Development of a High-Enthalpy Ground Test Facility for Shock-Layer Radiation



Peter Lyal Collen

University College

University of Oxford

A thesis submitted for the degree of

Doctor of Philosophy

Trinity 2021

Acknowledgements

First, a huge thank-you to my supervisor, Matthew McGilvray — for all of your efforts throughout the course of this thesis, for your ambitious targets, and for also showing up to the late nights and six-day weeks. You have taught me some valuable life lessons: to check new components actually fit *right away*, to always keep the beer fridge stocked,[1] and that choosing the beach house is always an option.

Secondly, I want to express my eternal gratitude to Luke Doherty for being — in the best possible way — the polar opposite of Matt. I especially need to thank Past Luke for his pain during construction of the tunnels and for answering my (hourly) annoying questions when I first started. You somehow managed to instil in me a level of attention-to-detail and precision which I never thought I'd have: I'm a better researcher and engineer for it.

To all of those in the (now huge) Hypersonics Group, thanks for making the last *mumblemumble* years so enjoyable. May we always remain 'Too Big to Fail'. Thanks especially to everyone who helped out with the various tunnel tasks and general moral boosts. Special mentions go to Chris Hambidge (for his 'really useful box' mentality), Matthew Satchell (for his conversations about shock tubes and development of the LASTA code), Seth 'The Floun-Dor' Wylie (for entertaining us with his identity crisis, and all the generosity), Rowlands (for being a great desk-buddy/teaching me hypersonics) and, of course, Alex 'Chai' Glenn (for selflessly pitching in during my final test campaign, staying positive and for his unwavering support of UK Garage Thursdays).

This thesis involved a vast amount of manufacture, technical expertise and administrative support — usually at short notice. Thanks to all the workshop guys (especially Dave, Leo, Dunc, Harry and James) for your awesome work and for bailing us out so many times. The same goes for Greg and Jason; I'm still impressed by your craftsmanship. I'm eternally indebted to the skills of Bill & Hal, for putting most of T6 together and for taking it apart when it *really* wanted to stay that way. Thanks also to Craig and Josh (putting all other IT support to shame with their competence), and to Kathryn, Alex and Anna for going the extra mile to keep everything running. For one last time: Sorry!

[1] And to actually own one in the first place...

The ‘Stand on the shoulders of giants’ quote is a cliché in academia; this is because it is entirely true. In particular, I would like to acknowledge Brett Cruden and Aaron Brandis at NASA Ames for their support, both in the form of their loan of the UV spectrometry equipment and their help and advice with the NEQAIR code. I am also grateful to the members of the Centre for Hypersonics at the University of Queensland, who have all provided so much expertise. I would especially like to thank Peter Jacobs, Richard Morgan, David Gildfind and Chris James for their help with the GDTk codes, advice on free-piston facilities and general sympathy for tunnel issues.

Finally, to my parents: for always supporting me in every way possible, for hosting me whilst I did the final write-up and for the constant supply of cakes as fuel. I’ll always remember our time together over these six months, and especially our attempts to circumnavigate the Glencree Valley mountain tops — we’ll get it done! I had been led to expect that the final few months of a doctorate (in a lockdown, no less) would be terrible, but I’ve genuinely had the best time. Thank you.

Abstract

This thesis details the establishment of a new, transient, high-enthalpy aerothermodynamic ground test facility at the University of Oxford: the T6 Stalker Tunnel. T6 is capable of operating as an expansion tube, reflected shock tunnel or in one of two high-enthalpy shock tube modes. This new facility was commissioned in each of these configurations, generating test conditions from 2.7 to 115.0 $\mathrm{MJ\,kg^{-1}}$. These correspond to trajectory points for a Mach 7 atmospheric flight condition and proposed Mars Sample Return missions. Overall, high-quality test flows were observed. This new facility now represents a unique resource within Europe for high-enthalpy aerothermodynamic ground testing.

The core aim of this work was to investigate 'radiative heating' effects. During planetary entry, the high-temperature gas around a return vehicle emits strong electromagnetic radiation, which can contribute significantly to surface heat flux. However, this heating mechanism is poorly understood, with high associated uncertainties.This thesis contributed to the resolution of this problem through development of a new mode of T6 — the Aluminium Shock Tube, or AST — which was designed specifically to investigate this phenomenon. The new mode was successfully commissioned; a thorough experimental assessment showed good comparison to computational predictions of performance and test time. Notably, the ability of the AST to achieve conditions of relevance for radiative heating in the atmospheres of Earth, Mars and Titan was demonstrated.

Utilising the new AST mode, shock-layer radiation experiments were undertaken from 7 $\mathrm{km\,s^{-1}}$ to 10 $\mathrm{km\,s^{-1}}$ in air. Using a newly developed dual-channel emission spectroscopy system, simultaneous measurements of spatially and spectrally resolved, absolute spectral radiance were made between 200 nm and 850 nm. These were performed at selected benchmark conditions from the literature to validate the new experimental results. In all cases, large extents of post-shock equilibrium were generated. In general, comparisons were favourable to the benchmark data from other facilities. Although some discrepancies were seen in comparison to numerical codes, these were consistent across the set of experimental data considered from all facilities. Reasons for these differences were proposed. The T6 AST is now one of the very few facilities in the world which has demonstrated the capability to produce validated shock-layer radiation data.

Lastly, a combined experimental-numerical study was undertaken to investigate the influence of shock deceleration on the measured post-shock radiance and electron density in shock tube experiments. This effect was conclusively shown to directly affect the measurement. The analysis was then extended to previous results from the NASA Electric Arc Shock Tube, thereby explaining historic discrepancies in that data.

Contents

List of Figures **xi**

List of Tables **xv**

Nomenclature **xvii**

1 Introduction **1**
1.1 Motivation . . . 1
1.1.1 The Radiative Heating Environment . . . 3
1.1.2 The Need for Ground Test Data . . . 7
1.2 Research Objectives . . . 10
1.3 Thesis Structure . . . 12

2 Literature Review **15**
2.1 Introduction . . . 15
2.2 Optical Diagnostics for High-Speed Flows . . . 16
2.2.1 Emission Techniques . . . 16
2.2.2 Laser Techniques . . . 22
2.3 Ground Testing for Shock-Layer Radiation . . . 24
2.3.1 Continuous Facilities . . . 24
2.3.2 Transient Facilities . . . 29
2.4 High-Enthalpy Shock Tube Facilities & Experiments . . . 35
2.4.1 Active Shock-Layer Radiation Facilities . . . 35
2.4.2 Shock Speed Variation Effects . . . 44
2.5 Summary . . . 49

3 Development & Commissioning of the T6 Stalker Tunnel **51**
3.0 Foreword . . . 51
3.1 Introduction . . . 52
3.2 Facility Overview . . . 53
3.2.1 The T6 Free-Piston Driver . . . 54
3.2.2 T6 Operating Mode Descriptions . . . 57
3.3 Free-Piston Driver Commissioning . . . 65

3.3.1 Driver Commissioning: Experimental Arrangement 65
3.3.2 Driver Commissioning: Results 67
3.4 Shock Tube Modes 70
3.4.1 Shock Tube Modes: Experimental Arrangement 70
3.4.2 Shock Tube Modes: SST Experimental Results 72
3.4.3 Shock Tube Modes: Facility Modelling 73
3.4.4 Shock Tube Modes: AST Experimental Results 77
3.5 Reflected Shock Tunnel Mode 79
3.5.1 Reflected Shock Tunnel Mode: Experimental Arrangement . . . 80
3.5.2 Reflected Shock Tunnel Mode: Experimental Results 81
3.6 Expansion Tube Mode 89
3.6.1 Expansion Tube Mode: Performance Envelope 90
3.6.2 Expansion Tube Mode: Experimental Arrangement 91
3.6.3 Expansion Tube Mode: Experimental Results 92
3.7 Conclusion 94

4 Aluminium Shock Tube Condition Development 97
4.1 Introduction 97
4.2 Aluminium Shock Tube Overview 98
4.2.1 Motivation for Development 98
4.2.2 Geometric and Experimental Design 102
4.2.3 Shock Speed Measurement 103
4.2.4 The Pitot Rake 104
4.2.5 Experimental Procedure 105
4.3 Facility Performance Envelope 108
4.3.1 A New High-Compression-Ratio Driver Condition 108
4.3.2 Tested Conditions 109
4.3.3 Ideal Performance Assessment 111
4.3.4 Nozzle Flow Discussion 111
4.4 Shock Tube Test Time Evaluation 115
4.4.1 Comparison of Test Time Determination Techniques 116
4.4.2 Test Time Assessment 121
4.5 Developed Conditions 123
4.5.1 Test Condition Facility Performance Assessment 126
4.6 Summary 128

5 Absolute Measurements of Air Shock-Layer Radiation 131
5.1 Introduction . . . 131
5.2 The Optical Emission Spectroscopy System . . . 132
5.2.1 General Arrangement . . . 132
5.2.2 Optical System Absolute Intensity Calibration . . . 136
5.2.3 Camera Triggering . . . 140
5.3 Spectral Comparison Methodology . . . 141
5.3.1 Definition of Shock-Layer Regions . . . 141
5.3.2 EAST Comparisons . . . 143
5.3.3 NEQAIR Simulations . . . 144
5.3.4 Spectral Fitting Routines . . . 146
5.3.5 Plasma Torch Comparison . . . 148
5.4 Condition I — Low Speed EAST Comparison . . . 149
5.4.1 Condition I: Equilibrium Comparison . . . 152
5.4.2 Condition I: Non-Equilibrium Comparison . . . 155
5.5 Condition II — Plasma Torch Test Case . . . 156
5.5.1 Condition II: Equilibrium Comparison . . . 158
5.5.2 Condition II: Non-Equilibrium Comparison . . . 164
5.6 Condition III — High Speed EAST Comparison . . . 165
5.6.1 Condition III: Equilibrium Comparison . . . 167
5.6.2 Condition III: Non-Equilibrium Comparison . . . 171
5.7 Summary . . . 171

6 On the Influence of Shock Speed Variation 175
6.1 Introduction . . . 175
6.2 Shock Speed Variation Condition Generation . . . 176
6.2.1 Mechanisms of Shock Speed Variation . . . 176
6.2.2 Condition Selection . . . 178
6.3 Spatial Radiance Variation . . . 180
6.3.1 Radiance Conditions . . . 181
6.3.2 Experimental Results . . . 182
6.3.3 LASTA-NEQAIR Coupling Methodology . . . 183
6.3.4 LASTA Radiance Results . . . 184
6.4 Shock Deceleration Effects on Test Slug Morphology . . . 186
6.4.1 Approach to Equilibrium . . . 187
6.4.2 Effect of Shock Deceleration Rate . . . 192
6.5 Electron Density Measurements . . . 194
6.5.1 Stark Broadening Methodology . . . 195
6.5.2 T6 Electron Density Experiments . . . 195
6.5.3 Revisiting EAST Electron Density Measurements . . . 200
6.6 Summary . . . 203

7 Conclusions & Recommendations 205
7.1 Conclusions and Contributions 206
7.1.1 A New Ground Test Facility 206
7.1.2 The Aluminium Shock Tube 206
7.1.3 Shock-Layer Radiation Experiments 207
7.1.4 Cross-Facility Comparisons 208
7.1.5 Shock Speed Variation Effects 208
7.2 Recommendations for Future Work 209
7.2.1 Facility Improvements 209
7.2.2 Further Work 215

Appendices

A Arrangement of Facility Infrastructure 221
A.1 Diagram Summary 221

B Spectroscopic Calibration & Uncertainty 223
B.1 Details of Calibration 223
B.1.1 Optical System Alignment and Characterisation 224
B.1.2 Absolute Intensity Calibration 229
B.2 Details of Uncertainty Analysis 235
B.2.1 Uncertainty Approach 235
B.2.2 Considered Uncertainties 236
B.3 Estimated Uncertainties 240
B.4 Summary 242

C Stark Broadening Approach 245
C.1 Line Broadening Considerations 245
C.1.1 Lorentzian Fitting Procedure 249
C.2 Stark Broadening: Uncertainty Quantification 249

References 253

List of Figures

1.1 Diagram of a blunt body during super-orbital atmospheric entry. 4
1.2 Computational analysis of radiative heating contribution to total peak heat flux for two vehicle nose radii during Earth entry. 7
1.3 Experimental results demonstrating an increase in shock-layer radiance at low velocity Martian entry conditions from the EAST and HVST facilities. 8

2.1 Image from testing of an MSR condition in the T6 ExT mode. 17
2.2 Diagram of the operation of a plasma wind tunnel. 25
2.3 Diagram of an inductive plasma torch OES experiment. 27
2.4 A radiating flow experiment in the X2 Expansion Tunnel 31
2.5 The NASA Electric Arc Shock Tube (EAST) facility 37
2.6 The JAXA Hyper-Velocity Shock Tube (HVST) facility. 40
2.7 Experimental arrangement for shock tube experiments in the X2 facility. 42
2.8 Diagram of the Mirels effect. 46
2.9 Diagram demonstrating the effect of shock deceleration on post-shock equilibrium in the EAST facility. 48

3.1 Selected mission trajectories and approximate ground test facility capabilities. 54
3.2 Performance comparison of common driver technologies. 55
3.3 Diagram showing the different T6 facility modes. 57
3.4 Distance-time diagrams of T6 facility modes. 59
3.5 Components used for T6 free-piston driver blank-off tests. 66
3.6 Representative results from free-piston blank-off tests with comparison to matched L1d3 model. 69
3.7 Performance predictions of T6 ST modes with air test gas, alongside Earth entry trajectories. 71
3.8 Finite opening time diaphragm simulations using L1d3 with comparison to experiment. 73
3.9 AST test data with comparison to numerical predictions. 78
3.10 Performance envelope of T6 in RST mode. 79
3.11 Pitot rake in the T6 test section with gauge positions labelled. 81

3.12 Shock speed comparison between shot T6s88 and the L1d3 prediction. . 82
3.13 Distance-time diagram of the L1d3 simulation of shot T6s88. 83
3.14 Nozzle supply pressure comparison between shot T6s88 and L1d3 prediction. 83
3.15 Stagnation-point heat flux using the DHTG compared to the analytic calculation. 84
3.16 Grid convergence analysis based on the mass-flow-weighted Mach number 87
3.17 Contour plot of the Mach number distribution for the T6 RST Mach 7 nozzle and test section flow-field. 87
3.18 Pitot-to-total pressure ratio comparison between shot T6s88 and axisymmetric CFD model. 88
3.19 Radial profiles of nozzle exit Mach number and static pressure. 89
3.20 Comparison of nozzle exit temperature distribution for the three thermochemistry models. 90
3.21 Comparison of proposed MSR Trajectories with T6 performance capability in ExT mode. 91
3.22 Experimental results for MSR expansion tube conditions. 93

4.1 Laminar Mirels analysis of large-diameter tube benefits. 101
4.2 Engineering drawing of the T6 AST. 106
4.3 T6 Aluminium Shock Tube tested conditions. 110
4.4 Comparison of measured AST performance with the ideal predictions. . 112
4.5 Comparison of shock timing station traces between the constant-diameter SST mode and the AST intermediate nozzle configuration. 113
4.6 Distance-time diagram of the AST nozzle region calculated using L1d3. 114
4.7 An example of the challenging nature of the AST testing environment. . 116
4.8 Comparison of shield and swirl cap geometries 117
4.9 Experimental Pitot rake data for two AST shots. 118
4.10 Example of test time assessment 122
4.11 Results from experimental assessment of facility test time 123
4.12 Measured shock speed variation for the selected test conditions. 127
4.13 Representative wall static and Pitot pressure measurements for the selected AST test conditions. 129

5.1 The optical emission spectroscopy systems used for the AST experiments. 133
5.2 Example of spatially and spectrally resolved, calibrated emission data . 139
5.3 Annotated experimental radiance plot for T6s186 142
5.4 Definition of nominal shock speed for T6 spectroscopy experiments . . 145
5.5 Data taken from Laux (1993) to enable NEQAIR comparison. 148
5.6 Emission results from the T6 AST at Condition I. 153

5.7 Comparison of experimental equilibrium spectral radiance between T6 and the predictions of NEQAIR for Condition I. 154
5.8 Excess radiance attributed to $N_2(1+)$ emission 156
5.9 Non-equilibrium metric comparison between T6 and EAST for Condition I. 157
5.10 Emission results from the T6 AST at Condition II. 159
5.11 Comparison of experimental equilibrium spectral radiance from T6 and the predictions of NEQAIR at Condition II. 160
5.12 Post-shock pressures measured at STS-15 for two Condition II shots. . . 161
5.13 Comparison of baseline and optimised NEQAIR spectrum with T6 experimental data at Condition II 162
5.14 Comparison of a NEQAIR with the plasma torch data of Laux (1993). . 164
5.15 NEM comparison between T6 shots at Condition II. 165
5.16 Emission results from the T6 AST at Condition III. 168
5.17 Comparison of experimental equilibrium spectral radiance between EAST, T6 and the predictions of NEQAIR at Condition III. 169
5.18 Comparison of the background continuum at equilibrium 170
5.19 NEM comparison between T6 and EAST at Condition III 172

6.1 The mechanisms used to vary the experimental shock speed profile. . . 179
6.2 The variation in equilibrium electron density with shock speed. 180
6.3 Measured shock speed variation for the SSV radiance test cases explored in this work 182
6.4 Experimental results of oxygen 777 nm multiplet emission for the radiance test cases. 183
6.5 Comparison of the experimentally-measured spatial variation in atomic oxygen radiance with the coupled NEQAIR/LASTA simulations 186
6.6 Investigation of SSV effects on the approach to equilibrium. 189
6.7 Numerical investigation of the influence of deceleration rate on the test slug length. 193
6.8 Measured shock speed variation for the T6 electron density measurements. 196
6.9 Experimental electron density results at the 0.1 Torr condition. 198
6.10 Experimental electron density results at the 0.2 Torr condition. 199
6.11 EAST shock speed profiles for electron density analysis. 201
6.12 Comparison between electron density measurements at EAST and the prediction of LASTA. 202

7.1 A microwave shock tracking system. 215

A.1 Infrastructure diagram of T6 in AST mode. 222

B.1 Summary of the spatial calibration arrangement and resulting image. . . 225

B.2 Comparison of measured and calculated line shapes for the AST OES systems. 228
B.3 Diagram of OES system calibration process above 300 nm. 231
B.4 Diagram of additional steps required to calibrate the Blue OES system below 300 nm. 232
B.5 Example error budget for the different stages of the calibration and shot data conversion processes. 240
B.6 Representative overall uncertainty in post-shock radiance. 242
B.7 Comparison of uncertainty as a function of wavelength. 243

C.1 An example of the measured and modelled instrument function used for Stark broadening measurements. 248

List of Tables

2.1 A comparison of high-enthalpy shock tube facilities. 36

3.1 Key dimensions of the T6 facility. 58
3.2 Developed T6 Driver Conditions. 67
3.3 L1d3 model tuning parameters to match blank-off data. 68
3.4 Flow properties of Mars Sample Return ExT conditions. 94

4.1 Comparison of T6 Driver Conditions C and C++ 109
4.2 Selected T6 Test Conditions. 126

5.1 Table of optical system characteristics used in this work. 137
5.2 Measured shock speeds for the T6 and EAST tests at Condition I 150
5.3 Measured shock speeds for the T6 tests reported at Condition II 157
5.4 Comparison of T6 Condition II equilibrium conditions to plasma torch parameters and nominal CEA values. 163
5.5 Measured shock speeds for the T6 and EAST tests at Condition III. . . . 166

6.1 Measured shock speed characteristics for the SSV radiance test cases. . 181
6.2 Measured shock speed characteristics for the SSV electron density cases. 197

B.1 Summary of the factors considered in the uncertainty analysis. 239

Nomenclature

Abbreviations

AST	Aluminium Shock Tube, an operating mode of T6.
CARS	Coherent Anti-Stokes Raman Spectroscopy.
CEA	Chemical Equilibrium with Applications, a computer program.
CFD	Computational Fluid Dynamics.
DHTG	Diamond Heat Transfer Gauge.
DLR	German Aerospace Center.
EAST	Electric Arc Shock Tube.
ESA	European Space Agency.
ESTCj	Equilibrium Shock Tube Calculator junior, a computer program.
ExT	Expansion Tube/Tunnel.
FOSTERS	Fast Oscillator Shock Timer Enabling Repeatable Spectroscopy.
FROSST	FRamework for Overset Simulation of Shock Tubes, a computer program.
FWHM	Full Width at Half Maximum.
HEG	High Enthalpy Shock Tunnel Göttingen.
HIEST	High Enthalpy Shock Tunnel.
HVST	Hypervelocity Shock Tube.
ICCD	Intensified Charge-Coupled Device, a camera technology.
ICP	Inductively-Coupled Plasma.
ILS	Instrument Line Shape.
IS	Integrating Sphere.
JAXA	Japanese Aerospace Exploration Agency.
LASTA	LAgrangian Shock Tube Analysis, a computer program.
LTE	Local Thermodynamic Equilibrium.
MCP	Micro-Channel Plate.
MSL	Mars Science Laboratory.

MSR	Mars Sample Return.
MWIR	Mid-Wave Infrared.
NASA	National Aeronautics and Space Administration.
NEM	Non-Equilibrium Metric.
NEQAIR	Non-EQuilibrium AIr Radiation, a computer program.
NIR	Near-Infrared.
NRST	Non-Reflected Shock Tube.
OES	Optical Emission Spectroscopy.
PWT	Plasma Wind Tunnel.
RST	Reflected Shock Tunnel.
sCMOS	scientific CMOS, a camera technology.
SNR	Signal-to-Noise Ratio.
SST	Steel Shock Tube, an operating mode of T6.
SSV	Shock Speed Variation.
ST	Shock Tube.
STS	Shock Timing Station.
TDLAS	Tunable Diode Laser Absorption Spectroscopy.
TPS	Thermal Protection System.
VUV	Vacuum Ultraviolet.

Latin Characters

A	Area, m^2
A_{ul}	Einstein Coefficient for Spontaneous Emission, s^{-1}
B	Background Signal, counts
C	Calibration Surface, counts $s^{-1}(W\,cm^{-2}\,sr^{-1}\,\mu m^{-1})^{-1}$
D	Diameter, m
D_{iris}	Aperture Diameter, mm
E	Camera Sensitivity, counts $electron^{-1}$
F	Intensifier Noise Factor, –
G	Camera Gain, electrons $photoelectron^{-1}$
H	Total Specific Enthalpy, $MJ\,kg^{-1}$
I	Calibration Source Spectral Radiance, $W\,cm^{-2}\,sr^{-1}\,\mu m^{-1}$
K_L	Launcher loss coefficient, –
K_a	Absolute Non-Equilibrium Metric, $W\,cm^{-2}\,sr^{-1}$

K_s	Spectral Non-Equilibrium Metric, $\mathrm{W\,cm^{-2}\,sr^{-1}\,\mu m^{-1}}$
L	Characteristic Length Scale, m
M	Molar Mass, $\mathrm{kg\,kmol^{-1}}$
M_s	Shock Mach Number, –
N	Number (of), –
P	Pressure, Pa
$R(x,\lambda)$	Spectral Radiance, $\mathrm{W\,cm^{-2}\,sr^{-1}\,\mu m^{-1}}$
S	Raw Camera Signal, counts
T	Temperature, K
U_{cs}	Conact Surface Speed, $\mathrm{km\,s^{-1}}$
U_{eq}	Flight-Equivalent Velocity, $\mathrm{km\,s^{-1}}$
U_s	Shock Speed, $\mathrm{km\,s^{-1}}$
V	Volume, $\mathrm{m^3}$
X	Generic Function Input, –
Y	Generic Function Output, –
$\mathscr{B}$	Rectangular/Boxcar Function, –
$\mathscr{G}$	Gaussian Function, –
$\mathscr{L}$	Lorentzian Function, –
$\mathscr{N}$	Principle Quantum Number
$\mathscr{R}$	Specific Gas Constant, $\mathrm{J\,kg^{-1}\,K^{-1}}$
c	Speed of Light, $\mathrm{m\,s^{-1}}$
d_i	Image Distance, mm
d_o	Object Distance, mm
f	Focal Length, mm
f_f	Piston friction factor, –
f_{wl}	Deuterium Lamp Wavelength Fit, –
f_x	Deuterium Lamp Spatial Fit, –
h	Static Specific Enthalpy, $\mathrm{MJ\,kg^{-1}}$
k	Opening Profile Exponent, –
m	Mass, kg
m_{GL}	Gaussian-Lorentzian Blending Parameter, –
$\dot{m}$	Mass Flow Rate, $\mathrm{kg\,s^{-1}}$
n	Number Density, $\mathrm{cm^{-3}}$
p	Pedestal Signal, counts
q_R	Radiative Heat Flux, $\mathrm{W\,m^{-2}}$
t	Time, s
v	Flow Velocity, $\mathrm{m\,s^{-1}}$
w	Line Width, nm
$w_{L,\alpha}$	Lorentzian Width Component of Hydrogen-α line, nm

x	Distance, m
CoC	Circle of Confusion, mm
FoV	Field of View, mm
Ma	Mach Number, –
T	Chai T-Factor, –
X	Mole Fraction, %
$\mathbf{\Delta U_s}$	Maximum Deviation of Shock Speed from Final Value, %

Greek Characters

Γ	Goulard Number, –
Λ	Compression Ratio, –
Ω	Solid Angle, sr
Θ	Image Rotation Angle, deg
β	Absolute Bias Limit, -
δ_{cs}	99 % Velocity Boundary Layer Thickness (at Contact Surface), mm
ε	Emission Coefficient, $\mathrm{W\,cm^{-3}\,sr^{-1}}$
γ	Ratio of Specific Heats, –
λ	Wavelength, nm
λ_0	Nominal Wavelength, nm
ρ	Density, $\mathrm{kg\,m^{-3}}$
σ	Absolute Precision Index, –
τ	Test Time, s

Subscripts

B	Rectangular/Boxcar
D	Doppler Broadening
$D2$	Deuterium Lamp Quantity
G	Gaussian
GL	Gaussian-Lorentzian
He	Helium
IS	Integrating Sphere Quantity
L	Lorentzian
N	Natural Broadening

P	Pressure Broadening
Res	Reservoir
SG	Smeared Gaussian
β	Bias Uncertainty
∞	Freestream
σ	Precision Uncertainty
avg	Averaged Quantity
c	Counts
cal	Calibration Quantity
e	Electron
exp	Experimentally Measured
f	Final Value
l	Lower State of Transition
m	Mean Value
n	Noise
nom	Nominal Value
p	Pitot Measurement
ph	Photons
r	Condition at Rupture
shk	Shock
sig	Signal
$source$	Calibration Source
t	Total Condition
u	Upper State of Transition
1	Driven Gas Initial Conditions
4	Driver Gas Conditions at Diaphragm Rupture
5	Acceleration Tube Initial Conditions
o	Diaphragm First Fully Open

I'm being quoted to introduce something, but I have no idea what it is and certainly don't endorse it.

— Randall Munroe, *xkcd #1942*

1 Introduction

Contents

1.1 Motivation **1**
1.2 Research Objectives **10**
1.3 Thesis Structure **12**

1.1 Motivation

There have been many reasons given as to why humanity should become a space-faring species. These range from the scientific (a better understanding of our Universe), to the economic (national employment creation and wider technology applicability) to the pessimistic (the diversification of humanity to protect against political or environmental catastrophe[1]). However, for many it is the idealogical argument — that to explore is a fundamental part of being human — that they find the most compelling. In the words of John F. Kennedy: *"Well, space is there, and we're going to climb it"*.

Whatever the ultimate motivation, the facts are these: in the coming decades, space travel will see significant change. The provision of space launch services is an industry already worth $13 billion, with significant further growth expected: a compound annual

[1] One day, there *could* be a 'Planet B'.

growth rate of 13 % is projected until 2027 (Fortune Business Insights, 2020), whilst the value of the space industry as a whole may reach $1 trillion by 2040 (Morgan Stanley, 2020). The rise in private launch providers has been identified as a major driver in this expansion. The increased competition and development of enabling technologies is driving down the cost of launches; mission viability is thus also increasing. Seven nations or political unions have now sent rovers to the moon, whilst in February 2021 three separate probes (from NASA, China and the United Arab Emirates) arrived at Mars in a single month (O'Callaghan, 2021).

Increased access-to-space has seen NASA develop its first national crewed launch capability in a decade, through the development of the Dragon capsule with SpaceX (Berger, 2020). The 'human element' of missions within the solar system is also seeing a resurgence: China is undertaking construction on a new space-station, Tianghe, which it aims to have operational by 2022 (Wall, 2021). The International Space Station has also seen repeated life extensions, with latest plans proposing its continued use until 2030 (Senate Committee on Commerce, Science & Transportation, 2019). Further afield, NASA and ESA have committed to send the first woman to the moon by 2024, with ambitions to have 'boots on Mars' by the middle of the following decade (NASA, 2020). As underpinning technologies are further proven, more challenging scientific missions are also either on-going or under serious consideration. Examples include atmospheric flight on other planets, such as the NASA Ingenuity and Dragonfly programmes (Witze, 2021), Mars Sample Return missions (discussed further in Chapter 3) and ESA proposals for 'Ice Giant' missions to Neptune and Uranus (ESTEC Concurrent Design Facility, 2019).

Fundamental to the success of each of these aspirations is the capability to enter a planetary atmosphere safely. The development cost of such programmes is extremely high[2] and the entry phase must be completed successfully on the very first attempt. This is especially critical in the case of crewed missions. However, our understanding of, and ability to predict, the aerothermodynamic heating environment for these missions — even for trajectories that were flown half a century ago — is still lacking (Gnoffo, 1999). Historically, this shortcoming has been addressed through increased thermal protection

[2]The recent Mars Perseverance mission cost $2.7 billion (Dreier, 2020).

system (TPS) design margins. However, as missions demand increased payload capability and undertake faster entries, the accuracy of vehicle heating predictions must similarly increase. Critical experimental and validation data for these problems has historically been sourced from ground test facilities. The capability of these must therefore also be expanded to enable improved reproduction of the flight environment for new missions.

Sections 1.1.1 and 1.1.2 give background on two key areas. The first describes the fundamental aspects of the flow around a vehicle during atmospheric entry, and highlights the importance of radiative heating mechanisms in particular. This section presents only the key physics which underpin the remainder of this thesis. For a full introduction to the topic, the reader is directed to the texts of Anderson Jr. (1989) and Park (1990).

The second section discusses the increasing requirement for ground test data, highlighting where large uncertainties may be found, and sets out the need for new ground test facilities for the study of these aerothermodynamic processes.

1.1.1 The Radiative Heating Environment

To remain in orbit, or to transit effectively between celestial bodies, space vehicles need to move at significant speeds. To land a vehicle on a planetary surface safely requires that essentially all of this relative velocity be removed before touch-down. Some of this can be achieved before entry (via extra-atmospheric braking manoeuvres) and then, once moving relatively slowly, with parachutes. However, the main deceleration phase for most missions involves using the blunt shape of the entry vehicle itself to generate large amounts of drag.

Atmospheric entry typically occurs at high velocities, in the range of $5\,\mathrm{km\,s^{-1}}$ to $10\,\mathrm{km\,s^{-1}}$. This is significantly faster than the speed of sound in the ambient gas, and so a strong bow shock forms ahead of the vehicle. Through this shock, the gas undergoes an irreversible compression process which significantly increases its static enthalpy and pressure. The latter allows deceleration of the vehicle, but the high temperatures result in large heat fluxes to the vehicle surface. Understanding this region of high temperature gas is the core aim of aerothermodynamic modelling for atmospheric entry.

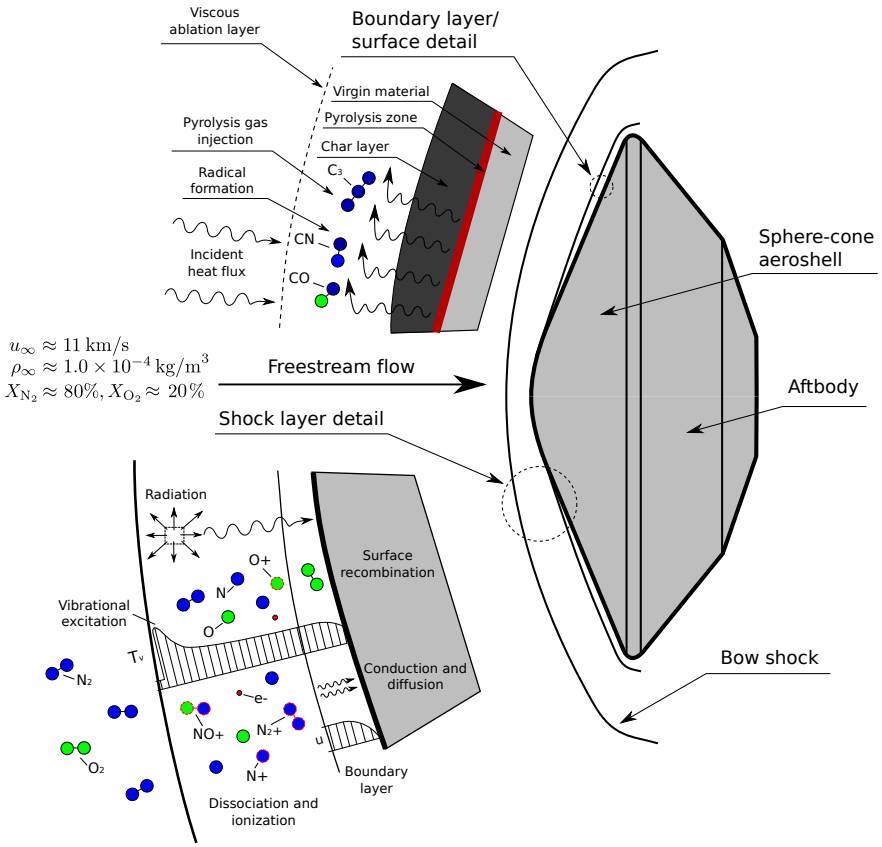


Figure 1.1 – Diagram of a blunt body during super-orbital atmospheric entry, with details of shock-layer and ablation processes shown (Potter, 2011).

For Lunar return trajectories, post-shock temperatures can be in excess of 10 000 K — twice the temperature of the surface of the sun. Under these conditions, the normal constituents of air (diatomic nitrogen and oxygen molecules) have enough energy to dissociate, forming atomic species and new radicals; notably NO. Electrons, usually fixed to orbits around heavier species, also gain sufficient energy to break free of these bonds. resulting in a significant degree of ionisation in the flow. The vehicle is thus sheathed in a high temperature plasma, which significantly changes the flow thermochemistry through electron-impact processes (Park, 1989) and can present barriers to communication during entry which are challenging to quantify (Ramjatan et al., 2020).

Although in most engineering applications the temperature is well defined, in high-enthalpy flows this is not always the case. Microscopically, the concept of ‘temperature’ is an expression of the distribution of internal energy states. At equilibrium, there is a linear relation between the energy of these states and the natural logarithm of their populations.

From a quantum perspective, all energy modes of a gas (the translational and electronic modes for atoms, and additionally rotational and vibrational for molecules) have discrete energy levels and can thus be assigned separate temperatures.

A characteristic of hypervelocity flight conditions is that the flow timescales become significant in comparison with the thermochemical reaction rates. These reactions occur in the flow due to collisions between gas particles. Danehy et al. (2013) give order-of-magnitude estimates for the number of collisions required for various processes of an O_2 molecule: 10 are required for the translational temperature to equilibrate, 20 000 for the vibrational energy mode and more than 200 000 for dissociation to occur. Consequently, when passing through the strong shock ahead of the entry vehicle, the translational temperature becomes very high as the kinetic energy of the species increases almost instantaneously. An initial thermochemical non-equilibrium state thus exists, which relaxes towards a thermal and chemical equilibrium at differing rates. This is also shown in Figure 1.1, where the vibration temperature is seen to decay to a steady state with sufficient distance behind the shock. Dissociation and ionisation are also identified in the shock-layer. For high-speed or high-altitude entries, significant portions of the flow-field may be in both thermal and chemical non-equilibrium.[3] Understanding and modelling these processes is thus essential to accurate prediction of the flow around these entry vehicles (Mitcheltree and Gnoffo, 1991).

In the post-shock flow, atomic and molecular excited states are continuously populated by collisions. This process must be balanced by a de-excitation mechanism: either through further collisions or via a radiative transition. In the latter case, the decay of an excited particle to a lower energy state results in the emission of strong electromagnetic radiation. Depending on the gas density, the wavelength of the radiation and the species present in the flow, this can be non-locally absorbed and re-emitted in different parts of the flow-field. An example of a radiating gas packet is also shown in Figure 1.1, where it can be seen that the gas emits in all directions. Some of this ‘shock-layer radiation’ is absorbed by the vehicle, contributing directly to the surface heat flux.

[3] That is, the internal energy distributions and/or species concentrations are still undergoing relaxation.

Historically, radiative heating has received less attention than that from convective sources. Whilst correlations for hypervelocity stagnation point convective heating have been long-established — notably in the works of Fay and Riddell (1958) and Sutton and Graves (1971) — the first engineering correlation for radiative heat flux was developed much later by Tauber and Sutton (1991). This correlation predicts a near-exponential rise in radiative heat flux above $9\,\mathrm{km\,s^{-1}}$, a trend which has been confirmed experimentally through data reduction of a large number of tests from the NASA Electric Arc Shock Tube facility in air by Brandis et al. (2017).

Figure 1.2 reproduces results of an analysis by Brandis and Johnston (2014) which examined the magnitude of this radiative heat flux in comparison to that from convective sources for two vehicles with nose radii of 1 m and 5 m. For the 1 m case, this analysis shows that the relative contribution of the radiative heating component to the overall vehicle peak heat flux increases quickly with flight velocity, becoming the dominant source after approximately $11.5\,\mathrm{km\,s^{-1}}$. The 5 m radius results show that radiative heating is even more significant for larger vehicles. Here, the majority of the heat flux is already due to radiative sources at $10\,\mathrm{km\,s^{-1}}$. This follows from a simple scaling analysis, where the volume of radiating gas ahead of the vehicle increases with L^3 but the surface area scales only with L^2. Crewed missions inherently require larger vehicles; better understanding of radiative heating will thus be crucial to their viability and success.

Although radiative heating is often considered a ‘high-speed’ phenomenon, the flight regimes in which it is important are highly dependent on the atmospheric composition. Computational analysis by Lino Da Silva and Beck (2011) and experimental measurements from Cruden et al. (2014) and Takayanagi et al. (2019) have shown that for Mars entries, a second radiative heat flux peak occurs around $3\,\mathrm{km\,s^{-1}}$. Their experimental data demonstrating this effect are reproduced in Figure 1.3. This additional radiative heating is due to high temperature, vibrationally-excited CO_2 which has not yet achieved sufficient energy to dissociate in large numbers. This heating mechanism was not originally considered for the Mars Science Laboratory entry in 2012, but was determined to a be a significant contributor to an excessive measured heating rate in the post-flight analysis by Cruden et al. (2015). For larger vehicles this mechanism is

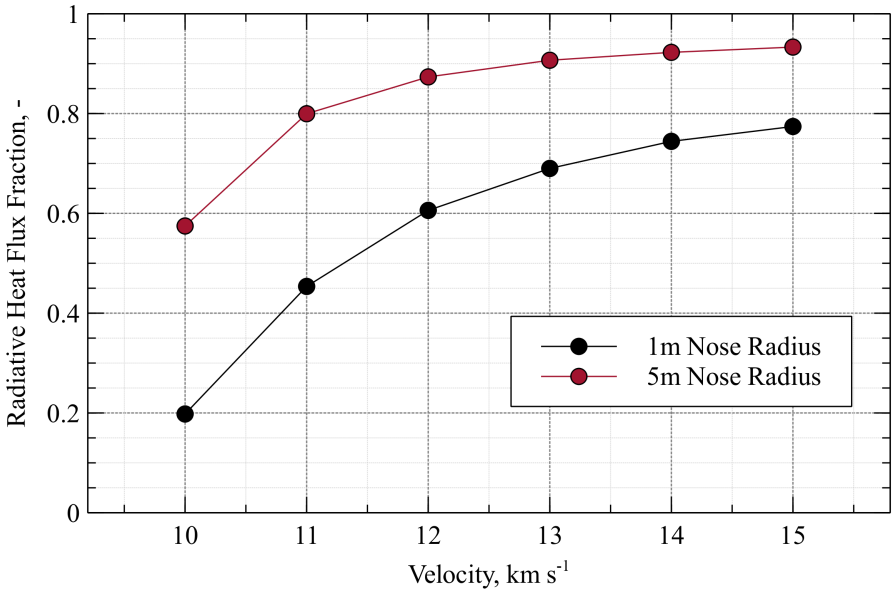


Figure 1.2 – Computational analysis of radiative heating contribution to total peak heat flux for two vehicle nose radii during Earth entry. Adapted from Brandis and Johnston (2014).

again anticipated to be the dominant source of vehicle heating at these speeds. Similar conclusions regarding the importance of radiative heating have been drawn for other atmospheres, with many studies notably undertaken for Titan entries (Olejniczak et al., 2003). These assessments further underscore the importance of accurate radiative heating predictions to future planetary exploration.

1.1.2 The Need for Ground Test Data

Despite the potential importance of radiative heating for the entry phase of many missions, the uncertainties in radiative heat flux are high. This directly impacts design margins and hence TPS mass. At the turn of the millennium, Gnoffo (1999) identified non-equilibrium radiation as a key future direction for NASA, citing uncertainties of over 100 % in some applications. Significant work has been undertaken in recent years to quantify this, notably by Brandis et al. (2015). Despite this, the uncertainty bounds on radiative heating predictions remain high: Cruden et al. (2018) identify velocities of around 9.5 km s^{-1} for Earth entry as particularly problematic, with uncertainties as high as 42 % and 69 % in the equilibrium and non-equilibrium regions respectively. They also note that an uncertainty cannot be assigned to equilibrium radiance (the largest contributor to vehicle radiative

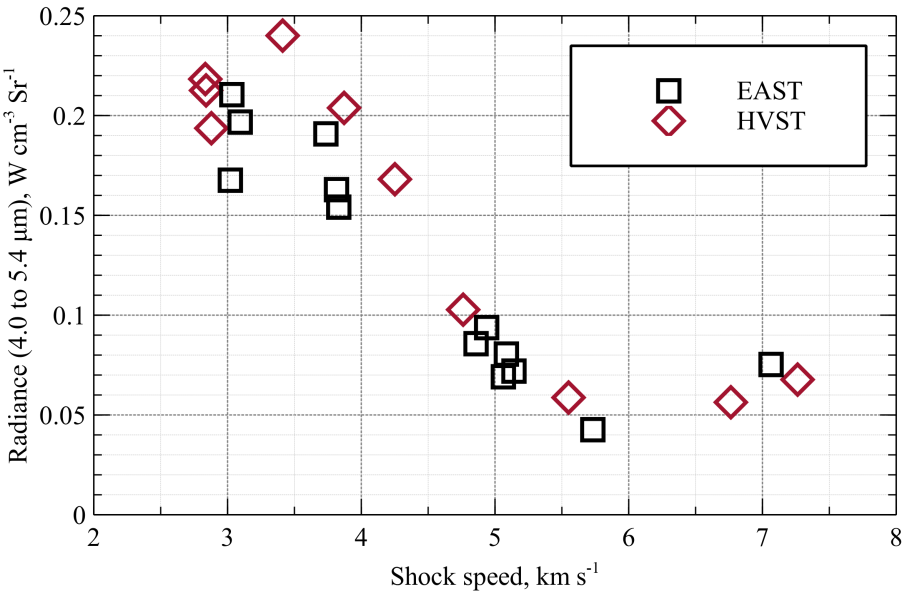


Figure 1.3 – Experimental results from the NASA EAST and JAXA HVST facilities, demonstrating a measured increase in shock-layer radiance at low velocity Martian entry conditions. Adapted from Takayanagi et al. (2019).

heat load for these conditions) below these speeds, due to difficulties in identifying the equilibrium region in the experimental data which forms the basis of the analysis. These conditions are commonly encountered during Lunar return.

The previously stated values apply just to stagnation-point radiative heat flux in air. Other cases have even greater uncertainty. Of particular note are high altitude Mars entries, to which Johnston et al. (2012) assign a bound of −78 % to 262 %. After-body radiation is also a recognised area of uncertainty: here, the flow expands around the vehicle shoulder and experiences thermochemical freezing. This region has presented a significant modelling challenge due to the coupling between radiation and highly non-equilibrium recombination mechanisms (Johnston and Brandis, 2015b). The wake of the vehicle thus consists of a large number of excited species which eventually decay radiatively. This wake can extend a large distance behind the vehicle, resulting in a large integrated heat flux (Brandis et al., 2020). West IV et al. (2017) estimate a radiative heating uncertainty bound of up to 125 % in this after-body region for Lunar return.

The preceding discussion has shown that radiative heating is a potentially large contributor to vehicle heat fluxes. However, development of accurate physical models

of this heating has proved challenging. In part, this is due to the coupling between a wide range of physical mechanisms, including compressible, hypersonic flow-fields, non-equilibrium thermochemistry and quantum theories of radiation (Johnston et al., 2013). As a result, different computational models can often show differences in excess of 100 %, especially in the case of complex molecules such as NO (Su et al., 2018) or CN (Brandis et al., 2014).

In terms of performing accurate measurements of vehicle heating, flight testing is the gold standard in experimental techniques. However, these programmes are exceedingly expensive and so are very rarely undertaken. Only a handful of flight test programmes relevant to atmospheric entry have flown in the past half century; notable examples for radiative heating include FIRE II, BSUV2 and Orion (Richardson, 1966; Erdman et al., 1993; Cruden and Brandis, 2019). It is more common for flight vehicles to carry some amount of diagnostic instrumentation to inform future aerothermodynamic predictions; these can include measurements of surface recession rates, embedded thermocouples or filtered spectrometers (Milos, 1997; Gazarik et al., 2008; Nelessen et al., 2019). However, in these cases the inclusion of additional instrumentation for the benefit of future design process must be balanced against the payload requirements of the current mission. Full datasets may also require prohibitive bandwidth to transmit during the actual entry; the vehicle therefore needs to survive the descent phase to receive the full benefits of the instrumentation (Gülhan et al., 2019).

Although flight testing provides actual measurements of vehicle heating through the trajectory, it has limitations. Referring again to Figure 1.1, it can be seen that a huge number of variables ultimately contribute to the measured heat flux. This includes non-equilibrium radiation, (possibly transitional) boundary layer influences, catalytic effects and heating augmentation due to ablation of the TPS ablative material, both by increasing surface roughness and by introducing radiating carbonaceous species into the flow (Hollis, 2012). Determining the contributions of each of these mechanisms in the post-flight analysis can present significant challenges (Cruden et al., 2015; Boyd and Jenniskens, 2010).

Ground-based testing offers an alternative means of generating high-quality validation data for computational tools and experimental predictions of vehicle heating. Test campaigns can be undertaken at a fraction of the cost of a flight test, and allow various geometric configurations and flow conditions to be explored. Advanced diagnostics, too complex for inclusion on a vehicle, can also be applied. This allows substantial de-risking of the vehicle design space. Whilst it is generally impossible to reproduce all of the relevant flow physics in one facility, this can be advantageous: fundamental mechanisms may be isolated and models developed based on these simplified test cases. The different types of ground testing options available for the study of shock-layer radiation are reviewed in detail in Chapter 2.

Finally, it is noted that several ESA-backed studies have highlighted the need for new European ground test capability to support future missions (Bugel et al., 2011; Reynier, 2016). Core capabilities which were identified as lacking included the ability to use non-air test gases, high speed aerothermodynamic testing, non-equilibrium thermochemistry and shock-layer radiation measurements. The latter was specifically highlighted, with no high-enthalpy shock tube facility currently extant on the continent. Furthermore, given the complexity of many atmospheric entry experiments, discrepancies are often found between experiment and modelling predictions, or even results from the same facility — for example, between numerical modelling, the NASA EAST and University of Queensland X2 facilities in the analysis of Brandis et al. (2019). Additional sources of ground test data can offer insight into these problems.

1.2 Research Objectives

The previous section demonstrated the importance of radiative heating for current and future mission proposals and the need for experimental data to inform and validate model development. Finally, the usefulness of ground testing and the specific opportunities for the development of a new European facility in the context of high-enthalpy flow experiments, and radiative heating, were identified.

Based on the above findings, four key objectives were defined for this thesis, as follows:

A. Develop & Commission a New, High-Enthalpy Ground Test Facility

Performing experimental studies of shock-layer radiation requires a suitable ground test facility. As the preceding survey showed, there was an identified requirement for such a capability within Europe. This need extended past the study of just shock-layer radiation to many other problems in high-enthalpy aerothermodynamics.

The first goal of this thesis is thus to develop and commission a new ground test facility, with capability of studying shock-layer radiation. This is to be achieved by commissioning T6 — a new high-enthalpy ground test facility capable of operating as a reflected shock tunnel, shock tube or expansion tube. This would provide a new source of ground test data for a wide range of atmospheric entry problems, addressing many of the previously identified gaps in European aerothermodynamic test capability.

B. Design & Characterise a Specific Facility Mode for Shock-Layer Radiation

The second objective of this thesis is to develop a new facility mode for T6, specifically for shock-layer radiation experiments. Known as the Aluminium Shock Tube, or AST, this mode will include features meant to maximise the quality of radiation experiments conducted within it. The design phase of this mode requires a performance assessment of the capabilities of the facility, as well as the development of test conditions to allow later benchmarking with other ground test facilities at flight-relevant conditions.

C. Perform Cross-Facility Comparison of Shock-Layer Radiation Experiments

Successful completion of the first two objectives would result in a ground test facility capable of reproducing conditions within the shock-layer of atmospheric entry vehicles. The third aim of this work is to establish non-intrusive optical techniques to measure the absolute emission from radiating air shock-layers. This data will then be compared directly to benchmark experimental measurements from other facilities and to numerical tools, thereby validating the results of the AST and demonstrating its utility for the study of shock-layer radiation.

D. Investigate Historic Ground Test Discrepancies

The final objective of this thesis is to extend the range of tested conditions to cover those where previous experimental measurements do not agree with predictions. Given the conclusions of Cruden et al. (2018) the equilibrium region of the shock-layer will be specifically targeted. This objective will either confirm a shortcoming in modelling approach (if the experimental results agree) or to highlight differences in the test conditions generated in different facilities (if they do not).

1.3 Thesis Structure

The remainder of this thesis consists of six further chapters, plus three appendices containing supplementary materials related to the main discussion. The contents of these are summarised below:

Chapter 2: Literature Review This chapter provides justification for the research pathway followed through the rest of this thesis. Different ground test facilities used for the study of shock-layer radiation are reviewed, as well various techniques for interrogating a high-enthalpy flow to determine thermochemical parameters of interest. Finally, shock tube experiments are reviewed in the context of super-orbital, high-enthalpy testing. This includes a summary of the current state-of-the-art in experimental results and an overview of the 'real-world' complexities inherent in these facilities.

Chapter 3: Development & Commissioning of the T6 Stalker Tunnel Achieving the research aims of this thesis required a means of reproducing flows normally experienced only during atmospheric entry. This chapter summarises the development and commissioning of T6, a new multi-mode, high enthalpy, transient ground test facility. After a short review of aerothermodynamic test facilities, commissioning tests of the driver section are discussed. Experimental data is then presented for each operating mode, with comparison made to numerical simulations. In general, high quality test flows are observed. The calculated enthalpy range of the experimental conditions achieved varies from $2.7\,\mathrm{MJ\,kg^{-1}}$ to $115.0\,\mathrm{MJ\,kg^{-1}}$.

Chapter 4: Aluminium Shock Tube Condition Development This chapter provides detailed information on the design and performance of a new T6 mode for shock-layer radiation studies. Whilst the Aluminium Shock Tube is discussed briefly in Chapter 3, here the aspects of its design and operation pertinent to the later shock-layer radiation experiments are detailed. The motivations for this mode's development are given, after which a performance assessment (in terms of achievable test conditions and usable test time) is undertaken. Finally, based on the facility operating envelope, test conditions for the benchmarking exercise of Chapter 5 are selected and the quality of their test flows analysed.

Chapter 5: Absolute Measurements of Air Shock-Layer Radiation With a new facility commissioned, novel operating mode developed and test conditions selected, Chapter 5 focuses on experimental measurements of shock-layer radiation in air. A description of the emission spectroscopy arrangement is first given, including specifics of the optical path. Experimental results from the selected test conditions are then given in the wavelength range 200 nm to 850 nm, spanning the ultraviolet to near-infrared regions of the electromagnetic spectrum. These results are shown to agree well with the benchmark datasets from other facilities and with the predictions of a computational radiation solver.

Chapter 6: On the Influence of Shock Speed Variation In this last core chapter, the benchmarked emission spectroscopy system is used to investigate the influence of the facility shock trajectory on the achieved test condition. The spatial variation of atomic line radiance through the shock-layer is measured for different shock speed profiles and compared with numerical predictions. This process is extended to determine spatial trends in electron density by measuring Stark broadening of the Balmer-α line of atomic hydrogen. It is shown that the shock trajectory is directly linked to the observed spatial trends, and that decelerating shock speed profiles result in radiative emission and electron densities in excess of equilibrium. Previously-published electron density measurements from the NASA EAST facility are then revisited and historic discrepancies in the measured data addressed.

Chapter 7: Conclusions & Recommendations Finally, the key findings from this thesis are summarised and assessed. Recommendations for further work are made, including suggestions for the improvement of the T6 facility, proposals for the enhancement of existing experiments and concepts for new avenues of investigation.

Appendix A: Arrangement of Facility Infrastructure The purpose of this appendix is provide a record of the arrangement of the T6 facility infrastructure during the first test campaign in Aluminium Shock Tube mode. This provides a comprehensive account of the experimental arrangement, with the relative positions of pressure gauges, vacuum pumps and gas mixture bottles shown.

Appendix B: Spectroscopic Calibration & Uncertainty This appendix contains complete details of the calibration process used for the emission spectroscopy measurements performed in this thesis. An uncertainty analysis of the spectroscopy measurement is also performed. The overall uncertainty is then assessed for the three main test conditions of Chapter 5.

Appendix C: Stark Broadening Approach The methodology used for extracting electron density using Stark Broadening is outlined in this appendix. A brief overview of line broadening mechanisms, an explanation of the approach taken in this thesis and an estimate of the uncertainty of the measurement are provided.

Everything in the world is exactly the same.

— Kanye West

2 Literature Review

Contents

2.1 Introduction 15
2.2 Optical Diagnostics for High-Speed Flows 16
2.3 Ground Testing for Shock-Layer Radiation 24
2.4 High-Enthalpy Shock Tube Facilities & Experiments 35
2.5 Summary 49

2.1 Introduction

The first chapter outlined the importance of radiative heating and chemical kinetics effects for space missions, the requirement for high-quality experimental results and the need for more ground test facilities to provide relevant data.

Here, the aim is to provide justification for the approach taken in the remainder of this thesis. Specifically, the different means of performing radiation measurements, as well as their advantages and disadvantages, are assessed. The different ground testing approaches for radiation are reviewed and the reasons why shock tube experiments were adopted highlighted. Finally, shock tubes in the context of high enthalpy testing are considered, reviewing both active facilities and non-ideal flow effects.

2.2 Optical Diagnostics for High-Speed Flows

Radiation is, by definition, an optical phenomenon; it therefore seems appropriate to study it optically. As discussed in Chapter 1, in a high-enthalpy flow the internal energy states of the constituent gas species are constantly excited through collisions with other particles. The qualities of radiative transport processes through the gas therefore allow inference of the thermodynamic properties and species concentrations in the flow (Levin, 2014). Optical diagnostics are also favourable as they are nonintrusive, therefore removing any influence of the measurement process on the flow-field. Here, optical diagnostics are divided into two main categories: emission techniques, which rely on the luminosity of the flow itself, and laser techniques, which require an external light source.

2.2.1 Emission Techniques

The ultimate motivation for the experiments in this thesis is that electromagnetic radiation from the hot post-shock gas ahead of a body during atmospheric entry can contribute significantly to the TPS heat load. Whilst this is inconvenient for vehicle designers, the inherent radiative nature of the flow enables meaningful analysis to be performed using emission-based methods. This is advantageous as these measurements are typically easier to set-up and cover a much wider range of the electromagnetic spectrum than laser techniques.

Figure 2.1 shows an image of a 15 km s^{-1} Mars Sample Return test in the T6 expansion tube mode. This is a single frame from a high-speed camera, using a frame-rate of 2 MHz and exposure time of 100 ns. The post-shock flow is seen to exhibit significant luminosity, even at these short gating times. It is this characteristic of high-enthalpy ground testing that makes it so tractable to emission-based approaches.

Here, emission measurement methods are split into two broad categories: those that measure spectrally-integrated radiance from the flow, and those that distinguish the contributions of different wavelength regions.

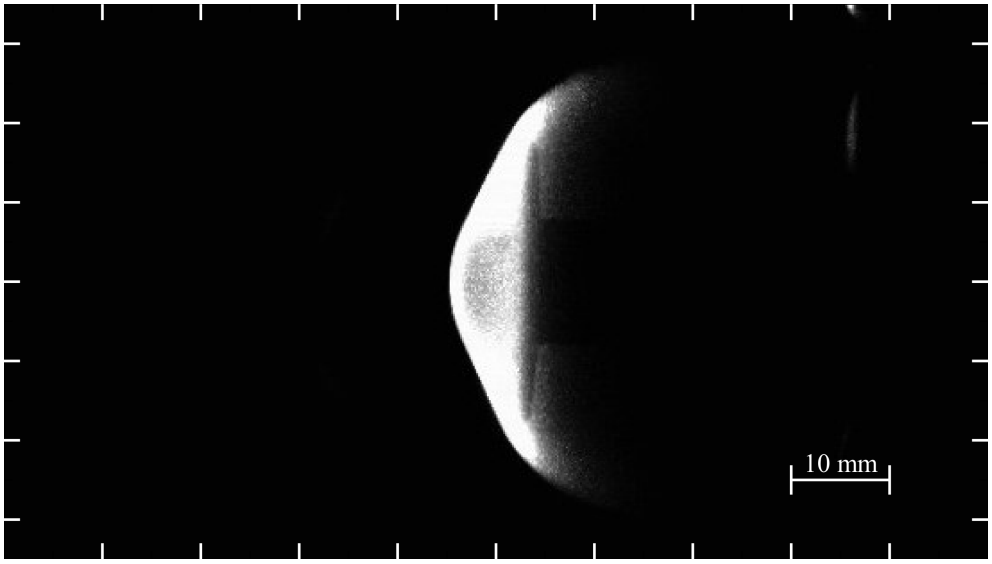


Figure 2.1 – Image from testing of an additively-manufactured aeroshell geometry at a 15 km s^{-1} Mars Sample Return condition in the T6 Expansion Tube mode. Flow is from left to right.

Spectrally-Integrated Techniques

The image of Figure 2.1 is an example of a spectrally-integrated technique, wherein radiation across the entire sensitivity range of the detector is collected. Typically, fully integrated camera measurements such as this are largely qualitative, allowing for flow visualisation (e.g. Zander et al., 2014) or test time evaluation (James et al., 2018a). However, more quantitative analysis can also be performed. For example, high-speed imaging measurements of shock stand-off distance have been used to assess free-stream non-equilibrium (MacLean et al., 2013). Takayanagi et al. (2017) has also used global imaging methods such as this to determine the distribution of mid-wave infrared radiation of CO_2 around a Martian aeroshell in an expansion tube.

Simpler even than camera imaging is the use of photodiodes. These are essentially single-pixel optical detectors with high gain and response times — 1 ns rise time devices are commonly available. Coupled to a focusing optic, the photodiode can be used to perform intensity measurements along a line-of-sight through the flow-field. In the work of Fujita et al. (2002), photodiodes are used to measure the spatial variation of emission behind a moving shock wave. This, coupled with a single spectrally-resolved measurement, ensures that the higher-resolution technique is located in the valid test flow region. The extent and magnitude of post-shock equilibrium can also be assessed.

Photodiodes are also useful in the characterisation of ground test facility performance due to their short rise times. James et al. (2019b) has developed optical methods for shock speed measurement using flush-mounted fibre-optic cables in the wall of an expansion tube; they are also useful for triggering of other experimental measurements such as fast-gated spectroscopic cameras.

Of perhaps greater utility than simple imaging methods is the use of spectral filtering to record only specific wavelength regions. In the thesis of Capra (2007), thin film gauges were placed behind optical windows of differing materials to determine the radiative heat flux on a scaled model of the Titan Explorer vehicle. These required replacement after every run due to the harsh testing environment. Further work by Tanno et al. (2015) used this approach during investigation of unexplained heat flux augmentation in the HIEST reflected shock tunnel at Apollo entry conditions. Here, thermocouples were mounted both on the model surface and behind flush-mounted windows set into the model. By examining the difference between the windowed and exposed gauges an estimate of radiative heat flux was made. Windows of differing transmissivity were also used to isolate the influence of different wavelength regions.

Generally, optical windows have wide transmission ranges. High quality optical filters can have full width at half maximum (FWHM) on the order of 1 nm, meaning that specific spectral features in the flow can be isolated. Many authors have coupled photodiodes to such filters. For example, Taylor et al. (1967) used an infrared arrangement to measure the radiative emission of the axisymmetric stretching mode of CO_2 behind a normal shock at Martian entry conditions in a shock tube. This method is particularly useful where specific wavelength regions are expected to be dominated by a single spectral feature of interest which changes rapidly throughout the test period; for example, in combustion (Kamel et al., 1995). The filtering technique can also be extended to two-dimensional imaging: James et al. (2018a) showed that test time in expansion tubes could be assessed across the entire core flow simultaneously by measuring the qualitative emission of atomic oxygen. Furthermore, Fahy (2016) used a range of bandpass filters to measure emission of several nitrogen and oxygen multiplets around scaled models of Hayabusa and Stardust aeroshells. Here, the optical system was fully calibrated, therefore allowing quantitative

measurement of absolute shock-layer emission and later comparison to computational fluid dynamic (CFD) simulations. Simultaneous use of several spectral filters can also be employed to perform spectroscopic analysis techniques: for example, Zander et al. (2017) determined the two-dimensional temperature distribution of a CO_2 plasma jet through measurement of atomic oxygen and carbon features. This work has recently been extended by Eberhart and Loehle (2019) to use a plenoptic camera with filtered imaging, allowing reconstruction of the distribution of atomic oxygen emission in a three-dimensional, high-enthalpy flow-field.

Optical Emission Spectroscopy

While spectrally-integrated measurements provide several advantages, the emission is not resolved as a function of wavelength. More complex spectroscopic analysis, as well as other assessments (such as identifying contaminants in the flow) requires that this be done.

By far the most common optical diagnostic used in high-enthalpy flow measurements is Optical Emission Spectroscopy (OES), where a spectrograph is used to provide spectral differentiation. Thorne et al. (1999) gives an excellent overview of this method. In summary: incident light is separated by wavelength by either refraction through a prism or, more commonly in research-grade instruments, diffraction from a ruled grating. This causes the outgoing light to be distributed spatially according to its wavelength. A detector array placed at the outlet of the instrument will thus register signal from different parts of the electromagnetic spectrum across its extent. Generally, the size of the detector is fixed and hence there is a trade-off between the bandpass of the measurement (i.e. the range of wavelengths measured) and the resolution. Low resolution measurements allow regions on the order of hundreds of nanometres to be observed simultaneously. In contrast, a high resolution measurement allows identification of finer spectral features, such as rotational lines of molecules. It should also be noted that this reduces the signal intensity, as the same amount of energy is spread across more pixels.

Emission spectroscopy can be used in combination with fibre-optic cables to provide a spectrally-resolved measurement at a single spatial location.[1] For example, Raiche and

[1] As with photodiodes, it should be remembered that this is a line-of-sight integration through the flow-field.

Driver (2004) used this technique to probe across the bow-shock of several test models in an arc-jet, allowing measurement of the comparative emission magnitudes of the stagnated air in the flow and the ablative species from the model to be made. Fibres can also be mounted within sufficiently large models; again in an arc jet, Winter et al. (2019) has measured the radiative heat flux incident on a test model and compared this to the convective heating. On-board OES measurements of radiative heat flux have also recently been performed in HIEST to determine the source of unexpected heating augmentations Cruden et al. (2021). In the recent work of Leibowitz (2020), an MSL geometry was instrumented with fibre-optics at different viewing angles — including on the back-shell. This was tested in both an expansion tube and reflected shock tunnel, and allowed direct measurement of wall-directed radiative heat flux on the model. This work also noted the coupling between the facility flow-field and the collection volume of the optical fibre, requiring computational rebuilding to determine the contribution of the boundary layer and nozzle expansion fan to match the experimental measurement.

A system of external optics can be used to map a linear region of the flow-field onto the slit of the spectrograph. This results in a spectrally-resolved measurement at each point on the slit. If a two-dimensional detector (i.e. a camera sensor) is coupled to the spectrograph, this allows simultaneous one-dimensional spatial resolution. This is known as an 'imaging spectrometer' arrangement. A full review of this widely-used technique is not attempted here, but some instructive examples in the context of shock-layer radiation are provided:

At NASA Ames, the EAST facility features four imaging OES systems, which allow simultaneous measurement from the vacuum ultraviolet to the near infrared. The spatial dimension is used to determine flow-field variations perpendicular to a normal shock (Greenberg et al., 2009). In model-based tests, radiation from different sections of the flow-field can be interrogated. Stagnation-line measurements are common e.g. Sasoh et al. (2001) and Sheikh et al. (2012), but other regions such as cross-sections of expansion fans (Wei, 2017) and the path of ablation products (Lewis et al., 2016) have also been probed. Imaging arrangements have also been used to observe actual re-entry of flight vehicles (Buttsworth et al., 2013), which has then been repeated in ground-based testing for comparison (Fahy et al., 2016).

Although in general a dichotomy exists between spectrometer bandpass and spectral resolution, echelle spectrographs avoid this issue. By utilising the entire two-dimensional array of a camera, higher-order diffractions can be used to measure significant bandpasses at high resolution. The disadvantage of this method lies in its use of the whole camera sensor for the spectral measurement, meaning that only one spatial location is measured (via a fibre-optic). This is particularly suited for continuous high-enthalpy facilities, where the fibre can be translated to measure different portions of the flow. For example, Loehle et al. (2016b) has demonstrated the applicability of this method in a plasma wind tunnel over the wavelength range 250 nm to 880 nm, achieving significant improvements in spectral resolution.

Using the measured emission spectrum, a wide range of spectroscopic analysis techniques can be used to extract key quantities of the flow. An excellent overview of some of the possibilities is given in the text of Griem (2005). In the case of flows related to atmospheric entry, the thesis of Laux (1993) applies many common techniques. For example, relative intensities of molecular and atomic features were used to extract (Boltzmann) vibrational and excitation temperatures. The optical system was also calibrated for absolute spectral radiance, allowing estimation of species number densities and direct comparison to numerical tools.

In the case of non-equilibrium flows, the wide spectral bandpass of OES is particularly useful. For air radiation, many excited upper atomic states of oxygen and nitrogen lie in the near infrared region over a range on the order of hundreds of nanometres. Using a sufficiently coarse grating, these can all be measured concurrently (see, for example, Hermann et al., 2016). The population of each excited upper state can thus be extracted, and compared to a Boltzmann distribution at varying temperatures. In the case of more complex thermochemical non-equilibrium, spectral fitting can be used; in the work of Tibère-Inglesse et al. (2018) the overpopulation of molecular nitrogen states was determined by fitting of the measured emission spectrum in a recombining air plasma. This has also been performed by several other authors in shock tubes and expansion tunnels e.g. Brandis and Cruden (2018), Yanes and Austin (2019), and Pannier and Laux (2019).

2.2.2 Laser Techniques

The techniques discussed up to this point relied on the self-emission of the high temperature test gas. In contrast, absorption methods use a secondary light source (typically a laser) to probe the flow. One of the most common laser techniques in use in high-enthalpy ground testing is tunable diode laser absorption spectroscopy (TDLAS). In this technique, a variable-wavelength laser is used to scan a relatively small portion of the electromagnetic spectrum in high resolution. The laser has a finite scanning rate, and so for high-speed flow experiments a balance must be typically struck between measurement frequency and bandwidth. TDLAS is a popular choice due to its simplicity (in comparison to other laser techniques) and relatively low cost in comparison to other systems. The technology is sufficiently robust to have been used as in-flight instrumentation for high-speed flight experiments (Kurtz et al., 2015). The tunable nature of the laser also allows the same system to be applied to a wider range of problems, thereby providing increased versatility in a single system (Krishna et al., 2016).

There are two key advantages of absorption spectroscopy over emission methods. First, the high spectral resolution of the laser allows detailed measurements of absorption line shapes to be made. The degree of line broadening can be used to assess various properties of the flow; for example, the Doppler width can be used to assess the translational temperature. This can be done to very low temperatures with reasonable accuracy: Parker et al. (2006) has characterised the free-stream of a reflected shock tunnel using this method, at a measured temperature of 190 K. Vibrational and rotational temperatures can also be characterised from measurement of molecular features, although in some cases more than one light source may be required (Allen and Kessler, 1996).

The second benefit of absorption spectroscopy is that species concentrations can be directly or indirectly measured. Even at the very high temperatures typical of re-entry, the vast majority of particles of a particular species are in the ground state (Danehy et al., 2013). As discussed in Section 5.3.3, the emission signal is proportional to the upper state of a particular transition. In contrast, absorption involves the excitation of populations from the lower state, and so if a light source of the correct wavelength can be used the ground state population can be directly measured. Species concentrations of

N_2, O_2, NO, N and O are measurable using absorption spectroscopy (Sharma and Park, 1990). Furthermore, in the case of low species concentrations multi-pass methods, such as cavity ring-down spectroscopy, can be used; this has been successfully demonstrated for the measurement of N_2+ number densities in non-equilibrium nitrogen arcs, as well as plasma torches (Yalin et al., 2002; Laux et al., 2003). Forbidden transitions, which are not observed in emission, are also accessible through absorption methods (Matsui and Morita, 2021). Finally, combinations of emission spectroscopy and TDLAS absorption have been used for the measurement of CO and CO_2 number densities in Martian gas mixtures (Danehy et al., 2013; Lin et al., 2013) Notably, this has been performed at the NASA EAST facility (see Section 2.4.1) in the work of MacDonald et al. (2018), wherein concurrent measurement of CO number density and translational temperature could be made with TDLAS. The excitation temperature could then be inferred from fitting of the simultaneous emission spectroscopy measurement, thereby giving a direct assessment of thermal non-equilibrium in the shock-layer.

From the baseline of TDLAS, absorption and laser diagnostics of essentially arbitrary complexity can be chosen to target specific attributes of the flow-field.[2] Danehy et al. (2013) provides a full and thorough review of molecular-based optical diagnostics for non-equilibrium hypersonic flows. The reader is directed there for a full review of different absorption methods and their applications. Here, a very broad overview of the key considerations for this work is outlined:

The major advantage to advanced laser techniques is their specificity. They allow direct measurements of translational, vibrational and rotational temperatures and species concentrations, as well as other flow properties, such as pressure. In some methods, these can be extracted simultaneously. Many of these are also point-based techniques, avoiding non-uniform flow features such as expansion fans near models or boundary layers. Conversely, higher spatial dimension measurements can be made using laser fluorescence methods. For example, Le Page et al. (2020) used laser sheet illumination to measure NO concentrations in a highly non-equilibrium expanding shock tunnel flow.

[2]Coherent Anti-Stokes Raman Spectroscopy (CARS) is an excellent example of this, with just some variants being BB-CARS, DBB-CARS, DPDB-CARS, SIDE-CARS, FAST-CARS, ULTRAFAST-CARS and BOX-CARS (Roy et al., 2010).

From the perspective of commissioning a new facility, a key disadvantage to advanced laser techniques is their specificity. In practice, these methods are best at determining a specific flow quantity of interest; often there are few other means of extracting this information. However — given the wide range of spectral features measured simultaneously using OES — emission measurements lend themselves better to the characterisation of a new facility. With OES, many radiating features and the spatial extent of the test flow can be simultaneously assessed. Furthermore, the financial cost of laser systems can be very high, as can the time required to establish them; in the same review, Danehy et al. (2013) comment that CARS techniques can take in excess of a year to apply properly. Given the recent development of T6, and hence the need for general characterisation, these techniques have not been investigated further at this time.

2.3 Ground Testing for Shock-Layer Radiation

A necessary requirement for a ground test facility which aims to study shock-layer radiation effects is that the total enthalpy of the flow be matched. While clearly of great import for all aerothermodynamic testing, it is especially critical for shock-layer radiation, given the strong dependence of radiation magnitude on flow temperature (Tauber and Sutton, 1991). Whilst many types of facility are capable of operating at total temperatures greater than atmospheric, only those useful for studying shock-layer radiation are considered further here. It should also be noted that this review approaches the types of facilities from the perspective of radiative heating studies specifically; a more general overview of the operation and use of the transient facilities is given in Chapter 3.

2.3.1 Continuous Facilities

As discussed in detail in Chapter 3 and reflected by Figure 3.1, continuous facilities are generally not capable of reproducing the hypersonic flight environment. As a result, when these facilities are used for the investigation of high-enthalpy effects the Mach number and/or total pressure of the resulting flow is typically limited. Nonetheless, useful data relevant to the problem of shock-layer can be generated. Here, two categories of continuous facilities are considered: plasma wind tunnels and plasma torches.

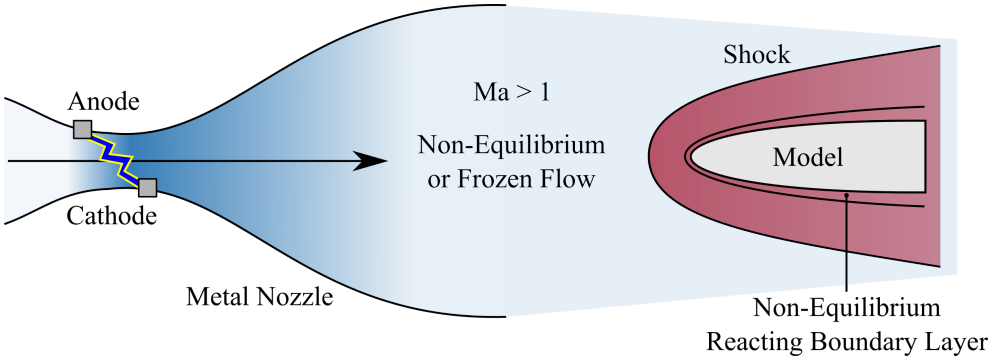


Figure 2.2 – Diagram of the operation of a plasma wind tunnel. Adapted from Marschall and Fletcher (2010). The case shown is supersonic; subsonic conditions are also common.

Plasma Wind Tunnels

Figure 2.2 shows a schematic of the operation of a plasma wind tunnel (PWT). In a PWT, cold test gas is fed through a plenum region, where it undergoes a heating process. The mechanism by which this heating occurs varies, but the most common is to use an electrical arc between an anode and cathode in the nozzle to increase the test gas enthalpy (Smith et al., 1998). The high temperatures and long run times mean significant cooling is required. Ablation of the materials within the nozzle also often occurs, to the extent that the level of free-stream impurities is a common metric used for comparison of these facilities. This is particularly pronounced for Huels (vortex-stabilised) designs, which show excessive erosion of all components as enthalpies are increased. Loehle et al. (2016a) provide a recent review of state-of-the-art PWT arrangements, highlighting that RF and magnetoplasmadynamic configurations offer the best flow purity and highest enthalpy capability, although they are limited in their total pressure range to approximately 5 kPa–10 kPa. As a result, the plasma flow and model are contained within a large vacuum vessel; the mass flow of the test gas must thus be low enough to be continuously removed by the facility vacuum pumping system.

The primary goal for the development of PWTs was historically for measuring stagnation-point heat flux rates, and for TPS performance assessment. Given the high static enthalpy of the test flow as it leaves the nozzle, the flow Mach number is not matched to flight; in many cases, it is subsonic. As a result, scaling of test conditions to flight is typically done based on the concept of local heat transfer simulation (Kolesnikov,

1999). This approach duplicates the boundary layer on the front of a vehicle using the static enthalpy, the velocity gradient at the boundary layer edge, and the stagnation pressure. This has been shown to reproduce the boundary layer and heat flux rates well for many standard geometries, although this is only strictly valid for convective heating (Loehle et al., 2018).

The low free-stream Mach number of a PWT flow means that the non-equilibrium region of the shock layer is not reproduced. In addition, work by Hermann et al. (2016) showed that there is a significant degree of non-equilibrium in the free-stream, with many atomic species exhibiting non-Boltzmann distributions of internal energy states. Free-stream unsteadiness was also observed due to the arc-attachment process. However, despite low total pressures it has been shown by Hermann et al. (2017) that near-equilibrium conditions can be achieved in the shock-layer, suggesting that these facilities can be used to measure shock-layer radiation away from the initial non-equilibrium peak. Indeed, given the challenges in generating sufficient test times at very low free-stream pressures in transient facilities (see Section 2.4.1), these tunnels may present the best means of studying equilibrium radiative heating at these altitudes. Specifically, the long run times allow extended camera exposures to be used, therefore allowing integration of the radiation signal over periods of minutes.

A final advantage of PWTs from the perspective of radiative heating is that they produce realistic heat fluxes and representative wall boundary layers. This means they can study coupled radiative heating effects related to the model itself. The heritage of PWT use for TPS development means they can create realistic wall temperatures, resulting in ablation of the model material. The presence of carbonaceous species in the flow has been shown to augment radiative heating effects in flight (Johnston et al., 2009) and can be studied for essentially any material in a PWT. This is typically done by comparing heating measurements using cooled and ablative probes (e.g. Loehle et al., 2014). In many super-orbital entries, the emission from the vacuum ultra-violet region (below approximately 200 nm) is the greatest source of radiative heat flux. However, this emission can be significantly absorbed by the colder gas near the wall; the boundary layer mass fractions thus directly influence the fraction of the radiative heat flux which

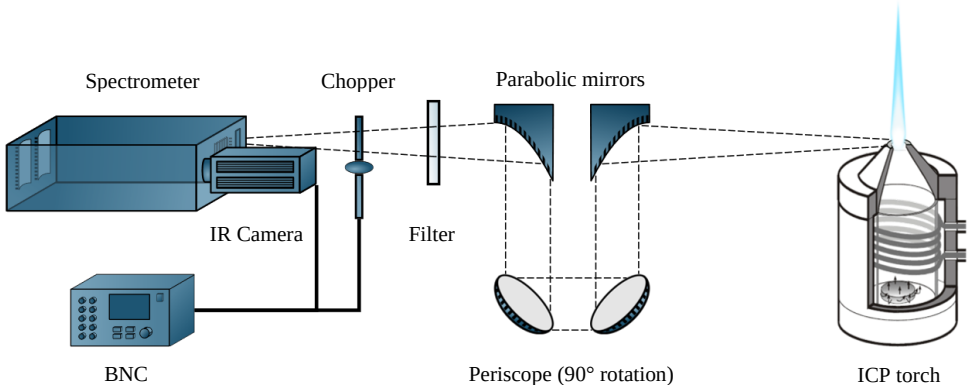


Figure 2.3 – Diagram of an inductive plasma torch OES experiment (Grimaldi et al., 2021).

actually affects the vehicle. Hermann et al. (2016) showed that this boundary layer profile could be measured using optical techniques in a PWT, thus allowing the estimations of the transmitted radiative heat flux to be made.

Inductively-Coupled Plasma Torches

The principle of an inductively-coupled plasma (ICP) torch is broadly similar to that of a PWT: a test gas is injected into a vessel, heated and then expelled through a nozzle. First proposed as a means of generating flows for spectroscopic analysis by Reed (1961), these torches have an advantage in that the plasma is generated by an inductive process, wherein the rapid oscillation of a magnetic field is used to accelerate free electrons. These fast-moving electrons cause further ionisation through collisions with heavier particles, which also increases their temperature. Eventually, a sufficient electron density is reached and the plasma becomes self-sustaining. This approach has an advantage over capacitive arc-heated PWT designs in that there are no metallic components exposed to the free-stream; instead, the flow travels through a magnetically-permeable quartz tube, maintaining flow purity. Various injector geometries are also used to promote mixing of the test gas, ensuring flow uniformity (McGuire et al., 2020). A diagram of a typical atmospheric plasma torch is given in Figure 2.3.

In general, the plasma torches used in research settings are comparatively small, with jet diameters on the order of 50 mm. The flow is also fundamentally subsonic; whilst flow velocities can be on the order of 1 km s^{-1} (Tibère-Inglesse et al., 2018), the high static

enthalpy prevents significant Mach numbers from being achieved. Because the torch exhausts to atmosphere, the total pressure is also fixed. These three factors combined mean that atmospheric plasma torches are not used for model testing, although some TPS and ablation work have been undertaken (MacDonald et al., 2015; Löhle et al., 2010). Larger versions of this technology have also been incorporated into PWT operation, with notable benefits for studies of catalytic effects (Loehle et al., 2016a).

In the context of shock-layer radiation, plasma torches can provide useful data. The high pressure of the jet results in a flow which is very close to equilibrium, which is useful for validating radiation models. For atmospheric entry, the work of Laux (1993) is often cited. His thesis extensively characterised the thermochemical state of an air plasma torch condition. This characterised flow was then used to substantially upgrade the NEQAIR2 radiation code in the ultraviolet to near-infrared regions. Since then, there have been extensions of this technique to other planetary atmospheres, such as Mars (McGuire et al., 2020) and Titan (Vacher et al., 2009). Gases can also be studied in isolation to investigate their specific properties; nitrogen has received significant attention (Yalin et al., 2002). The continuous nature of the design also permits very long exposures to be used, thereby allowing measurements of spectral regions with low signal-to-noise. Fine resolution spectra can also be measured by gradually transitioning the central wavelength of the instrument, allowing many spectroscopic fitting techniques (e.g. to extract rotational temperatures) to be used with narrow uncertainty bounds.

One disadvantage of the ICP arrangement is the relatively small diameter — this requires an axisymmetric characterisation of the temperature and species profiles throughout the flow-field, and complicates comparison of the spectra to other facilities and tools. The nature of the plasma torch also means that there is no shock front present in the flow, and as such no features of the post-shock non-equilibrium region can be investigated. This includes finite-rate radiative emission and thermochemistry. However, recent work by Tibère-Inglesse et al. (2018) has shown the potential for investigating recombining flows in a plasma torch. Here, a water-cooled tube of varying lengths is fitted to the outlet of the torch. The plasma undergoes recombination in the tube, and by measuring the emission at the outlet a determination of the degree of non-equilibrium in the flow

can be made. This suggests significant application of plasma torches as fundamental test cases for the problem of afterbody radiative heating. This is doubly true, as the initial equilibrium state of the plasma can be well characterised; this is a prerequisite for determining later recombination rates.

2.3.2 Transient Facilities

In the previous section, continuous facilities with application to the problem of shock-layer radiation were considered. In summary, it can be concluded that such facilities can produce useful data for the equilibrium region of the shock-layer, and for downstream processes such as ablative product radiation and recombination. The long run times also enable high resolution measurements over long durations, permitting detailed spectroscopic analysis of molecular features. However, the non-equilibrium region of the shock layer is not reproduced. The extent to which test conditions can be directly matched to flight is also limited, with Mach number never achieved and total pressure only matched for very high altitudes (in the case of PWTs) or coincidentally (for atmospheric torches).

Now, transient high-enthalpy facilities are considered. The first two types — reflected shock tunnels (RSTs) and expansion tubes/tunnels[3] (ExTs) — use a scaled model to generate a flight-representative flow-field. The last, shock tubes, instead use a moving shock to replicate a stagnation streamline. As shown in Figure 3.1, these transient facilities typically have run times ranging from microseconds to several milliseconds. These short timescales result in more stringent requirements for camera performance and ultimately present challenges to achieving good signal-to-noise characteristics.

Reflected Shock Tunnels

The operating principles of RSTs are discussed in greater detail in Chapter 3. For the purposes of the discussion here, the only background required is that a reflected shock process is used to provide the stagnation conditions feeding a hypersonic converging-diverging nozzle. This flow then passes over a model in the test section.

[3]The distinction between a ‘tube’ and a ‘tunnel’ is typically that the former maintains a constant diameter at the test section, whilst the latter ends in a nozzle.

As discussed in Chapter 1, radiative heating has historically been considered a high-speed phenomenon. In general, RST experiments at the very high enthalpies and total pressures experienced during super-orbital entry present problems. Because the gas is stagnated, the high total pressure and temperature of the flow at such conditions can cause severe melting of the nozzle throat components. Some campaigns have found this is sufficient to alter the throat geometry over the course of a single test, thereby changing the flow-field (Itoh et al., 1999). This can be addressed through use of different throat materials, but lifetimes of these components are still very short. In addition, at high enthalpies several RSTs have experienced issues with premature driver gas contamination of the test flow (Hornung, 2010). Despite this, some RSTs can match total temperatures representative of Lunar return — notably, HEG and HEIST at DLR and JAXA, respectively (Hannemann et al., 2016).

In general, atmospheric entry conditions are not tested at the correct Mach number in RSTs (Kliche et al., 2011). Instead, the total enthalpy of the flow is matched and the Mach number independence principle of Oswatitsch and Ruedinger (1980) assumed to apply. In practice, this means that the free-stream leaving the nozzle can remain at elevated temperatures. Furthermore, depending on the nozzle design, there can be a large degree of thermochemical freezing during flow expansion; vibrational temperature is often in non-equilibrium (e.g. Hurle et al. (1964) and MacLean et al. (2013)). This characteristic means that the non-equilibrium portion of the shock-layer is not typically matched to flight at these conditions. Heating discrepancies have also been identified in large shock tunnels — when operating at high enthalpies — which has been attributed to radiation from contaminant species by Cruden et al. (2021). These contaminants were found to produce an enhanced background continuum radiation, requiring fitting of species concentrations and therefore adding to the heating uncertainty.

For other planetary bodies, such as Mars, entries are typically slower and occur at lower pressures. RSTs are thus perhaps better suited to studies of these conditions, especially in the case where the dominant heating source will be due to the equilibrium region. Mars entry conditions have been tested in several RSTs to investigate surface heat fluxes (Hollis and Prabhu, 2013; Wright et al., 2005; Noeding and Martinez Schramm,

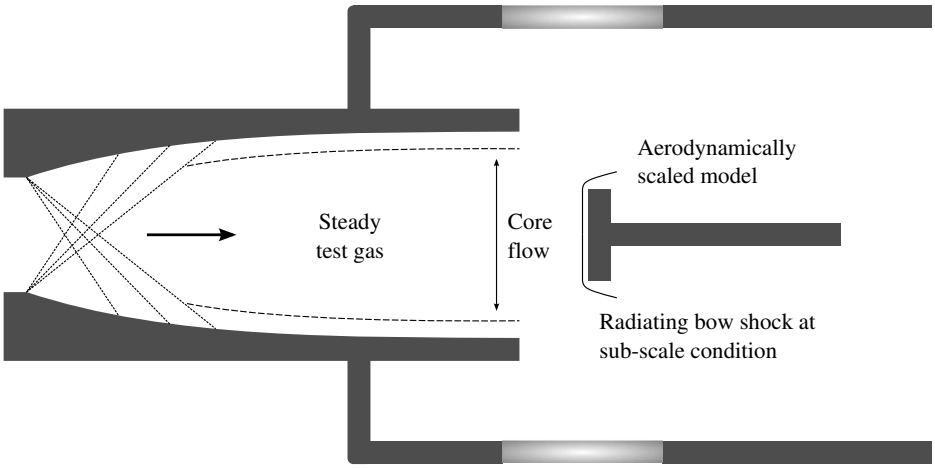


Figure 2.4 – A radiating flow experiment in the X2 Expansion Tunnel (Jacobs, 2011a).

2014). More recently, in the work of Leibowitz (2020), mid-wave infrared (MWIR) radiative heating was studied directly in the T5 shock tunnel using model-mounted fibre optics. Although numerical rebuilding is still on-going, this recommends RSTs as useful test-beds for relatively low-speed, equilibrium heating cases which require comparably long test times to establish the full flow-field.

Expansion Tubes & Tunnels

Unlike RSTs, ExTs do not stagnate the test gas. Instead, flow total enthalpy is increased through an incident shock and subsequent unsteady expansion process. This results in a much more 'chemically pure' free-stream flow and potentially allows reproduction of the entire shock-layer — including the non-equilibrium region. ExTs are capable of covering a wide range of flow conditions, from atmospheric scramjet flight to hyperbolic Earth entry (Gildfind et al., 2016), meaning it is generally possible to closely match the conditions for a mission of interest.

A range of model designs have been employed to investigate shock-layer radiation in expansion tubes. A common approach is to use a simple geometry to act as a stagnation point. The stagnation line can then be interrogated using a chosen optical technique. Selection of model size is crucial in these cases: it must be small enough to fit within the core flow of the facility, and to allow the flow-field to fully establish with sufficient time to perform the measurement before the end of the test period. Morgan et al. (2011)

provide a summary of the key considerations for model design when simulating radiating flows in impulsive test facilities. A larger shock stand-off distance results in a more equilibrated flow-field, which can help to reduce measurement uncertainties. This can be achieved by using a larger model, or through the use of two-dimensional geometries which inherently exhibit larger shock stand-off. However, in the case of a two-dimensional body some correction must be made for edge effects (Eichmann et al., 2007); axi-symmetric models avoid this issue, but a reconstruction technique (i.e. Abel inversion) is then required to rebuild the flow-field.

As well as stagnation line radiation measurements, more complex geometries can be tested. Scaled models of capsules for a range of entries including Earth, Mars and Titan have been studied in expansion tubes (Fahy, 2016; Banerji et al., 2018; Palmer et al., 2011a). In addition, recombining or expanding flows have been studied in the wake using this method (Takayanagi et al., 2017). For this problem in particular, Wei (2017) constructed a wedge model and measured the spatial evolution of radiance as the flow expanded around the corner. This work was undertaken for air and later extended to Mars entry by Gu (2018). Although promising, uncertainties were found in this work due to the unknown thermochemical state of the free-stream; similar conclusions were drawn in the results of Sheikh et al. (2012). Whilst expansion tube flows are generally much closer to equilibrium than RSTs, the unsteady expansion process results in thermochemical gradients through the test slug (Beck and Mackie, 1978). For small facilities, or rapid expansions, this can result in a non-equilibrium free-stream flow which ultimately impacts the similarity of spatial variations through the shock-layer.

Radiation Scaling Considerations

A key drawback of shock-layer radiation experiments using scaled models is that measurements of non-equilibrium thermochemistry and flow-field radiation do not scale directly to flight. In ExT experiments, binary scaling is typically used to match test conditions. Here, the ρL product is matched between flight and experiment; if reaction timescales are assumed proportional to the density, thermochemical rates are therefore appropriately scaled for the body size. If total enthalpy is also identical, this in effect also matches

Reynolds number (Stalker, 2006). However, work by Capra (2007), Morgan et al. (2008), and Andrianatos et al. (2015) shows that the radiative heat flux through the surface of a stream-tube scales with L: the radiative heat flux is therefore not directly matched to flight.

It should be noted that the severity of this effect on the flow-field is case-dependent, varying with the Goulard number as given by Goulard (1961) in Equation (2.1). This quantity expresses the relative magnitude of radiative energy from the flow to the total incoming energy flux. A large Goulard number implies a significant degree of radiative coupling in the flow; typically a value above 0.01 is considered sufficient for this effect to be important (Palmer et al., 2011b). Although negligible for certain entry cases e.g. low-speed Mars conditions (Leibowitz, 2020), for many applications this is not the case. Leyland et al. (2013) gives estimates for the Goulard number of 0.01 for Lunar return, 0.1 for Jupiter entry and 0.4 for Titan (at peak radiative conditions). It is interesting to note the compositional dependence of this value; despite the $48\,\mathrm{km\,s^{-1}}$ and consequent 60 000 K post-shock temperature of the Jovian entry, the Titan $6.4\,\mathrm{km\,s^{-1}}$ flight point exhibits far greater radiative coupling.

$$\Gamma = \frac{2q_R}{\frac{1}{2}\rho_\infty v_\infty^3} \tag{2.1}$$

In addition to differences in radiative effects, some chemical kinetic rate similarity is also not satisfied through ρL scaling. Three-body reactions are quadratic in density (Hornung et al., 1992) and so are not matched through the binary scaling parameter. Typically, the main non-equilibrium processes are binary, with only the final approach to equilibrium involving significant numbers of three-body reactions (De Crombrugghe et al., 2014). However, some areas of the flow-field — notably the recombination in the wake region — are dominated by three-body processes. This means that computational models must be matched to experimental scales and then extrapolated to flight.

Finally, it should be noted that recent work of Andrianatos et al. (2019) has avoided these scaling issues by simply testing a full-scale Hayabusa forebody in the X3 Expansion Tube. This is a significant advancement, as it permits direct assessment of the influence of the binary scaling approach and allows these differences to be assessed. However,

X3 is a very large facility — approximately 70 m long, with a nozzle exit diameter of 573 mm — and Hayabusa a relatively small geometry (400 mm in diameter). Full-scale testing is therefore not a viable approach for the majority of ground test facilities, or for larger vehicles.

Shock Tubes

Unlike the previously discussed transient facilities, shock tube experiments do not use a model. Instead, a normal shock is passed through a quiescent test gas at a density and composition matched to a flight trajectory point. This flow is thus used as an analogy to the stagnation line of an entry vehicle. This approach has three main advantages:

1. The shock-layer is reproduced almost exactly to flight, with no scaling of radiation or chemical kinetics required. The only difference occurs near the body, where the deceleration of the stagnation point flow results in a slight spatial compression of the gas packets. This is theoretically correctable using a simple residence-time transformation (Park, 1989), although this is not generally necessary in practice.

2. The boundary conditions for the experiment are significantly better defined, requiring only accurate measurement of the shock speed and fill pressure. This is in contrast to the ExT and RST experiments, which both involve the test gas undergoing a previous heating and expansion process. This can introduce uncertainties in the initial thermochemical state of the gas entering the shock-layer.

3. The flow behind the normal shock is effectively one-dimensional. This allows comparisons to simpler numerical tools and does not require axisymmetric treatment of experimental data, or concerns about edge effects.

There are short-comings in the use of shock tubes for shock-layer radiation studies. Only normal shocks can be produced, which means that expanding flows cannot be directly studied. In essence, only the stagnation streamline is recreated. However, for some atmospheres Johnston et al. (2019) showed that compressive cases can be used to study the wake region. Furthermore, recent work by Johnston (2021) has shown

that off-condition shock tube data can be applied to oblique shocks, thereby directly informing radiative heating predictions of other parts of the flow-field. Promising as these applications are, in practice measurements from shock tube experiments are generally used as fundamental test cases for the extraction of thermochemical rates and radiation data. These results then feed into computational models, which are later applied to non-equilibrium radiative heating simulations of entry vehicles (Barnhardt et al., 2019).

The potential advantages of shock tube experiments, in combination with the findings of Bugel et al. (2011) and Reynier (2016) regarding the lack of European shock tube facilities, ultimately drove this facility mode to form the focus of this thesis. A review of high-enthalpy shock tube experiments is thus undertaken in greater detail in the subsequent sections. In addition, although simple in principle, there are several experimental complications involved in the proper generation shock tube flows. These are also described in the following section.

2.4 High-Enthalpy Shock Tube Facilities & Experiments

In this section, the most active high-enthalpy shock tubes in the field of shock-layer radiation and atmospheric entry aerothermodynamics are reviewed. Summaries of their operating principles are provided, as well as an overview of past experimental campaigns. Finally, some of the more detailed considerations for performing shock tube experiments — specifically, shock deceleration — are discussed.

2.4.1 Active Shock-Layer Radiation Facilities

Shock tubes are very common tools for generating impulsive flows for a wide range of applications, a full review of which is beyond the scope of this work. Instead, the discussion here is limited to only those facilities which perform spatially resolved shock-layer radiation studies. These are scarce globally; Brandis (2012) identified only three facilities which had produced radiation data for Mars entry, at NASA, JAXA and the University of Queensland. Here, we consider the experimental arrangement and previous data of these three facilities in detail to establish the current status of these experiments in

the literature. An overview of the key parameters of these facilities is given in Table 2.1 to aid comparison.

In addition, it is noted that other types of shock tube experiments can provide highly valuable fundamental data for atmospheric entry applications. Notably, the use of reflected shock tubes in the study of high-temperature chemical kinetics (demonstrated initially by Windsor et al. (1957) and applied by several authors, notably in the recent work of Hanson and Davidson, 2014) directly informs thermochemical modelling development. These studies are typically more fundamental in nature — and do not recreate a realistic shock-layer — and so are also considered beyond the scope of this thesis.

NASA: Electric Arc Shock Tube

The EAST facility is a 101.6 mm diameter, 15 m long[4] shock tube based at the NASA Ames Research Centre. As described by Cruden (2014), the driver section consists of a 1.3 litre conical volume, initially filled with hydrogen or helium at pressures ranging from

[4]NB: As shown in Figure 2.5, the measurement location is actually mid-way along the facility, at approximately 8 m.

Table 2.1 – A comparison of high-enthalpy shock tube facilities. The presented information has been amalgamated from the body of referenced works discussed in this section. The T6 data is taken from this thesis. The performance figures are representative of the upper range of published data, but act as a rough comparison only. Unless otherwise stated, these are taken from tests in air. The bottom half of the table shows what atmospheres have been tested in each facility.

	EAST		**X2**			**T6**	
	4 in.	**24 in.**	**NRST**	**NRST-Al**	**HVST**	**SST**	**AST**
Bore, mm	101.6	609.6	85.0	155.0	70.0×70.0	96.3	225.0
Length*, m	8.0	18.1	9.1	4.7	3.7	8.8	5.5
U_s, km s^{-1}	15.5	9.24	10.0	9.0	13.0	13.3	10.5
P_1, Pa	13.3	18.6	53.2	4.0†	10.0	26.6	13.3
Earth	Y	Y	Y	N	Y	Y	Y
Venus	Y	N	N	N	N	N	N
Mars	Y	Y	Y	N	Y	N	Y
Titan	Y	N	Y	Y	N	N	Y
Gas Giants	Y	N	N	N	N	N	N

**Length defined from start of shock tube to measurement location.*

†Titan atmosphere (98 % N_2, 2 % CH_4)

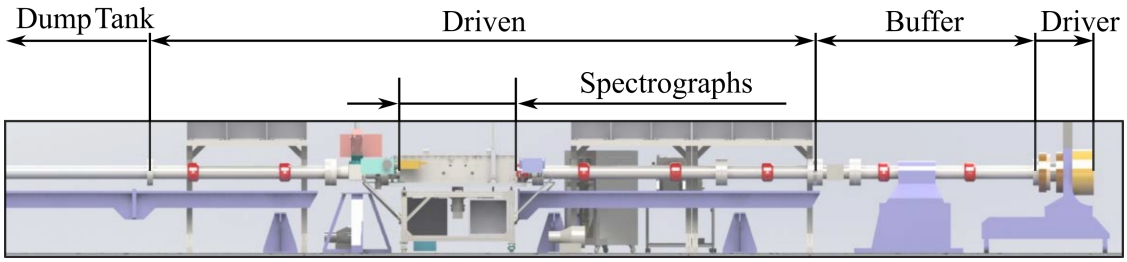


Figure 2.5 – The NASA Electric Arc Shock Tube (EAST) facility, with the spectrographs used for the emission measurement identified. Adapted from Cruden and Bogdanoff (2017).

30 psi to 200 psi. At the start of a test, a 40 kV, 1.2 MJ capacitor bank is rapidly discharged through a metallic filament inside the driver. This causes instantaneous vaporisation of the wire, rapidly heating the driver gas and causing rupture of a diaphragm. This drives a fast shock downstream. The electric arc technique is very powerful — with velocities in excess of 46 km s^{-1} recorded (Sharma and Park, 1990) — but the small volume of the driver and means of heating results in a rapid decay in pressure, causing substantial deceleration of the shock and short test times. However, these short durations have proven to be sufficient to produce significant amounts of useful data, especially of the non-equilibrium region.

Since its original development, EAST has undergone several significant upgrades, both in terms of better control of contaminants (notably through introduction of gas handling and plasma cleaning, which significantly improved cleanliness of spectra) and experimental methods. The last major upgrade of EAST is detailed by Cruden et al. (2009), which implemented simultaneous use of 4 imaging emission spectroscopy channels, housed in bespoke vacuum vessels to prevent absorption of radiation by atmospheric O_2 (in the vacuum ultra-violet, below 200 nm), water vapour and CO_2 (in the infrared). This covers a continuous wavelength region of approximately 120 nm to 1600 nm. As described by Greenberg et al. (2009), the improved EAST optical design utilises a telecentric optical set-up, which greatly reduces spatial blurring of the shock-layer due to the optical system. These optical components are focused on the test gas region through optical windows integrated into the tube wall. A diagram of EAST immediately following this upgrade is shown in Figure 2.5.

In the last decade, EAST has produced the majority of experimental data to inform investigations of shock-layer radiation. This work has chiefly been in support of proposed

NASA missions, covering Venus, Earth, Mars, Gas Giant and Titan entries (Cruden et al., 2012; Brandis et al., 2013; Cruden and Bogdanoff, 2017; Brandis and Cruden, 2017b; Brandis et al., 2017). More fundamental studies have also been undertaken; for example, tests in pure nitrogen to provide a simpler thermochemistry test case (Brandis and Cruden, 2018) and investigations varying the concentrations of atmospheric trace species (Brandis et al., 2016). A sufficient body of data has been generated to allow the definition of benchmark test cases for other facilities, and for numerical tools (Brandis and Cruden, 2017a).

Whilst some campaigns using laser-based techniques have been completed (MacDonald et al., 2018), the vast majority of studies undertaken at EAST have used emission spectroscopy, for the reasons outlined in Section 2.2.1. The knowledge gained over this period has lead to significant development in the understanding of how best to apply emission spectroscopy to shock tube experiments. Notably, Cruden (2014) outlines several methodologies for the calibration and characterisation of such arrangements, including considerations for spatial and spectral blurring due to various sources in the optical system. This foundation is drawn on heavily in the experimental results presented in Chapter 5 of this work.

Of particular relevance to the development of the T6 Aluminium Shock Tube discussed in Chapter 4 of this work is the use of a 24 inch (60 cm) shock tube at EAST. The substitution of the normal tube for a larger diameter counterpart produces an increase in radiation signal proportional to the diameter.[5] The main application of this configuration is very high altitude (and correspondingly low pressure) conditions, such as Mars aerocapture. Cruden (2012a) used the tube to study this problem, where it was found to improve the quality of emission measurements. However, later analysis by Bogdanoff and Cruden (2016) highlights that protuberances on the inner wall of the tube (such as weld beads) led to distortion of the shock at very low pressures. Furthermore, the very large diameter led to increased spatial blurring, and so the potential augmentation in radiance was not realised due to the need to include an aperture in the optical path. More

[5] If the radiation is optically thin, i.e. there is no self-absorption. The extent to which this is true is highly dependent on the specific spectral feature, the thermodynamic state of the gas and the path length.

recently, the larger tube has been used for higher-pressure, low speed Earth trajectories with better success. Results were found to be in overall good agreement with those from the 4 inch tube (Cruden and Brandis, 2020).

Measurements at EAST have largely contributed to the understanding, and serious consideration, of radiative heating for entry vehicles. The use of modelling tools developed from the EAST results has been able to explain discrepancies between flight data and simulations (e.g. Cruden et al., 2015). This has led to further inclusion of radiative heating measurements on newer flight vehicles, notably MARS2020 and Orion (Brandis, 2018). Furthermore, EAST experimental data directly inform TPS design margins through characterisation of uncertainties for a range of entry types.

Given the amount of data generated by EAST it is inevitable that discrepancies between models and the experimental data will exist. Some notable examples of this include an under-prediction of molecular emission at equilibrium at low-speed air conditions (Cruden and Brandis, 2017), radiation of the CO_2 overtone (2.7 µm) band which exceeds the frozen solution (Cruden et al., 2014), electron densities above equilibrium (Cruden, 2012b) and worsening agreement between numerical and experimental results below $10\,\mathrm{km\,s^{-1}}$ in air (Brandis et al., 2017). These cases highlight the need for cross-facility comparisons, which can either confirm these differences as physical effects or help to explain their origin.

JAXA: Hyper-Velocity Shock Tube

The free-piston driven Hyper-Velocity Shock Tube (HVST) was originally developed to support Mars aerocapture missions; the first commissioning is described by Yamada et al. (2011). Figure 2.6 shows a diagram of the facility, which is approximately 16 m in total length. The shock tube section is designated the 'low pressure tube' in this diagram. Unusually, the HVST design features a square cross section of $70\,\mathrm{mm} \times 70\,\mathrm{mm}$. More recently, the HVST was adapted to operate as an expansion tube, in which radiating flow experiments (notably of MWIR CO_2 radiation) have also been performed. A good level of agreement was observed between equivalent measurements in the two facility modes (Takayanagi et al., 2018).

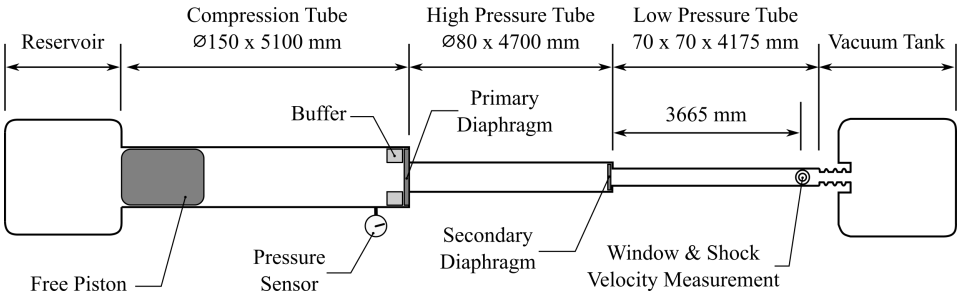


Figure 2.6 – The JAXA Hyper-Velocity Shock Tube facility. Adapted from Yamada et al. (2011).

The experiments in HVST are broadly similar to those from EAST: spectrally and spatially resolved emission is captured from a shock passing an observation window integrated in the tube wall. One notable feature of the HVST experiments in terms of the facility performance is the method of shock speed measurement and camera triggering. This is performed very accurately using laser-based techniques at the test section. This can, along with a high-precision delay generator, allow repeatable positioning of the shock within the test section to accuracies of ±0.5 mm (Yamada et al., 2012).

In terms of results, the majority of published research from the HVST has focused on Mars entries (Fujita et al., 2017). Investigations of MWIR radiance at lower speed entries has confirmed experimental results from EAST, and good agreement was found in the measured radiance between the two facilities (Takayanagi et al., 2019). Furthermore, the JAXA group has successfully made measurements in the VUV of CO (4+) emission at higher velocity Mars entries (Takayanagi and Fujita, 2012). This is a challenging region of the spectrum to measure, as the emitted radiation is absorbed by the Schumann-Runge bands of ambient O_2 molecules within the laboratory space. The optical path must therefore be entirely evacuated. In addition, Takayanagi et al. (2014) further extended the facility capability to rupture pressures in excess of 50 MPa, producing shocks of up to 14 km s^{-1} at a 5 Pa fill pressure. This upgrade enabled VUV measurements of emission from very high speed Earth return shock-layers to be made; HVST is thus the only shock tube other than EAST in which this has been achieved.

Although promising in its capability, the HVST experiments have a few idiosyncrasies which somewhat limit the wider applicability of its results. First, whilst the shock speed measurement and triggering technique is highly advanced, it is only performed at the test

section. The shock speed variation along the length of the facility is not therefore resolved. This limitation posed issues when undertaking the performance upgrades detailed by Takayanagi et al. (2014), wherein an increase in piston compression ratio and diaphragm burst pressure did not lead to a greater shock speed. This was hypothesised to be due to a loss of pressure a the piston face, but was not possible to characterise. Furthermore, as will be discussed in Section 2.4.2 and explored further in Chapter 6, shock deceleration is a proposed explanation for observed discrepancies in other facilities. The degree to which this happens in HVST is not possible to determine.

Finally, the imaging spectrometer arrangement used at HVST is different to other facilities. Here, a photodiode is used to perform an integrated intensity measurement at a single point. This rebuilds the passage of the shock-layer at a single spatial position with varying time. This contrasts with the approach used in other facilities in this section, wherein the entire spatial extent is imaged instantaneously. Given the very high repetition rate of the photodiode, this means the shock-layer is captured with minimal spatial blurring. However, as discussed in Section 2.2.1, photodiodes are an integrated measurement and cover a wide wavelength region. At HVST, the spectrally-resolved measurement is only made at discrete points behind the shock; in general, this is made at a single point by using a reflective condenser to focus light onto the spectrometer slit, although a fibre-optic coupler has also been used to provide approximately 10 mm resolution (Takayanagi and Fujita, 2012). Spatio-spectral resolution of radiance behind the shock-front thus relies on the accurate triggering system to vary the position of this point-based measurement in the shock-layer on consecutive shots. This inherently increases the sensitivity of the measurement to shot-to-shot variation and requires a significant number of tests to rebuild a reasonable representation of the shock layer.

University of Queensland: X2 Non-Reflected Shock Tube

The 85 mm diameter X2 facility primarily operates as an expansion tube; in that capacity, it has produced experimental data for a wide range of super-orbital and radiating flow problems. Some key examples of these was already provided in Section 2.3.2. It was later proposed by Morgan et al. (2006) that X2 could also be operated as a shock tube for the

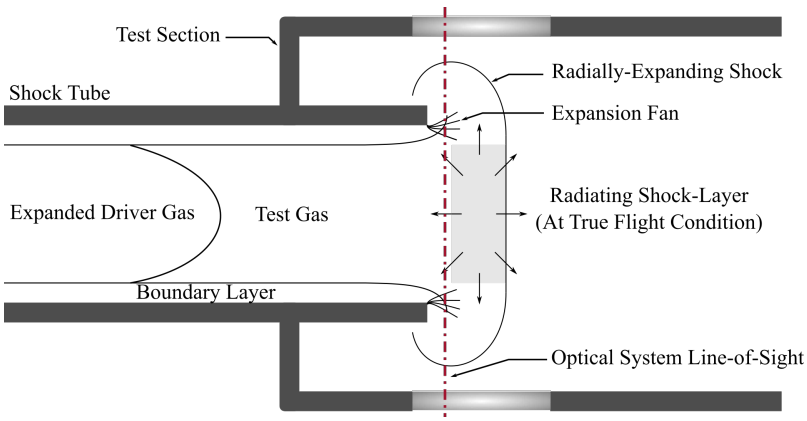


Figure 2.7 – Experimental arrangement for shock tube experiments in the X2 facility, wherein the shock is imaged as it emerges from the tube into the test section. Adapted from Jacobs (2011a).

study of shock-layer radiation. In this configuration, it is designated Non-Reflected Shock Tube (NRST) mode. Because the machine was originally designed as an expansion tube the wall does not feature integral windows. Instead, the flow is imaged as it emerges from the end of the tube and into the test section. This approach has the potential advantage that it does not look through the wall boundary layer[6] that forms behind the shock within the tube. However, this benefit is potentially offset by the presence of the supersonic expansion fan and radially-expanding shock which form at the outlet. A diagram of the facility in this mode of operation is shown in Figure 2.7.

X2 was first operated as a shock tube for the study of Titan entry conditions by Brandis et al. (2007). The concluding results of this work, later detailed in Brandis et al. (2010b), demonstrated excellent agreement between the data from the X2 facility and with EAST. The X2 Titan results later informed the development of non-equilibrium collisional radiative models for Titan entry, allowing comparison between datasets from facilities and modelling groups (Brandis et al., 2014). Furthermore, a set of experiments which captured the shock front at varying distances from the outlet of the tube determined that, at least for the tested Titan conditions, no adverse effect of the expansion fan at the outlet could be measured. This success led to the adoption of the technique in the T6 SST mode (Collen et al., 2019), also with good results.

[6] As is the case for the EAST, HVST and T6 AST experiments.

Aside from Titan entry, Earth and Mars radiation has also been studied in the X2 shock tube mode (McIntyre et al., 2011). Potter (2011) compared measurements of X2 air radiation at 10 km s^{-1} and 0.2 Torr to EAST, where good agreement was found between both facilities and the prediction of their one-dimensional post-shock relaxation solver. A much wider range of conditions was tested by McGilvray et al. (2010a) spanning pressures of 0.1 Torr to 0.4 Torr with velocities up to 11 km s^{-1}. A cross-facility comparison by Brandis et al. (2010a) between EAST and X2 was also performed, which showed good qualitative agreement between the two datasets. However, a need for a greater volume of comparative data was highlighted to enable deeper comparisons with the EAST results.

In general — and perhaps because of its more regular operation as an expansion tube — the facility characteristics of the X2 experiments have been well-characterised. In particular, shock speeds are measured along the length of the facility, and a combination of Pitot rake and high-speed imaging used to characterise test time and boundary layer thickness (e.g. Brandis et al., 2010a; Jacobs, 2011a). One key challenge in all X2 shock tube tests to date has been use of a radiant calibration source, which required optical components to be characterised individually and the solid angle of this system measured accurately. This has been a recognised source of uncertainty in several of the presented test campaigns.

Finally, again of particular relevance to the AST development presented in Chapter 4, Jacobs (2011a) constructed a 155 mm diameter aluminium shock tube for X2. Again, the shock was imaged as it emerged from the tube. This was designed to investigate upper-atmosphere Titan entry conditions, with initial fill pressures as low as 4 Pa (equivalent to an altitude of 359 km) tested. The larger diameter enabled useful test times, even at these low pressures. Notably, this new barrel was constructed from aluminium to reduce the amount of carbon contamination in the flow, which had been noted as a source of uncertainty by other authors (Bose et al., 2009). The interface between this tube and the original X2 facility was designed as a sudden expansion, which a computational study revealed leads to the formation of a shock train and possible deformation of the test slug, although this was not apparent in optical measurements. Despite this, the required Titan test conditions were achieved and large extents (approximately 100 mm) of shock-layer

generated. Jacobs et al. (2015) showed this data to agree well with comparable results from the 85 mm tube, validating its use for the investigation of high-enthalpy shock-layers.

Crucially, a key recommendation of the X2 Aluminium Shock Tube work was that the facility should be extended to other radiative flow problems given its utility for the studied conditions. This has not yet been implemented.

2.4.2 Shock Speed Variation Effects

The only three variables in a shock tube experiment are the initial shock tube fill pressure, the gas composition, and the shock speed. In general, the first two are reasonably simple to control, assuming leakage of atmospheric air into the facility is sufficiently avoided. Whilst some compositions — notably Titan (Brandis and Cruden, 2017b) — have chemistries particularly sensitive to air contamination, in general the gas variables are possible to manage within a sufficient degree of accuracy.

The main challenge in shock tube testing is thus to achieve the correct shock speed. The first obstacle to this goal is to have a facility with a sufficiently powerful driver section to achieve the condition of interest. Assuming this is the case, in an idealised scenario the shock speed would be constant along the length of the shock tube. However, in practice this is not observed. Here, some of the key reasons for this are discussed.

The first source of shock speed variation (SSV) is due to diaphragm opening. The vast majority of shock tube facilities use a diaphragm to initially separate the high pressure driver gas from the lower pressure test gas. Ideally, this is assumed to rupture instantaneously; however, in practice a finite opening time (on the order of 100 µs) is required. White (1958) performed an early analysis of this effect, showing that the diaphragm opening process leads to an initial ramp-up and later overshoot of the nominal shock speed, which is gradually reduced as the shock travels along the tube. This problem is considered in significantly more detail in the T6 commissioning experiments of Chapter 3.

The shock speed and the test time are closely linked. In a shock tube, the test time is defined by the distance between the shock and the contact surface, which forms the interface between the (shocked) test gas and the expanded driver gas. This can be seen in Figure 2.7. It could be reasonably assumed that the test time should be fixed by

conservation of mass: taking the density ratio of the shock and the length of the facility allows the length of the compressed gas slug to be determined. The test time would then be equivalent to the time required for this length to pass the measurement location, which occurs at the post-shock velocity.

In the middle of the last century, many authors noted that the aforementioned approach overestimated the test time significantly. It was also observed that lengthening the shock tube eventually resulted in no increase in the test time. The shock velocity was found to concurrently decrease along the length of the tube, again eventually reaching a steady state (Toennies and Greene, 1957; Duff, 1959). Work by several researchers, notably that of Roshko (1960) and Hooker (1961) linked these observations to development of a wall boundary layer behind the shock wave, which resulted in mass loss to the wall.

Mirels (1963) provided the most effective explanation of the influence of the wall boundary layer in shock tube flows, to the extent that these are now known as 'Mirels effects'. A diagram of his construction is reproduced in Figure 2.8. Here, a self-similar boundary layer is assumed to form in the flow behind the shock front. Mass is thus ingested into the boundary layer, eventually flowing around the contact surface and out of the test slug. As the shock progresses along the shock tube, the distance between the contact surface and the shock front increases; consequently, so does the boundary layer thickness at the rear of the test slug and thus the mass loss from it. The shock consequently decelerates due to pressure perturbations — as the boundary layer acts as a mass sink — which travel through the test slug. Finally, an equilibrium is reached wherein the mass flow entering through the shock is balanced by that exiting through the boundary layer. The shock thus reaches a constant speed, and no further increase in the distance between it and contact surface occurs.

Given that the Mirels effect is due to the wall boundary layer, it should be noted that the strength of this effect will vary depending on test condition and on tube geometry. In the case of low pressure test conditions, the post-shock Reynolds number will be lower which results in a proportionally thicker boundary layer. In addition, higher post-shock temperatures result in a greater density difference in the boundary layer (in the case of an isothermal wall) therefore causing larger proportional mass loss. However, given

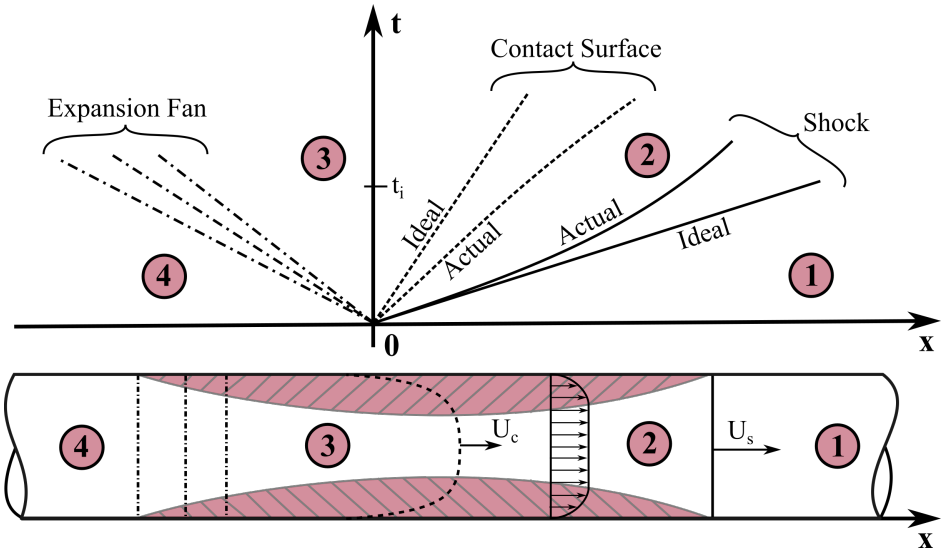


Figure 2.8 – Distance-time plot of the Mirels effect. Also shown is a diagram of the tube wall boundary layer, taken at a single moment in time (t_i). Here, region 1 denotes the initial test gas state, region 2 the shocked test gas, region 3 the expanded driver gas and region 4 the initial driver gas fill. Adapted from Mirels (1963).

the self-similarity of the boundary layer, tube diameter has the greatest effect. Over a fixed range of shock speeds, Mirels (1964) showed the test time to be proportional to $p_\infty D^2$ for a laminar boundary layer. Here, intuitively, the diameter is measured in inches and the pressure in centimetres of mercury. A larger tube is therefore the best means of minimising the influence of these phenomena on the shock-tube flow.

A final cause of shock speed variation is the production of expansion or compression waves due to changes in the driver. Some technologies — notably arc drivers — have highly transient pressure profiles, which result in a large degree of shock speed variation. Other approaches, such as free-piston facilities, can maintain steadier conditions. These are discussed in significantly more detail in Chapter 3.

An open question in the literature is: to what extent do variations in shock speed matter in shock tube experiments? Light (1973) considered this problem from the following perspective: in investigations of chemical kinetics, the rate parameters (which are the measurement objective) are functions of pressure and temperature. In arc-driven shock tubes, the rapid decrease in driver pressure caused decelerations far above those stemming from the Mirels effect. For the shock to decelerate to such a degree, strong expansion

waves must reduce the pressure throughout the shock-layer and thus this should change the apparent chemical kinetic rates.

To investigate the impact of shock deceleration, Light (1973) measured the electron density behind strong shock waves using a microwave interferometer. His results show differences in the observed trends of electron density through the shock layer at the varied conditions. However, the main mechanism of shock speed modulation between tests was to change the initial fill pressure in the tube. The presented results are thus at very different pressures, and the final shock speeds are also not equivalent. These factors, in combination with an overall poor agreement between a numerical model of the temperature variation in the test gas, has meant that these results have not convincingly proven any direct link.

In several test campaigns undertaken at EAST, shock deceleration has been posited as a potential source of disagreement between the experimental results and numerical predictions. There, changes in shock speed on the order of kilometres per second are common along the length of the facility. Cruden (2012b) measured electron densities in the shock-layer across a range of conditions, showing values significantly in excess of equilibrium. In a cross-facility comparison with X2, Brandis et al. (2010a) proposed shock deceleration as a potential cause of discrepancies in the EAST data. This mechanism is shown diagrammatically in Figure 2.9, wherein the changing shock speed leads to a gradient in temperature through the test slug. An improved agreement was seen in trends of background continuum radiation if this effect was modelled, but again a fully convincing argument was not possible.

Partly in an effort to investigate the shock deceleration influence, several authors have attempted computational simulations of EAST. However, the large aspect ratio of shock tube facilities makes full, viscous simulations incorporating thermochemistry extremely expensive (Kotov et al., 2014). In the two most recent attempts, one suffered from numerical issues (Bensassi and Brandis, 2019); this reflects the challenging nature of these simulations. The second successfully simulated the test slug, but because the driver was not fully modelled the shock deceleration trajectory was not reproduced (Chandel et al., 2019). One-dimensional simulation approaches have also been inconclusive (Sharma Priyadarshini et al., 2018).

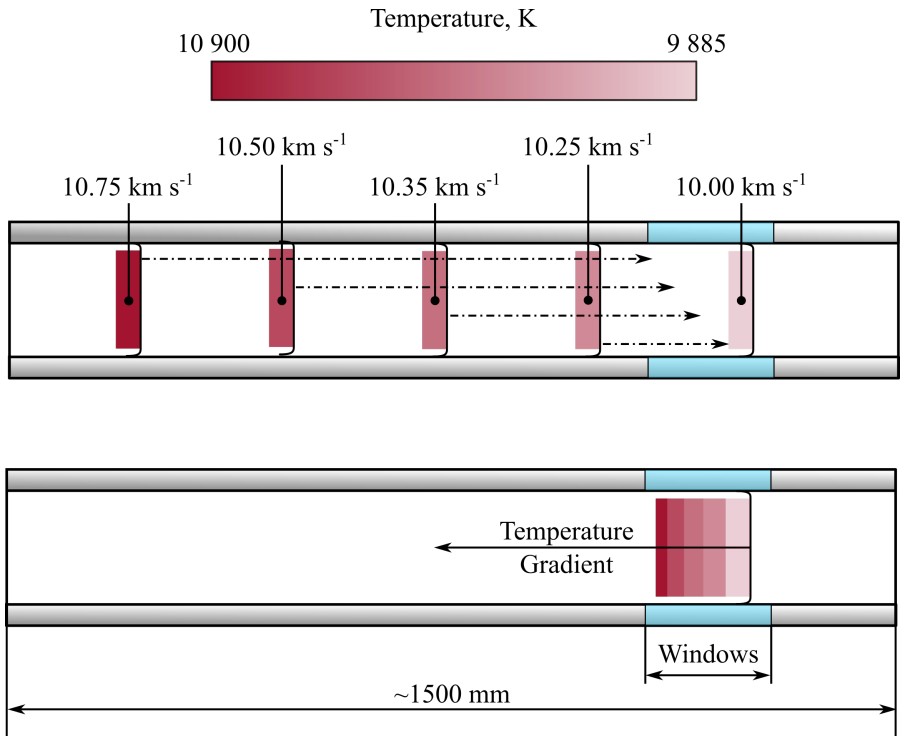


Figure 2.9 – Diagram demonstrating the effect of shock deceleration on post-shock equilibrium in the EAST facility. The upper diagram shows the variation in shock speed and the downstream movement of the shocked gas. The lower diagram represents the test slug as imaged when the shock is at the observation window. Adapted from Brandis et al. (2010a).

More recently, a new computational tool by Satchell et al. (2021c) and Satchell (2021) — LASTA — has been developed to investigate the problem of shock deceleration. This methodology uses the experimentally measured shock speed profile as an input, circumventing the challenge of reproducing the shock trajectory accurately via simulation. Through this analysis, it was demonstrated that the changing strength of the shock will generate an entropy gradient in the test slug; this persists despite pressure changes in the gas, and consequently so does a temperature variation. This result has been validated against data from T6, where it was shown to predict accurately increases in stagnation-point heat flux due to temperature gradients in the slug caused by shock deceleration (Satchell et al., 2021b). The new modelling approach has not yet been applied in the case of radiating shock-layer experiments.

2.5 Summary

This section reviewed both optical diagnostics for interrogating high-enthalpy flows and the types of ground test facility suitable for their generation. A wide range of experimental approaches are possible, all with distinct advantages depending on the specific measurement objective.

In terms of establishing a new facility for shock-layer radiation experiments, it was concluded that high-enthalpy shock tubes presented the best option. The full stagnation line shock-layer is reproduced, the flow is nominally one-dimensional and no scaling of the post-shock flow or radiation is required. Emission spectroscopy was also identified as the best flow diagnostic to implement in this work, given the wide range of information which could be extracted, the relative ease of establishment and the potential to compare directly to other facilities and to numerical tools.

Finally, previous shock-layer radiation experiments in high-enthalpy shock tubes were reviewed. Overall, it was found that a large body of data relating to shock-layer radiation has been generated over the last decade. Many cases have shown good comparability between datasets, and also with computational results. However, outstanding issues still remain. For certain conditions, e.g. lower speed air entries, the large uncertainties described by Cruden et al. (2018) still exist. Furthermore, there remain unknown influences — notably shock deceleration — which may affect experimental results. In the few cases cross-facility comparison has been possible, this analysis has contributed greatly to the better understanding of the underlying physics (Brandis et al., 2010a; Brandis and Cruden, 2017b). A further source of ground test data would therefore provide significant additional opportunities to reduce modelling uncertainty for future atmospheric entry applications.

Give me a lever long enough and a fulcrum on which to place it, and I shall move the world.

— Archimedes

3

Development & Commissioning of the T6 Stalker Tunnel

Peter Collen, Luke J. Doherty, Suria D. Subiah, Tamara Sopek, Ingo Jahn, David Gildfind, Rowland Penty Geraets, Rowan Gollan, Christopher Hambidge, Richard Morgan & Matthew McGilvray.

Contents

3.0 Foreword 51
3.1 Introduction 52
3.2 Facility Overview 53
3.3 Free-Piston Driver Commissioning 65
3.4 Shock Tube Modes 70
3.5 Reflected Shock Tunnel Mode 79
3.6 Expansion Tube Mode 89
3.7 Conclusion 94

3.0 Foreword

This chapter was originally written as a journal paper for the Experiments in Fluids special issue on Hypersonic Flight. Given the integral nature of the content of the article to this thesis, it is reproduced in full here. Although the layout has been altered to match

the rest of this work, the content remains unchanged. The original paper is referenced at the end of this document as Collen et al. (2021), with the authorship in full attributed above. In particular, Suria Subiah, Tamara Sopek and Rowland Penty Geraets are credited with the bulk of the work on Reflected Shock Tunnel mode, presented in Section 3.5.

The paper represents the development of a new, high enthalpy ground test facility. In the wider context of this thesis, the successful commissioning of T6 enables use of the new Aluminium Shock Tube, and hence all of the shock-layer radiation testing which follows.

3.1 Introduction

Further development of next-generation high-speed aircraft technologies, such as air-breathing access-to-space vehicles and atmospheric entry craft, requires greater understanding of hypersonic flow phenomena. Whilst flight testing remains the most desirable source of experimental data, the prohibitive cost limits the availability of relevant results for the multitude of possible flight trajectories. Ground test facilities can undertake hypersonic experiments at a fraction of the cost of flight test programmes, providing valuable data to inform vehicle development, understand the aerothermodynamic environment, and improve computational models.

Figure 3.1 presents several archetypal flight trajectories of interest to hypersonics research. It is clear that the peak heating conditions for all of the cases shown occur where there are significant thermochemical effects in the flow. In addition, the majority of these missions pass through high altitudes — at significant speeds — resulting in large non-equilibrium regions around the vehicle. Such flow-fields require accurate spatio-temporal reconstruction during ground testing. High-enthalpy test facilities are therefore required to properly recreate the flight environment and to enable relevant data to be obtained.

Stalker (2006) estimated that a continuous ground test facility capable of simulating re-entry conditions could require gigawatts of input power. This is evident in Figure 3.1, which shows that continuous facilities are currently limited to maximum speeds of around $1\,\mathrm{km\,s^{-1}}$. Achieving higher enthalpy test conditions therefore requires a shift to transient facilities, albeit with a general reduction in achievable test time. Hypersonic

pulse facilities of varying types are operated worldwide, by universities, space agencies and private companies (Lu and Marren, 2002) and all continue to provide invaluable data for vehicle development. However, for trajectories such as those shown Figure 3.1 it is not possible to simulate the entirety of the flight-path in any one type of ground test facility. This has led to the relatively recent conversion of existing ground test facilities to be multi-modal; examples include HEK-X (Tanno et al., 2016) and X3R (Stennett et al., 2018). This challenge has also formed a core motivation for the development of the T6 Stalker Tunnel described herein.

This paper first gives details of the new University of Oxford tunnel — T6 — in Section 3.2, describing the current arrangement and infrastructure of the facility. Results from the commissioning of the driver section with both 36 kg and 89 kg pistons are then presented in Section 3.3. Progress on the characterisation of each tunnel mode is then reviewed in Sections 3.4 to 3.6, with a range of experimental diagnostics discussed and comparisons to computational tools made. Data is presented which demonstrates the ability of T6 to simulate flight enthalpies in the range 2.7 to 115.0 $\mathrm{MJ\,kg^{-1}}$, corresponding to trajectory points for a Mach 7 flight condition and proposed Mars Sample Return missions respectively. Finally, Section 3.7 summarises the work and briefly discusses the next steps in the facility development.

3.2 Facility Overview

T6 is a new multi-mode, transient, high-enthalpy aerothermodynamic ground test facility at the University of Oxford. It can operate in four distinct modes according to test requirements: Reflected Shock Tunnel (RST), Expansion Tube (ExT) and in two specialist shock tube (ST) modes. These are compared diagrammatically in Figure 3.3, with the key dimensions provided in Table 3.1.[1] The specifics of each of these modes are discussed in subsequent sections. Also shown is the driver section, which is common to all modes. This modular nature results in a single facility capable of experimentally simulating flight conditions ranging from hypersonic atmospheric flight to hypervelocity re-entry.

[1] Note that the reservoir is in-line with the compression tube; these are labelled together in Figure 3.3 as 'Free Piston Driver'.

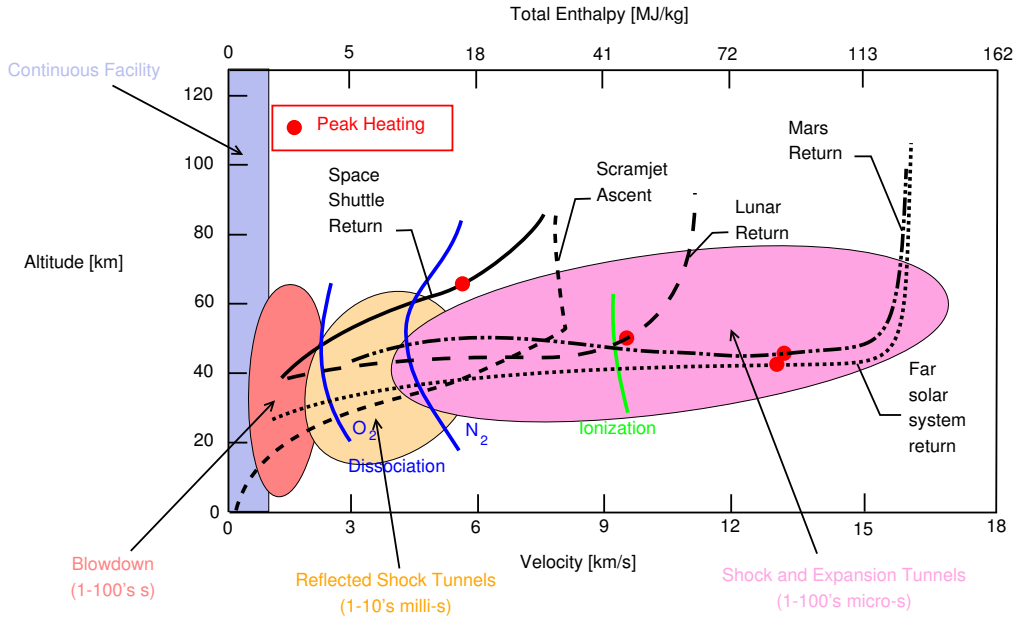


Figure 3.1 – Selected mission trajectories and approximate ground test facility capabilities. Adapted from Fletcher (2004).

3.2.1 The T6 Free-Piston Driver

The fundamental difficulty of high-enthalpy aerothermodynamic ground testing can be summarised as follows: it is impractical or impossible to generate and contain the high stagnation pressures and temperatures required to match flight conditions through steady means. Instead, these conditions must be generated transiently. This is almost universally achieved by passing a strong shock through the test gas, increasing its stagnation properties for sufficient time to provide a useful test flow. Many variations of this process are possible, as discussed in Sections 3.4 to 3.6. In all cases, a powerful driver section which is capable of driving a sufficiently strong shock through the test gas is required.

T6 Driver Selection

To maximise the shock speed achieved in the driven gas, the most important driver attributes are sound speed and — to a lesser extent — pressure. As a result, the operating principle of most driver technologies is to provide a source of high pressure and temperature, low molecular weight gas. The approach with the highest absolute performance is the arc driver, where the rapid discharge of electrical current through a filament greatly increases temperature and pressure in the driver section. This is the

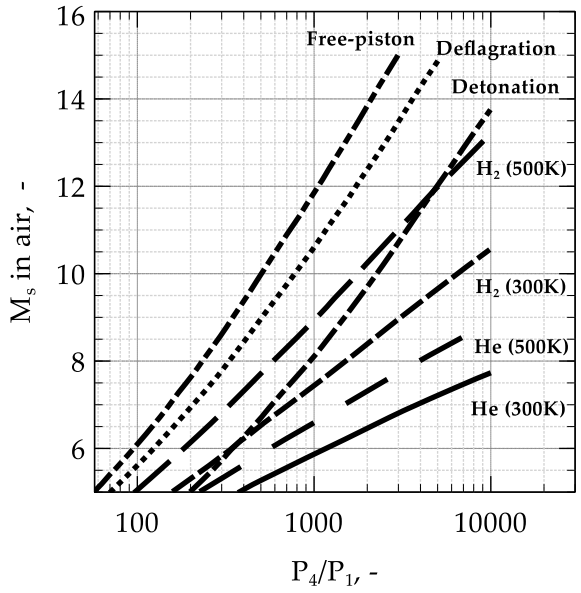


Figure 3.2 – Performance comparison of common driver technologies (adapted from Bakos and Erdos (1995)).

approach used by the NASA Ames EAST facility, which has recorded shock speeds in excess of 46 km s^{-1} (Sharma and Park, 1990). However, this technology is generally not suited for applications which require longer test durations (i.e. model testing) due to difficulties in maintaining steady flow properties in the driver gas.

Bakos and Erdos (1995) surveyed a range of driver technologies suitable for the HYPULSE facility, considering both performance and achievable test time. Their findings are reproduced in Figure 3.2, which plots the shock Mach number achievable as a function of the driver-to-driven pressure ratio. Noting the logarithmic scale of Figure 3.2, cold and heated helium as well as cold hydrogen require unfeasibly high pressures to achieve significant shock speeds. Heated hydrogen is a viable option, however this requires very high pressures to generate high velocity shocks. This approach is used by the CUBRC LENS tunnels, which operate at driver fill pressures up to 70 MPa (Holden et al., 2008). This approach also has the advantage of being low in complexity. However, handling hydrogen at these pressures poses serious safety concerns which are untenable in a university setting. Similar logic can be applied to combustion (deflagration) and detonation drivers, in which a mixture of hydrogen and oxygen is either burnt or detonated to achieve the desired rupture conditions. The authors also note that it can be challenging

in practice to operate a combustion driver at pressures above approximately 40 MPa due to the occurrence of local detonations. Of the options considered in Figure 3.2 the free-piston driver is shown to offer the highest performance. However, the mechanical complexity and hence capital cost of this approach is high. The knowledge required to develop driver conditions can also present significant challenges.

For the development of T6 a decommissioned but fully functional free-piston driver was fortunately available. This driver was originally part of the T3 Shock Tunnel, which operated at the Australian National University from the late sixties until the turn of the century. T3 used the first large-scale free-piston driver, which proved the performance benefits and operability of the technology (Stalker, 1966) and led to its adoption by several universities and national space agencies world-wide (Stalker, 2006). The availability of the T3 driver significantly reduced the capital cost of the free-piston design, therefore allowing the highest performance option to be chosen.

T6 Free-Piston Driver Description

In a free-piston driver, a heavy piston initially separates high pressure reservoir gas (air) from the lower pressure driver gas — typically a mixture of helium and argon. The tube holding this gas is termed the 'compression tube' and is bounded at the downstream end by the primary diaphragm: a metal sheet with a thickness on the order of millimetres. At the start of the test, the piston (currently either 36 kg or 89 kg) is accelerated by the reservoir gas to velocities in excess of $150\,\mathrm{m\,s^{-1}}$. As the piston nears the end of the compression tube the polytropic compression of the driver gas leads to a rapid increase in pressure and temperature, consequently decelerating the piston at rates exceeding 1000 g. The increasing driver gas pressure plastically deforms the primary diaphragm until rupture. Once ruptured, the driver gas ahead of the piston expands into the low pressure test gas in the shock tubes — driving the downstream flow processes — whilst the piston decelerates. This process is shown in the distance-time diagrams for each mode in Figure 3.4.

Tanno et al. (2000) describe two requirements for piston motion at the end of the stroke: (1) the velocity should be high enough to continue compressing the driver gas after diaphragm rupture (preventing generation of expansion waves which disturb the

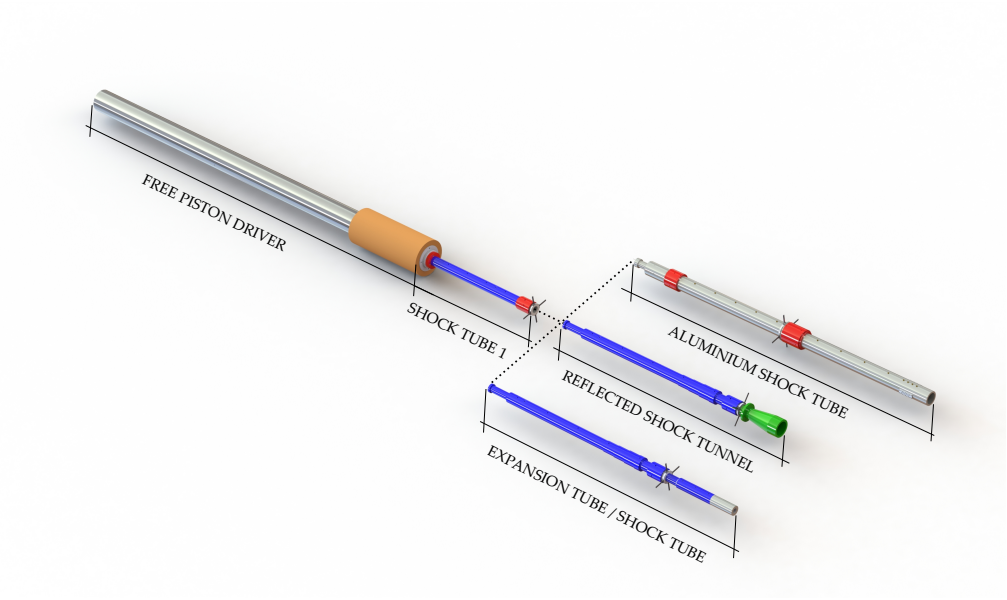


Figure 3.3 – Diagram showing the different T6 facility modes.

test flow) whilst (2) decelerating to a sufficiently low speed as to avoid damage to both the piston and compression tube/primary diaphragm station components upon impact with the buffers (located at the downstream end of the compression tube). Requirements 1 and 2 are often known as 'overdriving' and 'soft landing' respectively; driver conditions for which both are met are known as 'tuned' conditions.

The T6 driver is made up of a monolithic billet of stainless steel 9 m in length with an outer diameter of approximately 480 mm. This incorporates the 6 m, 300 mm diameter honed compression tube and an in-line high-pressure air reservoir. At the primary diaphragm station, a mild steel jacket of 730 mm outer diameter is shrink-fitted on to the driver billet. This jacket serves a dual function, acting as an inertial mass (to limit tunnel recoil and the generation of transient stress waves in the facility) and as structural reinforcement at the primary diaphragm station. This arrangement permits a maximum diaphragm rupture pressure of 270 MPa (Stalker, 1972).

3.2.2 T6 Operating Mode Descriptions

Figure 3.4 shows distance-time plots for the four operating modes of T6, starting from the moment of diaphragm rupture. These show the main wave processes which occur during a test. As shown in Figure 3.3, the driver and first shock tube are common to all modes and

Table 3.1 – Key dimensions of the T6 facility. Shock Tube 1 is integral to all modes; its length should thus be added to that of each mode to find the working length.

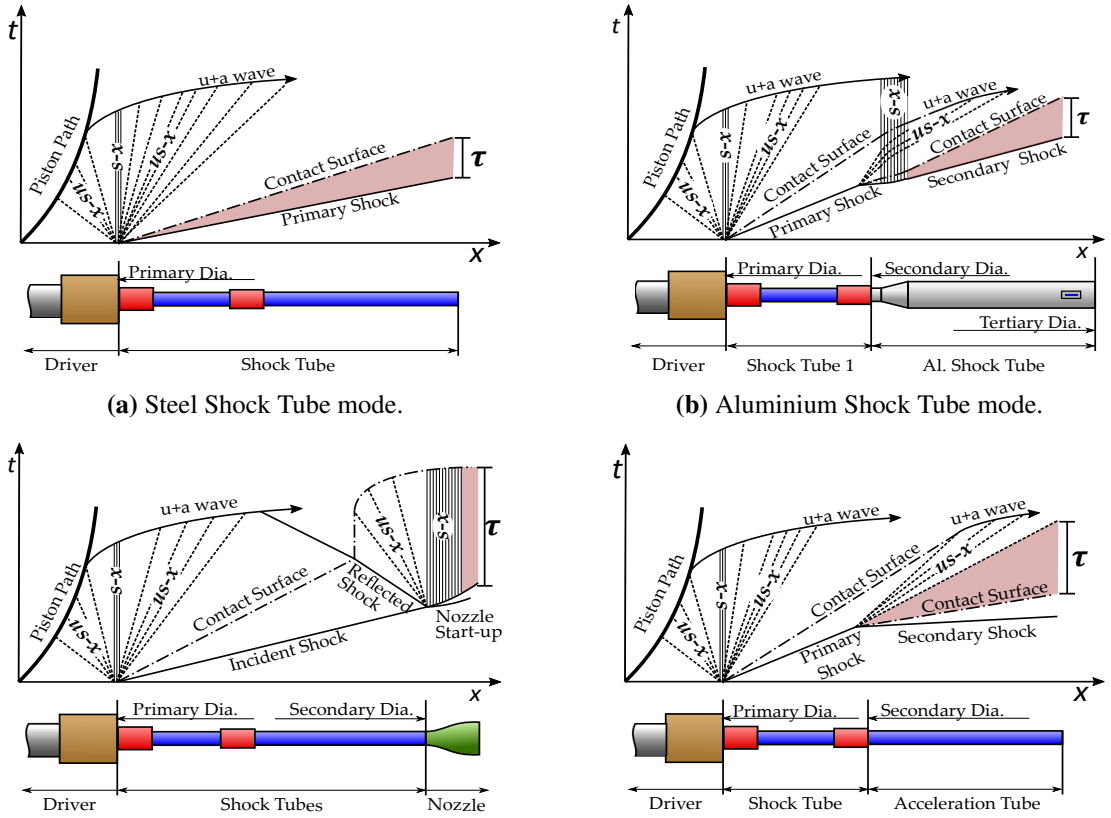
Section	Length, m	Internal Dia., mm	Outlet Dia., mm
Reservoir	2.8	342.9	300.0
Compression Tube	6.0	300.0	76.2*
Shock Tube 1	2.8	96.3	96.3
Reflected Shock Tunnel	5.3†	96.3	220.0†
Expansion Tube/Tunnel	6.0†	96.3	96.3†
Shock Tube	6.0	96.3	96.3
Aluminium Shock Tube	7.1	225.0	225.0

**Interchangeable orifice plate, currently matched to original T3 Shock Tube diameter.*
†Variable depending on nozzle chosen. Values shown representative of this work.

so the left portion of each figure is identical. At the highest level, the difference between the modes is the exact mechanism through which the test flow is generated. For example, in ST mode the test gas follows directly behind the primary shock, whereas in an ExT it must subsequently undergo an unsteady expansion to the desired condition. The location of the test flow region is coloured red in Figure 3.4 to aid comparison.

Shock Tube Modes

Shock tubes are used extensively for fundamental fluid dynamics research, chemical kinetics studies and computational code validation. This is in part due to their simplicity: they approximate one-dimensional flow phenomena, require relatively few input parameters and can — in the simplest cases — be modelled analytically. Whilst a large number of shock tubes are in use globally, the fraction active in the field of aerothermodynamics is small (Grinstead et al., 2010; Yamada et al., 2011; Brandis et al., 2010b). From the perspective of aerothermodynamic ground testing, shock tubes can be used to recreate the post-shock conditions ahead of an entry vehicle, permitting investigation of the thermochemical state of the gas. Notably, they are currently the best source of measurements of shock-layer radiation, which can contribute the majority of the peak heat flux on an entry vehicle (Brandis and Johnston, 2014) and cannot be accurately recreated with scaled model testing (Andrianatos et al., 2015). In general, shock tubes are not used for scale model testing; this is primarily due to the lack of an



(a) Steel Shock Tube mode.

(b) Aluminium Shock Tube mode.

(c) Reflected Shock Tunnel mode.

(d) Expansion Tube mode.

Figure 3.4 – Distance-time diagrams of T6 facility modes. The nominal test time, steady expansion regions and unsteady expansion waves are denoted by τ, s-x and us-x respectively. The region of useful test gas is shaded red.

expansion process following the shock-heating of the test gas. The test slug thus remains compressed, resulting in short test times. Additionally, the flow retains a high static enthalpy; the model shock-layer is therefore not correctly reproduced as the Mach number is limited and hence too low for the Mach number independence principle to apply. The free-stream is also highly dissociated which affects the non-equilibrium processes in the flow around the test article.

T6 has two distinct shock tube modes: the Steel Shock Tube (SST) and Aluminium Shock Tube (AST). The main purpose of these modes is to perform shock-layer radiation experiments, wherein a normal shock of desired velocity is passed through a quiescent gas of a pressure and composition chosen to match a trajectory point of interest. The goal of these studies is to make spatially- and spectrally-resolved measurements of the shock-layer as it passes the test section. An analogy is then made between the evolution of the

thermochemical state of the gas behind the normal shock and the stagnation line of an entry vehicle. This approach has the advantage of exactly matching the post-shock conditions to flight, with no scaling required. Depending on the measurement made, estimates of vehicle radiative heating, thermochemical rates and species populations can then be determined which ultimately gives a better understanding of the flight environment. Initial results from such experiments in T6 have previously been presented (Collen et al., 2019).

Shock Tube Modes: Steel Shock Tube Mode

The T6 SST mode consists of a steel barrel approximately 9 m in length with an internal diameter of 96.3 mm. For shock-layer radiation experiments, the approach as used in the X2 facility is followed, wherein the shock front is imaged as it emerges from the end of the tube (Brandis et al., 2010b). As will be shown in Section 3.4, the SST offers the better performance of the two shock tube modes — speeds in excess of 13 km s^{-1} have been achieved. Thus the primary purpose of the SST mode is to investigate shock-layer radiation at very high entry velocities, as would be typical for vehicles on hyperbolic Earth return or Ice Giant entry trajectories. In addition, the comparatively simple configuration of the SST (i.e. no nozzle or secondary diaphragm) make this mode ideal for the validation of computational tools and investigation of fundamental shock tube flow phenomena (Satchell et al., 2021a).

Figure 3.4a shows a distance-time diagram of SST operation. A test condition is defined by three parameters: test gas fill pressure and composition, and the incident shock speed. The test gas initially fills the shock tube. After rupture of the primary diaphragm, the driver gas expands into the shock tube, driving a strong shock through the test gas at the desired velocity. This produces a slug of shock-processed gas which travels behind the shock, undergoing the same non-equilibrium thermochemical processes as would be observed in the stagnation line shock-layer of an entry vehicle. The test time is therefore defined by the distance between the primary shock and the contact surface, which represents the boundary between the shocked test gas and expanded driver gas. The location of this test flow is shown in red in Figure 3.4a.

Shock Tube Modes: Aluminium Shock Tube Mode

The T6 AST mode was designed specifically for shock-layer radiation studies. The aluminium construction is intended to reduce the presence of carbon contaminants in emission spectra. A diaphragm at either end of the tube isolates the test gas from other sections of the facility, allowing ultimate pressures of approximately 10^{-3} Pa to be achieved with leak rates of 10^{-5} Pa s^{-1}. This minimises test gas contamination due to the ingress of atmospheric air, which can significantly influence the chemical kinetics through the shock for certain compositions of interest e.g. Titan (Brandis and Cruden, 2017b). The AST features two, 200 mm long windows at the downstream end of the tube, integrated into the tube wall. These permit optical access, with a range of window materials being available to allow transmission from the vacuum ultraviolet to the infrared (approximately 120 nm to 5500 nm). Finally, the key attribute of the AST is its large diameter, which is increased from the nominal shock tube bore through a 12° half-angle conical nozzle to 225 mm. The benefits of this are two-fold: firstly, the larger diameter leads to a greater integration path-length for optically thin radiation, which increases the achievable signal-to-noise ratio. Secondly, the boundary layer is relatively thinner in comparison to the tube diameter which results in a more uniform core flow, less shock deceleration and a longer slug of test gas (Mirels, 1963). This extends the range of conditions at which post-shock equilibrium can be achieved.

Whilst the large diameter of the AST is favourable for radiation experiments it results in a reduction in performance in comparison to SST mode. In the AST, the maximum shock speed achievable is reduced due to the lower pressure and temperature of the expanded driver gas downstream of the nozzle. Such a design is thus suited to the simulation of conditions where either the flight velocity or free-stream density is low but radiative heating effects may be significant. Examples relevant to currently proposed programmes include manned Mars missions, Titan entry or high-altitude aerobraking trajectories. Similar designs (in which the nominal diameter of the shock tube is increased through an expanding section) have been employed on both the NASA Ames EAST facility and the X2 expansion tube to investigate such conditions (Cruden, 2012a; Jacobs et al., 2015; Cruden et al., 2014; Brandis and Cruden, 2017b).

The distance-time diagram for the AST mode of operation is shown in Figure 3.4b. The experiment proceeds identically to those conducted in SST mode, with the exception that the test gas now initially sits in the AST. The shocked gas from the first tube — followed by the driver gas – then expands through the conical nozzle into the AST, driving the secondary shock into the test gas. As previously discussed, the expansion results in a reduction in shock speed. It is this shock that generates the test flow; this is again shown in red in Figure 3.4b.

Reflected Shock Tunnel Mode

Reflected shock tunnels have been used extensively over the past half-century to study a range of high-enthalpy aerothermodynamic problems, including scramjet engine testing, boundary layer transition and hydrogen ionisation studies — e.g. Stalker et al. (2005) and Stalker (2006). Physically, the difference between RST and SST modes is the presence of a converging-diverging nozzle at the downstream end of the facility, as shown in Figure 3.3. Currently, T6 has both Mach 7 and 8 nozzles available. Unlike the ST modes, RST mode is primarily meant for the testing of scaled models. The nozzle expansion provides a significant core flow region; models may therefore be made a sufficient size to permit high-resolution measurements of surface properties (e.g. pressure, heat flux) and aerodynamic forces. As RSTs typically have test times between 1 ms and 10 ms, they are particularly suitable for the investigation of relatively long time-scale phenomena where flow enthalpy is important, such as combustion. Many large-scale RST facilities operate world-wide, with capability to test up to orbital conditions (Hannemann et al., 2016; Stennett et al., 2020; Itoh et al., 1998; Mundt, 2016; Wang et al., 2017; Tsai et al., 2009).

Figure 3.4c shows an idealised distance-time diagram of T6 in RST mode. Initially, the test gas sits in the shock tube between the primary diaphragm and a secondary, Mylar diaphragm near the nozzle throat. As in SST mode, the test gas is first processed by the primary shock. This shock then reflects from the nozzle throat region, stagnating the test gas via a reflected shock process. This stagnated gas then acts as the supply reservoir for the nozzle flow, permitting aerothermodynamic testing of scaled models at matched total enthalpy and Reynolds number. The Mach number is often not matched as nozzles are

typically designed for fixed Mach numbers and are affected by variations in stagnation enthalpy. This is sufficient for many hypersonic aerothermodynamic studies due to the Mach number independence principle. However, it is possible to fully match a flight condition — including Mach number — when operating a properly designed nozzle at its nominal enthalpy e.g. Doherty et al. (2015).

The test time in a reflected shock tunnel is defined by the duration of steady conditions in the nozzle supply region. This is typically limited by three fundamental mechanisms: drainage of the available test gas and hence ingestion of the contact surface into the nozzle, the arrival of expansion waves from the decaying pressure in the driver, and the motion of the contact surface after passage of the reflected shock. The former is the scenario shown in Figure 3.4c and is defined by the geometry of the facility, in particular the shock tube length and the relative area of the nozzle throat and shock tube bore. The second effect – arrival of expansion waves from the driver (the $u+a$ wave in the plots of Figure 3.4) — can be sufficiently delayed through the use of a free-piston. This is achieved through the 'over-driving' technique discussed in Section 3.2.1. The final consideration — the motion of the contact surface — presents the greatest challenge for condition design. If the Mach number of the reflected shock in the expanded driver gas and shocked test gas is equal, the reflected shock will pass through the interface unhindered and stagnate it as shown in Figure 3.4c. Conversely, a mismatch in Mach number will cause the contact surface to either accelerate downstream or to reverse its motion. This leads to a corresponding departure from the nominal steady conditions in the test gas through an arrival of either a third shock or an expansion fan, respectively. The achievement of a stationary contact surface is known as tailoring (Wittliff, 1959). In reality, this process is more complex as the contact surface is an extended region of vortical structures; the shape of which is highly dependent on the upstream flow geometry and diaphragm opening processes (Goozée et al., 2006). In addition, the presence of a boundary layer can cause complex interactions when the reflected shock meets the contact surface, including jetting of driver gas near the wall (Stalker and Crane, 1978) which results in contamination of the test flow.

Expansion Tube Mode

As flight total pressure and enthalpy increase, it becomes increasingly difficult to reproduce test conditions of interest in a ground test facility which employs a nozzle stagnation region. From a practical perspective, the high temperature and pressure test gas must be safely contained for the duration of the test. Erosion of the nozzle throat has been observed in several large reflected shock tunnel facilities, increasing costs of test campaigns and resulting in uncertainty in flow conditions. In addition, reflected shock tunnels also exhibit issues with residual free-stream non-equilibrium thermochemistry as stagnation enthalpy is increased (Hornung, 1990; MacLean and Holden, 2006). Expansion tubes, first proposed by Trimpi (1962), offer the potential to reach significantly higher velocities, with total pressures on the order of gigapascals, whilst significantly reducing the level of thermochemical non-equilibrium in the free-stream. This is achieved by increasing the total enthalpy of the test flow through an unsteady expansion process which avoids stagnating the gas. These advantages come at the expense of test time, which is typically on the order of 10–100 µs. Expansion tubes are of particular use for conditions with high total pressures, such as low altitude, high Mach number scramjet experiments and atmospheric entry (Gildfind et al., 2016). In general, expansion tubes are used for scaled model testing. Although less common than RSTs, several research-level expansion tubes are in active use (Gildfind et al., 2016; Tanno et al., 2016; Tamagno et al., 1990; Dufrene et al., 2007; MacLean et al., 2013).

Figure 3.4d presents a distance-time diagram showing the theoretical operation of T6 in expansion tube mode. As in SST mode, the test gas is initially processed by an incident shock generated by rupture of the primary diaphragm. A thin secondary diaphragm (either aluminium foil or Mylar) at the end of the shock tube initially separates this test gas from a region of very low pressure lab air, known as the accelerator gas. When the primary shock reaches this diaphragm the diaphragm ruptures, allowing the high pressure, shock-heated test gas to unsteadily expand into the acceleration tube. This supersonic unsteady expansion process results in a net increase in total enthalpy, as given by Equation (3.1) (from Trimpi (1962)). The region of shocked and expanded shock tube gas makes up the test flow, as shown in Figure 3.4d. At high velocity conditions,

the test time is typically limited by the arrival of the unsteady expansion fan (which follows the test gas) at the test model.

$$dH = -(Ma - 1)dh \tag{3.1}$$

3.3 Free-Piston Driver Commissioning

A prerequisite for achieving high performance and safe operation of a free-piston driver is a thorough understanding of the piston dynamics. The multi-modal nature of T6 necessitates a range of driver conditions to enable testing across the wide range of desired flight trajectories. This section details the development and commissioning of four driver conditions using two different piston masses of 36 kg and 89 kg. Similar conditions were previously used in T3 and produced total enthalpies from 3.0 MJ kg^{-1} to 39.0 MJ kg^{-1}. This range is sufficient to meet current test requirements, however further driver conditions will be developed as necessary to support future test campaigns.

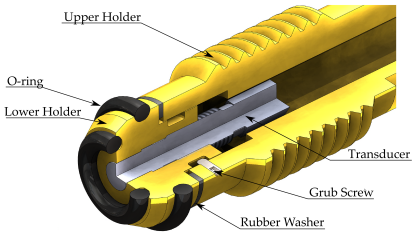
To characterise the motion of the piston, commissioning tests are performed with a thick blanking plate (designed to prevent rupture) in place of the diaphragm. This 'blank-off test' arrangement provides the necessary experimental data to calibrate numerical predictions of the piston motion. The approach is as follows: the greatest risk to the facility occurs after diaphragm rupture due to the loss of cushioning driver gas from in front of the piston. In a blank-off test, no rupture occurs and the piston is thus prevented from striking the buffers. The blanking plate contains a pressure transducer, which allows inference of the piston motion and is the primary measurement used to calibrate a computational model of the free-piston driver (Section 3.3.2). This can then be used to predict the piston impact speed during a real test. The plate must incorporate pressure instrumentation as, unlike more modern free-piston tunnels, the T6 driver does not feature a pressure transducer at the primary diaphragm station.

3.3.1 Driver Commissioning: Experimental Arrangement

The blanking plate used in lieu of the primary diaphragm is shown in Figure 3.5a and was manufactured from S355 mild steel with a total thickness of 70 mm. The blanking



(a) Photograph of blanking plate with nylon buffers, taken after testing.



(b) Detail view of blanking plate transducer mount.

Figure 3.5 – Components used for T6 free-piston driver blank-off tests.

plate was fitted with six nylon buffers, 60 mm in diameter and 55 mm in length to further reduce the risk of damage. The thickness of the plate allows for a design pressure of 100 MPa and permits inclusion of the pressure transducer. Previous studies employing piezoelectric pressure transducers in shock tunnels have experienced issues with excessive noise, which is typically attributed to transmission of high-frequency vibrations through the facility structure (Gildfind et al., 2013; Wagner, 12–13 April 2018). Based on these observations, attempts were made in the current work to ensure the pressure transducer was vibrationally isolated from the facility.

A section view of the resulting transducer holder assembly is given in Figure 3.5. Made of brass, this transducer mount was designed such that there was no path of continuous metal-on-metal contact between the sensor and the facility. The transducer (a PCB Piezotronics series CA102B03, removed from the factory-supplied threaded mounting adapter) is screwed into the lower half of the assembly, which is separated from the blanking plate by two nitrile o-rings. The upper half is isolated from the lower half by a rubber washer. The rubber washer offers some degree of vibration isolation while also allowing sufficient contact to retain the sensor against the high pressures experienced at the end of the compression tube. Two grub screws allow retrieval of the transducer and lower holder half sub-assembly. A circumferential groove ensures that these grub screws are not in contact with the lower half when the assembly is fully tightened.

The original 36 kg and 90 kg T3 pistons were refurbished for the testing reported here. The refurbishment consisted of re-skimming the outer diameter of the piston

Table 3.2 – Developed T6 Driver Conditions.

Piston	Condition	P_{Res}, kPa	P_4, MPa	X_{He} , %	Λ_r , -
Aluminium (36 kg)	A	730	9.8	0	60
	B	2100	29.6	100	60
	C	3500	46.2	100	60
Stainless Steel (89 kg)	HA	5500	20.6	19	22

body, replacing the downstream seal and wear rings and changing their material to oil-impregnated nylon. A screw thread was also added to the front face of each piston to facilitate retrieval from the compression tube. These modifications have resulted in a reduction in piston mass to 35.8 kg and 88.6 kg. Approximately 20 blank-off tests were conducted, leading to the development of four driver conditions. These are summarised in Table 3.2, where each condition is defined in terms of its helium mole fraction (with the balance made up by argon), nominal rupture pressure and compression ratio at rupture. For completeness, the required reservoir pressure is also included.

3.3.2 Driver Commissioning: Results

The purpose of blank-off testing is to tune computational models, building confidence in the predictions of piston trajectory. The numerical code chosen in this work to model the facility was L1d3, a quasi-one-dimensional transient Lagrangian code with equilibrium chemistry capability (Jacobs, 1998). This code has been shown to accurately reproduce experimental results in many other free-piston facilities at similar conditions (Mundt et al., 2007).

Translation of the three-dimensional geometry of a real facility into the one-dimensional code causes an inherent loss of fidelity. It has been shown that better agreement can be achieved by ensuring that the volume of each section of facility is reproduced accurately in the computational geometry (Andrianatos et al., 2016). However, fully two- and three-dimensional flow features can never be captured by L1d3 and so loss factors are used to account for their effect. The two sources of loss considered are the minor pressure loss coefficient (K_L) through the piston launcher (where the flow is forced to expand radially) and the piston seal friction factor (f_f). Table 3.3 presents the values of these

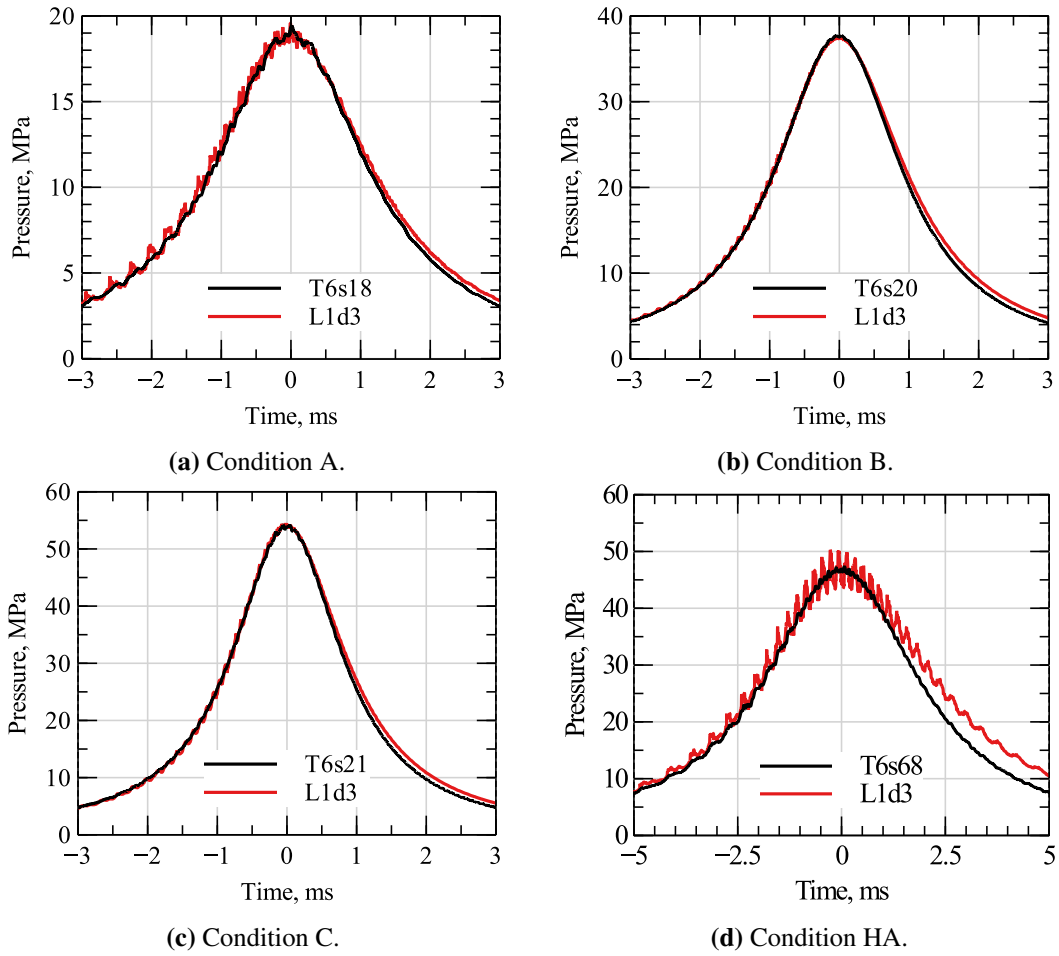
Table 3.3 – L1d3 model tuning parameters to match blank-off data.

Piston	K_L	f_f
Aluminium (36 kg)	3.4	0.275
Stainless Steel (89 kg)	3.7	0.880

tuning parameters which gave the best match to the experimental data for each piston. In the case of the aluminium piston, where multiple conditions have been tested, a single set of loss factors was found to match well across all conditions. These values also compare favourably with those found for the X2 expansion tube by Gildfind (2012), which has a similar launcher geometry. The results for the stainless steel piston launcher loss coefficient also show good agreement with these values. The piston friction factor is significantly higher for the stainless steel piston than that found for the aluminium piston. This difference is attributed to a tighter fit of the stainless steel piston's nylon wear rings in the compression tube bore due to a revision of manufacturing tolerances between the refurbishment of the two pistons.

Representative experimental pressure traces are shown in Figure 3.6 alongside the matched L1d3 results for the four conditions tested. In each case the pressure traces have been time-referenced to align the peak values of the numerical and experimental results. The secondary waves which occur when argon is used as the driver gas complicate manual identification of the peak pressure times. As a result, the peak was identified by fitting a curve (arbitrarily chosen as a fourth-order Gaussian) to the experimental and computational data for each condition. Whilst there is no specific physical basis for this choice of fitting function, it was found to give good agreement for the computational results for which the exact point of piston reversal is known. This approach was thus deemed sufficient to also fit the experimental traces.

The results of Figure 3.6 demonstrate good overall agreement between the computational model and experiments, as seen both in the peak pressure values and in the timing of the argon secondary wave processes visible in Figures 3.6a and 3.6d. The stronger damping of these secondary waves in the experimental data is due to the pressure transducer being mounted in a recessed cavity which results in a longer rise time. This was



(a) Condition A. **(b)** Condition B. **(c)** Condition C. **(d)** Condition HA.

Figure 3.6 – Representative results from free-piston blank-off tests with comparison to matched L1d3 model.

not modelled in L1d3. The initial pressure rise is well matched, however the computational model slightly over-predicts the pressure during piston rebound. This effect is likely due to heat loss from the driver gas; L1d3 uses a pipe flow model to calculate heat loss which performs poorly at the low velocities experienced during blank-off tests (Gildfind, 2012). In addition, during the pressure peak the sensor is exposed to high gas temperatures (in excess of 4500 K). This causes thermal strains to be generated in the piezoelectric transducer which can result in an apparent fall in pressure. Whilst this was mitigated by coating the front of the transducer with silicone grease, the extent to which this effect is still present is not easily quantified.

The close agreement with the experimental results suggest that the L1d3 model can be trusted to accurately predict piston motion. These tuned parameters have since been used

to model facility performance for the experiments presented in the subsequent sections.

3.4 Shock Tube Modes

Figure 3.7 shows theoretical performance predictions of both T6 shock tube modes at conditions of interest for shock-layer radiation studies calculated using PITOT: a state-to-state equilibrium analytic code for high enthalpy pulse facilities (James et al., 2018b). This analysis is based on driver condition C, i.e. that with the highest performance, as detailed in Table 3.2. These predictions are overlaid on example trajectories of Earth entry missions of interest. Also shown in Figure 3.7 are the test points reached to date in both modes. The vast majority of tests in SST mode have targeted $10\,\mathrm{km\,s^{-1}}$ and 0.2 Torr (26.6 Pa), a benchmark condition for shock-layer radiation (Brandis and Cruden, 2017a). Tests at similar conditions have also been undertaken in AST mode, where significant portions of the Orion return trajectory and low-speed Hayabusa entry conditions have been investigated. These are also identified in Figure 3.7.

Figure 3.7 also shows the theoretical performance achievable through addition of a secondary driver. The secondary driver is an intermediate tube (for T6, Shock Tube 1 is used; see Figure 3.3), typically filled with helium, between the main free-piston driver and the shock tube; this can permit faster shock speeds to be achieved in the test gas. A full analysis of the mechanisms by which this performance augmentation is achieved is provided by Gildfind et al. (2015). Commissioning of the secondary driver section is on-going. However, predictions suggest the majority of the presented flight trajectory points could be reached in SST mode with a secondary driver, with theoretical speeds in excess of $15\,\mathrm{km\,s^{-1}}$ achievable. To date, the fastest shock speed achieved in combination with a secondary driver is $13.3\,\mathrm{km\,s^{-1}}$.

3.4.1 Shock Tube Modes: Experimental Arrangement

The shock speed variation through the facility is determined using time-of-arrival calculations between PCB Piezotronics 113 and 132 series pressure transducers flush-mounted in the shock tube wall. In the SST mode, 12 shock timing station positions are distributed along the length of the facility. In comparison, the AST mode has 17 measurement

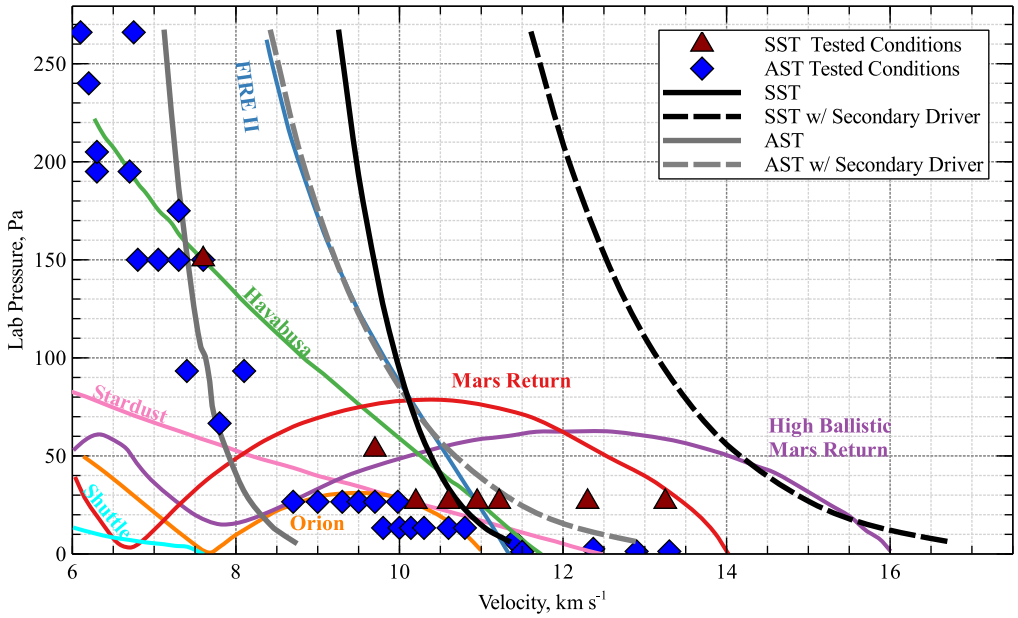


Figure 3.7 – Performance predictions of T6 ST modes with air test gas, alongside Earth entry trajectories (adapted from McGilvray et al. (2015)) with tested conditions shown.

locations; four of these are clustered around the optical windows at the end of the tube to better resolve the shock speed variation at the measurement location.

The arrival time of the shock at each sensor is extracted automatically using the method of James (2019), wherein the wall pressure traces are processed using a Canny edge detection algorithm to detect the shock location. The shock speed is then calculated using the time-of-flight between the transducer locations. In this work, the values for shock speed are plotted at the central point between the positions used for the calculation.

The uncertainties in shock speed are calculated using the method detailed in Appendix 2 of James et al. (2018b), which accounts for uncertainty in both the distance between transducers and the arrival time. Due to the similarity of experimental arrangement, the distance uncertainty was assumed to be identical to that of those authors with a value of ± 2 mm used for each transducer location. The error in the arrival time is made up of two components: the data acquisition system sampling period and the uncertainty in the shock arrival time itself. In this work, all data was recorded with a National Instruments 6368 series card at its maximum sampling frequency of 2 MHz. The uncertainty in the shock arrival time is assigned by the experimenter by manually selecting the period in which

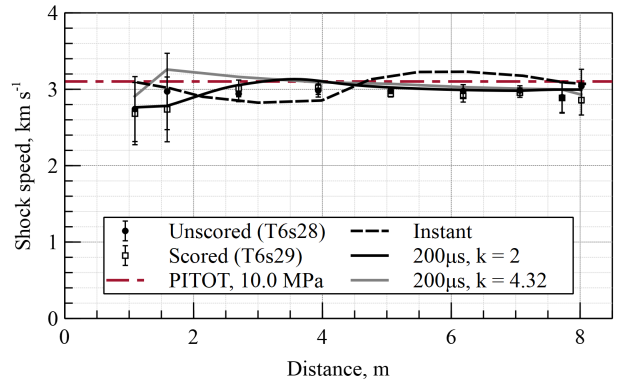
they are certain the shock has arrived. The error is typically largest at the downstream end of the tube (where the transducers have the smallest spacing, and therefore are most sensitive to uncertainties in transducer spacing and transit time) and at the beginning, where the sensors used in this work had a lower sensitivity and therefore the arrival of the shock cannot be identified with the same level of confidence.

3.4.2 Shock Tube Modes: SST Experimental Results

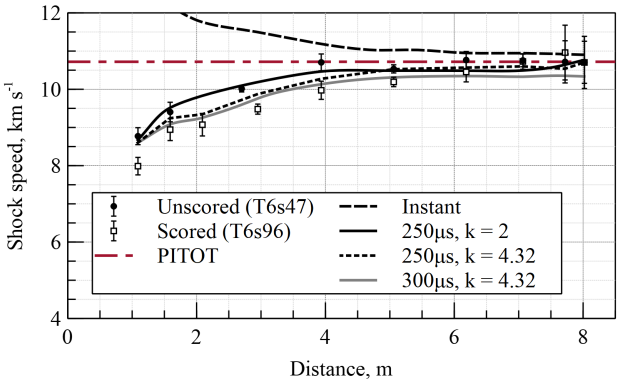
Representative shock speed data for driver conditions A and C (as detailed in Table 3.2) are given in Figure 3.8. For the tests reported here, lab air (defined in this work as ambient air from the experimental area) was used as gas purity was not expected to have a significant effect on the observed performance. In general, good agreement is observed between the experimental measurements and the predictions of PITOT at the downstream end of the tube. For all cases an initial ramp-up in shock speed is observed, which is attributed to the finite opening time of the primary diaphragm. This effect has been noted by several authors e.g. White (1958).

The T6 diaphragms are either unscored, where a plain sheet of material is used, or scored, in which case a mark is machined or stamped into the surface of the diaphragm. Scored diaphragms are generally preferred, as the rupture pressure can be more finely controlled via the depth of the score. Furthermore, smaller and fewer fragments of the diaphragm detach if it is scored, reducing the risk of damage to expensive models in the test section or to the tunnel itself. However, the rupture pressure of scored diaphragms is challenging to predict and can exhibit wide variation depending on the particular technician, manufacturing process, cutting tool and material used. While the T6 driver pressure is not measured directly, variability in rupture conditions is observed through the shock speed achieved. Other facilities using scored diaphragms have reported differences in burst pressure of up to 30 % (Boyer, 1965).

The plots of Figure 3.8 show shock speed variation for both unscored and scored diaphragms at both conditions. Whilst the differences between the aluminium diaphragm tests of Figure 3.8a are small, the qualitative trend of shock speed between scored and unscored shows greater differences for the case of Figure 3.8b. Here, the unscored test



(a) Condition A, P_1 = 1000 Pa.



(b) Condition C, P_1 = 26.6 Pa.

Figure 3.8 – Finite opening time diaphragm simulations using L1d3 (greyscale lines) with comparison to experiment (points). Also shown is the prediction of the PITOT code (dash-dot red line). All tests were conducted in lab air.

reaches an essentially steady speed by approximately 4 metres, whereas with scored diaphragms shock speed monotonically increases until almost 6 metres. The reasons for this are explored in greater detail in Section 3.4.3. In either case, for the majority of the tube length this variation is small in the context of other facilities which perform shock-layer radiation experiments (Chandel et al., 2019).

3.4.3 Shock Tube Modes: Facility Modelling

The ability to accurately predict shock speed variation is essential for the design of pulse facility experiments. The magnitude of shock-layer radiation is particularly sensitive to changes in shock speed (Brandis et al., 2010a). Shock speed variation is also critical when the facility is operated with a secondary driver or in expansion tube mode (see Section 3.6). In those tests, the secondary diaphragm is at a distance of approximately 3 m

along the tube. From Figure 3.8, diaphragm opening processes dominate the shock speed profile in this region and therefore the performance in these modes is strongly coupled to these opening effects. Understanding the mechanisms by which shock speed variation occurs in the test facility is thus fundamental to the design of high-performance test conditions. Furthermore, given the high capital and labour cost of tunnel test campaigns, it is desirable to develop a predictive capability for shock tube performance which can be used to investigate test conditions *ex ante*.

To investigate differences in shock speed variation a model of the whole facility was developed using the L1d3 code. The model used was identical to that used in Section 3.3.2 with the addition of the tunnel geometry downstream of the primary diaphragm. The test gas was modelled as equilibrium air, using a look-up table generated from the NASA Chemical Equilibrium with Applications (CEA) code of Gordon and McBride (1994). The boundary-layer mass loss models of Doolan and Jacobs (1996) were also applied in the test gas to better capture shock deceleration due to the Mirels effect. For the shots represented in Figure 3.8b their laminar correlation was used, whereas for simulations of the experiments of Figure 3.8a the turbulent formulation was applied due to the significantly higher shock tube fill pressure. This distinction was made based on the guidelines presented by Mirels (1964).

Two simulation methodologies were used: first, the diaphragm was modelled with the traditional approach used in the code, in which it ruptures instantaneously at a given pressure. Secondly, to better capture the influence of finite diaphragm opening time, a variable-area boundary condition was applied in place of the diaphragm. This feature was initially developed in the thesis of Doolabh (2016) and was primarily meant for the modelling of valves in Ludwieg Tube facilities. However, it essentially allows arbitrary transient variations in area to be applied which can be used to model diaphragm opening profiles from the literature.

Two factors influence the downstream variation of shock speed during diaphragm opening: the overall duration of the opening process and the variation in area during this time. The model used for the variation in area is given in Equation (3.2). Two approaches were used: the first was a parabolic curve (k = 2) which is a reasonable approximation

to the analytic calculation of Simpson et al. (1967). The second model was based on the experimental observation by Rothkopf and Low (1974) that whilst the aluminium opening behaviour closely followed the 'ideal' predictions of Simpson et al. (1967), the initial tearing of the petals of a ductile diaphragm can take up to 50 % of the total opening time, with only 5 % of the area being open by this point. This suggests a very different variation in area (or 'opening profile') for the same total opening time. Rearranging Equation (3.2) to solve for k and using 0.5 and 0.05 for the normalised time and area respectively (representing only 5 % of the full area being open after 50 % of the total opening time), a value can be calculated for k of 4.32.

For the T6 experiments, the aluminium diaphragms were of grade 1050-H14A with an elongation at failure of 10 % to 15 % according to the material certificate. The stainless steel diaphragms were manufactured from grade 304 2B sheet; these had an elongation at failure of 55 % to 60 %, again determined from the provided data for the specific batch of material. Given the large difference in ductility for the two diaphragm materials used it was anticipated that this property could be germane to the observed opening profiles of Figure 3.8. Although the findings of Rothkopf and Low (1974) regarding ductility were based on copper and brass diaphragms of unknown specification, the stainless steel used in the T6 experiments has a measured elongation equivalent to (or exceeding) common ranges for ductile alloys of these materials. In this work, we therefore assume that the scored stainless steel diaphragms can be modelled using the ductile value for k (i.e. 4.32).

$$\frac{A}{A_o} = \left[\frac{t}{t_o}\right]^k \tag{3.2}$$

The results of these simulations are also compared with the experimental data in Figure 3.8. For both cases of Figure 3.8 it can be seen that with the instantaneous opening model the initial trend in shock speed is not well captured, although there is reasonable agreement by the end of the tube. In contrast, the finite opening time results recreate the observed shock speed profile accurately along the entire tube length.

Considering the data of Figure 3.8a, a parabolic opening model with an opening time of 200 µs appears to provide the best match to the experimental data. The slower opening profile also produces a similar trend in shock speed, albeit with an additional brief increase at around 2 metres. Unfortunately, this was not resolved in the experiment given the transducer spacing used. The negligible difference in shock profiles is likely due to the relatively low overall shock speed: at a nominal velocity of 3 km s^{-1}, the shock will have travelled only 0.6 metres in the total diaphragm opening time. As a result, the largest differences in opening profile are upstream of the first pressure transducer and are therefore not observed experimentally.

The results for the L1d3 simulations at condition C are compared with the experimental data in Figure 3.8b. The unscored experimental results are best matched by a parabolic opening profile with a total duration of 250 µs. Notably, the steady-state velocity is achieved in both simulation and experiment by approximately 4 m. Conversely, the scored diaphragm results are best matched with the slower opening profile (k = 4.32) at an opening time of 300 µs. This model accurately captures the gradual rise in shock speed along the tube. Also shown for comparison is the effect of solely changing the opening profile, whilst maintaining the total opening time at 250 µs. It can be seen that the majority of the difference in the shock speed variation in the first half of the tube stems from the opening profile used, rather than simply the overall opening time.

The scored results are consistent with the conclusions of Rothkopf and Low (1974) regarding the slow initial opening of ductile materials. However, it is not immediately clear why the scored and unscored behaviour is so different, given that the material is identical. The majority of the disparity in opening profile is attributed to tearing of the score marks by Rothkopf and Low (1974), and so it may be that the failure mechanism of the unscored diaphragms is fundamentally different. In addition, the diaphragm opening is a complex, three-dimensional process for which the presented model presents a significant simplification. Nonetheless, good agreement with experiment is observed and the current level of fidelity is judged sufficient for the initial design of facility test conditions.

The results presented here demonstrate that to properly model the shock speed variation in a high-enthalpy shock tube requires consideration of the diaphragm opening

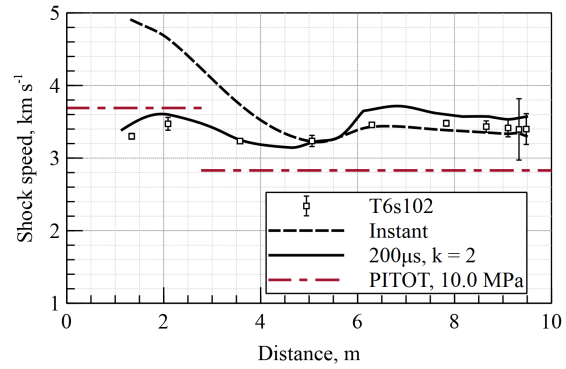
behaviour. Two parameters — the total opening time and the area variation throughout the opening — are shown to influence the evolution of shock velocity over the length of the facility. This modelling approach yields improved agreement with the experimentally measured shock speed profile. Based on the results of this study, work is currently ongoing to trial less ductile primary diaphragm materials for condition C, with the objective of further increasing facility performance.

3.4.4 Shock Tube Modes: AST Experimental Results

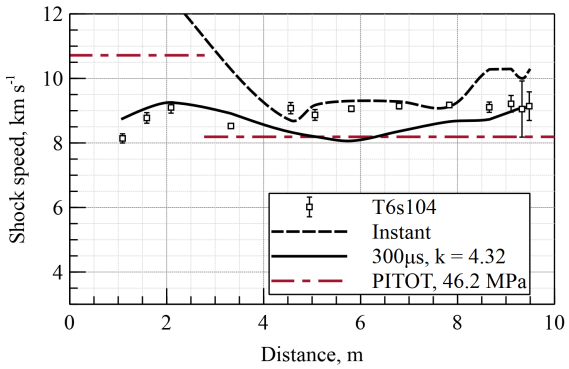
Representative shock speed variation for driver conditions A and C are shown in Figure 3.9. In both cases scored diaphragms were used. The behaviour up to 3 metres is equivalent to that observed in the SST, whereby the diaphragm opening process causes an increase in shock speed. For both conditions a dip is then observed in the velocity of the shock, after which there is a recovery to an approximately steady value by 5 m. In comparison with the SST results of Figure 3.8b, the scored diaphragms when used in the AST produce a flatter experimental shock speed profile. In the AST section, the maximum deviation from the mean shock speed is approximately 2 % and 5 % for Condition A and C respectively. This total variation is again low in the context of other similar facilities (Brandis et al., 2010a; Chandel et al., 2019).

Figure 3.9 also shows a comparison with both the PITOT and L1d3 codes. A positive result is that in both cases the shock speed at the end of the tube exceeds the ideal PITOT prediction. This is due to the state-to-state code's current implementation of the nozzle expansion process, which assumes the gas upstream of the shock tube steadily expands completely through the nozzle by an amount based on the area ratio between the AST and Shock Tube 1. The unsteady expansion into the AST test gas, and by extension shock speed, is then calculated based on these ideally expanded conditions. In reality, it is likely that the unsteady and steady expansion processes occur somewhat concurrently. Higher-dimensional effects, such as waves stemming from the driver, boundary layer growth and flow features in the nozzle may also moderate this behaviour.

Figure 3.9 also contains results of L1d3 simulations for each condition. In both cases, the diaphragm opening conditions — as determined from the SST data in Figure 3.8 —



(a) Condition A, P_1 = 26.6 Pa.



(b) Condition C, P_1 = 26.6 Pa.

Figure 3.9 – AST test data with comparison to numerical predictions. All tests were conducted in lab air.

were used. It can be seen that there is good agreement in the 96.3 mm tube (up to 3 m) and in the ultimate shock speed at the end of the AST. The flow is generally well-predicted for the experiments at Condition A, including with the instantaneous opening model (after approximately 5 m). However, for Condition C the finite opening time L1d3 results do not match the experimental data well in the region downstream of the nozzle. The agreement between 4 m and 8 m is better with the instantaneous model, but the arrival of a strong compression wave (from the driver) at approximately 8 m causes divergence from the experimental data. This behaviour has found to be consistent for a wide range of simulated rupture pressure and diaphragm opening parameters. A higher-fidelity computational assessment of the flow is underway to better quantify the nature of the wave processes through the nozzle and their influence on the shock speed downstream.

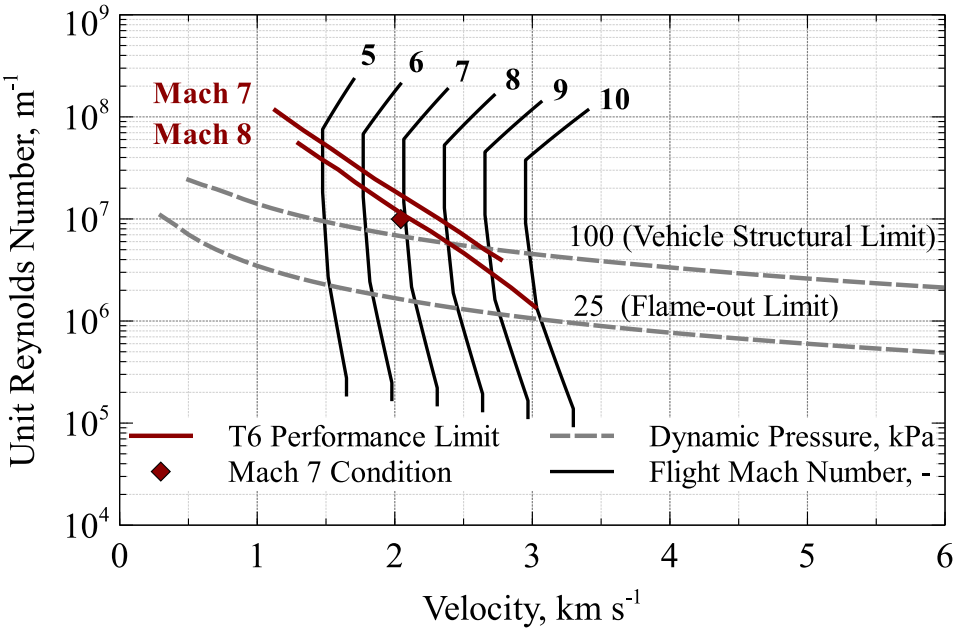


Figure 3.10 – Performance envelope of T6 in RST mode.

3.5 Reflected Shock Tunnel Mode

Figure 3.10 shows a comparison between the performance envelope of T6 in RST mode and typical air-breathing flight corridors across a range of flight velocities. Iso-curves of Mach number and dynamic pressure are given as a function of flight velocity and unit Reynold's number, calculated using the US Standard Atmosphere Model (NASA, 1976). At a given Mach number, the maximum and minimum unit Reynold's numbers are respectively defined by the structural strength of the vehicle and the ability to maintain combustion.

At the current time, contoured nozzles for nominal Mach numbers of 7 and 8 are available. Figure 3.10 also shows the maximum predicted performance envelope of T6 in RST mode with both of these nozzles. These performance curves have again been calculated using PITOT, using driver condition C (detailed in Table 3.2). An equilibrium expansion through the nozzle based on the ratio of the throat to exit diameters is also assumed. From these results, it can be seen that with the current infrastructure T6 is theoretically capable of reproducing the full air-breathing flight corridor up to Mach 8.

Finally, Figure 3.10 also shows the Mach 7 flight condition targeted in this work. The details of the measured properties at this test point are discussed in the subsequent sections.

3.5.1 Reflected Shock Tunnel Mode: Experimental Arrangement

For the experimental data presented here, driver condition HA (as detailed in Table 3.2) was used. The shock tube was filled to a pressure of 180 kPa, using a synthetic air mixture of 79.2 % N_2 and 20.8 %O_2 with total contaminants less than 2.2 ppm. This composition was used in preference to lab air to minimise errors in the thermochemical modelling of the nozzle discussed in Section 3.5.2. The analysis process used to select the facility filling conditions required for a desired test point has previously been presented (Subiah et al., 2019).

As discussed in Section 3.2.2, the nozzle supply conditions in a reflected shock tunnel are generated by passing a strong shock through the test gas and then causing said gas to stagnate upstream of the throat. The total conditions are typically calculated as follows: the total pressure is measured directly using pressure transducers upstream of the throat. The total enthalpy is inferred using the ESTCj code of Jacobs et al. (2011), wherein the measured initial shock tube fill pressure and shock speed are used as inputs to calculate the conditions through an ideal incident/reflected shock process. The nozzle supply conditions are then isentropically relaxed to the measured stagnation pressure, with the total enthalpy of the test flow calculated from these relaxed values. Proper characterisation of the test flow thus requires accurate measurement of the stagnation pressure and the incident shock speed along the facility.

The shock speed measurements are performed identically to those described in Section 3.4.1. In the nozzle stagnation region, PCB Piezotronics 102B03 series pressure transducers are used to measure the pressure behind the reflected shock. For these experiments, a Pitot rake was positioned in the test section at a distance of 25 mm from the nozzle exit. As shown in Figure 3.11, the rake consists of a steel wedge with 11 measurement positions, evenly spaced at 20 mm intervals from the centreline. For these tests both Pitot pressure (using 7 PCB Piezotronics series 113B27 piezoelectric transducers) and stagnation point heat flux measurements were made. The latter employed

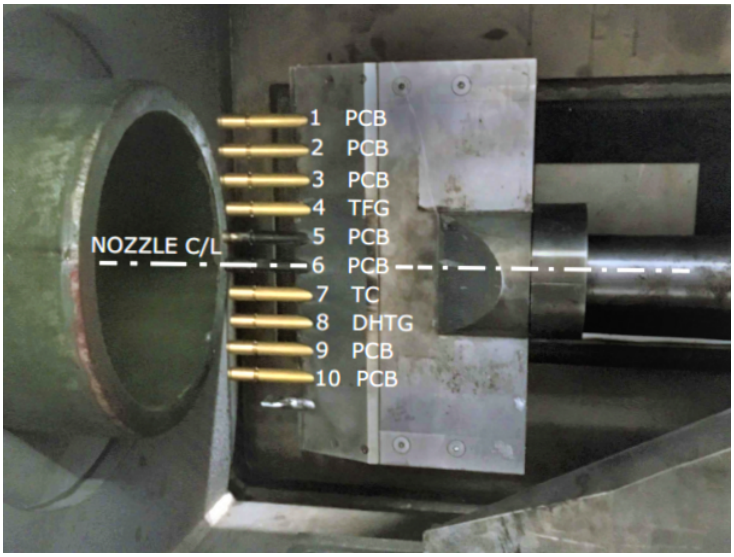


Figure 3.11 – Pitot rake in the T6 test section with gauge positions labelled (from Penty Garaets (2019)).

a platinum thin-film gauge, a coaxial surface-junction thermocouple (James et al., 2019b) and a novel diamond calorimeter heat transfer gauge (DHTG) developed by Penty Geraets et al. (2020). All sensors are held within brass probe bodies which extend upstream of the rake. In the post-test flow, impacts by fragments of metallic diaphragm material often occur. Consequently, the pressure transducers were protected by shield caps as described by Neely et al. (1991). The heat transfer gauges must be exposed to the flow to enable accurate measurements and so were flush-mounted in cylindrical bodies of diameter 10.50 mm and corner radius 0.13 mm.

3.5.2 Reflected Shock Tunnel Mode: Experimental Results

The measured shock speed variation through the facility is compared with an L1d3 prediction in Figure 3.12. For the L1d3 simulations, the finite opening model presented in Section 3.4.3 was used, with the slow opening profile and opening time of 180 µs applied. Good agreement is generally observed between the measured shock speed and the L1d3 prediction, although the simulation predicts a sharper acceleration at approximately 4 m. The reason for this feature can be identified in Figure 3.13, which plots the results of the simulation as a distance-time diagram using the log of static pressure. Here, a

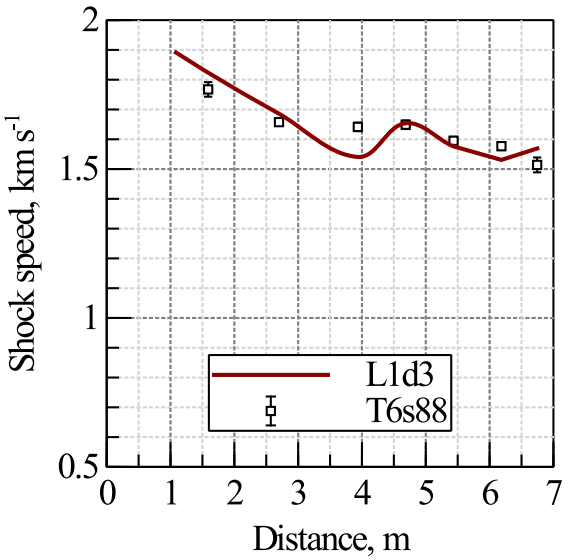


Figure 3.12 – Shock speed comparison between shot T6s88 and the L1d3 prediction.

compression wave — originating from the driver — is seen to reach the shock front at approximately 4 m, which causes it to accelerate. This effect appears earlier in the experimental data, though its precise position is not resolved given the spacing of the shock timing stations. The observed discrepancy is likely due to the tunnel geometry and diaphragm rupture model used in the simulation, which significantly simplifies the wave transmission processes occurring in this region.

Based on the experimental data, the shock speed for this condition is taken to be 1.52 km s^{-1}, which is the average value of the final three measurements. Using ESTCj, this results in a predicted stagnation enthalpy of 2.68 MJ kg^{-1} which is within 2 % of the target value of 2.7 MJ kg^{-1}.

Figure 3.14 shows a comparison between the experimentally measured stagnation pressure and the numerical calculation. Considering the experimental trace, the stagnation pressure aligns well with the target value of 26 MPa. The test time at the nominal condition, defined as $\pm$ 10 % of the target stagnation pressure value, is found from the experimental data to be 0.4 ms. This is also marked in Figure 3.14. Whilst this period represents the duration at the nominal condition, there is valid test flow after this period which can be analysed using quasi-steady methods before the onset of driver gas contamination (McGilvray et al., 2010b).

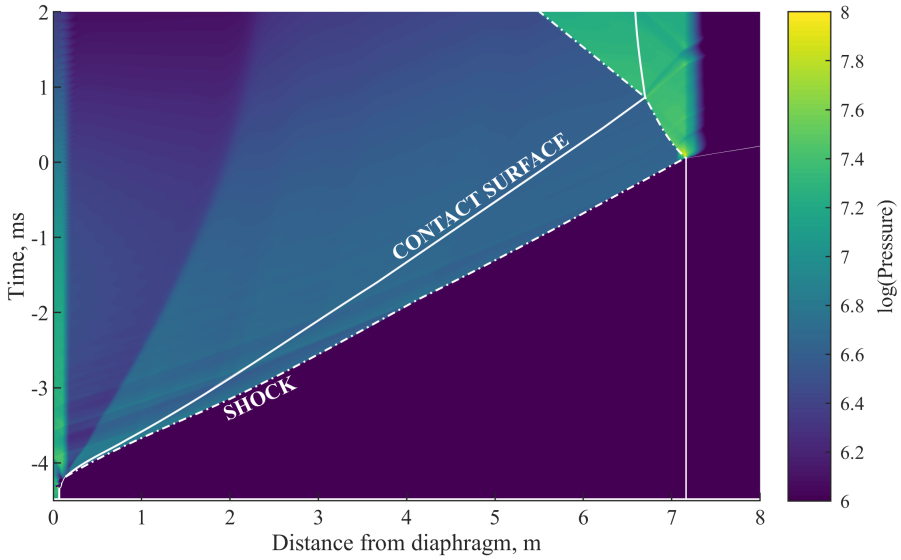


Figure 3.13 – Distance-time diagram of the L1d3 simulation of shot T6s88. The time axis is referenced to the arrival of the incident shock at the nozzle supply transducer, located at approximately 7 m.

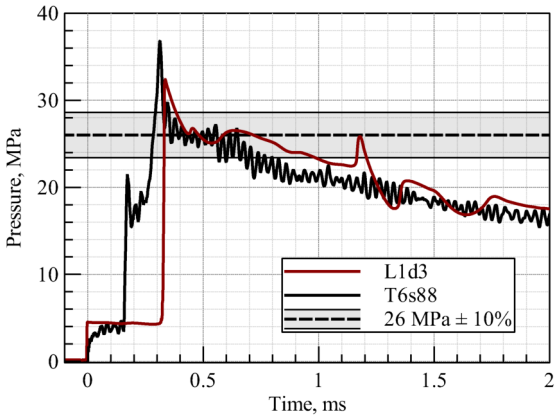


Figure 3.14 – Nozzle supply pressure comparison between shot T6s88 and L1d3 prediction.

In general, there is good agreement between L1d3 and the experimental results, both in terms of pressure magnitude during the test time and the decay rate. A sharp feature is present at approximately 1.2 ms in the simulated trace which is not observed in the experiment. The source of this wave is again visible in the distance-time diagram of Figure 3.13, where the stagnation pressure measurement is made at approximately 7 m. Here, the interaction of the reflected shock with the under-tailored contact surface generates a series of waves which travel downstream. These are significantly sharper in the computational result due to the idealised nature of the contact surface; in reality,

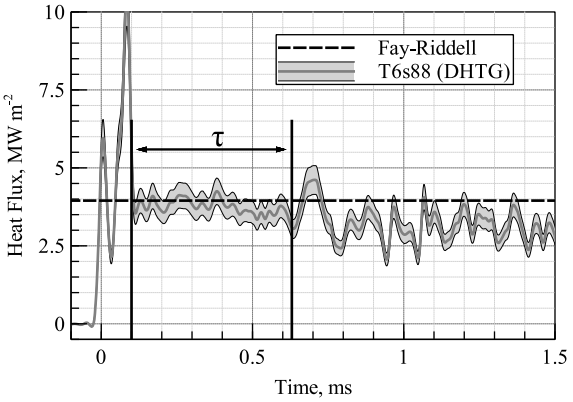


Figure 3.15 – Stagnation-point heat flux using the DHTG compared to the analytic calculation. The identified period of quasi-steady test flow is denoted by τ.

the boundary between the driver and driven gases is highly three-dimensional (Goozée et al., 2006), which tends to smooth out strong pressure reflections. This is not captured in L1d3 due to the quasi-one-dimensional nature of the code; similar discrepancies have been seen in the simulation of other facilities (Mundt et al., 2007).

Whilst the L1d3 results show a clean rise between the incident and reflected shock conditions, the experimental trace contains an intermediate pressure step. A similar feature is observed in some — but not all — other RST facilities and is not captured in other studies using L1d3 (Mundt et al., 2007). A full-facility numerical study of a reflected shock tunnel by Goozée et al. (2006) showed this feature to be caused by a complex interaction between the non-planar reflection of the shock from the end wall and the boundary layer, resulting in shock bifurcation. Further results presented in the thesis of Goozee (2003) using a combined experimental-numerical approach showed this pressure step to be significantly affected by the boundary layer thickness (and hence Reynolds number) and the end-wall geometry used. These factors explain both the inconsistencies in observation between facilities and why the (quasi-one-dimensional) L1d3 code does not reproduce the feature. Higher fidelity simulations to characterise this behaviour for the specific geometric case of the T6 RST mode are currently on-going.

Using the ESTCj code, the total enthalpy was calculated to be $2.68\,\mathrm{MJ\,kg^{-1}}$. Knowing the total pressure and enthalpy of the test condition, the method of Fay and Riddell (1958) was used to estimate the expected stagnation point heat flux on a spherical body.

As discussed in Section 3.5.1, the heat flux gauge holders are cylindrical; an empirical correction for an 'effective radius' (Zoby and Sullivan, 1966) — giving a value of 15.21 mm — has thus been used in the theoretical calculation.

The calculated heat flux for this condition is compared in Figure 3.15 with the experimental result from the DHTG. Good agreement is observed between the experimental heat flux measurements and the Fay-Riddell prediction during the test time. The measurement uncertainty for the DHTG is given by Penty Geraets et al. (2020) as 10 %, shown as the shaded region in Figure 3.15. This close agreement builds confidence in the calculated value of total enthalpy which will be further confirmed with direct measurements of total temperature via optical techniques in future experiments.

Reflected Shock Tunnel Mode: Nozzle Flow Analysis

To estimate additional properties of the test flow, a computational study was undertaken using an open-source Reynolds-Averaged Navier-Stokes computational fluid dynamics solver, eilmer4 (Jacobs and Gollan, 2016). The approach taken was identical to that used in previous studies of similar facilities, e.g. Chan et al. (2018), where the nozzle is simulated from the throat onwards. The measured stagnation properties are expanded to a Mach number of 1 to give a uniform inflow at the throat. The wall of the nozzle was assumed to be at a constant temperature of 300 K. A pseudo-space-marching approach was used to reduce the computational time needed to obtain a steady-state nozzle flow solution. The turbulence model used in the simulations was the k-ω turbulence model of Wilcox et al. (1998). To further reduce computational time, the wall functions of Nichols and Nelson (2004) was used to model the turbulent boundary layers. The application of wall functions is appropriate since boundary layer separation is not expected in the nozzle flow-field The turbulence intensity of the inflow to the nozzle was set to 5 %, with a ratio of the turbulent-to-laminar viscosity of 100. To examine the influence of boundary layer transition location on the core flow parameters, simulations with different transition locations downstream of the nozzle throat were performed. The boundary layer transition location was varied until a satisfactory agreement with the experimental Pitot pressure data was achieved. The final transition location is 380 mm downstream of the nozzle throat.

The computational grid which produced converged solutions for the flow simulations had 600 cells in the axial direction and 80 cells in the radial direction. Grid clustering was employed near the throat and initial expansion regions to resolve the larger flow gradients expected in these regions, and near the nozzle wall to ensure adequate resolution of the boundary layer. The grids near the nozzle wall were configured to be orthogonal to the wall to ensure that the near-wall flow parameters were properly approximated by the flow solver. The level of grid convergence is shown in Figure 16 with a plot of the mass-flow-weighted Mach number plotted against the inverse of the total cell number for each grid resolution. The coarse grid had 300 axial cells and 40 radial cells, the medium grid had 600 axial cells and 80 radial cells, while the fine grid had 900 axial cells and 120 radial cells. The mass-flow-weighted Mach number for the medium grid differed from the fine grid by only 0.7 %. It was thus concluded that the medium grid produced a flow-field at the exit of the nozzle that was sufficiently grid-converged for the analysis conducted in the present study.

The simulations were performed with three different thermo-chemical gas models to investigate the influence of high enthalpy chemical kinetics. These models were: equilibrium thermo-chemistry based on the 5-species air model from the CEA2 program of Gordon and McBride (1994), finite-rate chemistry based the Gupta et al. (1989) 5-species air model, and two-temperature thermo-chemistry based the 2-temperature, 5-species air model of Park (1989). The two temperatures considered are the translational-rotational and vibrational-electronic modes; it is assumed that these quantities represent the internal energy distribution for all chemical species. These thermo-chemistry models are referred to in this section of the paper as the *equilibrium*, *chemical non-equilibrium* and *thermo-chemical non-equilibrium models* respectively. The mixture transport properties (i.e. mixture viscosity and thermal conductivity) were calculated using mixing rules of Gordon and McBride (1994) which are a variant of Wilke's original formulation (Wilke, 1950).

Figure 3.17 presents a contour plot of Mach number iso-lines that were generated from simulations of the Mach 7 nozzle and the test section of the T6 facility using the equilibrium model. The test section flow-field was calculated separately, using the conditions from the nozzle simulation at a distance of 27.9 mm upstream of the exit as

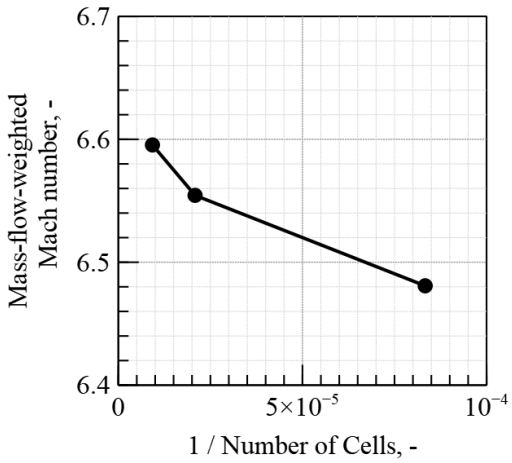


Figure 3.16 – Grid convergence analysis based on the mass-flow-weighted Mach number

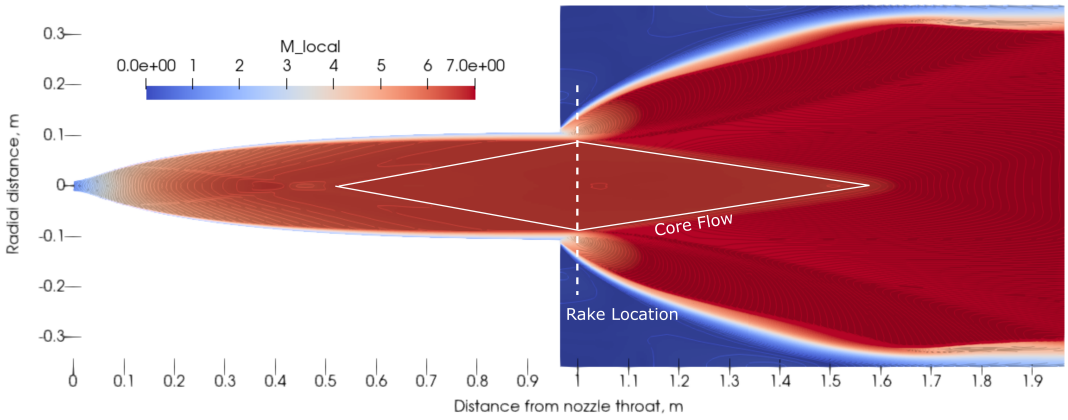


Figure 3.17 – Contour plot of the Mach number distribution for the T6 RST Mach 7 nozzle and test section flow-field. The solid white lines indicate the core flow region. The white dashed-dot line shows the position of the Pitot rake. Simulation performed by T. Sopek.

an inflow. The location of the Pitot rake is shown by a vertical dash-dot line and the bi-conic core-flow region by a dashed line. This region has a maximum axial length of 1050 mm and a maximum diameter of 180 mm.

A comparison of the experimental and simulated Pitot pressure at the measurement location is provided in Figure 3.18. The experimental values shown are the average Pitot pressure during the test time, normalised by the mean nozzle supply pressure over the same period. The results show good uniformity across the core flow region, which the

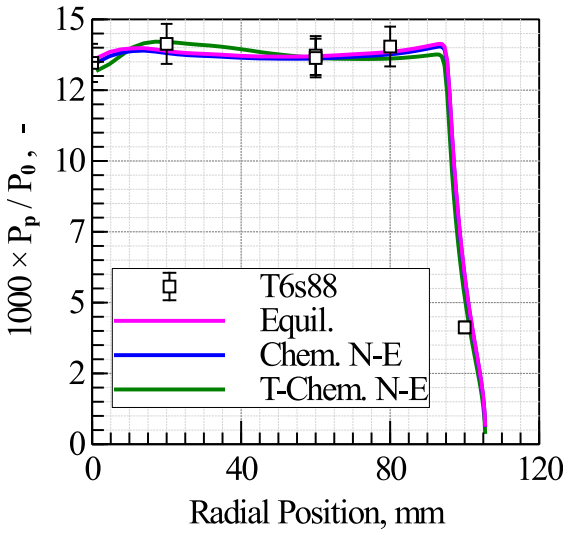
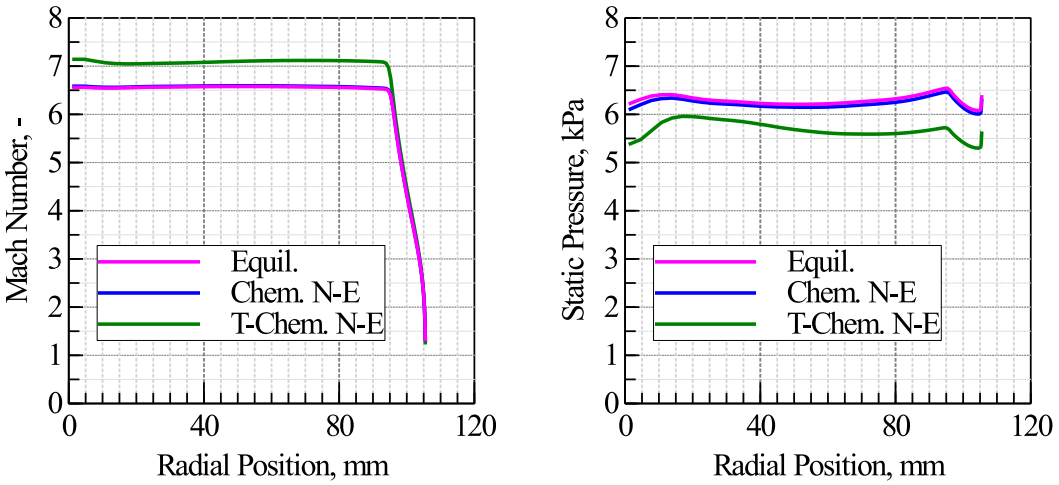


Figure 3.18 – Pitot-to-total pressure ratio comparison between shot T6s88 and axisymmetric CFD model.

experimental data suggests has a diameter of at least 160 mm. Also shown in Figure 3.18 are the Pitot pressure results from the three thermo-chemical models. To calculate these values, the flow over a simplified Pitot probe geometry was simulated using nozzle exit conditions for each of the three thermo-chemical cases. Figure 18 shows an excellent match between the experiments and the simulations, and that there is a good level of Pitot pressure uniformity in the core flow.

It is important to note that while the different thermo-chemistry models have little effect on the Pitot pressures (as shown in the comparison of Figure 3.18) they do have more significant influence on the free-stream flow properties – plots of nozzle-exit Mach number and static pressure from the three thermo-chemical simulations in Figure 3.19 reveal this. While the equilibrium and chemical non-equilibrium cases result in very small differences in Mach number and static pressure, the results for the thermo-chemical non-equilibrium model display significant departure from the other two models. The free-stream unit Reynold's number ranges from 8.9×10^6 m^{-1} for the thermo-chemical non-equilibrium simulation to 9.3×10^6 m^{-1} for the chemical non-equilibrium model.

Finally, Figure 3.20 shows (a) differences in temperature for the three thermo-chemistry models and (b) the amount of vibrational energy freezing for the thermo-chemical non-equilibrium solution. These simulations reveal that the free-stream static



(a) Mach number variation at nozzle exit. **(b)** Static pressure variation at nozzle exit.

Figure 3.19 – Radial profiles of nozzle exit Mach number and static pressure.

temperature is approximately 270 K in the case of the equilibrium and chemical non-equilibrium simulations, as well as for the thermo-chemical non-equilibrium translational mode. In contrast, at nozzle exit the vibrational temperature is frozen at 1270 K; for context, the static temperature at the nozzle throat is 2100 K.

The obtained nozzle exit flow properties display significant departure from the equilibrium, highlighting the need to take the influence of finite-rate thermo-chemistry into account when simulating hypersonic nozzle flows. These results show that these non-equilibrium effects are significant at the presented condition. This aligns with results from other RST facilities at similar enthalpies, for example Hannemann et al. (2010). Future experiments are planned to confirm the degree of thermal non-equilibrium in the flow-field, both through optical techniques and measurement of the free-stream static pressure. Based on the current data, good agreement is found between the targeted condition and the experimental results.

3.6 Expansion Tube Mode

The commissioning tests of T6 in ExT mode reported here focused on high-speed Earth return conditions. Both ESA and NASA are currently considering proposals for a Mars Sample Return (MSR) mission, a key challenge of which is the return of a sample capsule from Mars to Earth (Potter, 2020). Given that any gathered material must be returned from

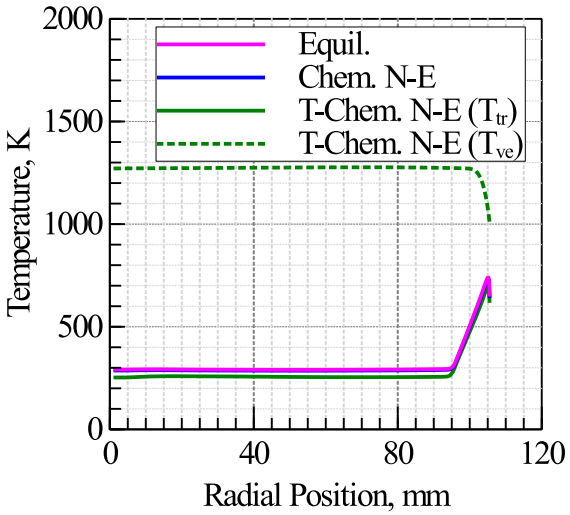
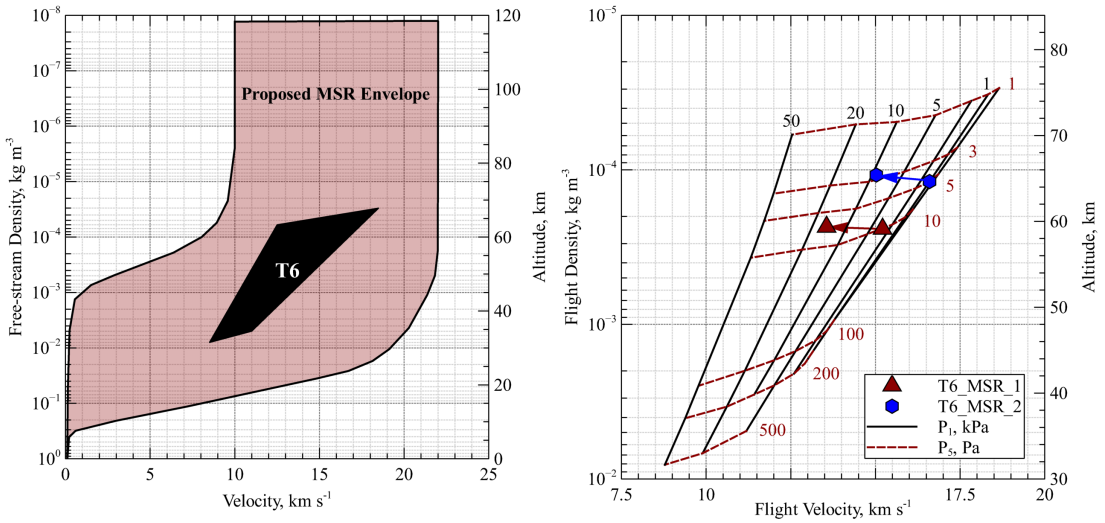


Figure 3.20 – Comparison of nozzle exit temperature distribution for the three thermo-chemistry models.

Mars, minimisation of vehicle mass to increase possible payload — through reduction of thermal protection system size — is desirable. The return section of the mission will likely occur at very high speed, with potential entry velocities up to 22 km s^{-1} (Johnston and Brandis, 2015a). At these velocities, the post-shock temperature can significantly exceed the limits of many of the thermochemical models used to predict vehicle heating. Johnston and Brandis (2015a) previously provided significant extensions to some of these models to enable their use for MSR trajectories. However, relevant ground test data will be required to validate predictions of the aerothermodynamic heating environment.

3.6.1 Expansion Tube Mode: Performance Envelope

The performance envelope of T6 in ExT mode in the context of MSR missions is shown in Figure 3.21. Figure 3.21a shows a likely bounding region for MSR flight trajectories. Overlaid is the capability map of T6 in expansion tube mode, employing the current highest performance driver condition, C. Figure 3.21b shows a more detailed representation of T6 performance prediction, wherein iso-curves of shock tube fill pressure (P_1) and acceleration tube pressure (P_5) are shown. This performance prediction has again been produced using PITOT, which has been extensively used for modelling of other expansion tube facilities (James et al., 2018b).



(a) Possible MSR trajectory envelope (adapted from Johnston and Brandis (2015a)) with T6 performance prediction.

(b) Detailed view of T6 performance capability region, showing tested conditions.

Figure 3.21 – Comparison of proposed MSR Trajectories with T6 performance capability in ExT mode.

It can be seen that the nominal capability of T6 lies in the centre of the map of possible trajectories for MSR missions. For stagnation point heat flux measurements the binary scaling parameter (the product of free-stream density and vehicle characteristic length scale) and flow total enthalpy is typically matched to flight to recreate the post-shock environment. The scaling in Figure 3.21 assumes a 35 mm diameter model is used with the density adjusted to match the conditions for a 900 mm diameter flight vehicle, corresponding to a proposed Earth Entry Vehicle (EEV) design (Dillman and Corliss, 2008). The model size is currently limited by the bore of the expansion tube (96.3 mm). Work is underway to design a nozzle, permitting an increase in outlet diameter to approximately 280 mm and thereby allowing significantly larger models to be tested.

3.6.2 Expansion Tube Mode: Experimental Arrangement

To validate the presented performance predictions an experimental study was undertaken in ExT mode. For the experiments detailed in this work, nominal shock tube pressures of 1 kPa and 3 kPa with acceleration tube pressures of 5 Pa and 10 Pa were used, respectively. The Pitot rake described in Section 3.5.1 was located in the test section, placed one tube

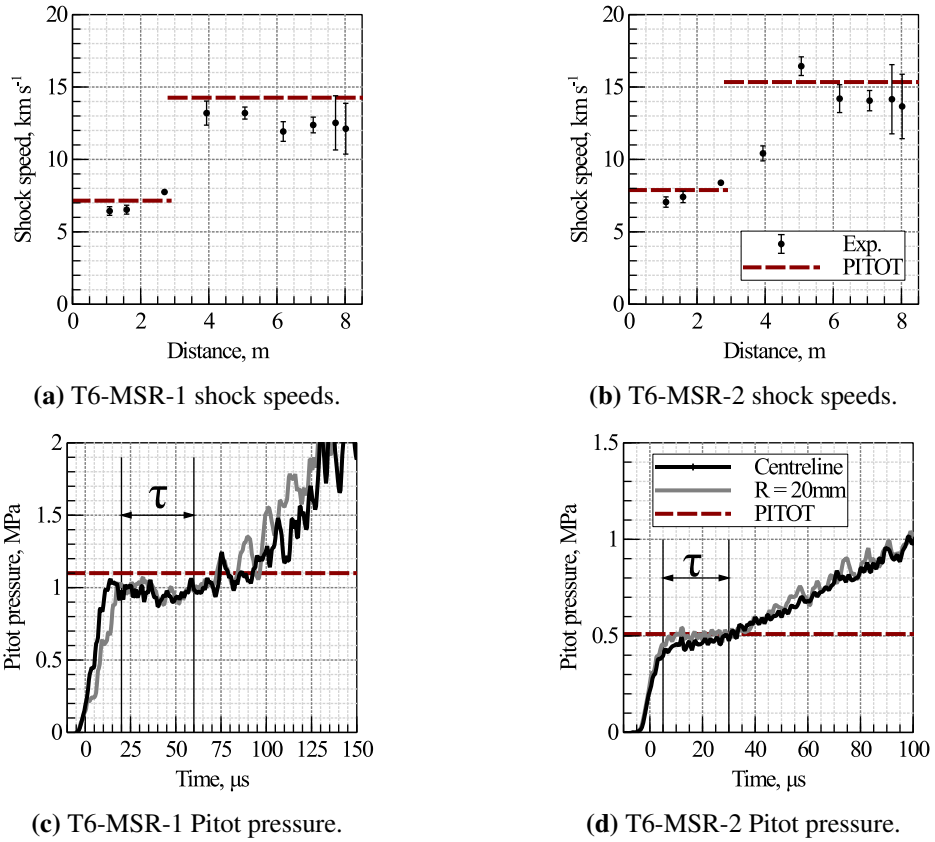
radius from the tube exit. Due to the smaller core flow diameter and higher pressures in ExT mode, two PCB Piezotronic 104 series piezoelectric pressure transducers were used for these tests. These were again protected using the shield cap design of Neely et al. (1991). For all experiments an aluminium foil secondary diaphragm with measured rupture pressure of 15 kPa was used.

3.6.3 Expansion Tube Mode: Experimental Results

The target test points, as well as the conditions achieved, are shown in Figure 3.21b. Here, the arrows denote the shift in the velocity and free-stream density from prediction to experiment; reasons for this difference are discussed below. Also note that, based on Mirels (1963) analysis, the actual velocity of the expanded test gas in the laboratory frame of reference is effectively the acceleration tube shock speed. In comparison, the velocity plotted in Figure 21b represents the 'flight-equivalent velocity' which accounts for the remaining static enthalpy of the test gas and is calculated by matching the experimental total enthalpy with flight.

Experimental results from the two conditions shown in Figure 3.21b are given in Figure 3.22. Figures 3.22a and 3.22b show the measured shock speed variation along the length of the facility, with comparison to PITOT calculations. Note that the secondary diaphragm is located at approximately 2.8 m. In general, it can be seen that PITOT over-predicts the achieved shock speed; this is to be expected given the idealisations in the code. As discussed in Section 3.4, the over-prediction in the shock tube is mostly due to diaphragm opening effects. A proportion of the test gas in the shock tube is thus processed by a weaker shock than expected, in effect reducing the performance of the driver. The second source of over-prediction by PITOT is that the code does not capture viscous or pressure losses. Notably, any loss through the secondary diaphragm — which is typically one of the largest performance loss mechanisms in an expansion tube — is not modelled. The mass of the secondary diaphragm is the main cause of this loss, and so ideally the lightest practicable[2] material is used.

[2] i.e. will not burst during facility evacuation or filling



(a) T6-MSR-1 shock speeds.

(b) T6-MSR-2 shock speeds.

(c) T6-MSR-1 Pitot pressure.

(d) T6-MSR-2 Pitot pressure.

Figure 3.22 – Experimental results for MSR expansion tube conditions. The identified region of quasi-steady test flow is denoted by τ.

Figures 3.22c and 3.22d show the measured Pitot pressure for each condition. Also shown in each figure is the value from the PITOT code, where the experimentally measured shock speeds and fill pressures are used to calculate the flow conditions. For both conditions good agreement is found between the experimental traces and the predicted Pitot pressure. Referring to the distance-time diagram of Figure 3.4d, it is expected that the Pitot trace should show first the arrival of the accelerator shock and gas, followed by the test gas and finally the unsteady expansion fan. The accelerator gas is not clearly observed in the Pitot pressure traces due to the filling time of the sensor housing (approximately 10 μs). Whilst a full characterisation of the flow-field at the tube outlet has not yet been undertaken these results suggest that the core flow diameter at this axial position is at a minimum 40 mm (based on the probe spacing). This implies that the choice of a 35 mm model for the performance scaling of Figure 3.21 is well within the limits required for the analysis to be valid. In both cases, the pressures show

Table 3.4 – Flow properties of Mars Sample Return ExT conditions.

Condition	P_1, kPa	P_5, Pa	P_0, GPa	H_0, MJ kg^{-1}	U_{eq}, km s^{-1}	τ, µs
T6-MSR-1	3	10	12.8	88.9	13.3	40
T6-MSR-2	1	5	14.1	117.6	15.3	25

good steadiness throughout the test time.

Table 3.4 shows the test flow properties for both of the conditions presented; these are taken from PITOT, again with the experimentally measured pressure and shock speed used as inputs. The test time is determined based on the period observed before the Pitot pressure traces begin to trend upwards; this is associated with the arrival of the unsteady expansion and hence the end of the test time. Although short in absolute terms, the determined test times are sufficient to establish the thermal boundary layer based on the work of Davies and Bernstein (1969). From these results, it can be seen that the ExT mode has achieved flow conditions in excess of 15 km s^{-1} with high-quality test flows of sufficient duration for aerothermodynamic ground testing. The experiments presented here thus demonstrate the capability of T6 to achieve hyperbolic atmospheric entry conditions.

3.7 Conclusion

This work has presented the development work to date on a new high-enthalpy, aerothermodynamic ground test facility — the T6 Stalker Tunnel. The facility is a combination of the original T3 free-piston driver, the Oxford Gun Tunnel barrels and newly designed components. Commissioning of the driver was first discussed, incorporating results using two pistons at nominal rupture pressures up to 46 MPa. Efforts to match a computational model of the driver to the experimental data were successful, with good agreement between the 'blank-off' test data and the model predictions shown.

Theoretical performance envelopes and experimental data from four distinct facility modes were then presented: reflected shock tunnel, shock tube, expansion tube and aluminium shock tube. In general, departures from the ideal predictions were attributed to 'real world' effects such as diaphragm opening and the presence of wall boundary layers. Good agreement with the experimental data and higher-fidelity simulations of the facility

was found. Notably, consideration of diaphragm opening effects and non-equilibrium thermo-chemistry gave close agreement to the measurements in the ST and RST modes. In all cases, high quality test flows were achieved.

The demonstrated flow conditions cover a wide range of mission archetypes and physical regimes, from recreating high-speed atmospheric flight to hyperbolic Earth entries. Future work will further extend capability, for example through construction of additional nozzles for RST and ExT modes and construction of a lighter piston. Extension and more detailed characterisation of flow conditions is also on-going. Of particular note is that this work presents the first European capability for super-orbital shock tube experiments — embodied in the T6 SST and AST modes. In addition, the ability to achieve MSR conditions in a ground test facility has also been demonstrated through expansion tube operation. These achievements highlight the unique value of T6 to support next-generation space missions through the provision of ground test data.

Funding Sources & Acknowledgements

The authors would like to acknowledge the UK National Wind Tunnel Facility for their support in the development of the T6 Stalker Tunnel under grant EP/L024888/1. Thanks also to the Oxford University John Fell Fund and Fluid Gravity Engineering for their support in the development of the facility.

Gratitude is extended to Peter Jacobs, Chris James and all at the University of Queensland for their support in the design and commissioning of the facility. We are eternally grateful for the contributions of the Oxford Thermofluids Institute Workshop and Building Services teams, with particular thanks owed to William Godfrey, Hal Surtell and James Carter for their substantial efforts expended over the course of making T6 operational.

Hammer time!

— M.C. Hammer, "U Can't Touch This"

4

Aluminium Shock Tube Condition Development

Contents

4.1 Introduction 97
4.2 Aluminium Shock Tube Overview 98
4.3 Facility Performance Envelope 108
4.4 Shock Tube Test Time Evaluation 115
4.5 Developed Conditions 123
4.6 Summary 128

4.1 Introduction

In the previous chapter, work to develop and commission a multi-mode, high enthalpy ground test facility was presented. It was shown that T6 could reproduce a wide variety of hypersonic flight environments, and that computational tools could be used to design test conditions and to model facility performance.

The remainder of this thesis builds on this foundation, focusing on the application of the newest facility mode — the T6 AST — to the problem of shock-layer radiation. The purpose of the current chapter is first to provide a detailed overview of the specifications

of the AST which are relevant to the later experimental work. The motivations for its development are first summarised, after which the particulars of the facility in terms of physical, experimental and operational arrangements are overviewed. The capability of the facility mode is then assessed against idealised predictions, both in terms of its performance and test time. Finally, three conditions which are used for the validation experiments of Chapter 5 are selected and the quality of their test flows confirmed using facility instrumentation.

4.2 Aluminium Shock Tube Overview

In this section, the AST mode is discussed in detail. This includes the motivations for, and expected advantages of, its design. The facility measurements used to characterise test conditions of the thesis are then discussed in detail.

4.2.1 Motivation for Development

In Section 2.4.1, existing high-enthalpy facilities in the field of shock-layer radiation were reviewed. As well as describing their operation and recent results of note, some of the experimental problems encountered in their operation were highlighted. To reiterate some of these, observed issues have included: low signal-to-noise (generally at low pressure, or low volumetric radiance), insufficient test time at low pressure, and contamination (due to either carbon from the tube wall or in the test gas itself). The wall boundary layer also has a potential impact on shock-layer radiation experiments, both through deceleration of the shock (via the Mirels effects of Figure 2.8) and because the test gas must be viewed through it. The motivation for the development of the T6 AST was to establish a purpose-built facility mode which would mitigate these issues.

The primary attribute of the new T6 AST which makes it particularly suitable for shock-layer radiation studies is its large diameter. Typically, existing high-enthalpy shock tubes have diameters of approximately 100 mm: for example, X2 (85 mm), T6 SST (96.3 mm) and EAST (101.6 mm). However — as was discussed in Section 2.4.2 — shock tube test time scales with D^2. A larger facility thus significantly reduces Mirels effects. More radiation signal is also available, scaling with the diameter in the case

of optically thin emission. This rationale has previously underpinned development of larger shock tubes for X2 and EAST (*c.f.* Table 2.1).

Based on preliminary performance studies using the PITOT code of James et al. (2018b), as well as structural requirements and the availability of material stock, the diameter of the new T6 AST was chosen to be 225 mm. The full rationale underpinning this design is discussed in more detail in Section 4.2.2. This modification, as well as several additional design features, solves or reduces many of the aforementioned problems, as follows:

- **Integration Length:** For optically-thin emission, the measured radiation signal is proportional to the optical depth. Thus, for a given optical system, the signal-to-noise of the measurement scales linearly with tube diameter. A similar argument can be made for many other non-intrusive measurement methods, e.g. absorption spectroscopy.

- **Boundary Layer Influence:** For a larger tube, the boundary layer is a smaller proportion of the overall radiating region, and thus the radiation is closer to the idealised assumption of one-dimensional post-shock flow. In addition, and as discussed in Chapter 2, Mirels effects have a strong influence on the development of shock tube flows. Given the size of the wall boundary layer is independent of tube diameter, a larger tube will experience significantly reduced Mirels effects. This increases test time and reduces viscous shock deceleration.

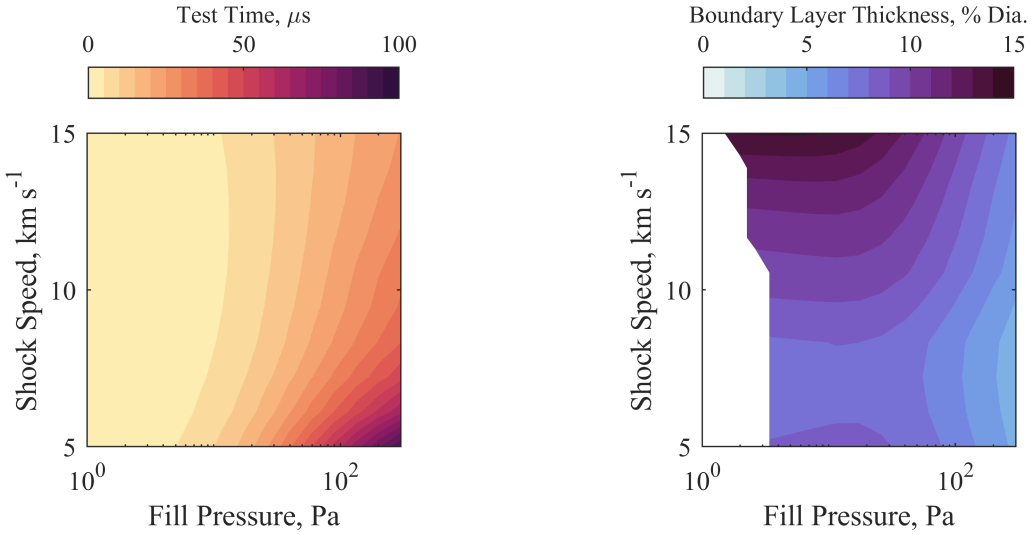
- **Contamination:** The tube is constructed from aluminium, therefore removing the wall as a source of carbon contaminants. Furthermore, the design features diaphragms at either end of the AST which, in combination with a high-vacuum pumping system, minimise the presence of contaminants in the test gas.

Figure 4.1 demonstrates the benefits of the AST through a laminar Mirels analysis using the code of Lewis (2017), where test time and the 99 % velocity boundary layer thickness are compared for the T6 SST and AST modes. Note that the T6 SST geometry is comparable to many of the existing facilities reviewed in Section 2.4.1. A range of

initial shock tube fill pressures and speeds representative of Earth entry were simulated, with the assumption of equilibrium air as the test gas. It assumed here that both the SST and AST are operated in 'straight-through' mode; as such, in the SST configuration Shock Tube 1 is utilised as an additional length of shock tube. This analysis thus uses a length of 8.8 m for the SST calculations, and 6.0 m for the AST.

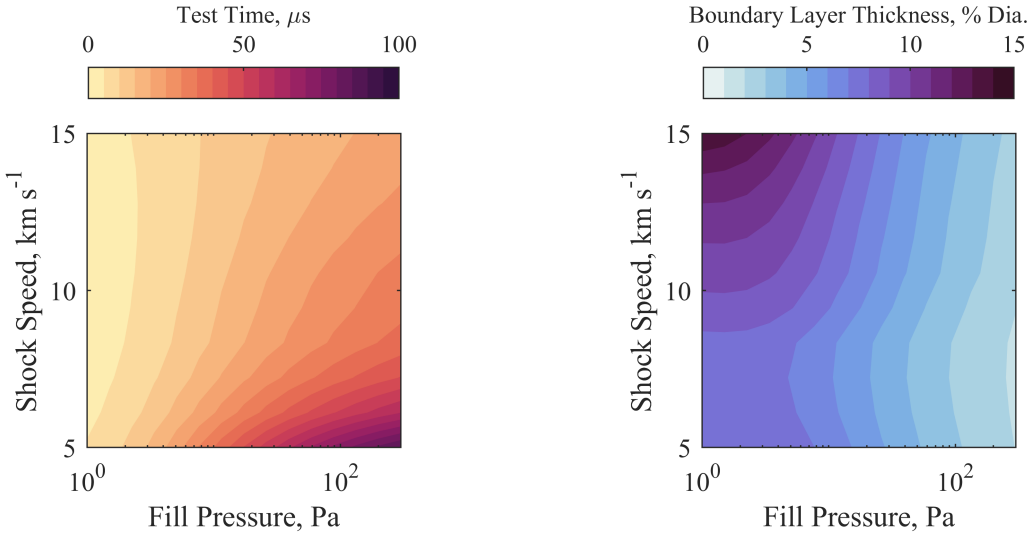
Figures 4.1a and 4.1c give absolute values of the calculated test time for the two tube diameters, whilst Figure 4.1e expresses these as a relative augmentation, i.e. the ratio of the 225 mm test time to that of the 100 mm result. From this analysis, it can be seen that the larger-diameter AST mode offers significant benefits in terms of the achievable test time, especially at lower pressures. For example, the predicted augmentation at 1.6 Pa and 11.7 km s^{-1} (a high-altitude condition representative of Hayabusa entry) is in excess of 4.5×. Given that low fill pressure conditions will have the longest equilibration times and lower volumetric radiance, this highlights the potential applications of the AST design for such cases.

The comparison of the relative boundary layer thickness in Figures 4.1b, 4.1d and 4.1f is also favourable, with the larger tube always exhibiting a smaller influence. Here, the boundary layer extent is expressed as the total thickness at the contact surface as a percentage of tube diameter. In the original analysis of Mirels (1963) the boundary layer is assumed to be self-similar, growing with the square root of the slug length; this is longer for the AST. The presented comparison is thus pessimistic (in terms of the potential AST performance), as for comparable distances behind the shock the benefit in relative boundary layer thickness is linear. However, this analysis explicitly highlights that the thickness of the boundary layer is always proportionally less for the AST. This means that the entirety of the additional test slug length gained through use of the larger diameter is (at least) as valid in terms of boundary layer influence. It should also be noted that the solver failed to converge for pressures in the 100 mm diameter tube below approximately 3 Pa. This is attributed to the boundary layer becoming a significant proportion of the tube diameter, which invalidates the 'thin' assumption inherent in the Mirels analysis.



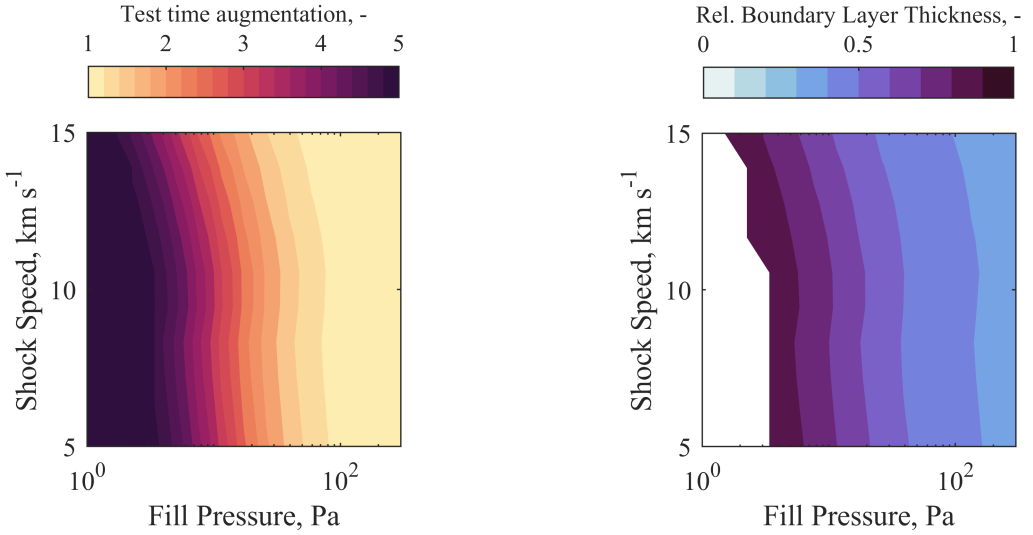
(a) Test time — 100 mm tube.

(b) $2\times\frac{\delta_{cs}}{D}$ — 100 mm tube.



(c) Test time — 225 mm tube.

(d) $2\times\frac{\delta_{cs}}{D}$ — 225 mm tube.



(e) Test time augmentation.

(f) Relative δ_{cs}

Figure 4.1 – Laminar Mirels analysis of large-diameter tube benefits.

4.2.2 Geometric and Experimental Design

The majority of the components of T6 are extensively modified versions of existing parts from either the T3 Shock Tunnel or the Oxford Gun Tunnel. In contrast, the AST was newly designed and manufactured to enhance the ability of T6 to investigate shock-layer radiation. Figure 4.2 shows a technical drawing of the facility (downstream of the primary diaphragm) in AST mode. Detail views showing the key features of the tube — namely the nozzle, windows (the equivalent of a 'test section' in this mode) and Pitot rake — are also provided. The specifics of these are discussed in subsequent sections.

The aluminium shock tubes themselves were manufactured from solid billets of 300 mm diameter, 7075–T6 aluminium. A 12° conical nozzle transitions the internal bore from 96.3 mm to 225 mm over a length of approximately 1 m. At the downstream end, two antipodal windows are held in removable holders, integrated into the tube wall. Historically, some shock tube experiments have shown issues with shock asperity due to the presence of rough features on the tube wall (Bogdanoff and Cruden, 2016). This was specifically addressed during the design of the AST, in two ways: firstly, all components forming the main internal flow-path of the shock tube have alignment features which ensure concentricity to within 0.05 mm. Secondly, these components — including the flush-mounted window holders — were honed as a full assembly to a diametric tolerance of 0.1 mm to ensure a smooth, continuous internal surface

The diameter of 225 mm was selected as a compromise between three core considerations: the potential boundary layer advantages, maintaining performance capability, and structural design requirements. The first of these has already been assessed in Figure 4.1. In terms of performance, it was accepted from the outset that the AST would not offer the same maximum velocity capability as the SST mode. However, an ability to reach some super-orbital conditions is still desirable — specifically, velocities of approximately $10\,\mathrm{km\,s^{-1}}$ with a fill pressure of 0.1 Torr to 0.2 Torr in air — to match the benchmark test conditions of Brandis and Cruden (2017a). Using the performance code PITOT, this was expected to be achievable with a diameter of 225 mm as shown in Figure 4.3a.

Above all, the design of the AST needed to satisfy the structural requirements for a pressure vessel. The largest diameter of stock material available was 300 mm — this

was sufficient to give acceptable safety factors throughout the facility assembly using the chosen internal diameter.[1] This was confirmed through hydraulic pressure testing of the AST components to 75 bar, providing a rated working pressure of 50 bar. Given the significant expansion of the driver gas through the nozzle this limit is far above any level which has been observed to date.

4.2.3 Shock Speed Measurement

A core theme which runs throughout this thesis is of the importance of shock speed measurement along the entire length of the shock tubes. These measurements directly contribute to characterising facility performance (Chapters 3 and 4), analysing radiation measurements (Chapter 5) and capturing trends in shock speed variation (Chapter 6). The means by which the shock speed and associated uncertainties are determined in all modes of T6 (using time-of-flight between shock timing stations (STS) flush-mounted in the tube wall) has already been discussed in Section 3.4.1. Here, more specific details of the use of shock speed measurement in the context of the AST are given.

Figure 4.2 gives the positions of the STS measurement locations for the T6 AST. Of particular note is the high number of measurement points, distributed along the entire length of the facility. This density of shock timing stations allows high resolution of the shock speed profile, allowing more accurate rebuilding of the trajectory for comparison to computational tools and for the SSV analysis conducted in Chapter 6. The sensor density markedly increases around the windows, providing enhanced characterisation at this key location and presenting the opportunity to use combinations of different measurements e.g. fibre-optic shock detection (James et al., 2019a). In this work, PCB Piezotronics 113B26 series transducers (with nominal sensitivities of 1.45 $\mathrm{V\,MPa^{-1}}$) were used in the wall of Shock Tube 1. In the AST, a combination of 113B27 and 113B28 transducers (with nominal sensitivities of 7.25 $\mathrm{V\,MPa^{-1}}$ and 14.50 $\mathrm{V\,MPa^{-1}}$ respectively) were used due to the lower pressures expected there. These have a stated rise time of no greater than 1 µs. These sensors are amplified by 8-channel, rack-mounted PCB Piezotronics

[1] The specifics of the structural design and the final safety factors are detailed in an internal report by Collen and Doherty (2018).

483C05 and 483C15 signal conditioners; in the AST, the latter was set at up to 10× gain to improve the reliability of the shock speed measurement. Based on the work of Hayne (2004), which used a similar arrangement on the X2 facility, the overall uncertainty in the static pressure measurement is estimated to be 7 %.

Closer spacing of the STS locations leads to greater uncertainty in the shock velocity measurement, as errors in arrival time and inter-sensor distance are more significant. As a result, in this work the stated shock speed for each T6 AST shot refers to the mean value measured on the last three transducers. For the vast majority of tests, this means in practice that approximately the last metre of shock travel is averaged. This is likely a good assumption, as the nominal test conditions presented in Section 4.5 have relatively flat shock trajectories over this region. The validity of this convention is discussed further in Chapter 6.

4.2.4 The Pitot Rake

Pitot measurements are an essential component of facility characterisation. Unlike wall static pressure measurements, they allow test time and flow uniformity (both radially and through the test slug) to be assessed. For AST mode, the usual T6 Test Section is removed and the tube inserted directly into the Dump Tank. This arrangement enabled the specification of longer tubes and hence maximised the available test time. However, given the usefulness of Pitot rake measurements, an alternate approach to that used in Section 3.5 was required.

Detail C of Figure 4.2 shows the AST Pitot rake. As visible in the main view, it sits within the Dump Tank on a cantilevered arm which extends downstream. This Mounting Arm is also visible in Figure 4.7a. The rake is asymmetric with respect to the AST bore, providing six measurement locations at 20 mm spacings from the tube centreline. In this campaign, the rake was nominally positioned at a distance of 112.5 mm (i.e. one radius) from the tube outlet. Again using the assessment of Hayne (2004), the uncertainty in the Pitot pressure measurement is taken to be 7 %.

Two measurement methods were used in the AST rake for this work. Primarily, PCB Piezotronics 113B24 and CA102B04 series transducers (with nominal sensitivities of

0.73 V MPa^{-1}) were employed to measure Pitot pressure. These locations are designated PP–0X in Figure 4.2. In addition, a coaxial surface-junction thermocouple (James et al., 2019b) was used to measure stagnation point temperature and thus infer heat flux. This is denoted 'SpT–02' in Figure 4.2. The sensor was again flush-mounted in a cylindrical geometry, as described in Section 3.5.

The thermocouple was sanded using 600 grit sandpaper to form the initial junction; typically, the resistance was approximately 6 Ω before the test. Based on the work of Palmer (1999) the gauge was electrically grounded to the body of the rake to minimise the impact of ionisation. The temperature signal was amplified using a Fylde FE-H379-TA amplifier, with stated bandwidth of 500 kHz. To calculate the heat flux, the inverse filtering approach of Oldfield (2008) was used. Based on the work of Capra (2006) and James et al. (2019b), the sensitivity of the thermocouple was taken as 62.5 μV $°C^{-1}$ and the value of the thermal effusivity as 8900 J m^{-2} K^{-1} $s^{-1/2}$. The presented heat flux results are smoothed using a 250 kHz moving average filter to reduce noise. The effectiveness of these measurement methods in the application of shock tube performance characterisation is discussed further in Section 4.4.

4.2.5 Experimental Procedure

In Section 3.2.1, the broad principles of the operation of a free-piston driven facility were described. Here, the specific procedure followed for these specific AST experiments is summarised. This overview is meant to capture the process followed and to give background for the tests presented in the remainder of this work. In Appendix A, a complete infrastructure diagram of the facility (representative of the current test campaign) is given as a companion reference to the description provided here.

Before a test in AST mode, the Compression Tube, Shock Tube 1, Aluminium Shock Tubes and Dump Tank are all under vacuum. The reservoir remains at atmospheric pressure. A large Edwards Vacuum GXS-160/1750 boosted dry scroll pump is the primary means used to evacuate the sections of the facility downstream of the primary diaphragm, whilst an Edwards E2M18 rotary vane pump is used for the compression tube. Depending on the specific test condition, a secondary or tertiary diaphragm may

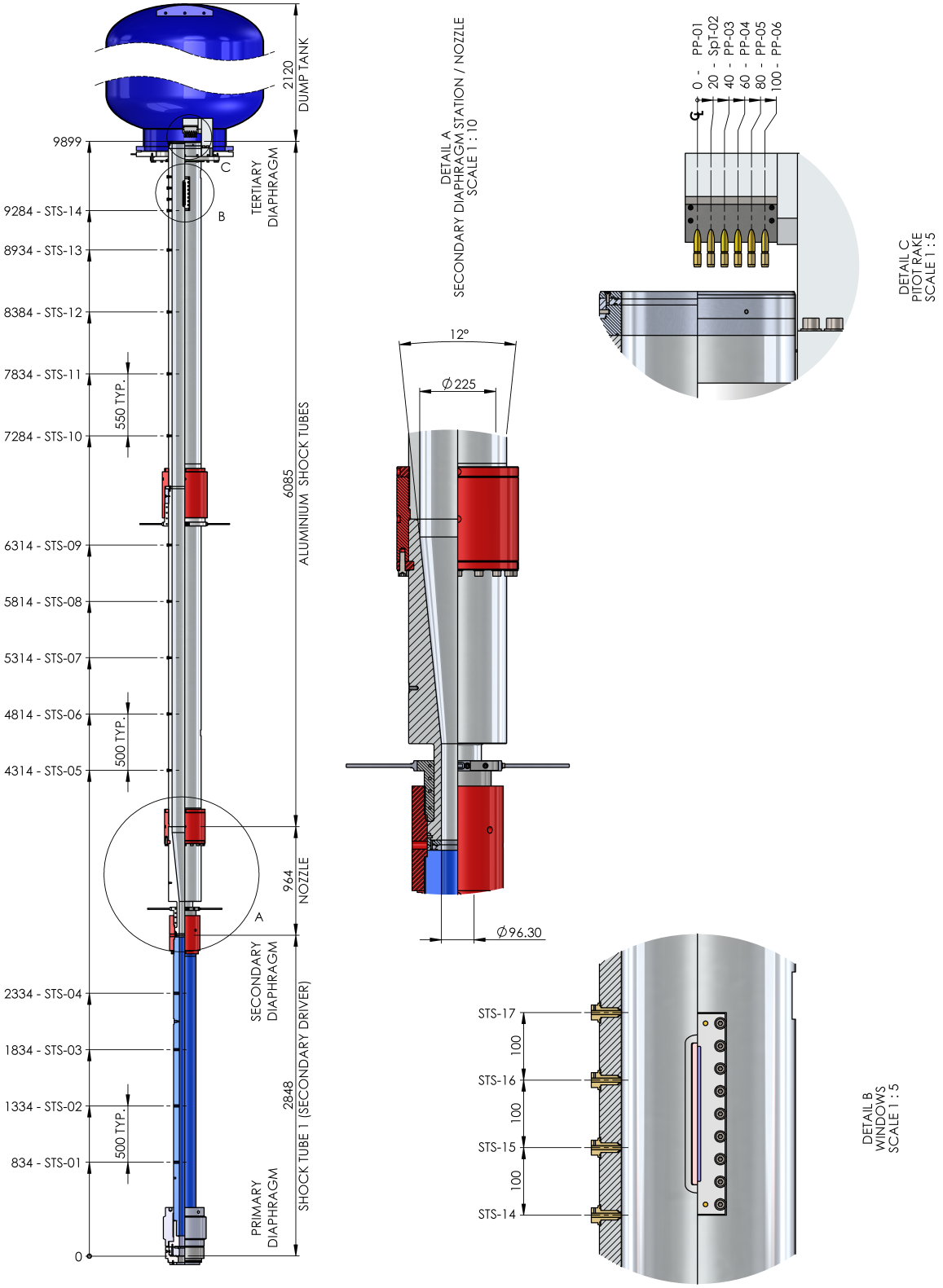


Figure 4.2 – Engineering drawing of the T6 AST, with shock timing station (STS) and Pitot rake measurement locations shown. The main drawing scale is 50:1. All dimensions are in millimetres.

also be used, positioned as shown in Figure 3.4b. Typically, the large facility pump can evacuate the shock tubes to less than 1 Pa. An Edwards EXT-75DX turbomolecular pump is then used to further reduce the pressure in the AST, to on the order of 0.01 Pa in the tests presented here.

The vast majority of experiments discussed in this thesis were undertaken in 'straight-through' mode, wherein a secondary diaphragm is not used and Shock Tube 1 and the AST form a single volume. If a secondary driver is used, Shock Tube 1 fulfils this function. A Mylar or aluminium foil diaphragm then separates this tube from the nozzle. This convention is reflected in the labelling in Figure 4.2.

In preparation for a test, the correct gases must be loaded into each section of the facility at the proper pressure. Typically in T6 the fill of the reservoir is completed last to minimise the amount of time the high-pressure gas is present in the laboratory. However, in this campaign the chief concern was minimising the opportunity for leakage of atmospheric air into the test gas. As a result, the order used was: first, filling of the compression tube. This was followed by the secondary driver (if in use). The high-pressure fill of the reservoir was then performed. Throughout this process, the turbomolecular pump continues to evacuate the AST. This pump is then isolated and the test gas is filled last, after which the facility is fired and then vented. The time elapsed between starting to fill the test gas and firing the facility was typically less than a minute.

The test gas fill pressure is measured using a 5 Torr Inficon CDG-025D, with a stated accuracy of 0.2 % of the reading. It was found during this campaign that the length of vacuum line between the AST and the gauge resulted in an unexpectedly long response time between filling gas into the shock tubes and the measurement settling. It is therefore conservatively estimated that the uncertainty in pressure is a maximum of ±1 Pa. The leak rate — measured by isolating the vacuum pumps and monitoring the AST pressure over a period of several hours — was determined to be between $0.2\,\mathrm{mPa\,s^{-1}}$ and $1.5\,\mathrm{mPa\,s^{-1}}$ at various points throughout the test campaign.

4.3 Facility Performance Envelope

In this section, the ability of the AST to reach test conditions of interest for shock layer radiation experiments is demonstrated. Firstly, test conditions achieved in the AST are presented to give an overview of facility capability. The experimental performance is then compared to the predictions of the PITOT code, and reasons for discrepancies discussed.

4.3.1 A New High-Compression-Ratio Driver Condition

The original intent for the AST test campaign was that Driver Condition C (as detailed in Table 3.2) would be used to maximise the achievable shock speed. This was an original T3 condition, and so there was reasonable confidence that it would provide high performance and good operability. Unfortunately, the high reservoir pressure required for this condition resulted in unacceptable leakage rates into the evacuated space behind the piston, causing premature firing of the tunnel during the reservoir filling stage.[2] It was also found that the performance gain realised through use of a secondary driver was less than theoretical predictions, which prevented some target test conditions from being achieved.

To address these problems, a modified version of Driver Condition C with a higher compression ratio was developed. This allows a lower reservoir fill to be used for the same diaphragm burst pressure, thereby resulting in an operable condition whilst maintaining performance. The same diaphragms could also be directly used, negating the requirement to revise thickness and score depths. The new driver condition, with a compression ratio of 75 and termed C++, is detailed in Table 4.1. The particulars of the original Condition C are also given for comparison. This was developed without the use of blank-off testing, solely using the tuned L1d3 model discussed in Section 3.3.2. The majority of tests presented in the remainder of this thesis utilised this condition.

It should be noted that it was not possible to produced a tuned piston trajectory for this condition. The higher a compression ratio that is used (for a given diaphragm rupture pressure), the lighter the piston must be to allow a soft landing whilst maintaining over-driving (Stalker, 1967; Itoh et al., 1998; Gildfind, 2012). This is due to the higher speed

[2] This has since been resolved through improved seal specifications.

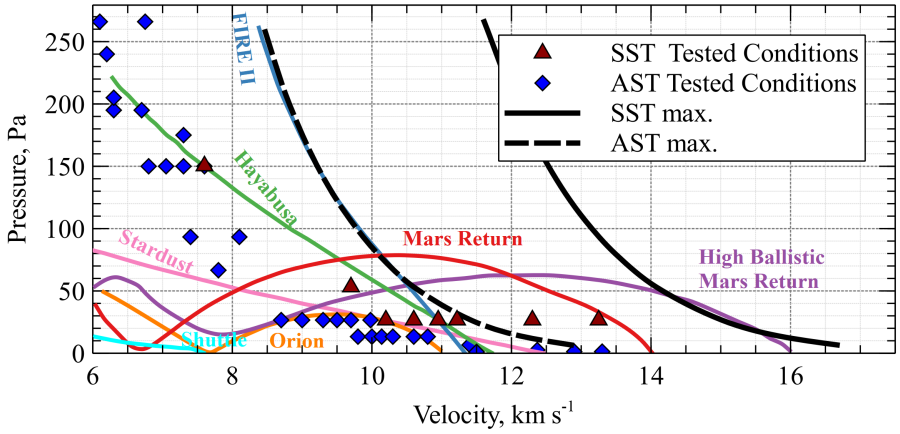
Table 4.1 – Comparison of T6 Driver Conditions C and C++

Condition	P_{Res}, kPa	P_4, MPa	X_{He} , %	Λ_r , -
C	3500	46.2	100	60
C++	2600	46.2	100	75

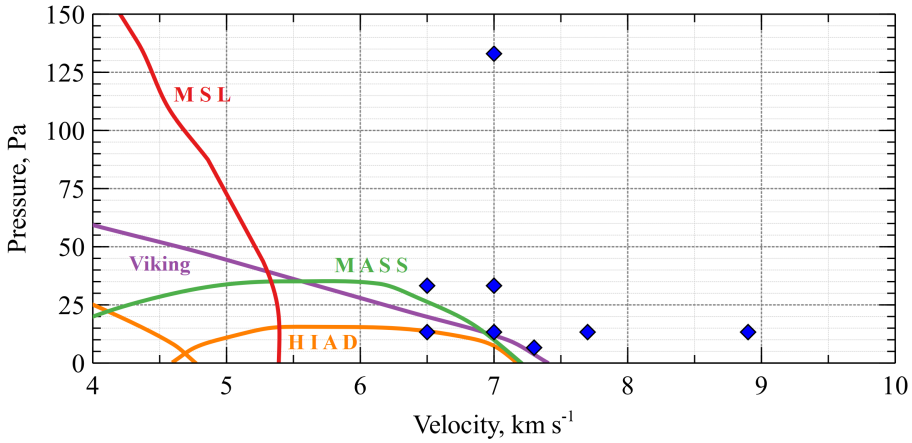
of sound in the driver gas (leading to greater mass flow through the orifice) and closer proximity of the piston to the buffers at diaphragm rupture. The lighter the piston used, the higher the velocity can be when rupture occurs — thereby balancing the mass flow out of the driver — whilst still being sufficiently decelerated by the driver gas pressure force at the end of the compression tube. As a consequence, with the current T6 piston mass of 36 kg a decision was made to prioritise the safe operation of the facility over increased performance. Some of the tests in this work show evidence of deceleration due to driver waves at the end of the tube; this was not deemed sufficiently large to be of concern for any of the experiments presented.

4.3.2 Tested Conditions

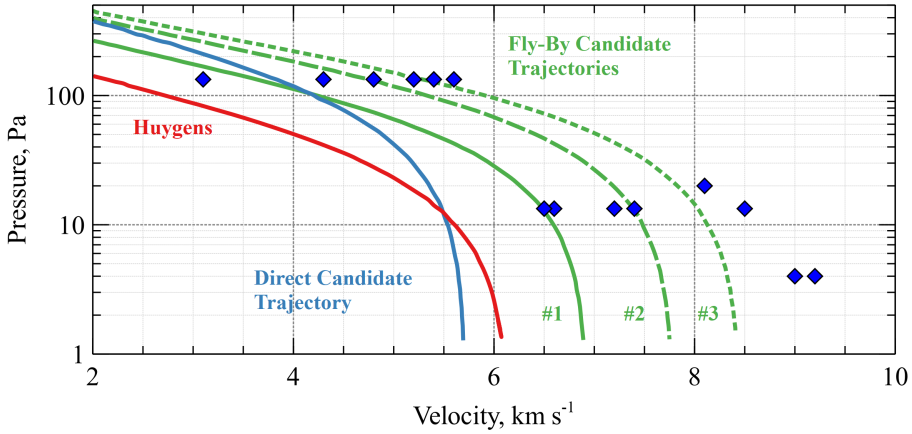
In total, the first T6 AST test series consisted of 165 shots. These tests were made up of several sub-campaigns, with objectives including facility performance assessment, computational code validation and emission spectroscopy measurements in air, nitrogen and the atmospheres of Mars and Titan. Figure 4.3 compares the tested points to various trajectories for past and present missions of interest. Note that all trajectories have been density-adjusted to lab conditions to account for temperature differences. In the case of the Earth testing of Figure 4.3a, markers with significant overlap have been thinned. It is beyond the scope of this work to fully analyse the performance of the facility across the totality of these experiments. Instead, these shots are shown to demonstrate what conditions have been achieved in the T6 AST, confirming its suitability for the investigation of the range of shock-layer radiation problems for which it was designed. For the air tests of Figure 4.3a, the performance limits (predicted using PITOT and assuming a secondary driver of pure helium at an initial pressure of 10 kPa is used) are given for both SST and AST modes.



(a) Earth: 79 % N_2, 21 % O_2. Adapted from Brandis and Johnston (2014).



(b) Mars: 96 % CO_2, 4 % N_2. Adapted from Cruden et al. (2012).



(c) Titan: 96 % N_2, 4 % CH_4. Adapted from Brandis and Cruden (2017b).

Figure 4.3 – T6 Aluminium Shock Tube tested conditions. The values for free-stream pressure along the trajectories shown are density-adjusted to laboratory conditions. The stated atmospheric compositions are by volume.

4.3.3 Ideal Performance Assessment

To assess the performance of the AST versus the predictions of PITOT a wide range of tests in air at the same driver condition were analysed. For many shots (especially those for Mars and Titan shown in Figures 4.3b and 4.3c), the primary driver was doped with varying amounts of argon to tune performance. However, a sufficiently large number of tests were undertaken using the nominal C++ driver condition (and to a lesser extent Condition B) to permit direct comparison.

Figure 4.4 presents a comparison between the performance curve calculated using PITOT and the experimental data for the AST. First, the experimental data was fit using a power law in the form $ax^b + c$. The resultant fit, as well as the experimental data, for Condition C++ is compared to the ideal prediction of PITOT in Figure 4.4. It is observed that the shock speed is over-predicted by the code at fill pressures above approximately 75 Pa and under-predicted below this value.

The ratio between the experimental and ideal prediction — termed the 'T factor' — as a function of shock tube fill pressure is given in a Figure 4.4. Also shown is the ratio found for an equivalent fit of Condition B, where only pressures above 66 Pa were tested. It can be seen that there is good agreement between the T-factors for the two conditions, suggesting that the discrepancy is a function of fill pressure rather than shock speed. In general, PITOT has previously been shown to give good agreement with experimental performance, including for the T6 SST mode as shown in Chapter 3. Typically, shock tube facilities are designed to have a constant diameter, and so the AST (with its intermediate nozzle) is somewhat unusual. The nozzle flow was thus investigated in more detail in order to explain these results.

4.3.4 Nozzle Flow Discussion

A fundamental difference between the T6 AST and the majority of other high enthalpy pulse facilities is the inclusion of an intermediate nozzle. As shown in Figure 4.2, this nozzle enables the larger diameter AST to be coupled to the rest of the facility. Here, the impact of this nozzle on the high-level performance of the facility is discussed.

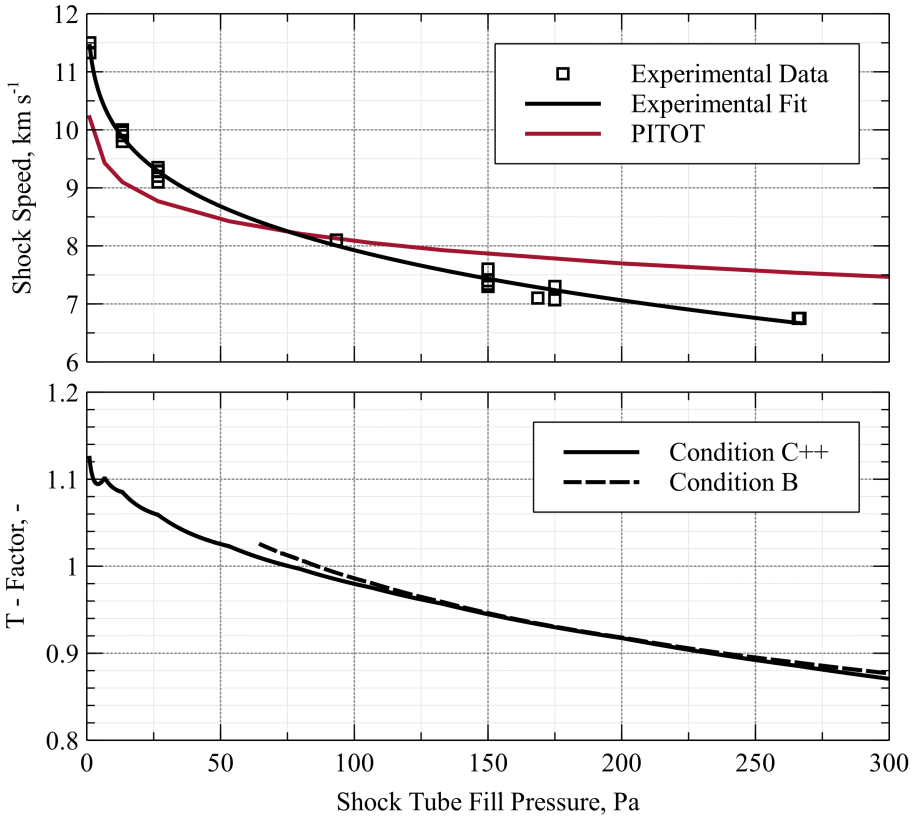


Figure 4.4 – Comparison of measured AST performance with the ideal predictions of PITOT. The constants used for the presented fit were: $a = -2.514$, $b = 0.1917$ and $c = 14.004$.

The flow-field and wave processes downstream of the AST nozzle is fundamentally different to that if a constant-diameter configuration is used. In Figure 4.5, example wall pressure traces for the T6 SST and AST modes are compared. The data shown is from STS-05 onwards, corresponding to positions downstream of the nozzle for the AST. It can be seen that, in the case of the SST mode, the pressure rises to a pseudo-steady plateau, after which the trace is seen to trend upwards. This is typical behaviour of any shock tube flow, closely following the canonical Sod's case. Inspection of the distance-time diagram in Figure 3.4a shows that these features correspond to the arrival of the primary shock and driver expansion fan which — the flow being supersonic — travels downstream.

In contrast, the behaviour in the AST is substantively different. The primary shock is followed closely by a second pressure discontinuity, which is seen to weaken as the distance from the nozzle increases. This feature is an inherent property of impulsive

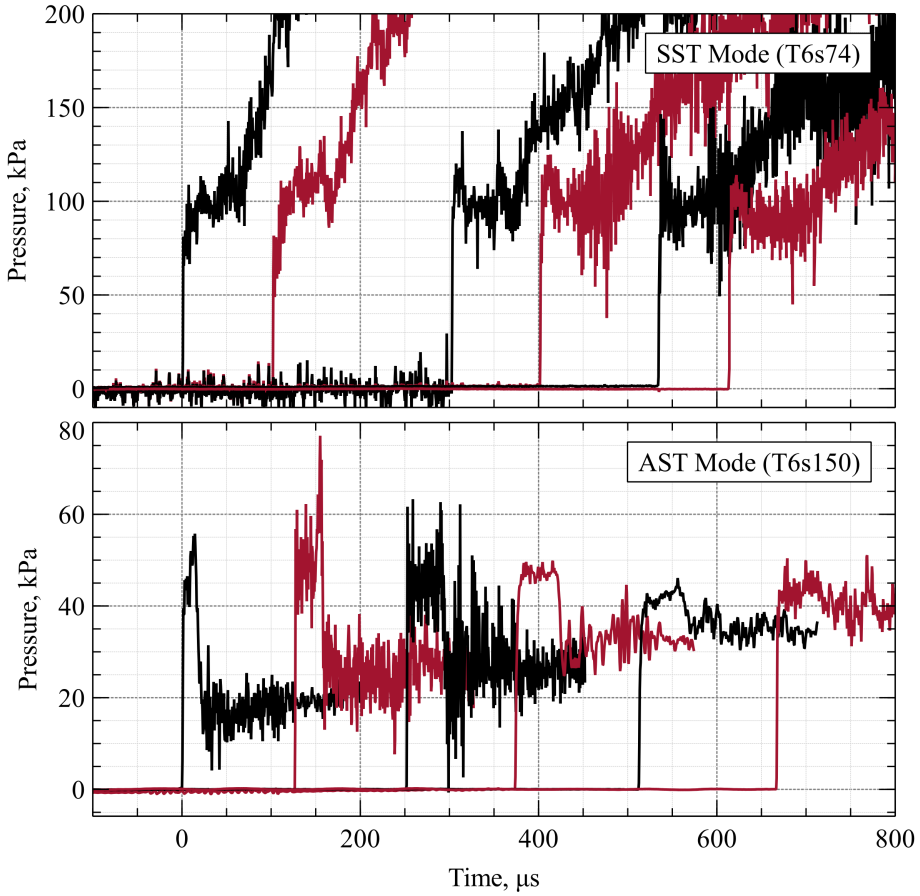


Figure 4.5 – Comparison of shock timing station traces between the constant-diameter SST mode and the AST intermediate nozzle configuration. Shown are wall static pressures from STS-05 onwards.The time axis is referenced to the arrival of the incident shock at STS-05. To aid clarity, consecutive traces alternate in colour, some measurement locations have been thinned, and for the AST data the traces are truncated after 200 µs.

nozzle flows, in which a second 'starting shock' is carried downstream behind the primary shock (Smith, 1966). This shock moves upstream in the primary shock frame of reference, causing the observed lengthening of the quasi-steady region of static pressure between the two discontinuities. This conclusion is supported by the results of L1d3 simulations, which show the formation and relative motion of these features. A representative distance-time diagram of the AST nozzle region generated from simulation results using the L1d3 code is given in Figure 4.6. The distance coordinate is referenced from the beginning of the nozzle expansion. The primary shock, contact surface and secondary starting shock are annotated. This starting shock is seen to form during the nozzle expansion

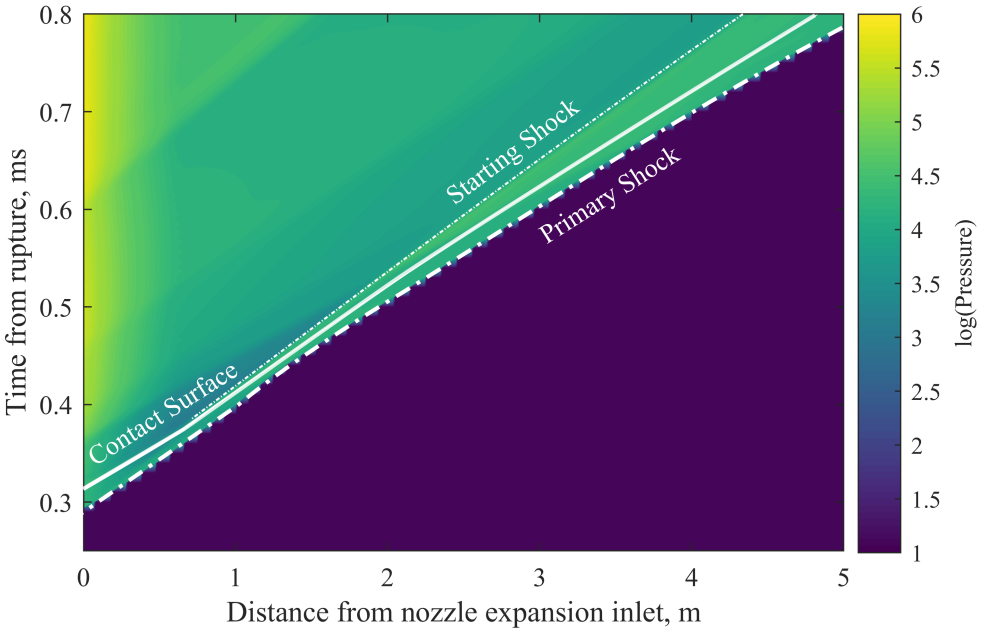


Figure 4.6 – Distance-time diagram of the AST nozzle region calculated using L1d3. The test gas fill is 13.3 Pa; the driver condition is C++. Here, the plotted data represents the base-ten logarithm of the static pressure. The primary shock, contact surface and nozzle starting shock are annotated.

process, after which these wave processes show good qualitative agreement with the AST static pressure results of Figure 4.5.

Given the complex flow phenomena which occur as the primary shock transits the nozzle, it is unsurprising that PITOT (which assumes an isentropic expansion based on the nozzle area ratio, followed by an unsteady process) does not fully capture the facility performance. The pressure dependence of the discrepancy between PITOT and experiment shown in Figure 4.4 is suggestive that viscous effects in the nozzle are an important factor in the observed performance differences. This is supported by the results of initial equilibrium L1d3 and inviscid axisymmetric CFD investigations, which both show similar trends to the PITOT prediction. Proper characterisation of the nozzle flow will require transient, viscous CFD simulations. There was insufficient time within this project to accomplish this and so it is left as a future work.

4.4 Shock Tube Test Time Evaluation

A critical attribute of any impulsive ground test facility is the duration of the valid test flow. In a shock tube, the test time is determined by the period required for the slug of compressed test gas (which sits between the shock and the contact surface) to pass the location of the measurement. For shock-layer radiation experiments, such as those reported here, the length of the test slug determines how much of the shock-layer is reproduced; this can be critical for matching thermochemical models. In Section 4.2.1, a discussion of the potential test time benefits of the AST was presented. In this section, these predictions are assessed experimentally. This investigation is a crucial component of the performance characterisation, as it demonstrates under what conditions useful test flows can be created and therefore informs the planning of future radiation studies.

The testing environment in a high-enthalpy shock tube is harsh. In measuring test time using physical instrumentation, there is typically a trade-off between survivability, response time and accuracy (Penty Garaets, 2019). In Chapter 3, brass shield caps based on the design of Neely et al. (1991) were used to protect the rake pressure sensors. Figure 4.7 shows these caps; the damage apparent in Figure 4.7b highlights why their use is required.

Although shield caps provide effective protection for the (expensive) sensors, their design results in a rise time of 10 µs to 20 µs, depending on the flow condition. This is due to the finite filling rate of the internal volume of the housing. This limitation is particularly problematic for shock tube experiments, as these typically have the shortest test times for the reasons given in Section 3.2.2. Inspection of Figures 4.1a and 4.1c reveals that the stated rise time can be a significant portion of the predicted test time, especially at low fill pressures and/or high incident shock speeds. The long rise time of the shield caps has presented challenges during characterisation of at least one other facility (Jacobs, 2011a); this motivated the inclusion of the coaxial thermocouple in this campaign, with which rise times of 1 µs can be achieved (James et al., 2019b). The utility of these measurement techniques for evaluating the test time in the context of high enthalpy shock tube testing is discussed in the following section.



(a) Pitot rake after first installation, with Mounting Arm visible in the lower half of the frame.

(b) Pitot rake, after impact from 80 µm Mylar secondary diaphragm fragments at 10 km s^{-1}.

Figure 4.7 – An example of the challenging nature of the AST testing environment. All probes shown use the shield caps of Neely et al. (1991) with the exception of position 2, where the coaxial thermocouple is flush-mounted.

Finally, it is acknowledged that optical techniques e.g. the filtered imaging approach of James et al. (2018a) have been shown to provide excellent means of assessing the duration of test flow over models. This solution was not possible due to the physical configuration of the AST: as shown in Figure 4.2, the Pitot rake is located within the Dump Tank. There is thus no current means of optical access, although modifications could be made in the future to permit this.

4.4.1 Comparison of Test Time Determination Techniques

The preceding discussion can be summarised as follows: characterising test time is important for shock tube facilities, but the very short flow durations pose challenges to this measurement. Given that optical techniques are not viable, it remains to be determined what the best instrumentation for performing this type of study in a high-enthalpy shock tube environment is.

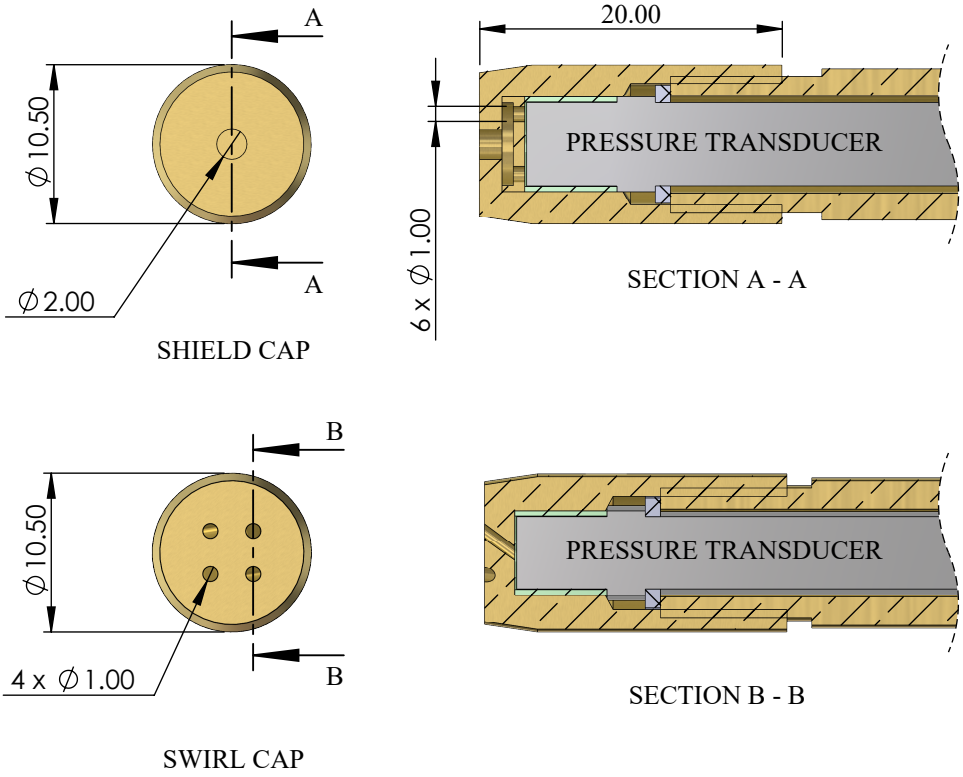
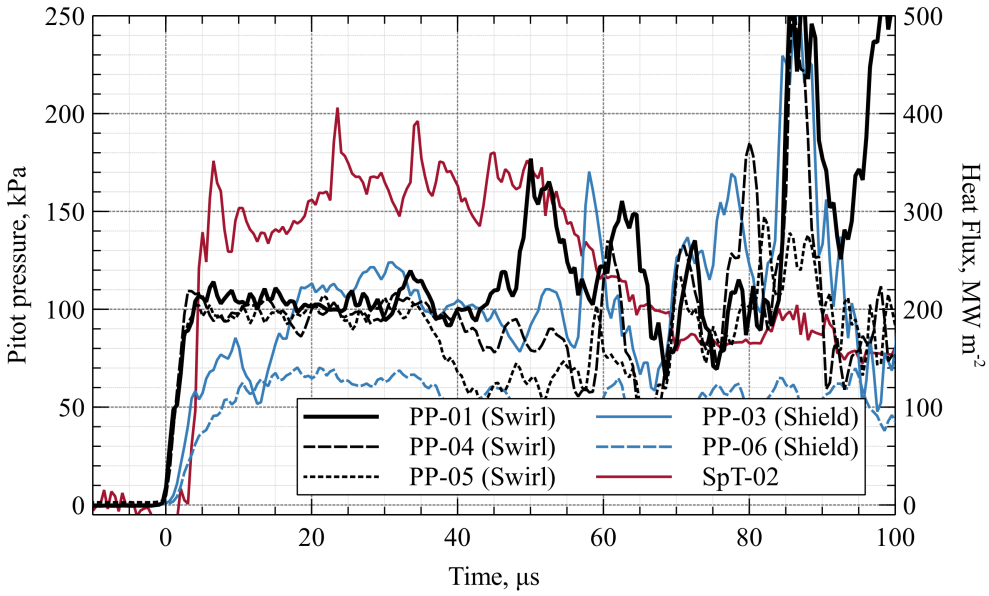


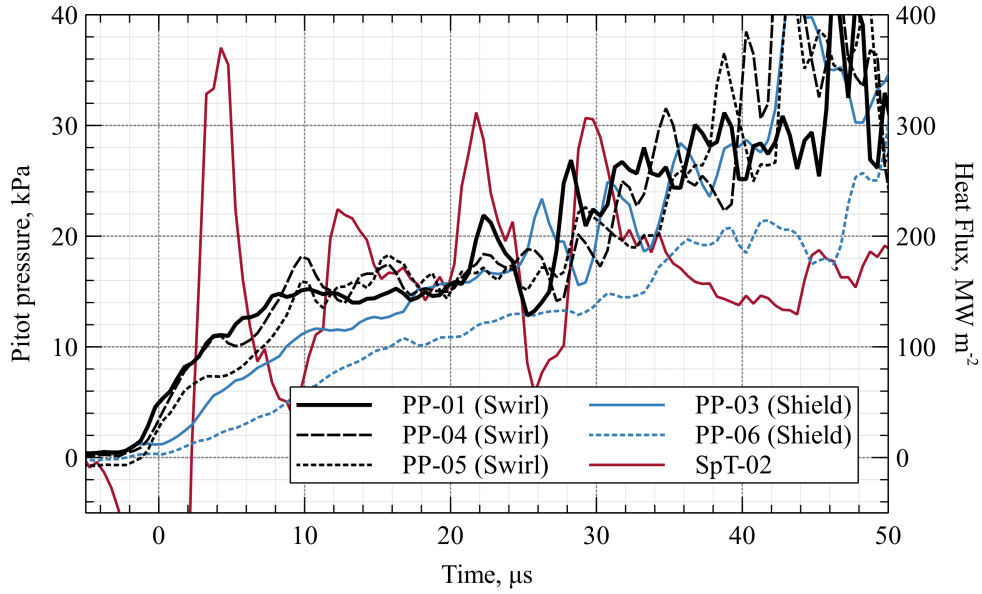
Figure 4.8 – Comparison of shield (upper, Neely et al., 1991) and swirl (lower, McGilvray et al., 2009) cap geometries. The former design requires additional volume to accommodate the shield: a thin disc with 6×1 mm holes which are radially offset from the centreline.

Here, the effectiveness of Pitot pressure and heat transfer measurements for assessing the test time is compared. For the pressure sensors, two protective cap designs were trialled: the aforementioned shield cap design of Neely et al. (1991) and the the 'swirl cap' geometry of McGilvray et al. (2009). The swirl caps were developed to avoid Helmholtz resonance issues which can affect the shield design under some test conditions. An incidental benefit of the modified geometry is a much shorter rise time, due to the reduction in internal volume. These have not extensively been used for shock tube experiments and so were also investigated here. A diagram of both cap geometries is given in Figure 4.8.

Figure 4.9 shows results from two consecutive shots of the T6 AST in which the test time measurement methods are compared. The presented data is representative of trends observed across the whole test campaign. Results from a relatively low-speed shot ($7.3\,\mathrm{km\,s^{-1}}$) are given in Figure 4.9a; here, PP–06 shows a much lower pressure than the rest of the sensors — this suggests that it sits outside the core-flow region. The other Pitot



(a) Shot T6s144: 7.3 km s^{-1}, 150 Pa



(b) Shot T6s143: 9.8 km s^{-1}, 13.3 Pa

Figure 4.9 – Experimental Pitot rake data for two AST shots, comparing Pitot pressure traces for two cap geometries. The results using an coaxial thermocouple are also shown.

measurements all agree well. However, the swirl caps demonstrate significantly shorter rise times than the shield cap geometry: 2 µs–3 µs versus approximately 18 µs. The PP–03 measurement using a shield cap also shows significantly more unsteadiness; this is not thought to be a physical effect, as the adjacent swirl cap measurements show no such fluctuation. Both cap designs give similar results for the end of the test time, occurring at

approximately 40 µs. Based on the swirl cap measurements of PP–05, –04 and –01 there is a gradual inward collapse of the core flow during driver gas arrival. Finally, the end of the test time based on heat flux agrees well with the pressure measurement. From the data, the rise time of the coaxial thermocouple is estimated to be approximately 5 µs. This is longer than the 'best case' for this type of gauge; previous authors have shown the rise time to be related to the thermal mass of the surface junctions (James et al., 2019b) so it is likely this could be reduced with further optimisation of the sanding technique.

The trends for the higher speed ($10\,\mathrm{km\,s^{-1}}$) case of Figure 4.9b are broadly similar to those already discussed, with a few key exceptions. Most notably, the coaxial thermocouple exhibits a sharp negative spike in heat flux at shock arrival, after which the trace recovers to a somewhat steady value — albeit with strong oscillations. This is observed consistently whenever the shock velocity is sufficiently high, and is attributed to ionisation. The post-shock test gas in a shock tube at super-orbital conditions is both at very high temperatures (approximately 10 000 K) and significant velocities in the laboratory reference frame (in excess of $9\,\mathrm{km\,s^{-1}}$). When this gas then stagnates on the front of the rake probes the calculated equilibrium temperatures can exceed 20 000 K, with electron mole fractions on the order of 20 %. During flow establishment, the formation of a reflected shock at the probe tip means these values are significantly exceeded. As the thermocouple is — by necessity — exposed to the flow, the free electrons can interact with the metallic surface of the gauge and thereby influence the heat flux measurement. Various grounding techniques proposed by Palmer (1999) were attempted, but proved unsuccessful for the very high temperature stagnation conditions tested here.

In terms of pressure measurement, the shield caps again show longer rise times than the swirl design. Critically, in the case shown in Figure 4.9b the PP–03 measurement never reaches a steady state. Whilst the driver gas arrival can be inferred in this trace by comparing the onset of increased flow unsteadiness with the swirl cap results, this data demonstrates that the sole use of shield caps for these short-duration flows significantly reduces the confidence in the assessment of the test period. For this purpose, a steady-state should ideally be achieved to permit comparison with the predicted Pitot pressure. The swirl caps achieve this aim. The centreline Pitot measurement (PP–01) shows a

moderately shorter test duration; this is attributed to the three-dimensional deformation of the contact surface on the centreline, which is more pronounced at lower pressures (see, for example, Satchell et al., 2021a).

Finally, the rise time of the swirl cap pressure measurement is found to be approximately 10 µs for this condition. The reduction in flow area of the narrow (1 mm) filling holes due to the lower pressure — and consequently thicker boundary layer — likely contributes to this; the effect of viscous area-reduction on rise time was confirmed computationally by McGilvray et al. (2009). However, it is thought that this effect is also partially caused by heat loss to the internal geometry of the probe. A simplified scaling analysis proceeds as follows: the rise time of the cap is essentially an unsteady filling problem, with the stagnation conditions on the probe tip driving mass flow into the internal cavity of the probe. Equation (4.1) gives an expression for the choked mass flow rate of an ideal, compressible gas. Assuming the final pressure after the filling to be equal to the Pitot pressure and the temperature to be some internal temperature, T_i, the final mass inside the cap can be determined using the ideal gas law. The flow rate, normalised by the final mass, can thus be written as shown in Equation (4.2). As expected, this is not a function of pressure. If the process is entirely adiabatic, then $T_i = T_t$ and the normalised mass flow rate should scale with the square root of stagnation temperature. However, if there is complete cooling to the wall temperature within the cavity then the inverse is true, and filling time actually increases by approximately the same factor.

Whilst this analysis completely ignores unsteady effects, it is sufficient to demonstrate the dependence of the pressure measurement rise time on the gas composition and the particular stagnation temperature. These factors should be accounted for when considering the applicability of these measurement techniques to new flow conditions.

$$\dot{m} = \frac{AP_p}{\sqrt{T_t}} f(\gamma, \mathscr{R}) \tag{4.1}$$

$$\frac{\dot{m}}{m} = \frac{AP_p}{\sqrt{T_t}} f(\gamma, \mathscr{R}) \times \frac{\mathscr{R}T_i}{VP_p} = \frac{A\mathscr{R}T_i}{V\sqrt{T_t}} f(\gamma, \mathscr{R}) \tag{4.2}$$

In summary, it was found that for the conditions considered in this campaign that Pitot pressure measurements using the swirl cap geometry gave the most consistent measure of

the test period. Notably, the rise time is significantly shorter than the shield cap design and as such they are recommended in the context of high enthalpy shock tube performance characterisation, despite a lengthening of rise time at higher stagnation temperatures. The coaxial thermocouple gave useful results under some – but not all – conditions. Other authors have resolved ionisation issues by sputtering the face of the gauge with SiO_2 e.g. Hayne et al. (2007), which is thermally conductive but an electrical insulator. The infrastructure to perform this process is not yet established at the Osney Thermofluids Laboratory. In any case, this technique would have necessitated frequent changeover of heat flux gauges due to their location on the stagnation point of the probe and the therefore inevitable ablation of the protective coating. Based on this assessment, the swirl cap measurements are used to assess the variation in test time across the range of tested conditions in the following section.

4.4.2 Test Time Assessment

To assess the test time performance of the T6 AST the rake data for a large number of shots was analysed. Here, only the data from the swirl caps was considered. The test time is determined by finding the time between the first arrival of the shock at the Pitot rake and the onset of driver gas contamination, visible as a sudden change in pressure magnitude and unsteadiness. This is performed manually using an interactive MATLAB script. The start and end points were not typically uniform for all radial positions. As a result, an error bound is placed on this nominal time interval by selecting the earliest and latest departure from the quasi-steady level at each end of the test period. This bound therefore constitutes both an uncertainty and a physically-significant range within the data. An example of this methodology as applied to a sample shot is shown in Figure 4.10.

The results of this analysis for initial fill pressures of 1.6 Pa to 266.6 Pa and shock speeds from 6.1 $\mathrm{km\,s^{-1}}$ to 11.5 $\mathrm{km\,s^{-1}}$ are shown in Figure 4.11. Here, the Mirels prediction of test time shown in Figure 4.1c has been reproduced; the tested conditions are overlaid as points. These are also shaded according to their measured test time. The folded views show the difference between the measured test time and the Mirels prediction, as a function of both fill pressure and shock speed.

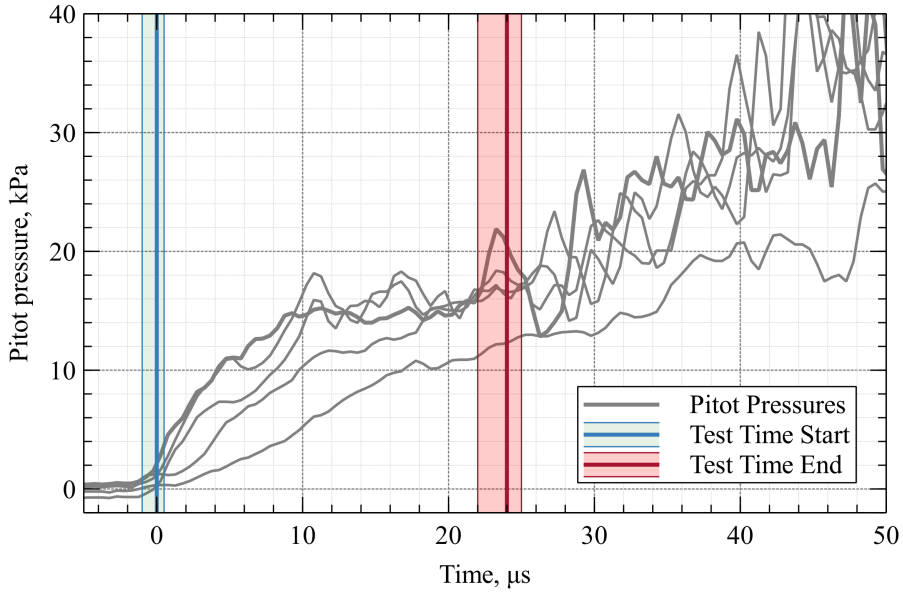


Figure 4.10 – Pitot pressure traces from T6s143. Overlaid is an example of test time assessment, with nominal values denoted by vertical solid lines. The identified region of uncertainty is shaded.

From these results, it can be seen that there is generally a good agreement between the Mirels prediction and the experimental measurements, which match within the uncertainty bound in all cases. There is increased scatter at higher pressures, which is due to additional noise in the flow; this makes confident identification of the test period challenging. Based on the criterion of Mirels (1964), at pressures of approximately 150 Pa the boundary layer would enter the transitional regime. This would both introduce unsteadiness and reduce the test time. There is also poorer agreement for the two shots at the lowest pressure of 1.6 Pa, as these have test times less than the rise time of the swirl caps.

Despite these discrepancies, in general the agreement is very good. This is especially true of the repeat conditions at 13.3 Pa and 26.6 Pa. Although in some individual cases the uncertainty in test time estimate can be high, generally these are on the order of ±3 µs. This overall good agreement with the analytic prediction of test time, both in terms of magnitude and the overall trend, suggests that useable test flows are produced across a wide range of conditions in the AST, and builds confidence in the use of these tools for the planning of future test campaigns.

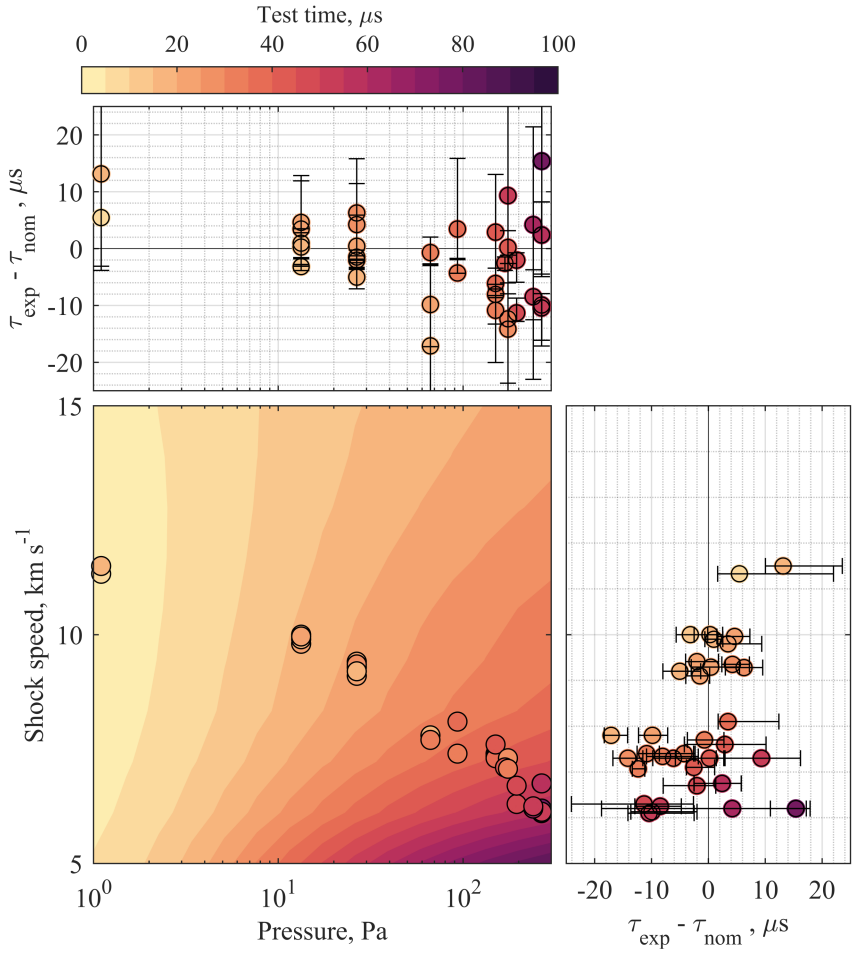


Figure 4.11 – Results from experimental assessment of facility test time, with comparison to laminar Mirels prediction. The tested conditions are shown as points, shaded according to their experimentally measured test time. The folded views show the absolute difference between the measured and nominal values of the test time for each experimental point, including uncertainty bounds based on manual assessment of driver gas arrival.

4.5 Developed Conditions

This section discusses the selection and development of test conditions for the shock-layer radiation experiments presented in Chapter 5. The main purpose of these experiments is to benchmark the AST emission results against established data sources and to provide another source of cross-facility comparison. The criteria for selection of these test conditions are as follows:

1 **Mission Relevance:** Any conditions investigated must be of interest for past or planned flight programmes. Typically, this is satisfied for many of the datasets that

meet criterion 2.

2 **Comparability:** There must be sufficient data from other facilities which is available in the open literature.

3 **Complexity:** The complexity of the conditions (both in physical phenomena and facility operation) would ideally be minimised to reduce the number of potential factors influencing the final result.

4 **Feasibility:** Conditions must be achievable using the T6 AST. They must also be sufficiently within the performance envelope to allow the test point to be reached reproducibly.

5 **Utility:** The conditions studied in the AST should be of wider use than simple benchmarking of the facility.

Considering the aforementioned factors, the selection of test conditions was undertaken as follows: ideally, there should first be a test condition with a large region of nominal equilibrium for comparison. This reduces the influence of spatial resolution effects (i.e. optical system f/# and the motion of the shock) and eliminates the need to consider non-equilibrium thermochemistry in the initial analysis **(3)**. Cruden and Brandis (2017) previously presented air data between 7 km s^{-1} and 9 km s^{-1} in pressures ranging from 0.01 Torr to 0.90 Torr, which shows substantial areas of equilibrium **(2)**. In addition, these datasets are freely available online (Cruden, 2017) and are of direct interest to proposed Earth entry trajectories **(1)**. Based on the performance map shown in Figure 4.3a, these conditions are well within the capability of the AST **(4)**. Finally, although there are significant regions of equilibrium in the flow, some discrepancies have been observed in the data of Cruden and Brandis (2017), both between the two diameters of tube used at the EAST facility and when comparing to numerical predictions. Specifically, the equilibrium radiance level is under-predicted in the majority of cases. The ultraviolet/visible region is also much less optically thick in the non-equilibrium region than computational simulations suggest. A further source of cross-facility comparison could therefore contribute to the resolution of some of these uncertainties **(5)**. Of the

available data, a condition at nominal fill pressure of 66.6 Pa was selected. This is detailed in Table 4.2 as Condition I.

As discussed in Chapter 2, when considering equilibrium radiation measurements atmospheric plasma torches can provide a useful source of experimental data. Notably, the thesis work of Laux (1993) has been extensively referenced for the development of radiation models. Additionally, that thesis implemented modifications to the NEQAIR2 code, the successor of which is employed extensively in Chapter 5. A condition was thus developed to recreate the conditions of these experiments in the post-shock equilibrium region of the AST. Given the aim is to compare to an atmospheric plasma torch, the first requirement was to generate an approximately 1 bar post-shock pressure. Laux (1993) reported the temperature of the torch to be between 6500 K and 7500 K. Based on this, a target condition of 175 Pa and 7.2 km s^{-1} was chosen, corresponding to a nominal post-shock equilibrium temperature of approximately 7000 K. This is also shown in Table 4.2, where it is designated Condition II. By reproducing established results in a different type of facility, this condition inherently satisfies criteria **(2)**, **(3)** and **(5)**. Referring again to Figure 4.3a, it can be seen that said condition is also within the performance bounds of the AST **(4)** and lies on the nominal Hayabusa flight path **(1)**.

At the low speeds typical of Conditions I and II, the majority of the emission is dominated by molecular species and the influence of ionisation is reasonably small. Above approximately 9.5 km s^{-1} (in air), there is a notable regime change wherein the majority of the equilibrium emission stems from atomic transitions. The electron number density is also significantly increased. It was also desired to validate the AST experiments in this regime, as well as to investigate whether equilibrium conditions could be achieved in the shock-layer.

Such higher-speed conditions are representative of many high velocity Earth return trajectories **(1)**. Brandis and Cruden (2017a) proposed a set of benchmark shock tube experiments at these conditions, at fill pressures of 0.1 Torr and 0.2 Torr, with the majority of the tests in the range 9 km s^{-1} to 12 km s^{-1} **(2)**. Given the inherent nature of the AST (better signal-to-noise and test time at the expense of performance) a condition at the lower end of the speed and pressure regime would be most suitable **(4)**. Furthermore, analysis of

Table 4.2 – Selected T6 Test Conditions.

Condition	P_1, Pa	U_s, km s^{-1}	Comparison	Reference Study
I	66.6	7.7	EAST (Low Speed)	Cruden and Brandis (2017)
II	175.0	7.2	Plasma Torch	Laux (1993)
III	13.3	10.0	EAST (High Speed)	Brandis and Cruden (2017a)

the equilibrium region by Brandis et al. (2017) found that models mostly disagreed with the experimental data from EAST below these velocities — a source of comparable data would thus assist in determining the generality of this effect **(5)**. The chosen condition was selected to be 13.3 Pa and 10.0 km s^{-1}. It was anticipated that this could be reached without the use of a secondary driver, therefore minimising operational complexity and the time between shots **(3)**. This test case is designated Condition III in Table 4.2.

4.5.1 Test Condition Facility Performance Assessment

The facility performance and the quality of its test flows are inextricably linked. Here, three key measurements are reported for the test conditions selected in Section 4.5 and listed in Table 4.2: shock speed variation, static pressures at the observation window, and centreline Pitot pressure. These are compared to the predictions of analytic tools to confirm that the targeted conditions are achieved.

Figure 4.12 shows the measured shock speed variation for the three conditions presented in Table 4.2. Shown are all shots discussed in Chapter 5; it can be seen that there is excellent shot-to-shot repeatability. The portion of the test gas which originates in Shock Tube 1 and the nozzle (i.e. the first four shock speed measurements) is not considered part of the valid test flow. Within the AST itself, the shock speed profile shows good steadiness along the length of the tube, as well as close agreement with the target conditions. This is especially true within the last 2 m, which typically is the maximum extent of test flow visible through the observation windows. There is a slight deceleration in shock speed near the measurement location, which is associated with expansion waves travelling from the driver. As discussed in Section 4.3.1, it was not possible to produce over-driving at the high compression ratio of Driver Condition C++,

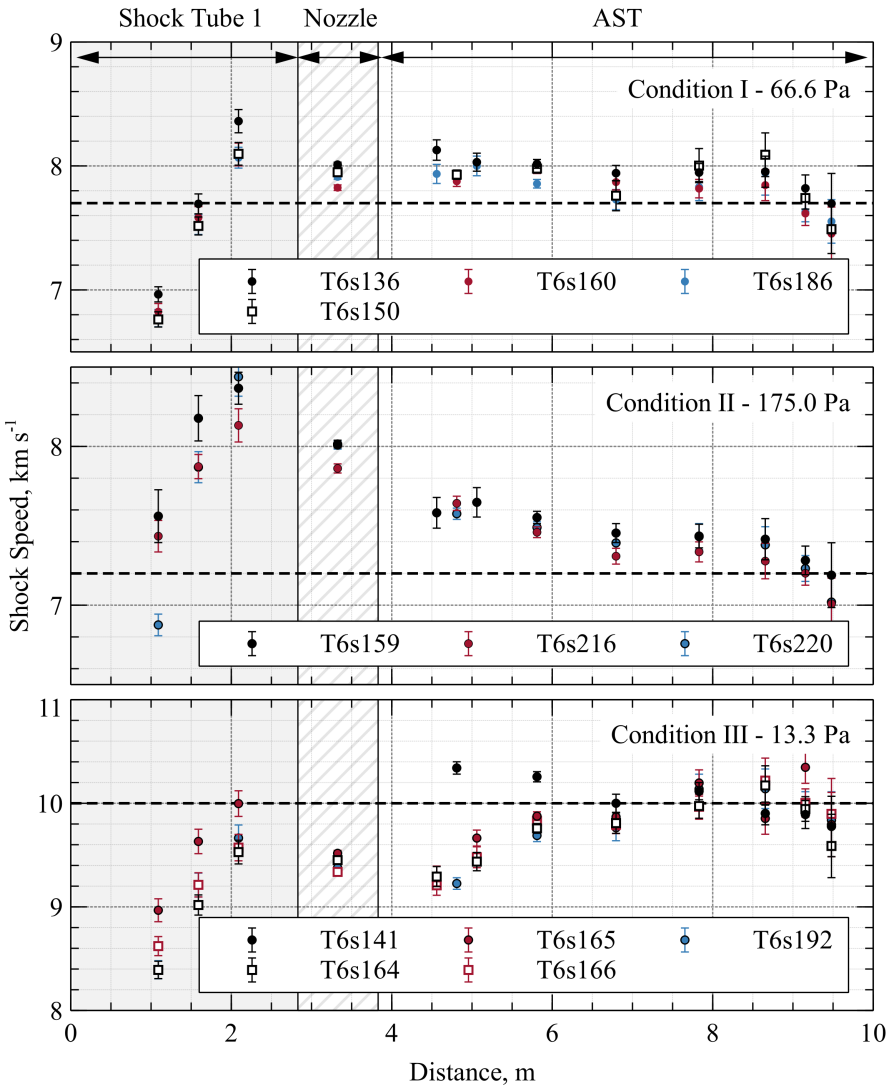


Figure 4.12 – Measured shock speed variation for the conditions shown in Table 4.2. The target shock speed for each case is shown as a dashed line. The portion of the trajectory which occurs in Shock Tube 1 and through the nozzle are shaded. The centre of the windows is located at 9.4 m.

which causes this effect. Despite this slight deviation, the overall variation at the window is still within the measurement uncertainty.

Representative pressure measurements for the three conditions are given in Figure 4.13. The wall static pressures at the observation window are shown in Figure 4.13a, where they are compared to the expected post-shock value for each case. The nominal value is determined from the equilibrium post-shock conditions calculated using the NASA CEA code. It can be seen that in all three cases there is excellent agreement between the predicted value and the experimental measurement. This validates the accuracy

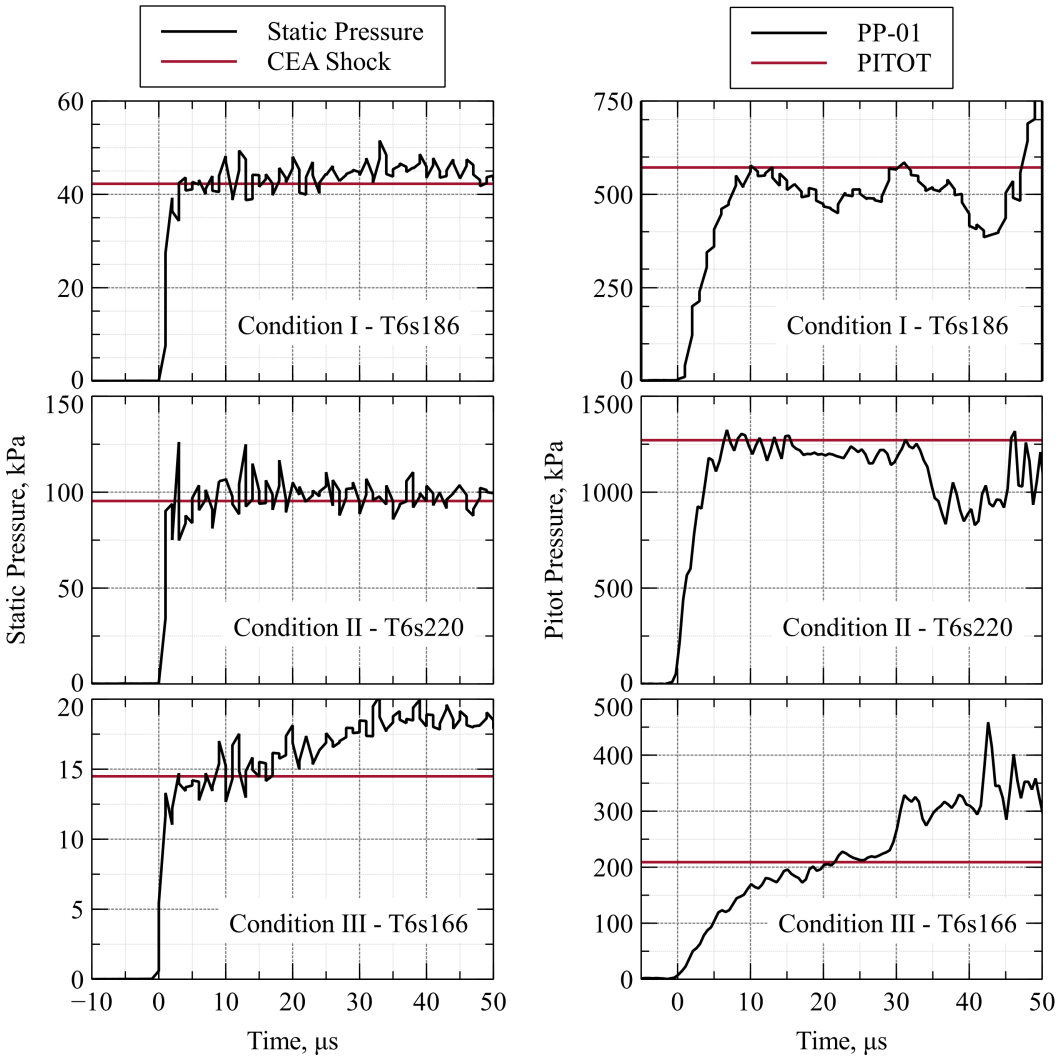
of the shock speed measurement and, in the case of the lower density of Condition III, the fill pressure.

Finally, the measured centreline Pitot pressures are shown in Figure 4.13b. It can again be seen that there is good agreement between the expected and measured values. Here, the nominal values for Pitot pressure are calculated using the PITOT code, based on the experimentally measured shock speed. In the case of the lower speed conditions (I and II), there is a gradual reduction in Pitot pressure from the nominal over the test period; this is again attributed to the lack of over-driven conditions in the free-piston driver. Condition I also exhibits some unsteadiness in the trace which is not apparent in the other tests. Paull and Stalker (1992) have shown that different conditions at the interface between the driver and test gas result in changes in the acoustic impedance. This varies the transmission efficiency of waves from the driver, which may be why this condition exhibits greater sensitivity to these waves. Of particular note is that the Pitot pressure for Condition III agrees well the the nominal value, despite the low fill pressure and high shock speed. This again recommends the swirl cap geometry as a useful instrumentation choice for high-enthalpy shock tube testing.

4.6 Summary

In this chapter, the particulars of a new operating mode for the T6 free-piston facility were presented. Details of the design relevant to shock-layer radiation experiments were highlighted, and the specifics of its use in the remainder of this work given. The shock timing arrangement, the design of a new Pitot rake and the operational methodology used in the experimental campaign were specifically highlighted.

The results of a performance study for the AST were presented, in which it was shown that the design was capable of achieving test conditions relevant for both low-speed and super-orbital Earth re-entry. In addition, tests for high-altitude Mars cases and Titan trajectories demonstrated capability to perform experiments at conditions of particular relevance for radiative heating. These results also validated the suitability of the AST for its designed purpose, i.e. measurement of emission under either low pressure or limited volumetric radiance conditions. Comparisons with the PITOT code were reasonably good,



(a) Wall static pressures.

(b) Centreline Pitot pressures.

Figure 4.13 – Representative wall static and Pitot pressure measurements for the three developed conditions of Table 4.2, with comparison to calculated values.

however some disagreement was observed which is attributed to complexities in the nozzle flow which require more detailed analysis. An assessment of the test time was shown to give good agreement with the laminar predictions of Mirels (1964).

Finally, the rationale for the selection of three test conditions to perform benchmark emission spectroscopy experiments was outlined. Representative shock speed profiles, static pressure and centreline Pitot measurements were also shown for the three cases, demonstrating close agreement with the nominal values. These conditions are now employed in the following chapter to perform measurements of radiating air shock-layers.

A photon walks into a hotel.

The clerk says, "Can we help you with your luggage?"

The photon replies, "No thanks, I'm travelling light."

— Anon.

5 Absolute Measurements of Air Shock-Layer Radiation

Contents

5.1 Introduction 131
5.2 The Optical Emission Spectroscopy System 132
5.3 Spectral Comparison Methodology 141
5.4 Condition I — Low Speed EAST Comparison 149
5.5 Condition II — Plasma Torch Test Case 156
5.6 Condition III — High Speed EAST Comparison 165
5.7 Summary 171

5.1 Introduction

The preceding chapter demonstrated the ability of the new T6 AST to generate flows relevant to the problem of radiative heating. Three test conditions were selected for benchmarking experiments; the aim of these is to compare results of shock-layer radiation measurements from this new facility to established data.

The approach taken in the AST experiments is as follows: a shock is generated, which travels along the tube. The final shock speed, initial fill pressure and gas composition are matched to a trajectory point of interest. As the shock passes windows in the tube wall, a

line along the tube axis is imaged onto the slit of a spectrograph using a system of mirrors. The incident light is thus resolved spectrally, resulting in a two-dimensional map of the light intensity (as a function of axial position and wavelength) being imaged onto the sensor of a camera. In these experiments, the shock can travel in excess of 10 mm μs^{-1}. This imposes significant challenges on the optical system, both in terms of measuring sufficient intensity and in achieving shot-to-shot repeatability.

This chapter first describes the optical system used to perform measurements of shock-layer radiation in the T6 AST. The methodology used to compare the experimentally measured spectra to both other facilities and to numerical tools is then outlined. Results at the three conditions of Chapter 4 are then presented, with comparisons made in both the equilibrium and nonequilibrium regions of the shock-layer. Finally, conclusions based on the experimental comparisons are given.

5.2 The Optical Emission Spectroscopy System

The shock layer radiation experiments undertaken in the AST employed a dual-channel optical emission spectroscopy (OES) system. This permitted two regions within overall spectral range of 200 nm–900 nm to be measured simultaneously for each shot. In this study, these will be referred to as the 'Blue' and 'Red' systems, after their primary wavelength regions (200 nm to 500 nm and 550 nm to 900 nm respectively).

A detailed description of these systems is first given, including measured characteristics of the optical system. A concise outline of the calibration approach is then presented. For full details of this process, the reader is directed to Appendix B.

5.2.1 General Arrangement

The T6 AST features two diametrically opposed optical windows, integrated into the tube wall at a distance of 9.6 m from the primary diaphragm. The clear aperture of these windows is 190 mm or 200 mm axially[1] and 10 mm vertically. Depending on the wavelength region of interest, MgF_2, UV-grade Fused Silica and CaF_2 windows are available, covering the wavelength range 115 nm–8000 nm. In the long term, it is

[1] The length variation is a result of variability in available optical material ingot size.

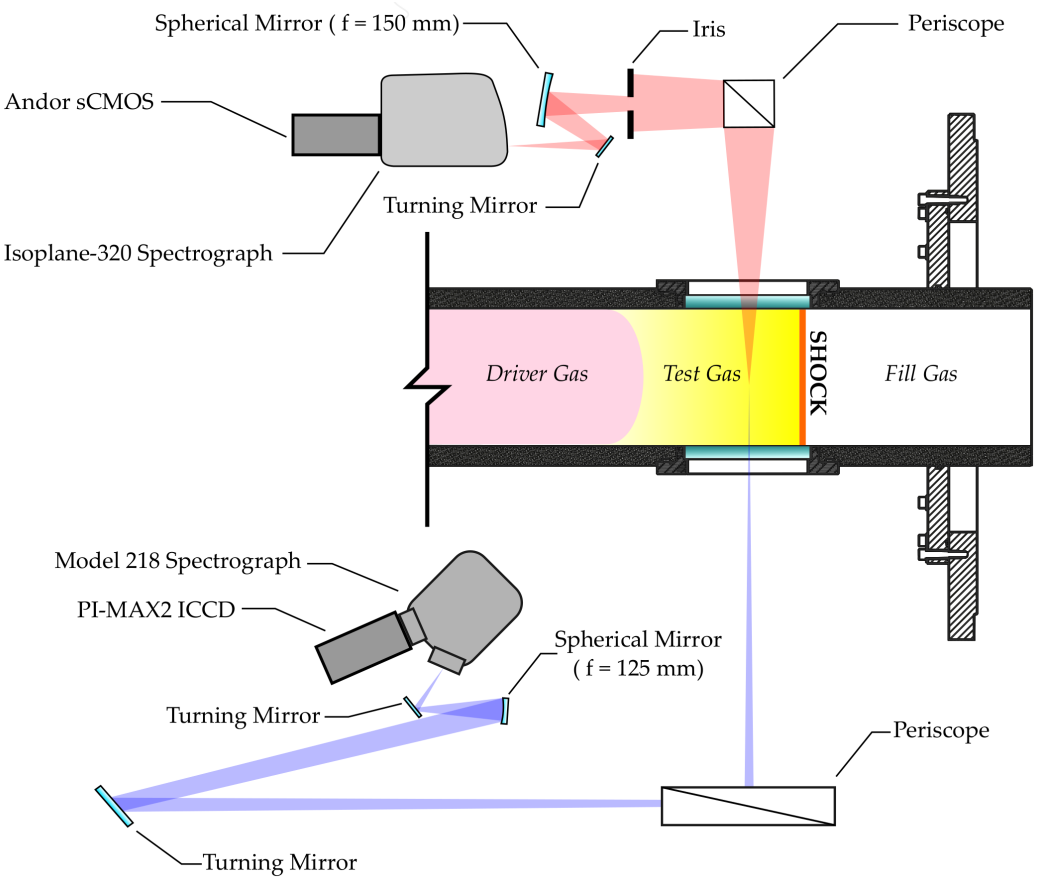


Figure 5.1 – The optical emission spectroscopy system used for AST experiments. The Red OES is shown above the tube and the Blue OES below. Not to scale.

intended that multiple spectroscopy systems be installed on each side; see Greenberg et al. (2009). In these experiments, where two OES channels were used, these were arranged on opposite sides as shown in Figure 5.1.

The function of the OES system is to capture spectrally and spatially resolved emission data from the shock-layer. The former objective is achieved by use of a diffraction spectrometer, which uses a ruled grating to disperse incident light by wavelength. For more information on the operating principles of these instruments the reader is directed to Thorne et al. (1999). Spatial resolution is achieved in the experiment through use of a system of mirrors; these image a line along the tube axis onto the spectrometer slit. Each point along the slit (and hence the tube axis) is thus resolved spectrally. Mirrors are used in preference to lenses — given the wide wavelength ranges observed — as this avoids chromatic aberrations.

Red Optical Emission Spectroscopy System

The Red OES system is shown in the top half of Figure 5.1. An Andor sCMOS intensified camera[2] with a Gen 2 W-AGT photocathode and P46 phosphor is coupled to a Princeton Instruments Isoplane-320 spectrograph. For this work, diffraction gratings of 150 Grooves/mm and 1200 Grooves/mm were used, both with blaze wavelengths of 500 nm. The sCMOS camera used has a sensor resolution of 2560×2160 pixels, with the larger dimension oriented in the wavelength direction. However, in practice the sensor is limited as by the intensifier: this is circular, meaning the corners of the (rectangular) sensor are unusable. The sensor also oversamples the intensifier, which has a resolution of 1280×1080 pixels.

Whilst the loss of resolution due to oversampling of the intensifier is undesirable, it does permit 2×2 binning to be used with no loss of resolution. This is a software-based post-processing step performed during data readout from the camera, which down-samples the sensor data by summing 2x2 squares of pixels. Physically, each pixel can only hold 30 000 electrons before saturating. The brightest spectral line must be less than this threshold, which sets a limit on the maximum signal-to-noise achievable using 1x1 binning at a given intensifier gain. Assuming that the noise on each pixel is statistically independent, using binning can increase the signal-to-noise ratio by a factor given by Equation (5.1), where N_{px} is the number of binned pixels and S_{sig} and S_n are the signal and noise counts on one pixel respectively. As this step is performed in the software, the digitisation can be increased from 16-bit to 32-bit which maintains the dynamic range of the image.

$$SNR = \frac{N_{px} S_{sig}}{\sqrt{N_{px} S_n^2}} = \sqrt{N_{px}} \frac{S_{sig}}{S_n} \tag{5.1}$$

Radiation emitted from the hot gas within the tube is imaged onto the slit of the Isoplane using a 150 mm focal length spherical mirror. Two 50 mm diameter flat mirrors in a periscope arrangement account for vertical offset between the optical table and AST

[2] It should be highlighted that intensified sCMOS cameras have not typically been used in high-enthalpy ground testing, with only ICCD designs historically available. However, in the course of this work they were found to offer substantially improved noise and dynamic range characteristics, as well as the ability to capture significantly more calibration images in a shorter time.

centreline. The periscope also rotates the incoming light by 90°, mapping a horizontal line along the tube axis onto the vertical spectrometer slit. A key consideration for an optical arrangement of this type is that the angle of incidence of the spherical mirror should be minimised to reduce coma. This is achieved with an additional 1 inch diameter flat mirror, which is used to fold the optical path. This allows sufficient space to position the spectrometer and camera at the focal point without excessive turning of the focussing mirror. In all cases, the mirrors used were Thorlabs protected silver (-P01 series) which have a guaranteed average reflectance greater than 97.5 % in the range 450 nm to 2000 nm. Finally, a 550 nm long-pass filter (Thorlabs FEL0550) was included in the optical path. This prevents higher-order spectral features being superimposed on the measured spectrum.[3]

At the shock there exist very strong spatial gradients along the axis of the tube. As a result, a sufficiently large depth of field is required to minimise the size of the so-called 'circle of confusion' (CoC) at the tube wall. An iris of variable diameter on the object side of the focussing mirror allows the depth-of-field of the system to be varied. This iris is placed as near as physically possible (i.e. touching) the focusing mirror in order to reduce vignetting. Improvements in the depth-of-field require reduction of the solid angle of the captured radiation, reducing signal intensity. A balance must therefore be found between the spatial resolution and signal-to-noise ratio of the measurement. The Isoplane has an aperture ratio of f/4.6; the external imaging optics must also have a value greater than this to ensure the spectrograph is under-filled. This limits the scattering of stray light inside the instrument, which can affect the measured intensity. The characteristics of the Red OES, as determined from measurements of the installed system, are given in Table 5.1.

Blue Optical Emission Spectroscopy System

The Blue OES system is shown in the bottom half of Figure 5.1. A Princeton Instruments PI-MAX2 ICCD camera with Gen 2 UV intensifier is coupled to a McPherson Model 218 spectrograph. The ICCD has a pixel resolution of 1024×256, with the larger dimension again used for the wavelength component of the measurement. For shots after number

[3]For example, light of 400 nm wavelength entering the spectrometer will generate second-order diffractions at 800 nm, which are challenging to remove *post hoc*.

T6s216, a new Andor intensified sCMOS with a WE-AGT photocathode and P43 phosphor was available and so was substituted for these later tests.

The optical system used is in principle identical to that used for the Red arrangement, with a few key differences. These were largely driven by the smaller slit size of the Model 218 spectrograph — 12 mm in comparison to 24 mm for the IsoPlane. This required a greater magnification to maintain a similar field-of-view (FoV). This was achieved through use of a spherical mirror with a focal length of 125 mm at a distance of 3815 mm from the tube centreline. Space constraints within the laboratory area meant that an additional folding mirror was required to fit this object distance in the area available beside the tunnel. This is reflected (pun intended) in the optical path shown in Figure 5.1. The periscope consists of two rectangular 200 mm×25 mm mirrors. These differ from the design used on the Red OES as they were manufactured to order for operation in the VUV; the large axial extent permits use in a future telecentric optical arrangement. All optical components were Al-MgF_2 coated, with a rated reflectivity greater than 85 % in the region 200 nm to 650 nm. A filter was not required for measurements in the UV region, as a combination of attenuation from ambient atmospheric oxygen and a decrease in mirror reflectivity effectively eliminated incident light below 200 nm.

In the Blue OES, no iris is used; the spherical mirror has a diameter of 1 inch and hence gives a smaller f-number than the spectrometer, given the larger object distance. The characteristics of the Blue OES are again given in Table 5.1. The measured data shows that the two optical systems provide roughly equivalent field-of-view capability. In both cases, the CoC on the optical axis is on the order of 1 mm at the tube wall. In the case of the Blue OES camera, this equates to less than one pixel in size after demagnification through the optical chain.

5.2.2 Optical System Absolute Intensity Calibration

The shock tube windows, optical mirrors, spectrograph diffraction gratings and camera intensifiers all possess a wavelength-dependent efficiency with which they transmit incident light. A calibration standard with known emission as a function of wavelength is thus required to determine the transfer function of the system and hence relate the intensity

Table 5.1 – Table of optical system characteristics used in this work. The object and image distance, as well as iris diameter, were measured directly from the optical arrangement; the solid angle and CoC (assessed on the optical axis at one tube radius from the focal point) were calculated from these values. The FoV is determined from the spatial calibration.

Channel	f, mm	d_o, mm	d_i, mm	D_{iris}, mm	Ω, 10^{-5} sr	CoC, mm	FoV, mm
Red	150	1856	154.4	20	9.12	1.14	159.1
Blue	125	3815	136.0	—	3.37	0.71	167.0

measured in the experiment (in sensor counts) to a meaningful value of spectral radiance (in $\mathrm{W\,cm^{-2}\,sr^{-1}\,\mu m^{-1}}$). This needs to be undertaken for every unique combination of optical system parameters, e.g. spectrograph grating angle, camera gain, spectrometer slit width and iris diameter. Having an absolute measure of spectral radiance enables direct comparison to both other facilities and to numerical tools. The value and utility of the dataset is thus greatly enhanced. Again, a full description of the calibration process is given in Appendix B; a brief overview is provided here for context.

Some authors have used an irradiant source (calibrated in units of $\mathrm{W\,m^{-2}\,nm^{-1}}$) for the purpose of absolute calibration (e.g. McGilvray et al., 2010a). However, this approach requires an accurate determination of the solid angle captured by the optical system. This is sometimes achieved by calibrating each optical component in a bench-top setting and then combining the individual efficiencies to form a representative curve for the system as a whole. An alternate approach, applied here, is to use a source of known spectral radiance which is placed on the tube centreline. This allows the entire optical path to be calibrated in-situ and does not require the solid angle to be known, thus circumventing this potential source of error. This approach also allows the calibration operation to be completed after each test, thereby compensating for any change in optical properties. Lastly, by translating the calibration lamp along the tube axis any variation due vignetting effects can be corrected; this extends the useable field-of-view.

Above 300 nm, a Bentham Instruments SRS8 quartz-tungsten-halogen integrating sphere with spectral radiance calibration in the range 300 nm–2500 nm was used. This lamp features a 50 mm diameter outlet window and so spatial calibration of the optical path is achieved by imaging the integrating sphere at several overlapping locations within the

field-of-view. These individual images are then stitched together during post-processing to give a continuous, smooth surface. At each location, 100 accumulated images are taken and averaged to reduce noise. A background image is also taken and subtracted from the calibration images to account for noise generated during the exposure (primarily due to thermally generated electrons and read noise in the digitization process) and any ambient light sources. The camera gain must be equivalent in both the experiment and calibration. The radiance standards used are significantly dimmer than the post-shock gas imaged during a test. As a result, a longer exposure time must be used during the calibration to yield a reasonable signal level. Both the calibration and experimental images must therefore be normalised by their corresponding exposure times. It has been shown that this reciprocal relationship becomes less accurate at very short exposures, due to the transient opening process of the intensifier gate. However, at the times used in this work ($>$500 ns) this effect is expected to be negligible in comparison to the overall experimental uncertainty (Cruden, 2014).

Whilst the integrating sphere calibration was valid to 300 nm, the Blue OES required calibration down to 200 nm. To achieve effective calibration in this wavelength range, a McPherson Model 632 deuterium light source was used. This standard had a valid calibration between approximately 115 nm and 400 nm. The effective diameter of the deuterium source is approximately 1 mm; this makes entirely covering the field-of-view impractical. Instead, images are taken at approximately 10 mm intervals. This results in calibration curves across the whole wavelength range at discrete spatial locations, with positions corresponding to the individual D_2 images. These discrete curves are then fit at each spatial pixel using either a polynomial function or smoothing spline.

For the vast majority of shots presented in this work, the above calibration procedure is performed before each test. This accounts for any changes in window transmissivity due to residue from the post-test flow which coats the tunnel wall between tests. The windows are also cleaned between each shot (before the calibration) using acetone, which effectively removes this residue. The cleaning process also minimises the difference between calibrations, allowing a degree of redundancy in the case of a bad set of calibration data.

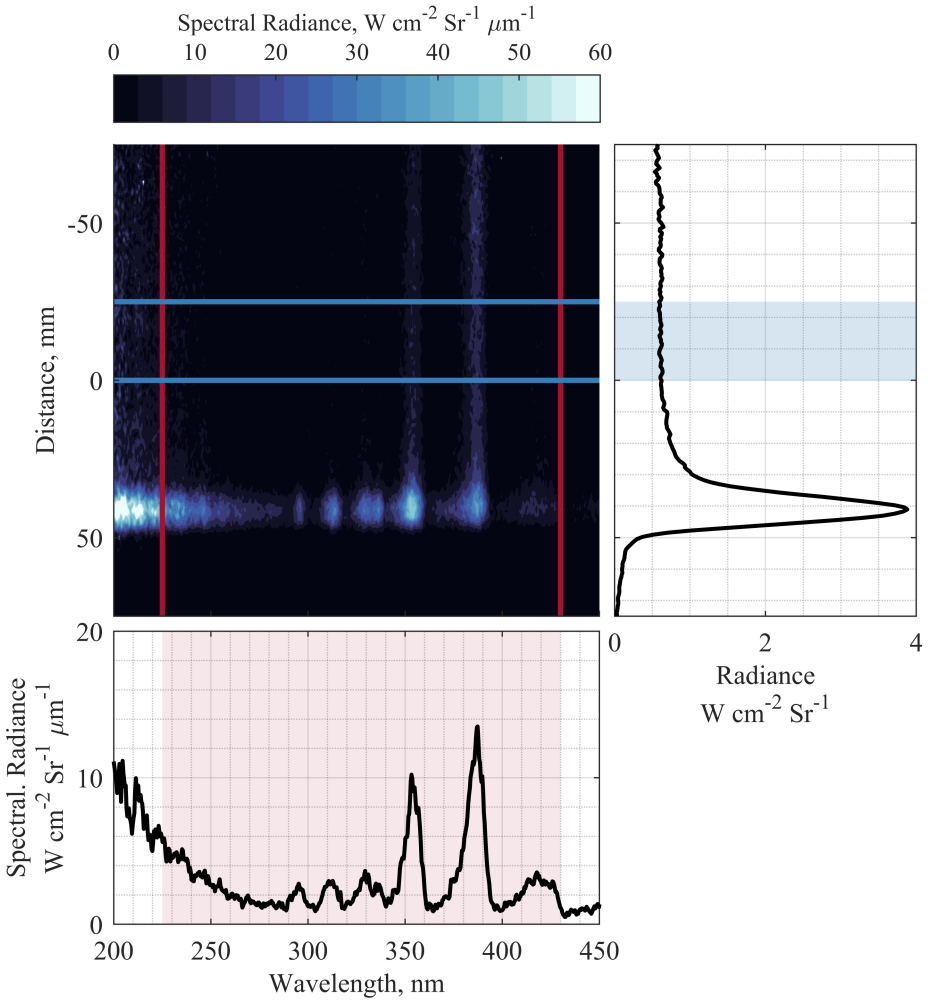


Figure 5.2 – Example of spatially and spectrally resolved, calibrated emission data from the Blue OES for shot T6s186. The mean equilibrium spectral radiance between the two horizontal blue lines is shown on the bottom graph. The right-hand plot shows the integrated radiance between the vertical red lines.

An example of a calibrated spectrally and spatially resolved emission spectrum generated by applying all of the stages in the preceding discussion is shown in Figure 5.2. This data can then be applied to study which spectral regions radiate most strongly in different parts of the shock layer. Alongside the 2D data, plots of the equilibrium spectral radiance and the integrated radiance are shown. The limiting bounds for these are given as horizontal blue and vertical red lines, respectively.

5.2.3 Camera Triggering

A challenge for shock-layer radiation experiments in a shock tube is that the flow is highly transient: at 10 km s^{-1}, the shock traverses the 200 mm AST window in 20 µs. The objective is to image a sufficient amount of the pre-shock gas to confidently identify the shock front, the whole non-equilibrium peak, and as much of the equilibrium region as possible. As a result, it is desirable to position the shock to within 25 mm (at worst) from test-to-test. These factors place stringent requirements on the accuracy of the camera triggering system. Given also the effort required to perform every test, the trigger signal should be robust to shot-to-shot variation in shock speed to maximise the proportion of useful tests.

For these experiments, a trigger box (Fast Oscillator Shock Timer Enabling Repeatable Spectroscopy — FOSTERS) was built based on the design of Jacobs (2011b). FOSTERS houses a Microchip Technology PIC16F1769 microcontroller, which monitors the signal on two shock timing stations upstream of the window. The distance between these timing stations is equal to the distance between the second timing station and the centre of the window. When the shock passes the first transducer, an internal 8 MHz clock begins counting. After the shock passes the second timing station, the count value is recorded. When the timer reaches double this value (i.e. when the shock should be in the centre of the window), a trigger signal is sent to the cameras. This also allows a pre-trigger signal to be sent immediately when the shock reaches the first transducer, which is required to prepare the Red OES camera for fast gating.

This microcontroller-based triggering approach is necessary, as different shock speed profiles and/or shot-to-shot variation can result in poor positioning of the shock in the window and hence the need to repeat a test. A simple delay is vulnerable to this issue. In addition, the fast motion of the shock prohibits higher-level software programs and/or triggering approaches: even simple calculations/input-output processes require orders of magnitude greater computational time than is available. In practice, the only mathematical operation which has sufficient time to be performed (even using the microcontroller) is a multiplication by two i.e. a bit shift, which can be completed in a single clock

cycle. Using this approach it was generally possible to position the shock to within a few millimetres between repeated tests.

5.3 Spectral Comparison Methodology

In this work, spectral data from the T6 AST are compared to various sources. This section summarises the approach taken in each comparison.

5.3.1 Definition of Shock-Layer Regions

This chapter compares emission data from several regions of the shock-layer. Here, the conventions used to define these portions of the test slug are outlined. Figure 5.3 shows an example of the typical experimental trend in radiance observed through the shock-layer; the annotations show the main regions of the test slug. Ahead of the shock, a slow rise in radiance is typically observed. In this work, the location of the shock front is taken to be where a significant rise above this trend (shown as the red line in Figure 5.3) is first observed. Immediately following the shock front, there is a region of non-equilibrium. This is typified by a transient excitation and subsequent relaxation process; the non-equilibrium peak is thus taken to be the first local maximum in radiance directly behind the shock.

With sufficient distance away from the shock front, the finite-rate thermochemical processes are complete and no further change in radiance is expected. The timescales required for this to occur are dependent on the specific flow conditions: from one-dimensional simulations[4] using the 11-species, two temperature model of Park (1993) the relaxation distance is predicted to be 14 mm, 5 mm and 9 mm for Conditions I, II and III respectively. However, a key output of these shock tube experiments is often the thermochemical rates; this makes definition of the non-equilibrium extent based on such simulations tenuous. Additionally, in a real experiment the measured test slug is blurred spatially by both the resolution of the optics (which changes across the field-of-view due to the telescopic nature of the set-up) and by the motion of the shock during the exposure time. For the experiments reported here, the latter causes a minimum

[4]These are discussed in more detail in Section 6.4.1.

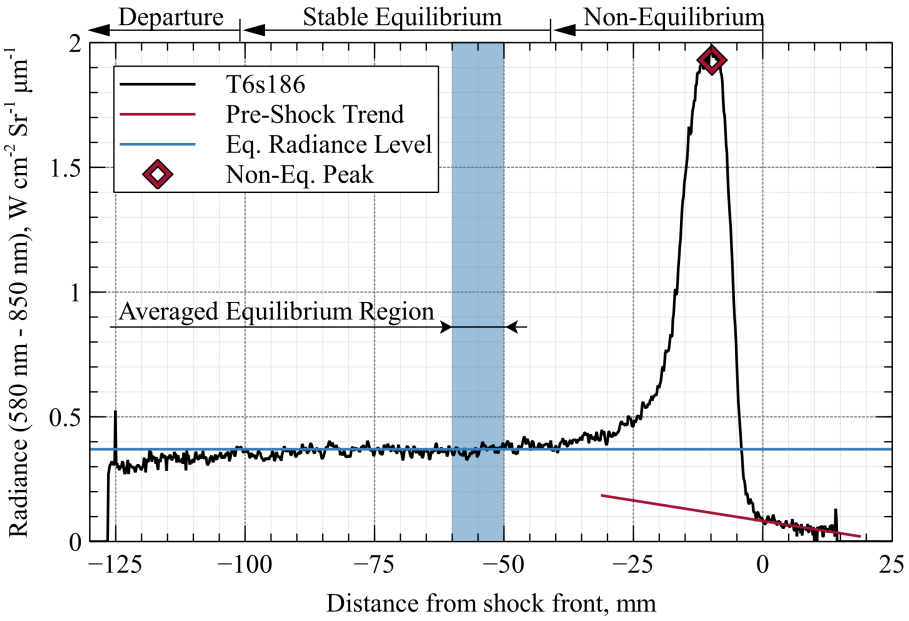


Figure 5.3 – Annotated experimental radiance plot for T6s186, showing main features of the shock-layer: the shock front, non-equilibrium region and stable equilibrium plateau.

smearing of 3.6 mm (for the Red camera, at Condition II). This is on the same order as the expected relaxation distance.

The inherent variability in the emission data from shock tube facilities presents challenges to robust, automated identification of the equilibrium plateau. This is thus typically performed manually; see, for example, Brandis et al. (2010b). The location of 'stable equilibrium' is here defined an extent of approximately constant radiance directly after the non-equilibrium region. In this work, the end of this equilibrium plateau is assumed to occur after a sustained change in gradient which causes a significant departure (i.e. $\sim$10 %) from the identified equilibrium level. In the case of the experimental data of Figure 5.3 this occurs at approximately −100 mm. In general, the AST experimental results presented in the subsequent sections showed excellent repeatability and long extents of steady equilibrium. As such, the mean equilibrium spectral radiance has been calculated between 50 mm and 60 mm behind the shock front in all cases for consistency. This region is represented by the shaded blue areas in Figures 5.2 and 5.3.

5.3.2 EAST Comparisons

The tests conducted at EAST used for comparison in this work are detailed in each section. It should be highlighted that only shots either designated as benchmark cases in published works (Brandis and Cruden, 2017a; Cruden and Brandis, 2017) or given the highest quality rating in the datasets are used for comparison here.

The equilibrium spectra are not directly comparable as the use of differing optical equipment results in different amounts of instrumental broadening, which change the sharpness of the observed features. In addition, the difference in tube diameters result in approximately double the emission measured in the AST for the same condition. This does not scale exactly with tube diameter due different degree of optical thickness in the gas and the proportionally different amount of boundary layer absorption. For the conditions discussed here, NEQAIR simulations were performed to determine the expected optical thickness. Following the approach of Cruden and Brandis (2020), the results of each simulation were normalised by their diameter to give an effective 'spectral radiance per unit depth'. The ratio of this quantity for the AST to that from EAST gives an effective metric for the optical thickness, with a value of 1 implying optically thin emission. These simulations suggest that molecular features will be effectively optically thin for these conditions (on the order of 2 % difference). However, atomic lines in the near infrared are predicted to show up to 35 % less radiance per unit depth for the AST cases.

Considering these factors, the following methodology is used: in the equilibrium region, the results from both T6 and EAST are compared to their NEQAIR simulations. This is discussed further in Section 5.3.3. The EAST equilibrium spectra are taken as specified by the NASA researchers in the online database (Cruden, 2017). These have been averaged by the original authors at differing distances behind the shock front, depending on the position of the apparent 'equilibrium' portion of the shock layer. As discussed in the work of Brandis et al. (2010a), this is identified manually This approach is expected to make less difference for the low speed comparisons of Sections 5.4 and 5.5 (where a steady equilibrium can typically be identified) but may introduce more uncertainty for other cases.

In the immediate post-shock region, the non-equilibrium metric (NEM) proposed by Brandis et al. (2013) is used for comparison. The metric takes two forms: the spectral NEM and the absolute NEM, as defined in Equations (5.2) and (5.3) respectively. In the case of the spectral NEM, the integration limits are chosen to be ± 2 cm of the shock front, to account for differing amounts of spatial blurring due to optical resolution or the motion of the shock during the gating time. The normalisation by tube diameter means that in the case of optically thin radiation direct agreement would be expected between facilities; in practice, absorption often results in a lower value of this metric for larger-diameter tubes.

$$K_s(\lambda) = \frac{1}{D} \int_{x_{shk}-2cm}^{x_{shk}+2cm} R(x,\lambda)\, dx \tag{5.2}$$

$$K_a = \int_{\lambda_1}^{\lambda_2} K_s(\lambda)\, d\lambda \tag{5.3}$$

The absolute NEM is a scalar value that accounts for the total radiance within the non-equilibrium region of the shock layer in a given wavelength range. Physically, this can be considered equal to the radiative heat flux incident on the stagnation line of an entry vehicle, if said vehicle had a shock stand-off distance of 2 cm and the plasma can be considered optically thin (Brandis et al., 2013). In this work, the absolute NEM is plotted cumulatively, which allows more direct comparison of the EAST and T6 data across the range of spectral features presented.

5.3.3 NEQAIR Simulations

All computed spectra in this thesis were generated using the Non-EQuilibrium AIr Radiation (NEQAIR) program, first developed by Park (1985). The current version (15.0) used in this thesis is maintained by Brandis and Cruden (2019). NEQAIR is a line-by-line spectral code with the capability of simulating one-dimensional radiative transport. The full capabilities of the code are summarised by Cruden and Brandis (2014).

For the equilibrium comparisons presented here the NASA CEA code of Gordon and McBride (1994) was used to generate an equilibrium composition for the shock speed and fill pressure of the chosen test. For the T6 shots, the average shock speed at the last three transducers is again taken. This is shown for a representative case at each condition

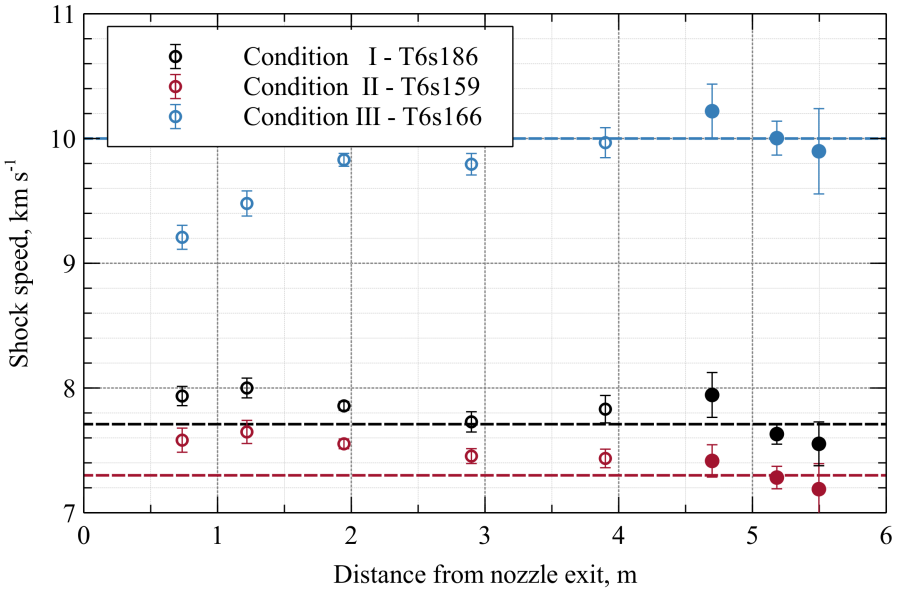


Figure 5.4 – Definition of nominal shock speed for T6 spectroscopy experiments. The dashed line shows the mean value of the final three measurements; these are shown as filled markers.

in Figure 5.4. The validity of this choice is explored further in Section 6.4.1. For the comparisons between NEQAIR and the EAST facility, the stated shock speed in the shot summary (as estimated by the NASA investigators) is used.

The NEQAIR simulations undertaken here assume a radiating depth equal to the tube diameter. The computations were performed using the recommended solver settings, specifically the non-Boltzmann, flux-limited method in combination with a local escape factor approximation with a characteristic distance of 1 cm. The solution is not expected to be particularly sensitive to these settings as the analysis was performed using an equilibrium composition which should be at local thermodynamic equilibrium (LTE).

The calculated spectrum from NEQAIR is convolved within the code with the instrument function to enable direct comparison with the experimental results. In the case of T6, the instrument function determined using the method detailed in Appendix B.1.1 is used. For EAST, the low speed condition instrument functions are taken from the online dataset (Cruden, 2017). The high speed test data used in comparisons with Condition III are processed using the slit function parameters detailed in Brandis and Cruden (2017a).

5.3.4 Spectral Fitting Routines

A core aim of this thesis was to investigate whether a stable, post-shock equilibrium could be achieved at the tested conditions, and to what extent this region was similar to the prediction of CEA. This is straight-forward for pressure measurements, however assessing the temperature of hypervelocity flows is a complex exercise. Physical instrumentation typically measures temperature change, from which heat flux can be calculated and then flow temperature inferred based on assumptions of heat transfer coefficient. Several key unknowns, notably catalytic effects, complicate this process in the context of high enthalpy shock tube experiments (Penty Garaets, 2019). Spectroscopic analysis offers the ability to infer temperature from the measured emission of a high temperature plasma, and — if appropriately high resolution measurements across a sufficiently broad set of wavelengths are made — can be used to determine species number densities, excited state populations and, if appropriate, assign an effective Boltzmann temperature for an internal energy mode of interest. In the optically thin case, the upper state population can be calculated directly from the integrated line or multiplet emission using Equation (5.4), where $\mathscr{H}$ is the Planck constant and c the speed of light. Here, the emission coefficient is only a function of the upper state population and known spectroscopic constants, which allows the former to be directly calculated.

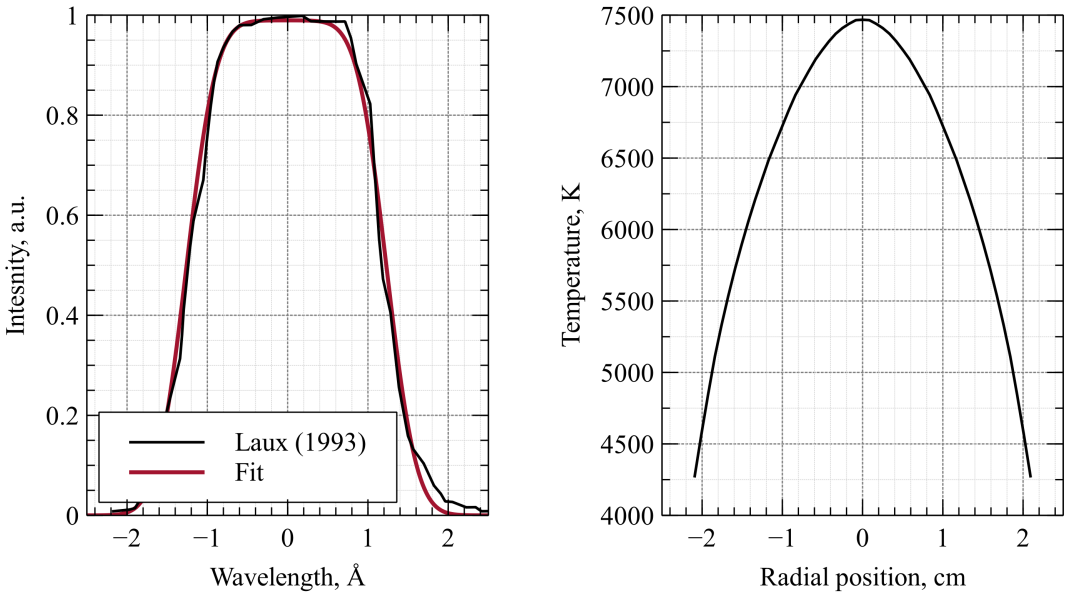
$$\varepsilon = \frac{n_u A_{ul} \mathscr{H} c}{4\pi\lambda_0} \tag{5.4}$$

In practice, however, the AST emission is not generally optical thin. This significantly complicates the described analysis as in this case the lower states of the transition absorb a portion of the radiation. In addition, this absorption has a non-linear dependence on intensity, such that the variation in emission and absorption across the shape of the measured line must be fully considered. Often in the literature this is performed from first principles, where the known parameters of the plasma and spectroscopic constants are used to calculate broadening mechanisms, and hence the radiative transport through the gas (e.g. Hermann et al., 2016).

In this work a different approach is applied, wherein the python-based optimisation routines of Brandis and Cruden (2018) are used. These scripts interface with NEQAIR and attempt to minimise the error between an experimental spectrum and the solver output. Using this interface has the advantage of working with a validated tool and should produce results consistent with other comparisons in this work. Under the multi-temperature assumption, translational, rotational, vibrational and excitation temperatures can all be varied independently, as well as species number densities. Non-Boltzmann and state-specific populations can also be individually perturbed.

In this work, the fitting is undertaken as follows: an initial guess for the temperatures and number densities are provided by calculating the CEA equilibrium composition. The temperatures are then fixed and the number densities of the species optimised to provide a best fit to the experimental spectrum. The temperatures are then also included in the optimisation. Given the much stronger sensitivity of the solution to temperature, this significantly improves the agreement between the number density sample mean and the CEA predictions in equilibrium, albeit the uncertainties are typically large enough that this is not particularly significant. As noted by Brandis and Cruden (2018), these fits are not unique solutions but can be used to find likely bounds on the plasma parameters.

For the analysis presented in this work the default non-linear least squares optimiser, in combination with a Trust Region Reflective algorithm, was used. The standard error of each fitting parameter is determined from the Hessian matrix, evaluated at the optimal values for the inputs. These are used to compute a 95 % confidence bound for the fitting result. Typically, these bounds are large for number densities but much smaller for temperatures. In this work, the number density uncertainties are reported as the root-sum-square of the fit confidence interval and the maximum experimental uncertainty over the considered wavelength region. The temperature fits are achieved though fitting a Boltzmann distribution, and are hence dependent on the ratio of emission lines rather than their absolute magnitude. This minimises the influence of the experimental error and thus only the uncertainty of the fit is reported.



(a) Monochromator ILS, with fit.

(b) Plasma torch temperature profile.

Figure 5.5 – Data taken from Laux (1993) to enable NEQAIR comparison. The temperature profile is taken from Figure 4.5 of that work; the measured ILS is taken from Figure E1.

5.3.5 Plasma Torch Comparison

In this thesis, the original plasma torch data of Laux (1993) is used as a benchmarking case. Following similar logic to the equilibrium comparisons with EAST, it is not expected that there would be a direct correspondence between the torch data and that from T6: the diameters are substantially different, and the conditions are not exactly matched. Instead, the plasma torch data is also compared with NEQAIR. This section describes the modelling approach taken to enable this comparison.

The approach used to simulate the plasma torch closely follows the original method of Laux (1993). To create an input to NEQAIR, the measured temperature profile (replicated in Figure 5.5b) was used to calculate the equilibrium species number density at 50 points across the torch diameter. This was done using the CEA program, assuming a pressure of 101.3 kPa and composition of 78.084 % N_2, 20.946 % O_2, 0.934 % Ar and 0.033 % CO_2. All settings used for the NEQAIR simulations are identical to those used for T6 and EAST. In the original work of Laux (1993), it is stated that the large f-number (f/50) allows the simulation to be treated with a tangent-slab approach. This is replicated here. It should also be highlighted that the experimental measurement has already been Abel-inverted.

In the original work of Laux (1993), the instrument line shape (ILS) was measured and used in the convolution of numerical spectra directly. This is reproduced in Figure 5.5a. Whilst an approximate trapezoidal function is provided in the original work, this is not an available input option in the NEQAIR code. Instead, the approach outlined in Appendix B.1.1 was followed and the line shape fit using a smeared Gaussian function. The resulting fit is also shown in Figure 5.5a. Lastly, in the original work this line shape was not normalised by its area; this has been done here to allow direct comparison to the NEQAIR output.

5.4 Condition I — Low Speed EAST Comparison

The results of emission spectroscopy measurements at Condition I (7.7 km s^{-1}, 66.6 Pa) are shown in Figure 5.6 for both the Red and Blue optical systems. A summary of the measured shock speed for each shot, as well as for the EAST tests used as comparison, is provided in Table 5.2. Considering first the spatially-resolved radiance presented in Figure 5.6a, it can be seen that the measured emission extends up to approximately 125 mm behind the shock front. For the shots undertaken in the UV, the central wavelength was varied depending on the region of interest; the radiance in the region 200 nm to 300 nm (corresponding to NO emission) is thus plotted separately to enable direct comparison between shots. In all cases a steady level is reached after the initial non-equilibrium overshoot, suggesting the shock layer has reached equilibrium. The enhanced emission at the shock front is a fundamental feature of hypervelocity air shocks, and is present in all spectral features throughout the measured spectrum. This phenomenon is due to the very high translational temperature at the shock front, which leads to increased collisional excitation of electronic states (Park, 1990). There is a difference observed in the maximum value of this peak depending on the spatial position of the shock, for example between shots T6s160 and T6s136. This is attributed to the combination of a wide field-of-view and a telescopic optical arrangement, which results in increased spatial blurring away from the optical axis. In general, the shock position is found to be consistent across both the Red and Blue OES. Large differences in shock position between shots are caused by intentional variation of the camera delay to adjust the

Table 5.2 – Measured shock speeds for the T6 and EAST tests compared at Condition I (66.6 Pa). The nominal shock speed is 7.7 km s^{-1}. The EAST tests only report the final shock speed at the window.

T6				
Test	T6s136	T6s150	T6s160	T6s186
$U_{s,m}$, km s^{-1}	7.84 ± 0.08	7.78 ± 0.07	7.69 ± 0.06	7.69 ± 0.06
$U_{s,f}$, km s^{-1}	7.69 ± 0.24	7.49 ± 0.20	7.45 ± 0.21	7.55 ± 0.18

EAST		
Test	E59-43	E59-46
$U_{s,f}$, km s^{-1}	7.75	7.71

shock position in the field-of-view; when these settings are equivalent, very good spatial repeatability is achieved (*c.f.* T6s160 and T6s186).

The magnitude of the measured radiance agrees well between all shots for the Red OES. In the case of the Blue data, more variability is observed. This reasons for this are explored further in the subsequent discussion. However, it is known that the some of the scatter observed in the data from 300 nm to 450 nm is caused by cyanogen radiation. The CN Violet ($B^2\Sigma^+ - X^2\Sigma^+$) band head occurs at 388.29 nm. This is known to originate from the tube wall; specifically, if Mylar secondary diaphragms are used in a preceding test then a hydrocarbon residue coats the AST bore. This contamination is then advected downstream during the next test, forming CN in the high-temperature boundary layer. This issue was largely resolved through improved shot-to-shot cleaning of the tube using a foam pigging device and acetone. The aluminium construction of the tube enables very low levels of CN with proper cleaning techniques. This solution was only identified midway through the test campaign; a future modification of the facility to incorporate a plasma cleaner (based on the solution of Cruden et al., 2009) is planned to fully eliminate this source of error.

The mean spectral radiance in the equilibrium region is presented for each shot in Figure 5.6b, where both the spectrally-resolved emission and its cumulative integral are shown. For these cases, the equilibrium region has been taken to be from 50 mm to 60 mm behind the shock front.[5] At this condition, the primary contributors to the

[5]Note: the plots show absolute distance from the centre of the window.

measured radiance are molecular features. Atomic lines of oxygen and nitrogen are also observed in the Red data. The most prominent features are labelled for each OES channel in Figure 5.6b.

The continuous background emission underlying the Red OES data of Figure 5.6b is caused the N_2 (1+) molecular band, resulting from vibronic transitions between the $B^3\Pi_g - A^3\Sigma_u^+$ excited states. This feature makes up the majority of integrated emission in this region. Atomic lines of nitrogen and oxygen are also observed. In general, the data shows excellent consistency between shots. Slight differences in the magnitude of the integrated radiance spectra is attributed to natural variations in the shock speed. However, these variances are very small across the range of tests at this condition.

Considering the Blue spectral data, this again consists mostly of molecular features, dominated below 275 nm by the superposition of the NO γ, β, δ and ε bands. The remainder of the spectrum — above approximately 300 nm — is made up of the overlapping N_2 (2+) and N_2+ (1-) systems, relating to the $C^3\Pi_u - B^3\Pi_g$ and $B^2\Sigma_u^+ - X^2\Sigma_g^+$ transitions of molecular nitrogen and its ion respectively. Although there is no direct overlap, there appears to be a good agreement between the magnitude of the emission between the blue and red data in the visible region, best observed through comparison of data from T6s150. The influence of CN contamination is seen through enhanced integrated radiation in the 300 nm to 400 nm region; this is not evident in the data from shot T6s186.

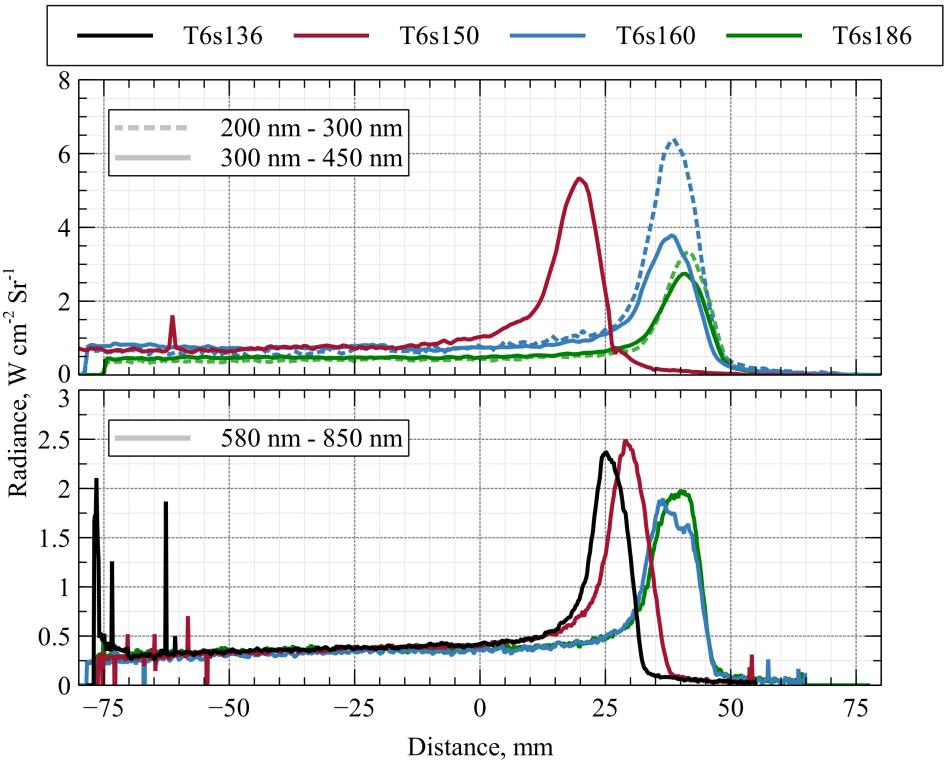
The data from the Blue OES using the PIMAX-2 ICCD camera appears to be affected by an intermittent issue, wherein occasionally a test will be notably lower in magnitude than other repeats at the same condition. This is not seen in the Red data comparisons for the same tests, which eliminates shot-to-shot variation as a root cause. A full uncertainty analysis was undertaken (detailed in Appendix B) to investigate whether this scatter in the Blue OES data is reasonable; it was found that the overall differences are, at best, on the limit of the uncertainty bounds. Substitution of calibrations from the same day does not substantially change the result. In general, it has been found that a constant factor of 1.6 corrects these tests to agree exactly with others at the same condition. This is true over the course of several mirror adjustments and a number of weeks, suggesting that a camera issue (either a gating problem or non-linearity) is the root cause. These tests are

reported here, for two reasons: first, they agree with the predictions of NEQAIR. Whilst this is almost certainly fortuitous, these tests are included for completeness. Second, although the absolute magnitude of these experiments may be erroneous the spectral features and spatial extent of the shock-layer can still be used to demonstrate the quality of the equilibrium region and make to comparisons of spectral features. Further efforts to characterise this issue are on-going.

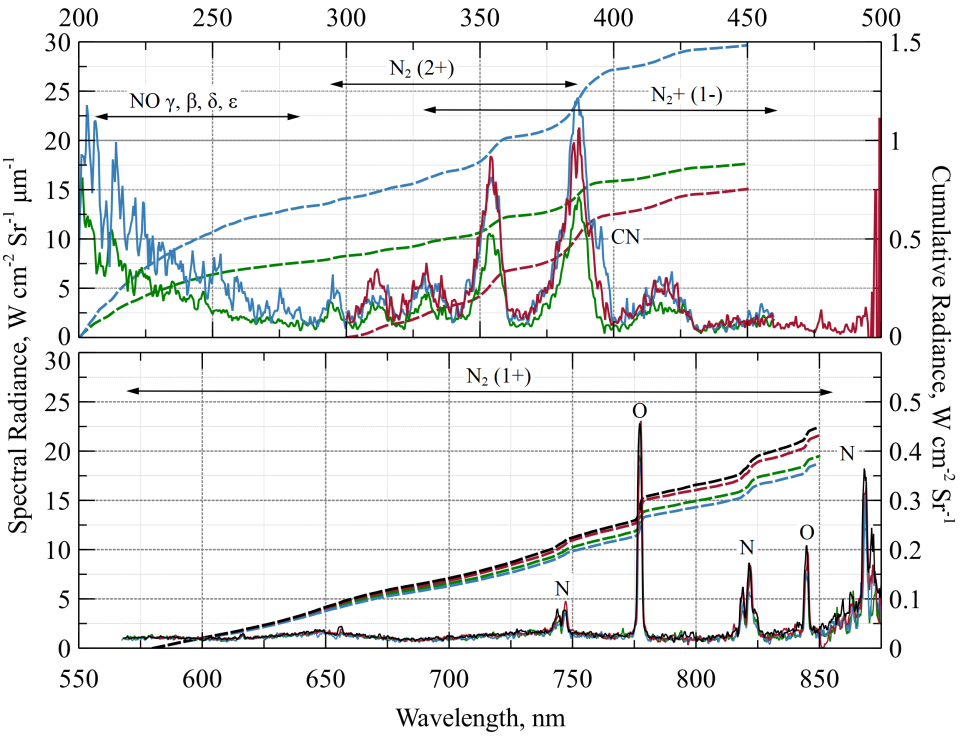
5.4.1 Condition I: Equilibrium Comparison

Figure 5.7 shows a comparison between two representative T6 shots and NEQAIR. Here, the tests from T6 which have simultaneous data from both wavelength channels are shown. Condition I was selected to give direct comparison to shots from the EAST facility; thus also shown is the comparison between NEQAIR simulations and two shots from EAST. These are the designated benchmark test (E59-46) and a repeat at the same condition (E59-43). The graphs of Figure 5.7 are plotted on a log scale to enable comparison across the full spectrum. It can be seen that there is close similarity in the results from the two facilities in terms of the observed spectral features. On the red channel, the T6 data is moderately better resolved due to the use of a finer grating; this is counterbalanced by the wider spectral bandwidth available using the EAST arrangement, which permits the overlap to be measured between the two spectrometers.

Considering first the ultraviolet portion of the spectrum, the observed spectral features compare well between the T6 experiments and the prediction of the NEQAIR for the two tests. As previously discussed, it is thought that the data from T6s186 is erroneously low, which improves the apparent agreement. However, this is also the condition with the lowest carbon contamination and so it is included here. The trends for T6s160 are more similar to those seen for EAST, wherein there is a slight under-prediction of the NO radiance and some of the N_2 (2+) features. There is also good qualitative agreement with the EAST results, albeit these seem to sit slightly above the NEQAIR prediction. These differences aside, both T6 tests agree with their NEQAIR predictions within the uncertainty of the measurement — a positive result.



(a) Radiance. The wavelength ranges included in the integral are inset.



(b) Equilibrium spectral radiance, averaged between 50 mm–60 mm behind the shock front. The solid lines are spectral radiance; the dashed lines show their cumulative integral.

Figure 5.6 – Emission results from the T6 AST at Condition I. The results from the Blue and Red OES systems are shown in the upper and lower portion of each plot respectively.

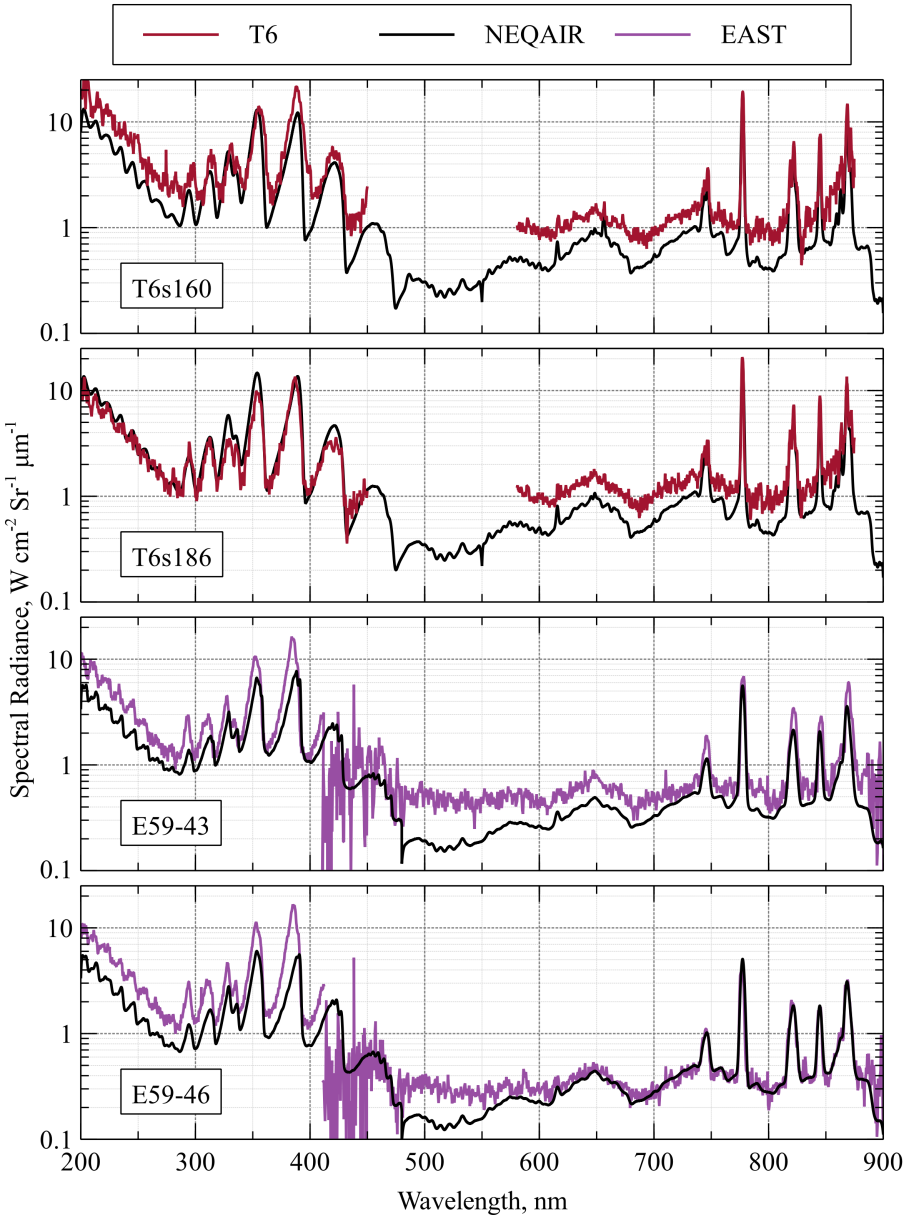


Figure 5.7 – Comparison of experimental equilibrium spectral radiance between T6 and the predictions of NEQAIR for Condition I.

In the Red region, it can be seen that the atomic oxygen and nitrogen features are well matched between both facilities and NEQAIR. In comparison to the T6 experiments, the $N_2(1+)$ band is under-predicted. For the nominal EAST benchmark condition, this is not the case. However, the alternative test at Condition I from EAST (E59-43) shows the same excess of $N_2(1+)$ emission. This data appears more consistent with the T6 results, both at this condition and Condition II (see Section 5.5), which is at a similar velocity.

This conclusion is also supported by the much broader range of experimental data from both the 10 cm and 60 cm tubes studied in the literature (Cruden and Brandis, 2017). This suggests that the agreement of E59-46 is perhaps fortuitous. Figure 5.8 compares the excess radiance of the $N_2(1+)$ emission for a range of cases in all three tubes. It can be seen that in all cases the $N_2(1+)$ contribution is significantly greater than the prediction. There appears to be a worsening trend above approximately 8 km s^{-1}, whilst at lower speeds the T6 AST data suggests the excess of N_2 radiance remains constant at approximately 1.5. At the higher velocities it is likely that bound-free reactions become more prevalent due to increased ionisation. This continuum radiation overlaps the $N_2(1+)$ band in the integrated region, which would explain these results. Shock deceleration effects also likely contribute to this trend; these are discussed further in Chapter 6.

Given that many of the T6 cases have post-shock pressures on the order of 100 kPa, and that the radiance is flat in the equilibrium region, this is not thought to be a non-equilibrium effect in the core flow. Gessman (2001) has shown that nitrogen atoms can preferentially recombine into the N_2 (B,$v = 13$) state through inverse pre-dissociation, although higher-resolution spectral measurements would be needed to fully investigate this effect in the AST. This over-prediction is discussed further in Section 5.5.1.

5.4.2 Condition I: Non-Equilibrium Comparison

For the comparison of the non-equilibrium region the metrics defined in Section 5.3.2 are applied. The results of the comparison between EAST and T6 for both the absolute and spectral NEMs are given in Figure 5.9. In general, there is good agreement between the presented T6 data and between the two facilities. In the red, the integrated atomic features show excellent consistency between the two datasets. Again, the EAST test E59-46 is lower than the rest of the dataset. The absolute NEM is approximately 20 % greater for the T6 data in the considered wavelength region, largely due to the cumulative effect of the $N_2(1+)$ band. This feature is not expected to be optically thick, and so given the construction of the metric these values would nominally be identical. This is the case within the uncertainty of the measurement, and so the presented results can be said to show very close agreement.

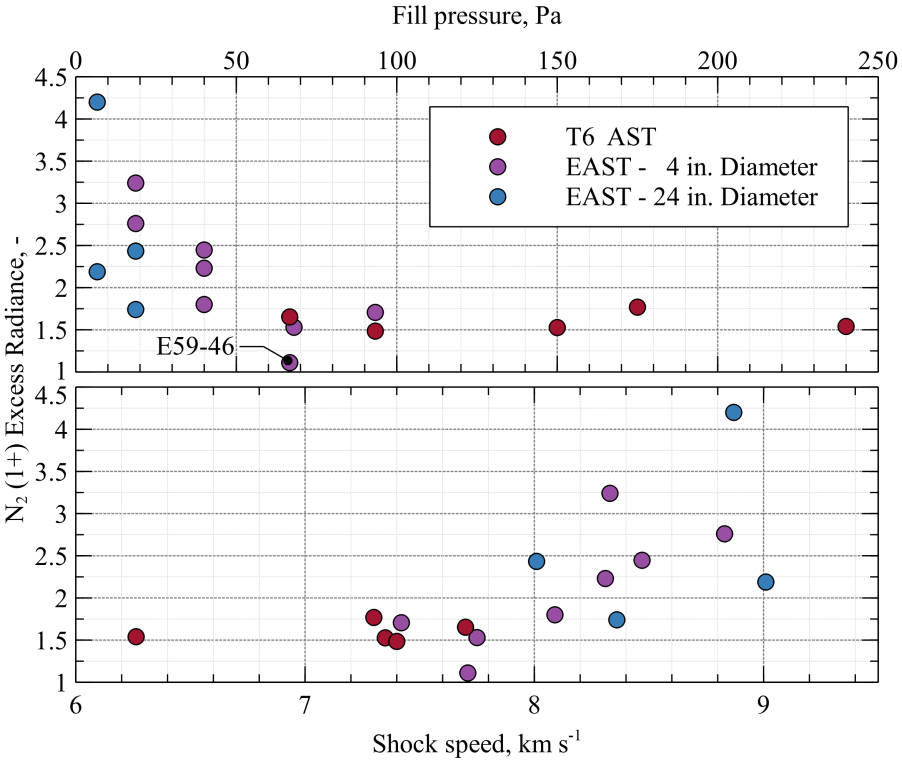


Figure 5.8 – Excess radiance attributed to $N_2(1+)$ emission for a range of tested conditions in T6 and EAST. The excess factor is determined as the ratio of the integrated experimental radiance to the computational prediction in the range 580 nm–730 nm.

The blue data shows overall good agreement in the non-equilibrium between T6 and the data from EAST. A slight excess of integrated radiance for T6s160 is observed due to increased noise at approximately 225 nm. The data for T6s186 is again seen to be lower across all wavelengths. This aside, good correspondence in both the observed spectral features and their relative magnitudes is seen. Given that the majority of the molecular features should be optically thin at this condition, the close agreement of the data from T6s160 with that from EAST aligns better with the anticipated trends.

5.5 Condition II — Plasma Torch Test Case

The shock layer emission data for Condition II (7.2 km s^{-1}, 175.0 Pa) are presented in Figure 5.10, which again shows the data in terms of the equilibrium spectral and cumulative radiance as a function of wavelength. The measured velocities at this condition are provided for reference in Table 5.3 The spatial variation in the integrated radiance

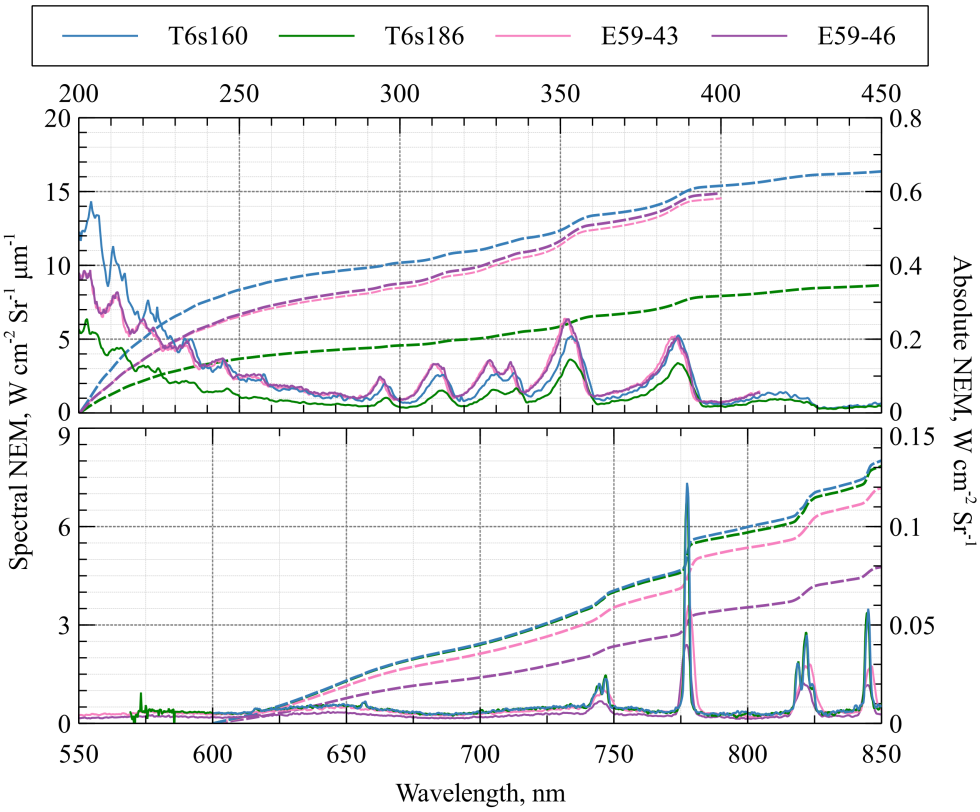


Figure 5.9 – Non-equilibrium metric comparison between T6 and EAST for Condition I, in terms of the Spectral (solid lines) and Absolute (dashed lines) NEM.

Table 5.3 – Measured shock speeds for the T6 test reported at Condition II (175.0 Pa). The nominal shock speed is 7.2 km s^{-1}.

	T6		
Test	T6s159	T6s216	T6s220
$U_{s,m}$, km s^{-1}	7.29 ± 0.05	7.17 ± 0.05	7.23 ± 0.05
$U_{s,f}$, km s^{-1}	7.19 ± 0.20	7.01 ± 0.16	7.02 ± 0.15

is also given. The observed spectral features and trends are essentially identical to those seen in Section 5.4, although the increased post-shock pressure leads to a shortened non-equilibrium region in comparison to the Condition I results of Figure 5.6a. Again, both channels show that a significant extent of post-shock equilibrium is achieved.

In the red, T6s216 used an exposure time of 400 ns (half that of the other low speed shots presented in this work), leading to a sharpened non-equilibrium peak. The measured radiance for this shot is also approximately 10 % lower. This is due to a combination of trialling a lower shock tube fill pressure of 168 Pa (*c.f.* the nominal value of 175 Pa)

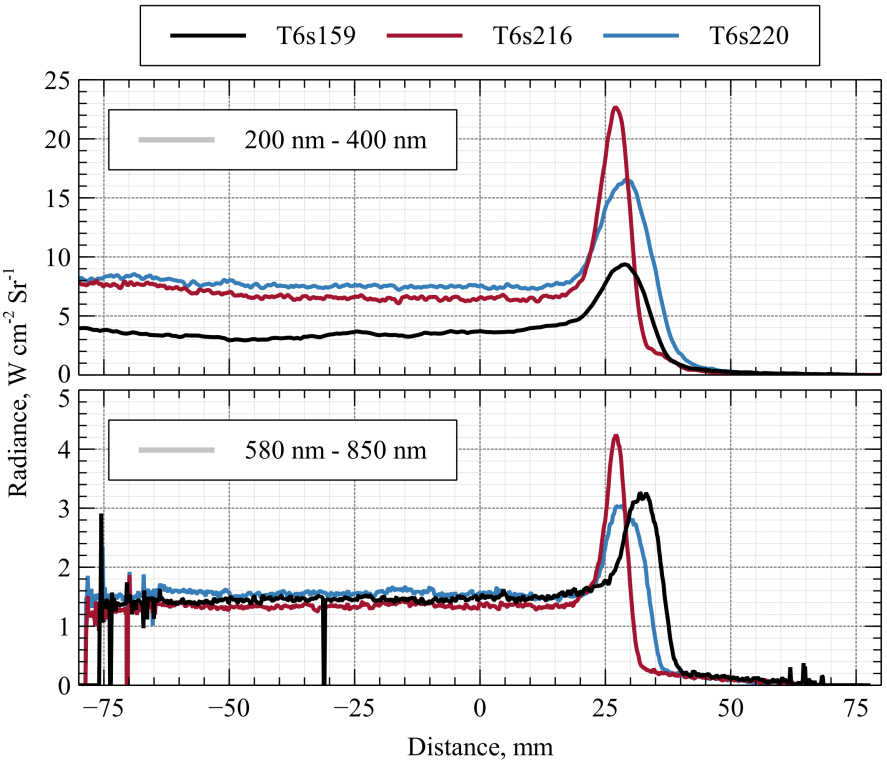
and a slower overall shock speed due to natural shot-to-shot variation. This is reflected in the stated values of static pressure shown in Table 5.4. Again, the Red spectra show excellent shot-to-shot repeatability. Given the number of tests between T6s159 and T6s220, this is a promising result.

In contrast, the Blue OES data of Figure 5.10a there is a disparity between test T6s159 and the later shots. The reason for this is apparent in the equilibrium data of Figures 5.10b and 5.11, where a vertical offset is seen between the two groups of data. For the later experiments, the PIMAX-2 ICCD camera described in Section 5.2 was replaced by a new Andor sCMOS. The reasons for this difference are not immediately clear. The PIMAX camera was operated using an MCP gating mode, with enhanced UV rejection outside the gating time. Conversely, the Andor model is newer and exhibits better signal-to-noise characteristics. The same aforementioned scaling factor aligns test T6s159 exactly with these later shots, which is again suggestive of a gating issue in the original camera.

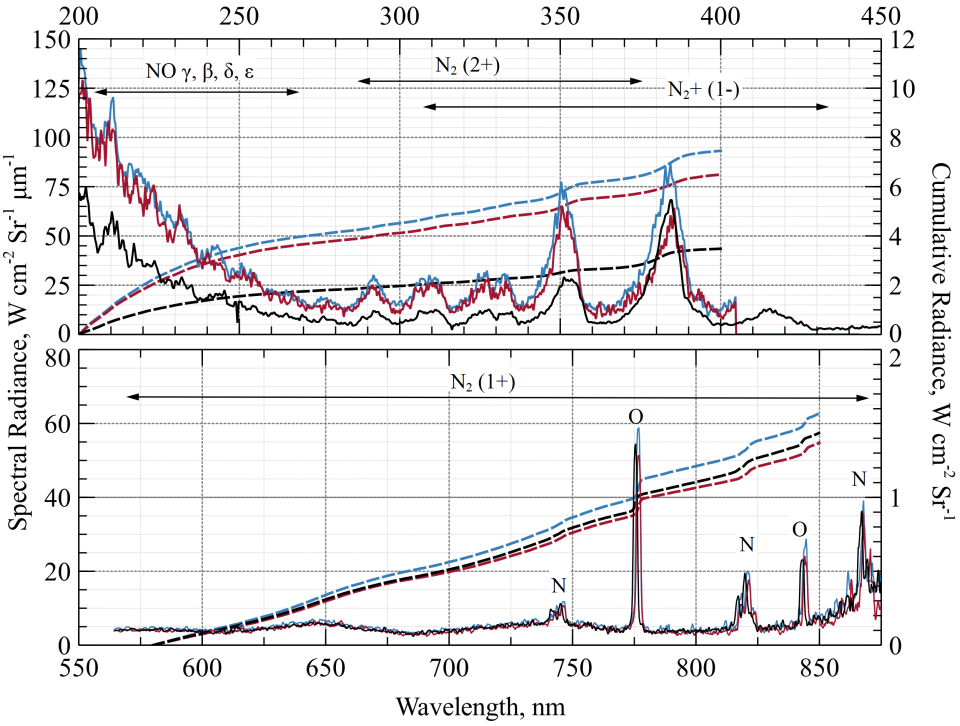
5.5.1 Condition II: Equilibrium Comparison

Figure 5.11 shows a comparison between the T6 data at equilibrium and the predictions of NEQAIR. The trends and conclusions are again equivalent to those for Condition I. Notably, the $N_2(1+)$ is under-predicted. In the data from the Blue OES, the newer camera appears to give results closer to the EAST data of Figure 5.7; the radiance in that region is under-predicted by approximately a factor of two. The qualitative similarity between the trends for the later T6 tests and the EAST experiments further promotes the idea of an intermittent problem with the PIMAX-2 camera; again, all tests are included for completeness.

As discussed in Section 4.5, the purpose of Condition II is to provide a directly comparable test case to the atmospheric plasma torch data of Laux (1993). This would therefore ideally have a post-shock pressure of 1 bar and temperature of 6500 K to 7500 K, with a region of clear equilibrium. There are fundamental differences in the flows produced in the shock tube case and the torch: the former has an transiently generated shock-layer, regions of significant non-equilibrium, and is influenced by the boundary layer; the latter



(a) Radiance. The wavelength ranges included in the integral are inset.



(b) Equilibrium spectral radiance, averaged between 50 mm–60 mm behind the shock front. The solid lines are spectral radiance; the dashed lines show their cumulative integral.

Figure 5.10 – Emission results from the T6 AST at Condition II. The results from the Blue and Red OES systems are shown in the upper and lower portion of each plot respectively.

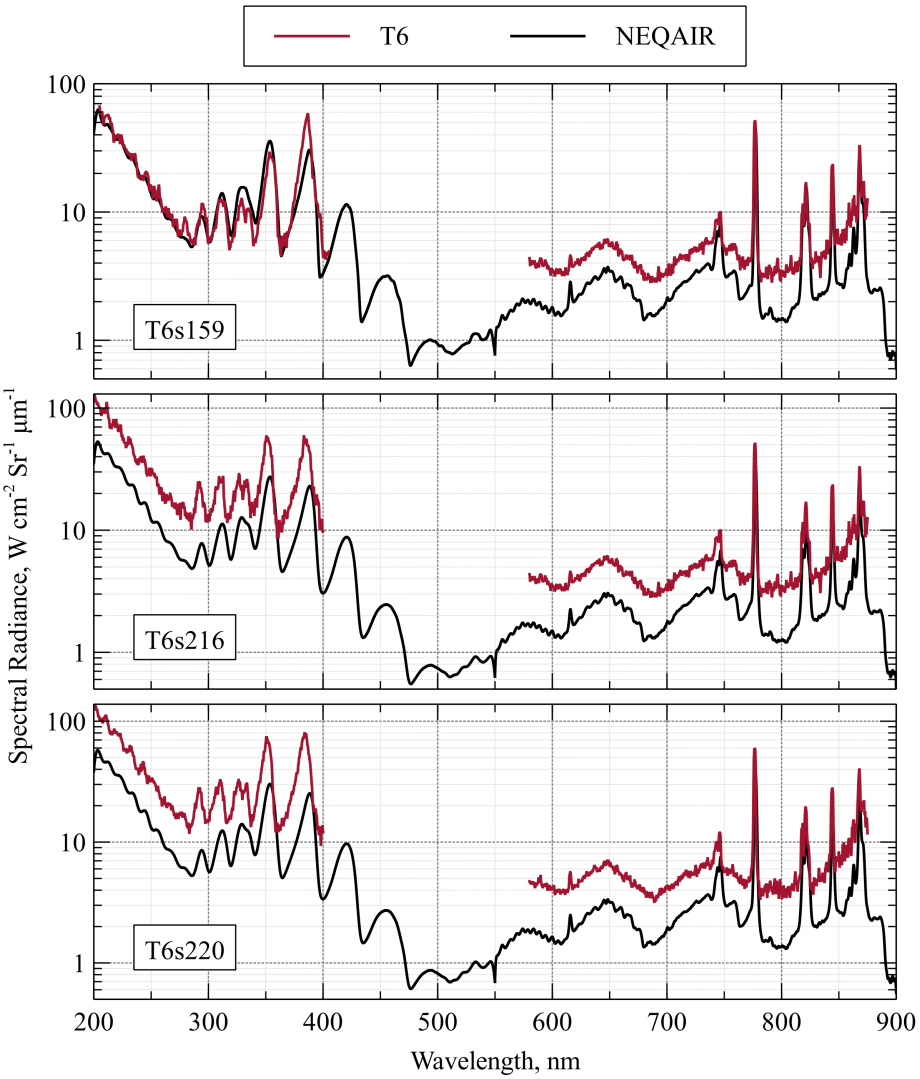


Figure 5.11 – Comparison of experimental equilibrium spectral radiance from T6 and the predictions of NEQAIR at Condition II.

has a smaller spatial extent and a stronger radial temperature gradient. By providing as similar a test case as possible, these more subtle differences can begin to be investigated.

Figure 5.12 shows the static pressure traces for two shots, T6s216 and T6s220. These traces are taken from STS-15, shown in Figure 4.2 and located at an axial position of approximately −50 mm on the spatial axis of the presented spectra. Here, it is observed that the pressure rises to 100 kPa in the post shock region. There is an initial transient period in the pressure rise; however, the steady pressure is reached within 5 µs, which equates to approximately 35 mm of distance at the nominal post-shock velocity. This is significantly less than the observed region of equilibrium.

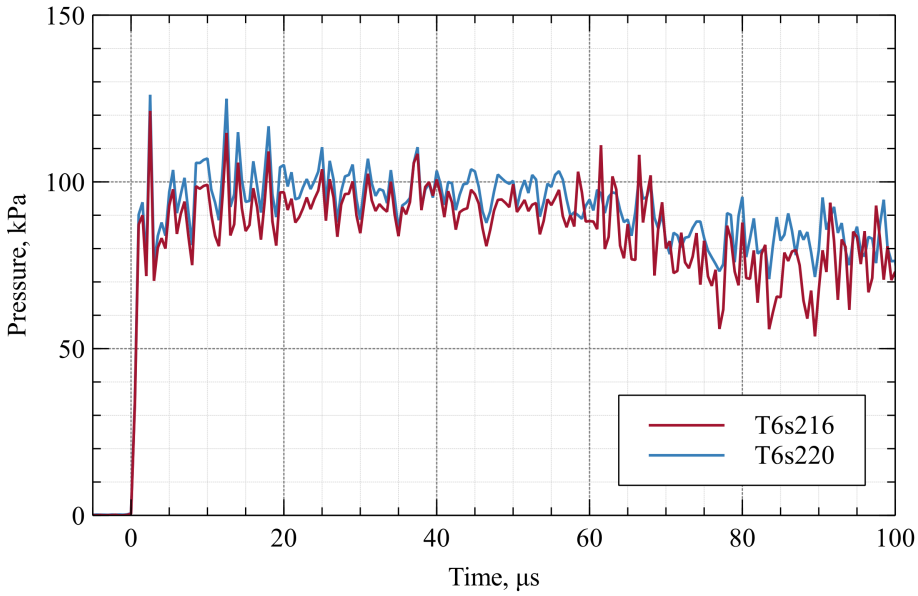


Figure 5.12 – Post-shock pressures measured at STS-15 for two Condition II shots.

In this work, the red emission spectrum is used to assign a temperature to the post-shock equilibrium region. In the case of Condition II, the pressure is measured to be approximately atmospheric. It is therefore assumed that two Boltzmann temperatures (the combined translational-rotational and vibrational-electronic modes, T_{tr} and T_{ve}) are sufficient to describe the internal energy distributions of the gas. Typically, at the temperatures considered here a 7 species model (incorporating N_2, O_2, N, O, NO, NO+ and e-) is considered sufficient to describe the thermochemistry. Based on the observed spectral features shown in the Red spectra of Figure 5.10, only the number densities of N_2, N, and O were varied in the optimisation. Given the disparity between the NEQAIR predictions of the N_2 (1+) emission and the experimental data demonstrated in Section 5.4, this approach alone resulted in an erroneously high estimate for T_{ve}. The optimisation was thus modified to treat the N_2 $B^3\Pi_g$ state separately. Given the goal of comparing the equilibrium spectra, for the fitting procedure the experimental spectral radiance was averaged between 20 mm and 50 mm behind the shock to further reduce uncertainty.

Figure 5.13 show the results of the fits of the red emission spectra for T6s216 and T6s220. These are compared to both the experimental measurement for each shot and the original NEQAIR spectrum based on the CEA equilibrium composition. It can be seen that the optimisation provides good agreement with the experimental measurement,

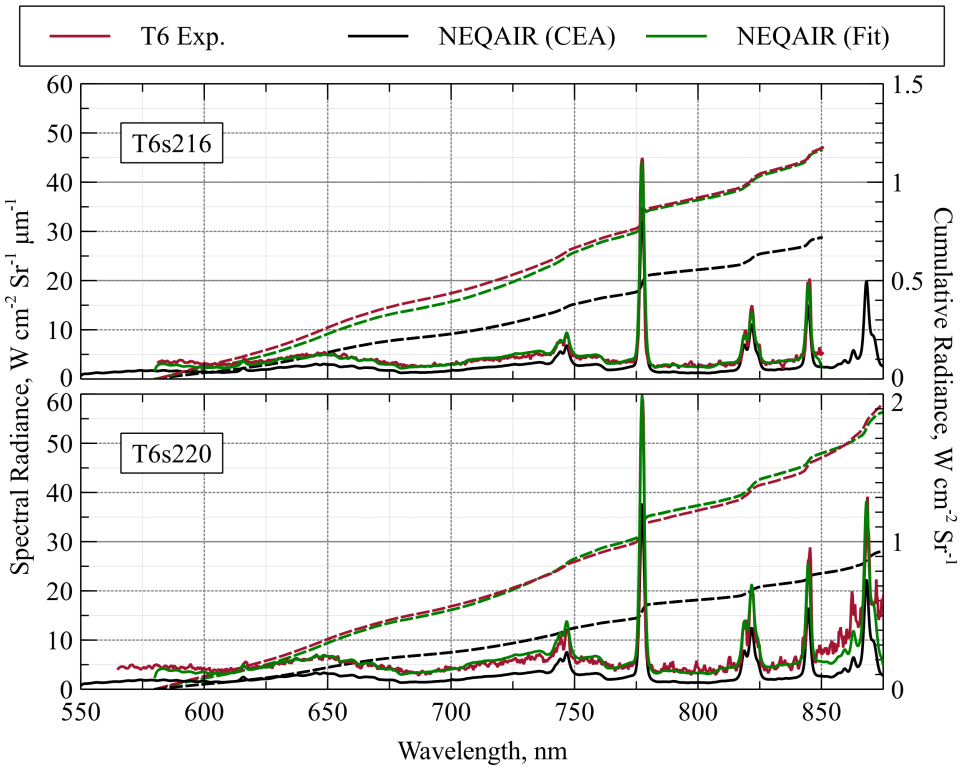


Figure 5.13 – Comparison of baseline (from CEA) and optimised NEQAIR spectrum with T6 experimental data at Condition II. The cumulative integrated radiance is shown as dashed lines.

suggesting that the plasma can be accurately described using the modelling parameters chosen. The calculated number densities and temperatures for these fits are shown in Table 5.4, where they are again compared to the nominal CEA predictions. It is determined that both shots agree with the predicted equilibrium temperatures (and, consequently, the temperature of the plasma torch) within the fit uncertainty. As far as can be determined from this fit, these appear to be in equilibrium. Of note is that the N_2 (B) population does not agree within the confidence of the fit; this is expected given the results of Figure 5.8. The number densities of the other considered species also agree with CEA, albeit with large uncertainties. This is due to the use of the higher energy states in the NIR for the spectral fitting. Due to the assumption of a Boltzmann distribution, the total number density must change significantly to cause a discernable variation in the spectrum. However, the fit is much more sensitive to temperature, and especially to T_{ve} via the atomic excitation component, leading to lower errors in this parameter.

The aim of this investigation was to estimate the post-shock temperature. Based

Table 5.4 – Comparison of T6 Condition II equilibrium conditions to centreline plasma torch parameters (Laux, 1993) and nominal CEA values. The T6 pressure is determined from shock timing stations, with error equal to one standard deviation of the steady signal. The remaining measurement values are inferred from the spectral fitting procedure.

		T6s216		**T6s220**	
Parameter	**Plasma Torch**	**CEA**	**Exp.**	**CEA**	**Exp.**
P, kPa	101.3*	95.6	93.5 ± 7.2	100.8	99.1 ± 7.3
T_{tr}, K	7300 ± 300	6960	7002 ± 740	6989	7095 ± 939
T_{ve}, K	7500 ± 100	6960	7016 ± 243	6989	7000 ± 265
n_N, 10^{17} cm^{-3}	—	4.85	4.55 ± 3.48	5.09	7.84 ± 6.38
n_O, 10^{17} cm^{-3}	—	2.59	2.61 ± 1.87	2.67	3.69 ± 2.87
$n_{N2(B)}$, 10^{13} cm^{-3}	—	1.19	1.79 ± 0.46	1.29	2.52 ± 0.65

**Varies with local barometric pressure. Assumed here to be at the standard atmosphere.*

on the presented uncertainties, the fitting approach was judged sufficient to provide a reliable estimate for this quantity. The results of this analysis thus confirm that the shock tube flow is close to that of the atmospheric plasma torch and therefore provides a comparable test case.

Lastly, the plasma torch data of Laux (1993) are compared to the NEQAIR simulations in Figure 5.14. These spectra were measured in much greater resolution than the shock tube experiments, as evidenced by the differentiated rotational features. There is good agreement between the atomic nitrogen and oxygen lines in the near-infrared, and with the NO bands. The latter is not the case for the shock tube data; this could therefore be a boundary layer effect, given this is the main difference between the two facility types. A computational simulation of the boundary layer incorporating thermochemistry is required to confirm this.

Several molecular features are similarly under-predicted for this plasma torch case as they were for the shock tube conditions, including the N_2(2+) and N_2+ (1-) bands in the UV and the N_2(1+) in the NIR. Whilst the full region used to calculate the excess N_2 radiance in Figure 5.8 was not measured in the plasma torch data, using the range 715 nm to 740 nm results in an excess ratio of 1.69. This agrees well with the measurements of EAST and T6 at similar post shock temperatures (i.e. approximately 7.5 km s^{-1}) shown in Figure 5.8. This result is of interest, as simulations using the SPECAIR code have

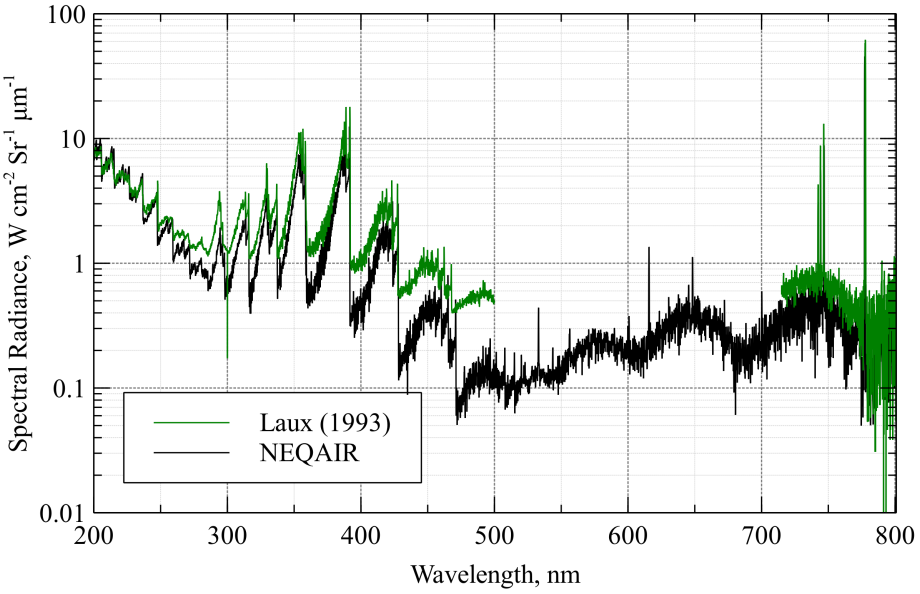


Figure 5.14 – Comparison of a NEQAIR simulation to the plasma torch data of Laux (1993).

been shown to agree well with experimental measurements at the exit of the torch (e.g. Tibère-Inglesse et al., 2018). It is therefore possible that a disparity in spectroscopic constants is the root cause of the observed differences at these conditions. Future work will simulate the T6 data with the SPECAIR solver and contrast the results.

5.5.2 Condition II: Non-Equilibrium Comparison

Figure 5.15 shows a comparison of the T6 experimental data using the non-equilibrium metric. Again, the Red data shows excellent consistency. Despite the greater magnitude of the non-equilibrium peak for shot T6s216 in Figure 5.10a the absolute NEM is observed to be lower; as previously discussed, this is due to the differing exposure times used. The trends in the blue data are equivalent to those seen for the equilibrium spectral radiance of Figure 5.10b; T6s159 is again lower than the other two tests. T6s216 is apparently the cleanest measurement, showing no evidence of CN contamination. Whilst there is no comparable test case for the non-equilibrium region at this condition, the results appear consistent with those previously presented for Condition I in Figure 5.9.

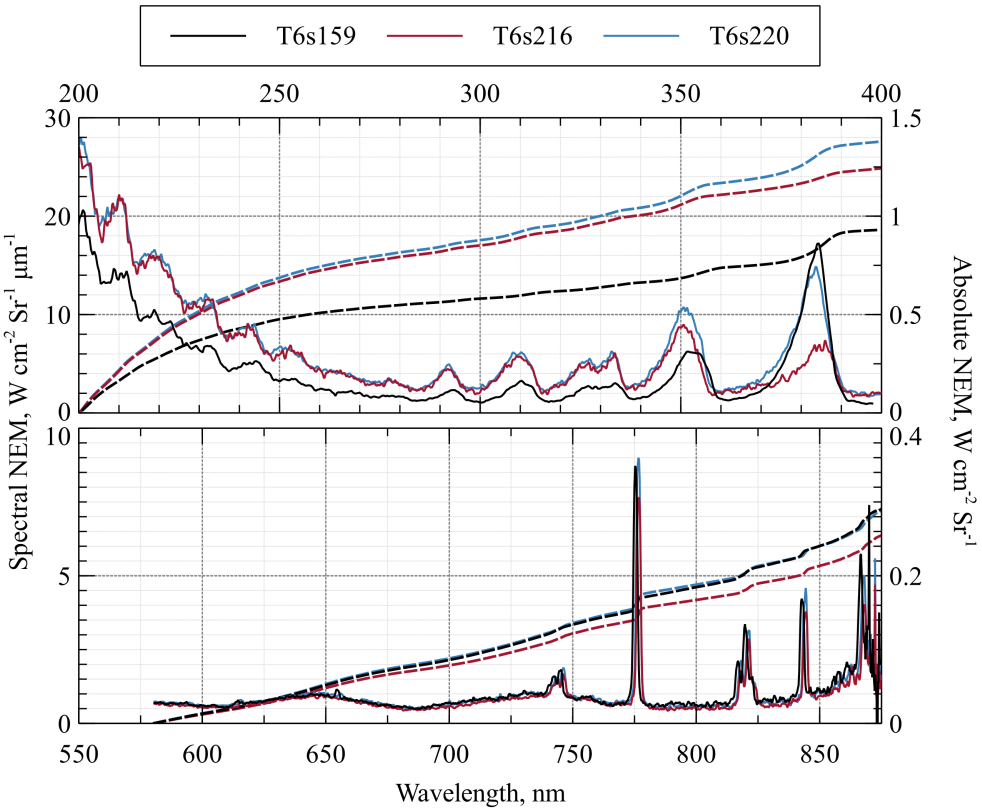


Figure 5.15 – Non-equilibrium metric comparison between T6 shots at Condition II, in terms of the Spectral (solid lines) and Absolute (dashed lines) NEM.

5.6 Condition III — High Speed EAST Comparison

Figure 5.16 presents the emission measurements at Condition III (10.0 km s^{-1}, 13.3 Pa) in the T6 AST. The shock speeds of the presented experiments and the comparison EAST tests are again given in Table 5.5. In comparison with the low speed experiments of Sections 5.4 and 5.5, the spectral emission and spatial variation in radiance show qualitative differences. This is most marked in the red results of Figure 5.16b, which show that the equilibrium radiance is now dominated by atomic emission. Considering the Red radiance profiles of Figure 5.16 it can be seen that the non-equilibrium is no longer necessarily the strongest source of emission the shock-layer, with this ratio showing significant sensitivity to the shock speed. Generally, there is a local minimum in radiance approximately 20 mm behind the shock front; this is discussed further in Chapter 6. Overall, a large extent of equilibrium is achieved — especially considering the low pressure and high velocity of this condition. A maximum of ∼100 mm of valid test flow

Table 5.5 – Measured shock speeds for the T6 and EAST tests compared at Condition III (13.3 Pa). The nominal shock speed is 10.0 km s^{-1}. The EAST tests only report the final shock speed at the window.

T6					
Test	T6s141	T6s164	T6s165	T6s166	T6s192
$U_{s,m}$, km s^{-1}	9.88 ± 0.10	9.94 ± 0.11	10.02 ± 0.12	10.02 ± 0.12	9.98 ± 0.11
$U_{s,f}$, km s^{-1}	9.78 ± 0.29	9.59 ± 0.31	9.79 ± 0.31	9.90 ± 0.34	9.84 ± 0.27

EAST			
Test	E50-26	E50-102	E50-104
$U_{s,f}$, km s^{-1}	9.98	9.71	10.13

is visible for shot T6s141. This is a positive result, as it demonstrates the ability of the AST to achieve high-quality, equilibrium test flows even at relatively low pressures. This condition shows more variability in the post-shock radiance, attributed to the greater proportional error in fill pressure and the larger sensitivity of the atomic emission to shock speed. This is, however, within the uncertainty of the measurement.

The UV radiance is much more similar in appearance to the low speed data, with the emission in this region being dominated by the non-equilibrium peak. This is due to the molecular species being largely dissociated at this velocity. The equilibrium spectrum is made up of a combination of (significantly weakened) N_2 (2+) and N_2+ (1-) molecular emission and atomic nitrogen and oxygen lines. These atomic lines are largely from higher energy states, with lower transition probabilities, than the lines observed in the red spectrum. These are not sufficiently populated at this temperature to exceed the non-equilibrium emission. There is also little evidence of NO (the dominant radiator at the low speed conditions) at this velocity, with any radiation present being indistinguishable from the noise floor. Considering shot T6s166 (for which data is presented for both spectral channels) there is good agreement observed in the axial extent of the shock-layer in comparison with the Red data. There is again a 1.6x discrepancy observed in the data from T6s192. All other parameters compare well for this test.

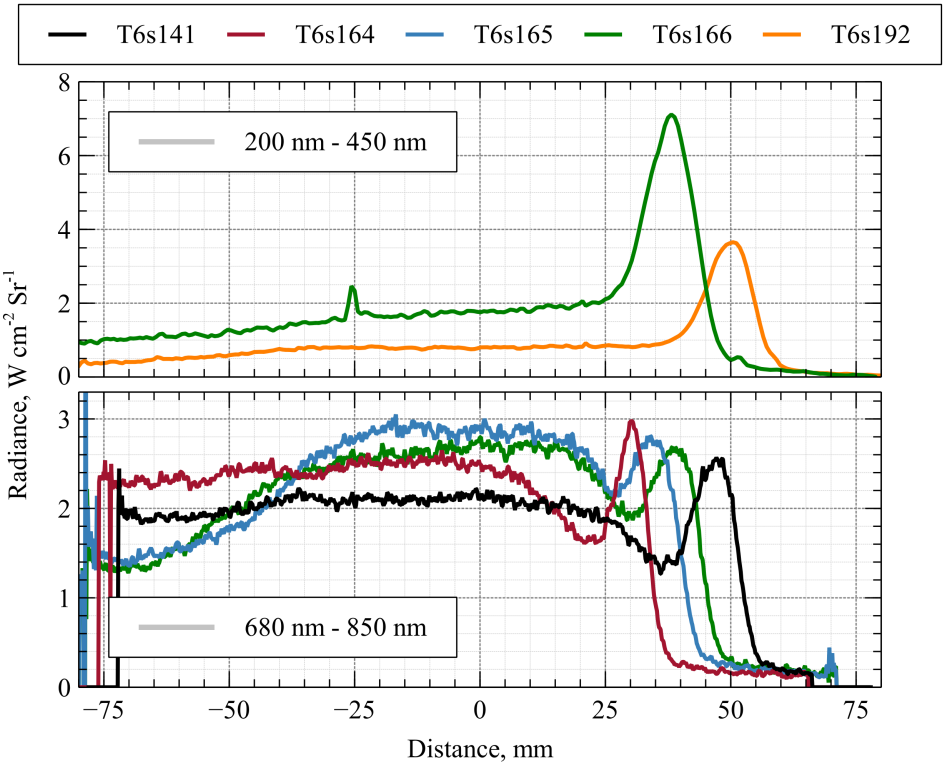
In terms of contamination, the red spectrum shows evidence of the Balmer-α line of atomic hydrogen at 656.6 nm. This is despite evacuation to pressures on the order of 0.01 Pa, testing in a synthetic air mixture, and flushing the AST several times with

test gas before the shot. It is thought that the bulk of this effect caused by water vapour which is adsorbed onto the tube wall during turn-around, as calculations using the measured ultimate pressure and leak rate predict significantly less hydrogen emission than is observed. On the blue channel, carbon is also evident as a contaminant line at approximately 247.8 nm. This proved challenging to eliminate entirely using current cleaning methods. However, inspection of the EAST data presented in Figure 5.17 shows that the level of these contaminants is of the same order of magnitude, albeit with slightly elevated levels in T6. As commented in the preceding sections, a plasma cleaner (as used in EAST) is planned as part of a future upgrade of the facility which should help to reduce these effects.

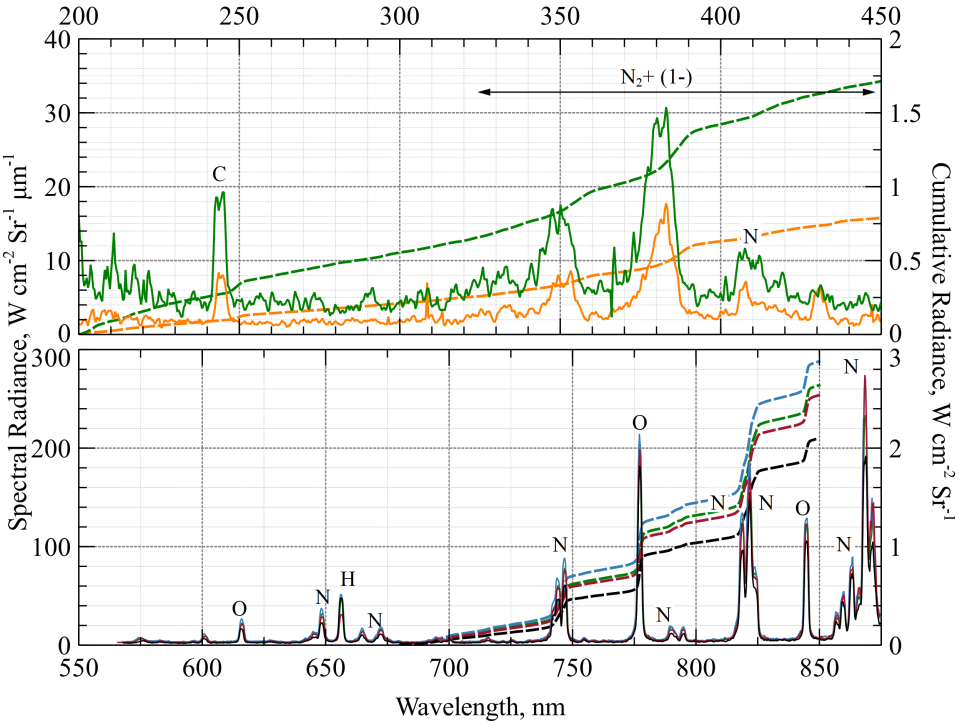
5.6.1 Condition III: Equilibrium Comparison

The radiation in the post-shock equilibrium region is compared to the predictions of NEQAIR in Figure 5.17. A composite spectrum of benchmark EAST data is also compared to simulation. Overall, the vast majority of radiating species are identical between both facilities and are reproduced well by the computational code. Both T6 and EAST experimental spectra exhibit an additional atomic line at approximately 795 nm which is not predicted by NEQAIR, although it has not been possible to conclusively identify what species causes this feature. It may be the oxygen 794.7 nm line, although silicon also has a transition close to this wavelength, which could be ablated from the UV-fused silica window surface. This aside, the atomic lines are reproduced well. Of note is that the NEQAIR simulation appears to under-predict their magnitude in comparison with the EAST experimental results, whilst the T6 data is over-predicted. This may be related to shock deceleration and is discussed further in Chapter 6.

In the case of both facilities, there is a greater background level than is predicted by NEQAIR. In the NIR region, the use of a higher resolution grating for the T6 experiments better resolves the contributions of the atomic line instrument broadening to the background continuum. Here, it can be observed that the calculated background emission is under-predicted in NEQAIR. This difference is also visible in the EAST data, a discrepancy which has been previously noted by Cruden (2011). In that work,



(a) Radiance. The wavelength ranges included in the integral are inset.



(b) Equilibrium spectral radiance, averaged between 50 mm–60 mm behind the shock front. The solid lines are spectral radiance; the dashed lines show their cumulative integral.

Figure 5.16 – Emission results from the T6 AST at Condition III. The results from the Blue and Red OES systems are shown in the upper and lower portion of each plot respectively.

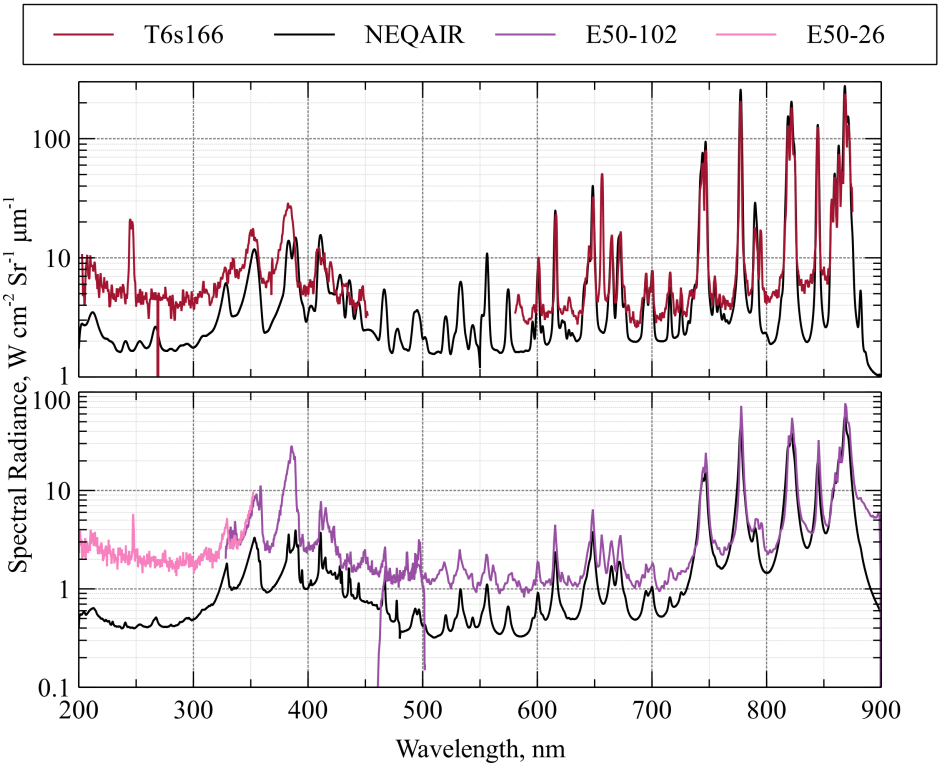


Figure 5.17 – Comparison of experimental equilibrium spectral radiance between EAST, T6 and the predictions of NEQAIR at Condition III.

the additional background continuum was attributed to the radiative recombination reaction of N+ ($N^+ + e^- \rightarrow N$), hypothesised to be in excess due to a measured electron density greater than equilibrium. This was improved through closer modelling of the instrument line shape and inclusion of the TOPbase database in NEQAIR, as reported by Brandis et al. (2015).

Figure 5.18 again shows a comparison of the data from T6s166 to the NEQAIR code, with a focus on the NIR region. The uncertainty bounds on the measurement are also shown. In several areas, the predicted background continuum does agree reasonably well with the lower range of the uncertainty. This is in line with expectations: although the N_2 (1+) band was shown to be under-predicted by NEQAIR, and lies in this region, this is expected to form a negligible contribution to the overall emission at this condition. From equilibrium simulations, the N_2 (1+) band has a peak spectral radiance of 0.03 W cm^{-2} sr^{-1} µm^{-1} at approximately 640 nm for this case. Additionally, the electron density was determined to be equilibrated for an equivalent shot at this condition — this is

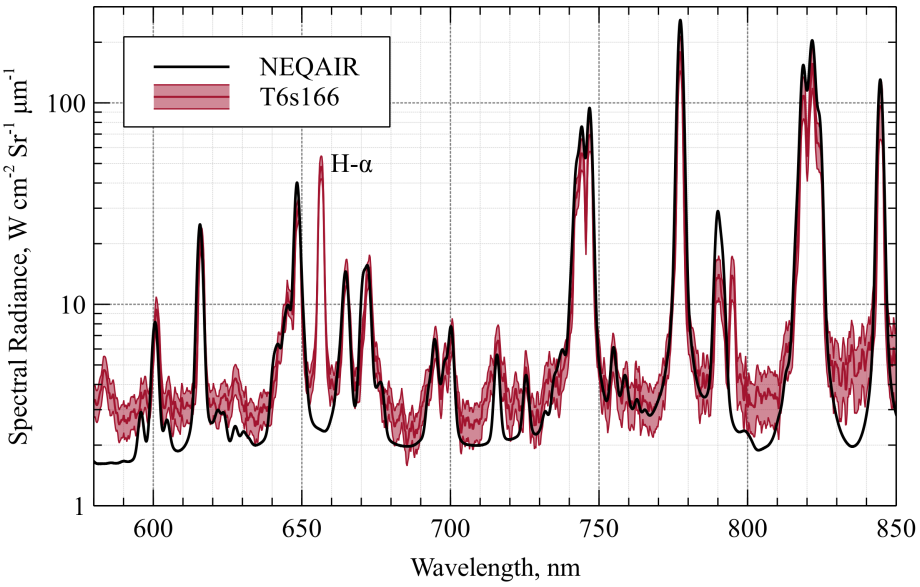


Figure 5.18 – Comparison of the background continuum at equilibrium for Condition III. The results of NEQAIR are compared to the experimental data from T6s166, with uncertainty bounds.

fully detailed in Section 6.5. This measurement, in combination with the comparatively flat shock trajectory for the T6 data (shown in Figure 4.12), eliminates excess electron density and shock deceleration as potential factors leading to enhanced radiative recombination.

Although the agreement is generally good, there are several points at which the predicted background continuum is lower than the measurement. This may simply be due to errors in the nominal shock speed. It is also possible that — given the large difference in magnitude of the atomic lines and the background — a secondary peak in the ILS could introduce additional radiation away from its primary location. This would not be captured with current fitting techniques; the instrument point-spread function should be assessed to investigate this. The remaining probable causes are the presence of contaminant species and the magnitude of the bound-free reactions which generate the background continuum, which may occur excessively in the boundary layer. The former will be investigated after the upgrade of the T6 facility with a plasma cleaner; the latter would require additional modelling. Overall, however, these effects are reasonably small in the overall context of the spectral measurement. It can thus be said that the agreement between the predictions of NEQAIR and the data from T6 is close for the background continuum at this condition.

5.6.2 Condition III: Non-Equilibrium Comparison

The non-equilibrium regions for both T6 and EAST are analysed in Figure 5.19 in terms of the non-equilibrium metrics. As would be expected from the results shown in Figure 5.16, T6s192 is significantly lower in radiance in the Blue OES results. Again, this is attributed to a technical issue with the camera. This aside, there is excellent agreement between T6s166 and the composite EAST spectrum across the entire wavelength range. There is also good agreement in the observed spectral features between both T6 tests, and in comparison to EAST. In contrast to the equilibrium spectra of Figure 5.16b, the non-equilibrium shows more dominant contributions of N_2 and N_2+ emission; these are caused by the presence of as-yet-undissociated molecular species. There is also evidence of non-equilibrium NO emission, although the relative magnitude of this is significantly lessened when compared with the lower speed tests.

In the red region, the two facilities again compare very well. The radiance of T6 is effectively bounded by EAST tests 50–102 and 50–104, corresponding to nominal shock speeds of 9.71 km s^{-1} and 10.13 km s^{-1} respectively. This appears reasonable given the measured shock speeds in the AST at this condition. In contrast to the low speed data, the non-equilibrium region is dominated by atomic radiance at this condition. Some small contribution from the N_2 (1+) is observed, but this again is negligible for this case. It is expected that the majority of the observed atomic features would be optically thick, resulting in a comparatively higher value for the NEM results at the EAST facility. The experimental comparison is consistent with these expectations.

5.7 Summary

This chapter detailed the first measurements of shock-layer radiation in the new T6 AST. An overview of the dual-channel emission spectroscopy system used in these experiments was first provided, including details of the optical design and a short summary of the calibration and operational procedures. An overview of the methodology used to compare experimental measurements from T6 was also given. Of particular note is

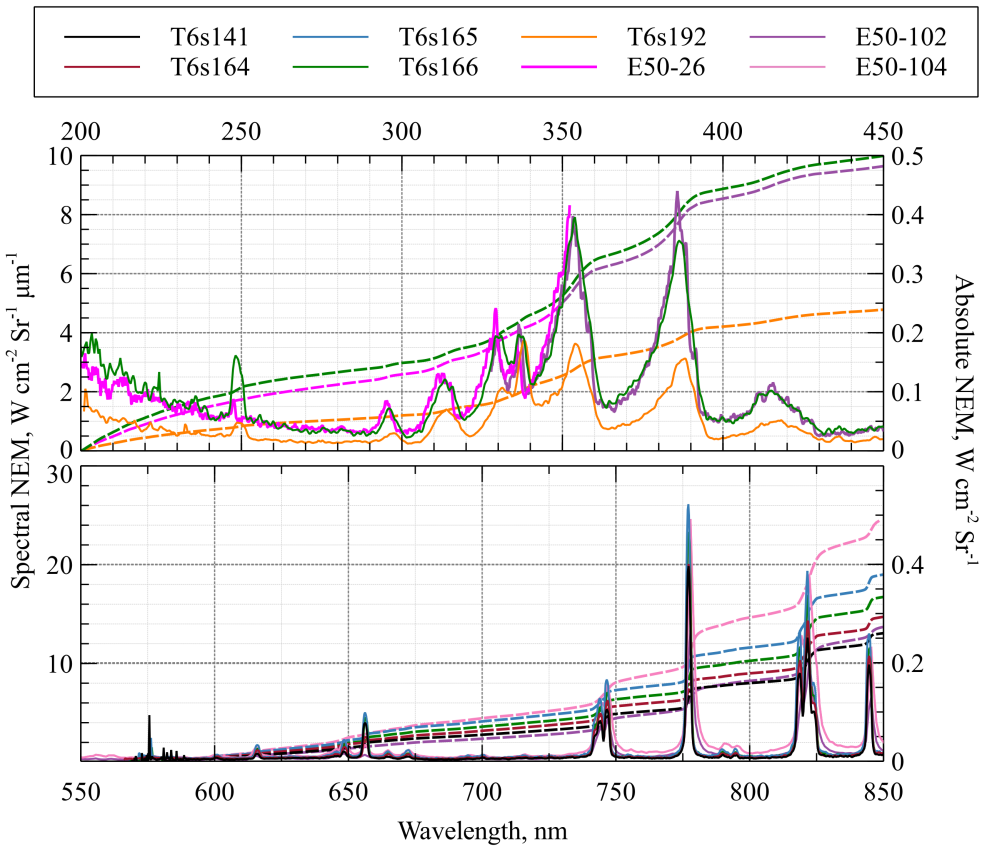


Figure 5.19 – Non-equilibrium metric comparison between T6 and EAST at Condition III, in terms of the Spectral (solid lines) and Absolute (dashed lines) NEM.

that the developed system yields a measurement of absolute spectral radiance, thereby allowing direct comparison to other facilities and to simulation tools.

Emission results from 200 nm to approximately 850 nm were then presented for three test conditions relevant to Earth entry. In all cases, the new data from T6 was shown to exhibit extended regions of steady post-shock equilibrium. This confirmed that the T6 AST is able to properly produce these super-orbital shock-layers with abundant test time, in which optical diagnostics can be used.

Overall, comparisons to benchmark experiments from the NASA EAST facility and that from the atmospheric plasma torch were very good. Qualitatively similar spectra were found in all cases. In the case of the Blue OES data from T6, an intermittent variability (attributed to the intensified camera) was found to alter the overall magnitude of some test results. These have also been reported for completeness. However, it was noted that the relative magnitude of both the spectral features and the spatial variation in radiance

is consistent with other T6 tests and with data from other facilities; the results thus retain some value for the benchmarking of the facility. In the case of the consistent Blue tests, as well as every test in the Red region, excellent agreement was found between facilities. Comparisons to the NEQAIR solver were largely equivalent, with similar areas of both agreement and disagreement observed.

The results presented here have successfully benchmarked the emission results from the T6 AST to previous data from the literature. In several areas, notably the under-prediction of the N_2 (1+) band, the initial cross-facility comparisons presented here have helped to isolate the source of these discrepancies. This demonstrates the value of the newly established source of experimental data. Future test campaigns may now build from this foundation, applying the newly developed facility mode and optical diagnostics to other test conditions. The experimental dataset generated through this test series can also be used to plan future experimental campaigns, allowing more accurate bounds to be placed on the minimum measurable levels of spectral radiance. Finally, the data presented here represents a selected portion of the overall dataset; these validated experimental results can be utilised in future numerical modelling efforts.

The past is never where you think you left it.

— Katherine Anne Porter

6 On the Influence of Shock Speed Variation

Contents

6.1 Introduction 175
6.2 Shock Speed Variation Condition Generation 176
6.3 Spatial Radiance Variation 180
6.4 Shock Deceleration Effects on Test Slug Morphology 186
6.5 Electron Density Measurements 194
6.6 Summary 203

6.1 Introduction

In the preceding chapter, the shock-layer emission measurements from the AST were benchmarked against data from the literature. Overall, the presented results validated the ability of the new facility to generate high quality test flows and to accurately measure the radiative emission from hypervelocity air shock-layers at Lunar return conditions.

Here, the preceding validation cases are used as a baseline from which to investigate the influence of the facility itself on shock tube radiation experiments. In particular, the effect of shock speed variation on the measured emission is studied experimentally. This chapter seeks to answer two questions: firstly, can any effect of shock deceleration be significantly linked to the observed test flow in these shock tube experiments? Secondly:

what conditions influence the strength of this effect, and can approximate bounds be set on the acceptable level of variation?

This chapter describes a series of experiments undertaken in the T6 AST, in which various shock trajectories were generated and their impact on spatial trends through the shock-layer investigated. The methodology for achieving this aim is first outlined, after which the rationale behind the selection of conditions is assessed. Emission spectroscopy measurements from these tests are then presented, with comparison to numerical tools. The same computational methods are then used to investigate the effect of deceleration on the final test slug, and some preliminary recommendations for future shock tube experiments made. Finally, spatial trends in electron density are also assessed in the T6 AST, after which the same methodology is applied to previously published data from the EAST facility.

6.2 Shock Speed Variation Condition Generation

The central aim of Chapter 4 was to develop the 'best' test conditions possible, minimising the variation of the shock speed from the nominal and maximising repeatability.[1] In this chapter, the opposite approach is taken wherein large variability in the shock speed profile is intentionally introduced. This section discusses several means through which this may be achieved in these shock tube experiments. The rationale underpinning the choice of the test cases explored in the rest of this chapter is then laid out, with the achieved conditions summarised.

6.2.1 Mechanisms of Shock Speed Variation

The distance-time diagrams of the T6 operating modes shown in Figure 3.4 represent a significant simplification. In reality, the main flow processes in high-enthalpy pulse facilities are superimposed by highly complex patterns of acoustic waves which ultimately influence facility performance. These can either be relatively large — typically caused by variations in the core facility processes, such as the piston compression and diaphragm opening — or be effectively 'acoustic noise' generated by boundary layer growth and

[1] Insofar as this is possible in a transient, high-enthalpy facility.

the 3D interaction of the hypervelocity flow with the facility itself. The impact of these waves can range from negligible, to severe disturbances of the test flow and, potentially, to premature departure from the nominal test condition. These effects have been studied by many authors, for example Bakos and Erdos (1995), Erdos et al. (1994), Paull and Stalker (1992), and Gildfind (2012).

In this work, the secondary driver was the primary means used to tune the shock speed profile in the AST. This was achieved through two main mechanisms: the secondary driver fill pressure and the thickness of the secondary diaphragm. Depending on the fill pressure, the addition of a secondary driver can either augment or reduce the shock speed in the shock tube (Gildfind et al., 2015). In addition, Paull and Stalker (1992) studied the use of a secondary driver as an 'acoustic buffer', which could prevent waves from the driver generating noise in the test flow. The upper plot of Figure 6.1 shows the influence of varying the secondary driver fill pressure in the T6 AST from 5 kPa to 20 kPa. In all cases, the primary driver condition was C++ (as per Table 4.1), the secondary driver composition was helium, the same 10 µm Mylar diaphragm was used and the AST fill pressure was 26.6 Pa of air. It can be seen that the final shock speed, and the rate of deceleration, are dependent on the fill pressure used. Experience has shown that the lower fill pressure cases are more likely to show a sharp deceleration at the end of the shock tube. This is due to the faster shock speed in the secondary driver gas, which results in a shorter, hotter slug; this completes the expansion process — and transmits expansion waves from the driver — more rapidly, reducing performance.

The second means through which the shock speed was varied was through the thickness of the secondary diaphragm. Bakos and Morgan (1994) present a thorough analysis of the rupture mechanisms of secondary diaphragms, showing that a reflected shock initially forms which is gradually weakened due to the expansion of the downstream gas. The thicker the diaphragm (or lower the fill pressure), the larger the difference in density between the diaphragm material and the post-shock gas in the secondary driver. This consequently impacts the relative strength of the reflected shock. A study by Roberts et al. (1995) showed that a strong reflected shock at the secondary diaphragm results in an initial overshoot in shock speed, as the continuously-weakening reflection produces

a temperature gradient in the secondary driver gas. Through varying the secondary diaphragm thickness the initial part of the shock trajectory could thus be modified. In this work, thicknesses of 5 µm to 80 µm were used, corresponding to approximate burst pressures of 15 kPa and 240 kPa.[2] The effect of changing this thickness on the shock speed profile is also shown in the bottom half of Figure 6.1. Here, the secondary driver was 10 kPa helium and the AST fill 13.3 Pa air. Note the apparently lower speed measured across the nozzle (at approximately 3.25 m) due to the longer rupture time of the thicker material. Ultimately, use of the 80 µm thickness was discontinued due to the excessive damage which resulted to the Pitot rake due to diaphragm fragment impact. An example of the resulting degradation after several runs was shown in Figure 4.7b.

6.2.2 Condition Selection

To compare the effect of shock deceleration, the approach taken is to generate different shock speed variation profiles and then investigate spatial trends through the test slug. In selecting suitable test conditions, the following key points were taken into consideration:

1. Based on the work of Mirels (1963) the test slug will be most compressed for low shock tube fill pressures. As a result, the greatest sensitivity to any deceleration effect is likely under these conditions.

2. As has been extensively discussed throughout this work, the magnitude and distribution of radiation through the shock-layer is a strong function of shock speed. Furthermore, the spatial extent of non-equilibrium processes is influenced by the initial fill pressure. These should thus both be as similar as possible at the end of the tube (where the optical measurement is made).

3. Excess electron density has been measured at velocities under 10 km s^{-1} at EAST. This effect has been preliminarily attributed to shock deceleration. It would thus be desirable to overlap with these conditions to cross-validate these results.

[2] The former value was measured experimentally by gradually evacuating the shock tube whilst keeping the secondary driver open to atmosphere. The latter is calculated based on the thickness ratio.

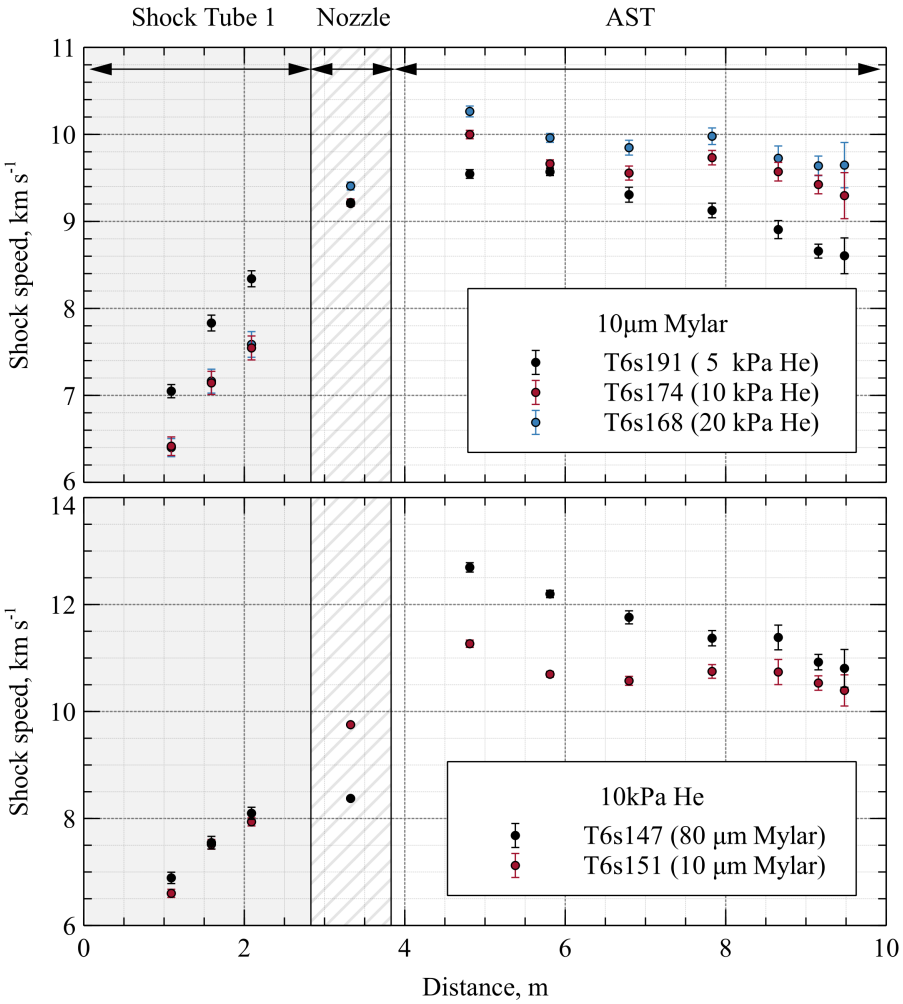


Figure 6.1 – Example of the mechanisms used to vary the experimental shock speed profile. The upper graph hows the impact of varying secondary driver fill pressure with all other parameters held constant. The lower demonstrates the impact of the secondary diaphragm thickness.

Based on the above considerations, a nominal shock speed of 9 km s^{-1} and fill pressure of 0.2 Torr was targeted. It was intended that this be the final shock speed at the AST window, with variations in deceleration upstream of this point. These tests would thus all — in theory — be at the same condition.

Figure 6.2 adapts a plot from Brandis et al. (2010a) which shows the variation in equilibrium electron density with shock speed at 0.1 Torr and 0.2 Torr, calculated using CEA. It can be see than that between approximately 8.5 km s^{-1} – 10.0 km s^{-1} there is a significantly steeper gradient in electron density. It was therefore intended that by varying the upstream shock speed through this region that differing distributions of

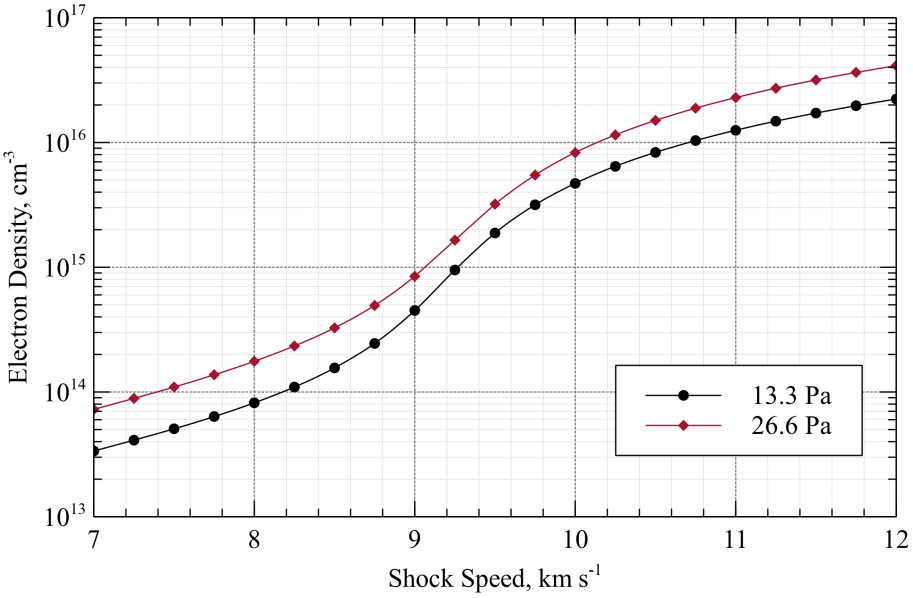


Figure 6.2 – The variation in equilibrium electron density with shock speed, calculated using the CEA program. Adapted from Brandis et al. (2010a).

electron density could be measured, which may help to explain discrepancies observed in other facilities. This is discussed further in Section 6.5. Finally, it should be noted that comparisons to electron density are likely more robust than those against radiation: accurate prediction of the radiance magnitude involves errors in spectroscopic constants whereas the equilibrium electron density is theoretically known exactly.

6.3 Spatial Radiance Variation

In this section, emission spectroscopy measurements are presented for a series of tests exhibiting varying degrees of shock deceleration. For this study, data from the Red OES system described in Section 5.2 is used, focusing on the spatial trends of radiance. Here, the oxygen 777 nm line has been selected for comparison. The emission of this multiplet has been very well characterised, and as such any errors in spectroscopic constants are low (Kramida et al., 2020).

The approach to calibration and post-processing is identical to that described in Appendix B. It is reiterated here that prior to each test the windows are thoroughly cleaned with acetone, after which the full spatial field-of-view is calibrated in-situ. The

Table 6.1 – Measured shock speed characteristics for the SSV radiance test cases, all at an initial fill pressure of 26.6 Pa. Here, $U_{s,f}$ is the final shock speed, $U_{s,m}$ the mean of the last three measurements and $\Delta U_{s,max}$ the maximum percentage variation of the profile from the final measurement.The absolute NEM is calculated from 700 nm–850 nm.

Shot	$U_{s,f}$, km s^{-1}	$U_{s,m}$, km s^{-1}	$\Delta U_{s,max}$, %	Abs. NEM, W cm^{-2} sr^{-1}
T6s129	9.23 ± 0.28	9.31 ± 0.09	2.5	0.166
T6s130	9.09 ± 0.26	9.32 ± 0.10	4.2	0.177
T6s132	9.41 ± 0.24	9.45 ± 0.09	4.7	0.186
T6s138	9.17 ± 0.24	9.41 ± 0.09	4.2	0.184
T6s174	9.30 ± 0.26	9.46 ± 0.10	7.6	0.232
T6s188	9.49 ± 0.28	9.71 ± 0.12	11.2	0.334

possibility that observed differences in spatial trends are due to calibration artefacts or changes in window transmissivity are thus considered highly unlikely.

6.3.1 Radiance Conditions

The shock speed variation (SSV) for the conditions considered in this section are shown in Figure 6.3. The measured final shock speeds at the AST windows are all nominally within the range of 9.0 km s^{-1} to 9.5 km s^{-1}. The spread of shock speeds varies from approximately 9.0 km s^{-1} to 10.5 km s^{-1} along the length of the AST. The final shock speed, average value calculated on the final three transducers and the maximum percentage deviation from the final value are also tabulated in Table 6.1 to aid identification. From the measurements, it can be seen that the final values all vary by less than 0.4 km s^{-1} (or 4 %$\sim$) and agree within the measurement uncertainty. The mean velocity at the end of the tube is even more consistent, differing by at most 0.15 km s^{-1} and again agreeing within the stated error bounds. The exception to this trend is shot T6s188, which ends at a slightly higher velocity. Also shown are the overall absolute NEM values, calculated as per Equation (5.3). These are generally very similar, again suggesting that the shock speeds are approximately the same at the measurement location. The exceptions to this trend are shots T6s174 and T6s188, which show notably higher values. The reasons for this are discussed further in the following section.

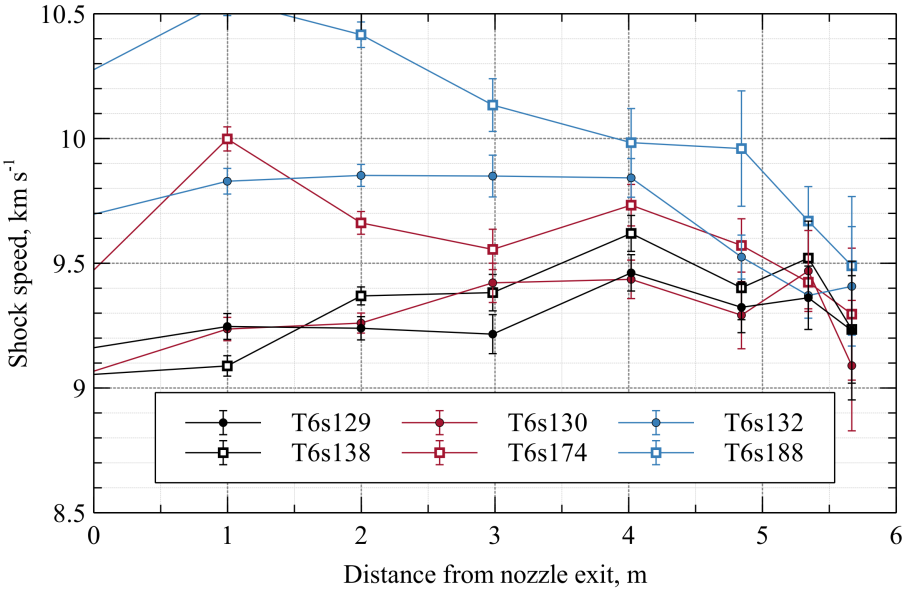


Figure 6.3 – Measured shock speed variation for the SSV radiance test cases explored in this work. In all cases, the AST fill composition was 26.6 Pa of synthetic air. Lines are included here for ease of identification of each trajectory.

6.3.2 Experimental Results

The measured emission for the SSV radiation test cases is shown in Figure 6.4. Presented is the spatial variation in integrated emission from 760 nm to 785 nm, corresponding to the oxygen 777 nm multiplet. Here, the non-equilibrium peaks have been aligned to aid comparison. From the presented data, it can be seen that the trends in radiance through the shock-layer show distinct differences. Comparison between the SSV profiles in Figure 6.3 and the radiance results qualitatively suggests a strong link between the observed emission and the shock trajectory. It can also be seen that the magnitude of the non-equilibrium peak is more similar than the absolute NEM values shown in Table 6.1 suggest; the integration between ±20 mm of the peak results in a significant amount of the rising spatial trend being included in this value, which offsets the result.

These results show that differing shock speed trajectories can influence the distribution of radiance through the shock-layer. The following analysis in Section 6.3.3 strengthens this conclusion substantially. It should be noted that, whilst shock-layer radiation is a strong function of velocity, it is not expected that the small differences in measured shock speed at the AST windows could account for the differences observed. These results

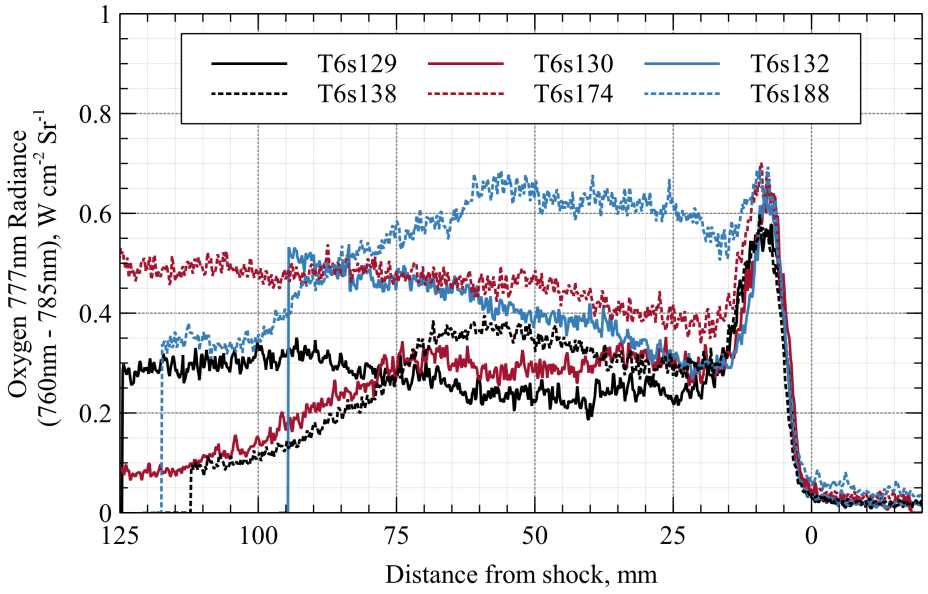


Figure 6.4 – Experimental results of oxygen 777 nm multiplet emission for the radiance test cases.

clearly highlight the intrinsic link between the facility performance (i.e. how the test condition is generated) and the measured characteristics of the resulting shock-layer.

6.3.3 LASTA-NEQAIR Coupling Methodology

The experimental results shown in Section 6.3.2 are strongly suggestive that variations in shock speed influence the characteristics of the shock-layer. However, further analysis is required to definitively connect the observed trends with the variations in the shock velocity.

To perform this analysis the LAgrangian Shock Tube Analysis (LASTA) code of Satchell et al. (2021c) is used. LASTA is a quasi-one-dimensional flow solver which uses the experimentally measured shock speed profile an input. As the shock progresses along its trajectory, slices of isentropic shock-processed gas — placed at pre-determined intervals along the length of the facility — are activated and tracked. Each slice is given an initial total enthalpy, and the properties of the slice are updated at each time step to accommodate changes in the total enthalpy from wave and boundary layer effects. Slice velocity is determined by a mass balance of the core flow with the boundary layer, which is modelled analytically using the approach of Mirels (1963). The code assumes equilibrium chemistry and has been validated for high enthalpy shock tube flows

against an array of experimental measurements (Satchell et al., 2021b). The only inputs required, in addition to the measured shock speed profile, are the initial fill pressure and composition of the test gas, and the tube diameter.

To generate the radiance comparisons in the subsequent section, LASTA is combined with NEQAIR using the following approach. First, the shock speed profile for each case (as shown in Figure 6.3) is interpolated, and extrapolated past the final measurement location. This is required to allow LASTA to correctly generate a distribution of pressure waves in the test slug. The spatial distribution of temperature, density and species concentrations are then used as inputs to NEQAIR. Here, NEQAIR is run in its 'shock tube' mode, wherein each spatial location behind the shock is assumed to radiate with an optical depth equal to the tube diameter. The other simulation settings used were identical to those already described in Section 5.3.3.

To compare to the experimental radiance, both the simulated and measured spectra were integrated between 760 nm and 785 nm. Previously, some disagreement has been found between the background continuum radiance in NEQAIR and experimental data from EAST (Brandis et al., 2010a). As a result, the integral here has a linearly-interpolated background removed from both sets of data to eliminate this source of error.

6.3.4 LASTA Radiance Results

The comparisons between the experimentally-measured spectra of Figure 6.4 and LASTA-NEQAIR are shown in Figure 6.5. LASTA is currently only capable of simulating equilibrium chemistry; as a result, the initial non-equilibrium peak is not expected to be matched. This difference aside, there is in general excellent agreement between the simulated radiance and the experimental measurement. The absolute magnitude of the emission is generally well captured, suggesting that the population density of the radiating transition is close to equilibrium through the majority of the shock-layer.

The key result shown in the results of Figure 6.5 is that the spatial trend in radiance is very well captured. This confirms that the observed differences in the measured radiance are a direct consequence of the shock speed variation. If these are compared to the shock trajectories of Figure 6.3, direct correspondence can be made between variations in

the shock profile and those later seen in the test slug. This is true not only in cases of continuous deceleration (e.g. T6s132) but also in more oscillatory cases, as exemplified by the trends of T6s129. These results also establish the importance of accurate, high-resolution shock speed measurement for shock-layer radiation experiments. Errors in the shock speed can cause deviations of the LASTA-NEQAIR prediction from the experiment; the differences at 25 mm for T6s138 and 174 mm are attributed to this source.

Finally, it can be seen that the more sharply decelerating cases (i.e. T6s130, T6s138 and T6s188) exhibit foreshortened test slugs. This is evidenced by the premature termination of the LASTA result. The mechanisms for this are discussed in Section 6.4.2. In general, it can be seen that LASTA predicts the location of the rear of the slug reasonably well, to within approximately 15 mm. The largest discrepancy in the presented data is present in the comparison with T6s188, which shows approximately 33 % difference at the rear of the slug. This is also the case with the greatest deceleration. The deviation of the experimental data from the LASTA prediction is attributed to the formation of a vortical mixing region at the contact surface between the driver and test gas. Work by Satchell et al. (2021a) has shown that greater rates of shock speed variation lead to increased deformation of this region, which can be on the order of the tube diameter. Because the driver gas in the AST must expand through the nozzle, it is generally much colder than the test gas. This results in a mixing region at a lower bulk temperature — and with reduced concentration of oxygen atoms — resulting in a reduction in the radiance. This is not captured in LASTA due to the one-dimensional nature of the code.

In summary, the close agreement between the experimental radiance results from T6 and the combined LASTA-NEQAIR simulations conclusively demonstrate the impact of shock speed variation on the shock-layer. The good comparison is also suggestive that the shock-layer trends can be largely modelled using an equilibrium thermochemistry assumption, after the non-equilibrium peak. As commented by Satchell et al. (2021b), the extension of LASTA to include a non-equilibrium model would allow more accurate determination of thermochemical rates through the shock-layer. These results also show the importance of adequate shock speed measurement if the radiance variations in the test slug are to be properly rebuilt.

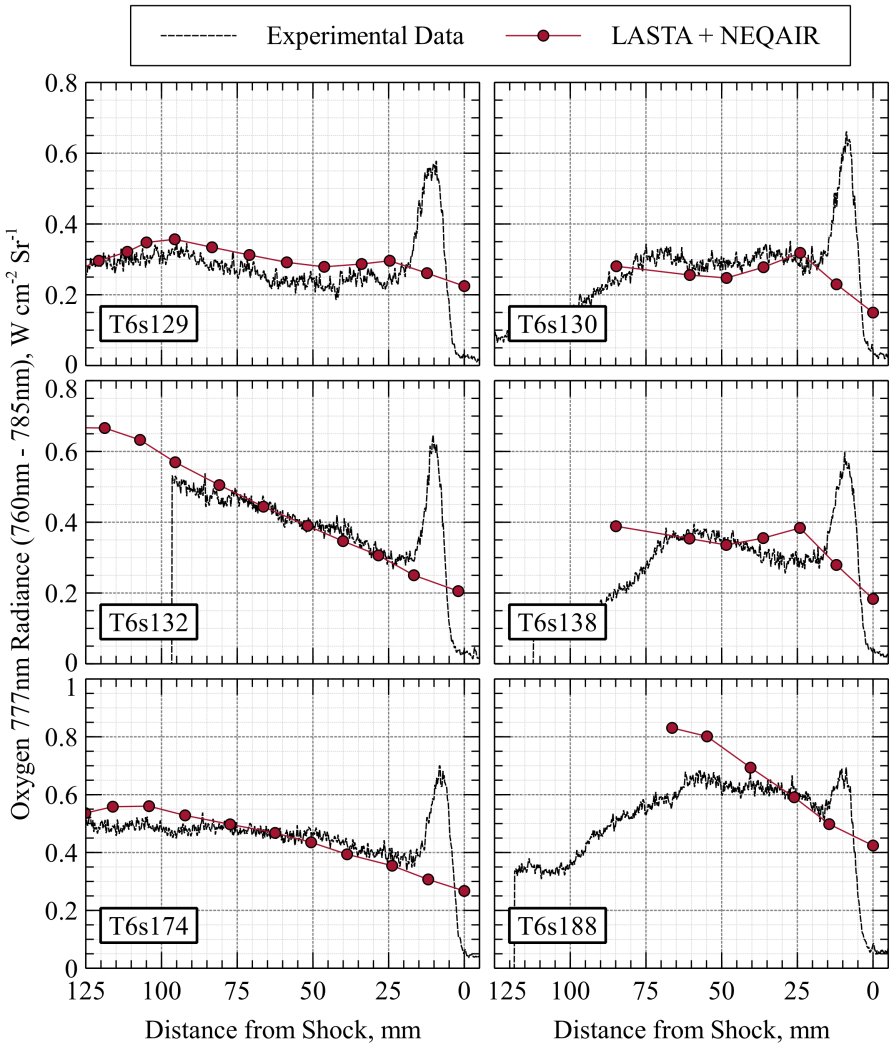


Figure 6.5 – Comparison of the experimentally-measured spatial variation in atomic oxygen radiance with the predictions of the coupled NEQAIR/LASTA simulations. All data has been referenced to the same shock location. A premature termination of the experimental trace indicates the upstream edge of the field of view; the LASTA data ends at the rear of the simulated test slug. In all cases the LASTA points were distributed at 200 mm intervals along the shock tube.

6.4 Shock Deceleration Effects on Test Slug Morphology

In this section, the preceding analysis is extended to examine the effect of shock deceleration on the ultimate shape of the measured shock-layer. First, one-dimensional non-equilibrium simulations are performed to give a baseline case for what variation should be seen in the shock-layer in the absence of SSV effects. These are then contrasted with the measured trends in post-shock radiance. This comparison is used to propose guidelines on the appropriate choice of nominal shock speed for comparison to computational tools.

A numerical study is then undertaken to investigate what impact the shock deceleration rate has on the length of the final test slug.

6.4.1 Approach to Equilibrium

Here, the measured trends in post-shock radiance are compared with the prediction of a one-dimensional, finite-rate thermochemistry solver. The purpose of this analysis is to demonstrate the form of the 'ideal' shock-layer i.e. one without shock deceleration effects. This is then contrasted with experimental data and with LASTA.

In this analysis, three sources of data are presented. The first two are identical to those shown in Figure 6.5: experimental measurements of the oxygen 777 nm radiance and corresponding values from coupled LASTA-NEQAIR simulations. The third set of data is generated using the finite-rate one-dimensional shock solver Poshax3 of Potter (2011). These latter simulations provide a representation of a typical analysis approach, in which SSV is not considered. The establishment of post-shock equilibrium under these conditions is then compared.

Poshax3 Simulation Methodology

Given an incident velocity, temperature and pressure Poshax3 calculates the one dimensional thermal and/or chemical relaxation behind a normal shock using a chosen set of reaction rates. The field of non-equilibrium thermochemistry is vast and a proper treatment and assessment of thermochemical modelling is not attempted here. Instead, a common model in the literature is compared with the experimental trends. For this analysis, the 11-species, two temperature air model of Park (1993) was chosen. The translational-electronic exchange rates are from the same source, with the translational-vibrational reactions taken from Gnoffo (1989).

The outputs of the Poshax3 simulations (i.e. number densities, translational-rotational temperature and vibrational-electronic temperature — all as a function of distance behind the shock) were then used as an input to NEQAIR. The result is convolved with a 5 mm rectangular and 5 mm triangular blurring function to account for the motion of the shock during the camera gating and for the off-axis position of the non-equilibrium peak. The

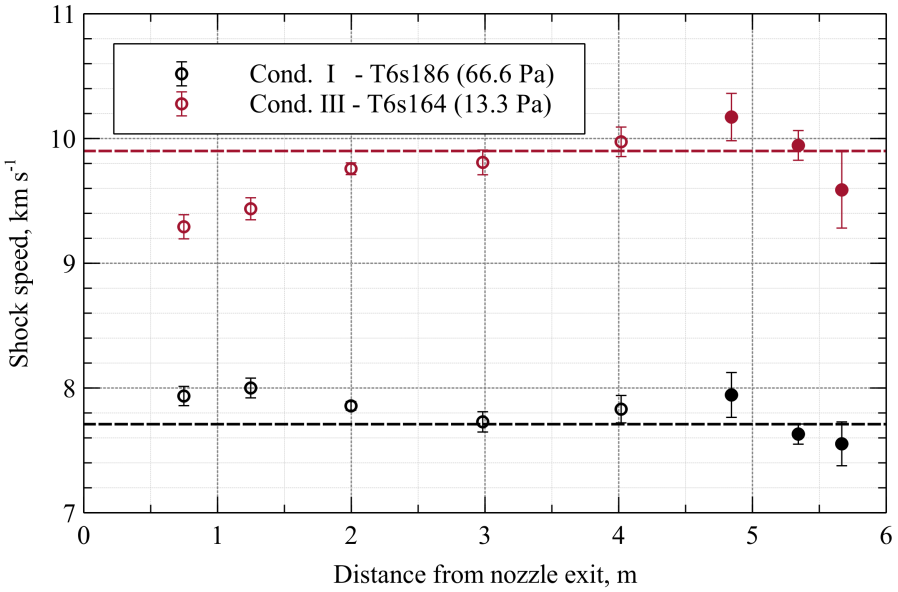
triangular blurring value was calculated based on the characteristics of the Red OES system optical path, as detailed in Table 5.1.

In Sections 4.2.3 and 5.3.3 the convention for reporting the nominal shock speed values in this work was defined. For the T6 experiments, this value has been chosen as the average of the last three shock speed measurements closest to the window (the 'mean' value). Generally, the T6 tests exhibit relatively flat shock speed profiles; this averaging approach was thus expected to reduce the uncertainty inherent in the closely-spaced time-of-flight calculations without introducing errors due to velocity gradients. The alternative method would be to select the 'final' shock speed at the window (either from measurement or fitting of the trajectory) as the nominal, as is done at EAST.

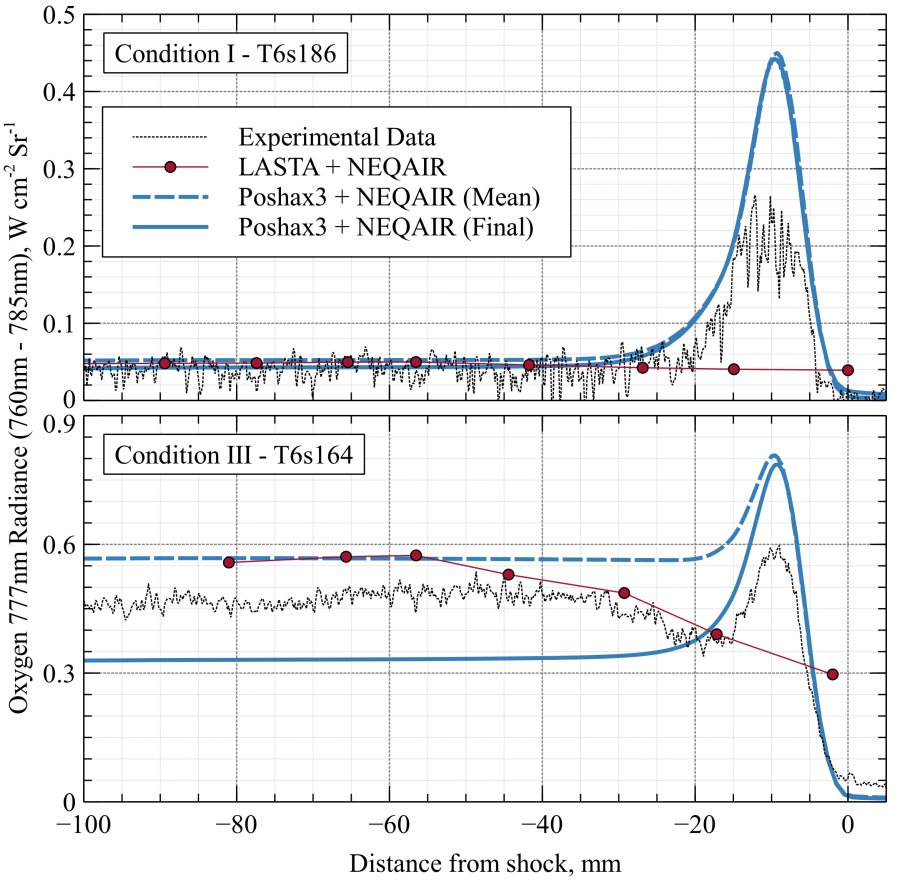
To investigate the impact of these conventions, differences between 'final' and 'mean' shock speed values were assessed for two of the conditions presented in Chapter 5. In Figure 6.6a, shock profiles for two tests are reproduced at Condition I (T6s186) and III (T6s164). It can be seen from these measurements that T6s186 is reasonably flat, whereas T6s164 was found to deviate slightly from the nominal value of the condition at the last transducer. In both cases, the mean value describes the shock velocity along the majority of the tube well. For these conditions, both the the mean and final values were simulated using Poshax3 to enable comparison with the experimental measurement.

Shock-Layer Comparison Results

Figure 6.6b shows the results of the comparison between the T6 experiments and NEQAIR, using both LASTA and Poshax3 solutions as inputs. Considering Condition I, the Poshax3 simulations predict a shock-layer which is qualitatively identical to that observed experimentally: a non-equilibrium peak, followed by a decay to stable equilibrium. The simulations using the final and mean shock speeds show close similarity; this is to be expected, given the relatively flat shock speed profile and low sensitivity of the post-shock equilibrium radiance to shock velocity at this condition. The LASTA result reflects this, predicting an essentially constant radiance. Again, the non-equilibrium peak is not modelled due to the equilibrium nature of the code. However, this analysis does show that based on the shock speed profile the thermodynamic properties should be constant



(a) Shock speed variation. The dashed line shows the mean value of the final three measurements; these are shown as filled markers.



(b) Comparison of experimental oxygen 777 nm radiance with NEQAIR predictions. Simulations are performed with LASTA and with Poshax3 at the final and mean shock speeds. The LASTA initial Lagrange point spacing is 200 mm.

Figure 6.6 – Investigation of SSV effects on the approach to equilibrium.

through the initial non-equilibrium region; extraction of reaction rates could thus be performed accurately without consideration of SSV.

The non-equilibrium peak is over-predicted by the Park 93 model in combination with the default NEQAIR non-Boltzmann (Quasi-Steady-State) excitation rates. It should be noted that the Poshax3 simulation does not account for hydrodynamic influences, notably the axial compression of the test gas through Mirels effects, which would also affect the peak shape.

For the results of Condition III, the form of the shock-layer predicted by Poshax3 is qualitatively identical to that for Condition I: after an initial non-equilibrium region, a monotonic decay occurs to a steady equilibrium. As presented in Chapter 5, at velocities around $10\,\mathrm{km\,s^{-1}}$ the equilibrium radiance first exceeds that from the non-equilibrium peak as atomic line emission becomes dominant. The ratio of the non-equilibrium and equilibrium regions shows thus greater sensitivity to shock speed at this condition. The presented test (T6s164) exhibited a deceleration at the last transducer; this is reflected in the Poshax3 results, which predict very different equilibrium radiance. Overall, there is better agreement with the mean velocity prediction at equilibrium. However, the experimental result shows a local minimum at approximately $-20\,\mathrm{mm}$ between the non-equilibrium peak and the equilibrium region. This is not captured by the chosen thermochemical model. This is also a feature of EAST experiments (e.g. Brandis and Cruden, 2017a). Typically, this feature becomes less distinct at higher velocities, as the magnitude of the equilibrium radiance further exceeds that from the non-equilibrium peak.

As would be expected, LASTA agrees with the equilibrium level of the final-velocity Poshax3 simulation at the shock. The LASTA result then trends towards the mean-velocity value with increasing distance through the shock-layer. There is good agreement in the mean-velocity simulation and LASTA after approximately $55\,\mathrm{mm}$; this validates the choice to average a $50\,\mathrm{mm}$ to $60\,\mathrm{mm}$ distance behind the shock for the equilibrium spectra at this condition presented in Section 5.6.

Comparison of the LASTA result to the experimental measurement again shows good agreement in the observed trends. Interestingly, the LASTA analysis predicts that the non-equilibrium region should decay to an equilibrium radiance close to the value

at the local minimum, before again trending upwards. This is of interest, as work by Lemal et al. (2016) reproduced this 'dip' feature (where other models did not) for VUV atomic radiance at similar test conditions to those that are presented here. That analysis did not include deceleration effects, and only considered thermochemical modelling — specifically, various heavy-particle impact excitation models were applied. This warrants further investigation, ideally using a set of state-of-the-art thermochemistry rates within a future version of LASTA.

In summary, the cases presented here have demonstrated the nominal trends which would be expected for one-dimensional, thermochemically reacting shock-layer. In the case of Condition I, which had a flat trajectory, the morphology of the predicted and measured post-shock radiance profiles is similar. Good agreement is also found between all predictions and experiment at equilibrium. In contrast, the case presented for Condition III — which does show evidence of deceleration — exhibits shock-layer trends which are matched less well by the Poshax3 simulation. In addition, the choice of nominal shock speed has a greater impact on the final numerical prediction. LASTA was found to again reproduce the observed trends well.

When combined with the experimental findings of Section 6.3.3, these results suggest some broad guidelines which may be established when considering the appropriate nominal shock speed for shock-layer radiation experiments. From Figures 6.5 and 6.6b it can be seen that the initial non-equilibrium region consists of approximately two Lagrange points upstream of the measurement location. In these simulations, this equates to roughly 400 mm of shock travel. Therefore, if only the non-equilibrium region is of interest, a large deceleration somewhere upstream of this point may not greatly impact the results. In this case, the sensible 'nominal' shock speed for the condition is the value as close to the measurement location as can be determined. For equilibrium measurements, an average is more appropriate.

Finally, it should be noted that the above guideline is highly condition dependent. In addition, these conclusions will not necessarily be applicable for other atmospheres, where in some cases equilibration can require significantly longer distances. For example, the Mars experiments of Brandis et al. (2013) required more than 60 mm of post-shock

distance to approach a steady equilibrium. This suggests that shock deceleration may influence the observed chemical-kinetic rates for these conditions; the impact of this should be investigated in more detail using a code which combines shock deceleration modelling with finite-rate thermochemistry.

6.4.2 Effect of Shock Deceleration Rate

The preceding discussion investigated the influence of SSV on the initial approach to post-shock equilibrium. This section demonstrates the effect of shock deceleration rate on the overall slug length. This is done through a numerical investigation with LASTA. A set of simulated shock trajectories was developed, all beginning at a velocity of $10\,\mathrm{km\,s^{-1}}$ and ending at a nominal speed of $9\,\mathrm{km\,s^{-1}}$ at the measurement location. Each trajectory decelerated linearly between these two values, beginning at a different position along the shock tube. A flat trajectory for each velocity was also considered. These trajectories are shown in the top half of Figure 6.7.

The resulting temperature distributions predicted by the LASTA code are also shown in Figure 6.7. Again, the effect of shock deceleration on the post-shock properties is clear. It can also be observed that greater rates of deceleration exacerbate the shortening of the test slug. This is because expansion waves must reduce the pressure at the rear of the slug to cause the shock to decelerate, forcing the gas slices to expand axially along the tube. This expansion causes a corresponding increase in mass consumption by the boundary layer. In the majority of the deceleration cases, the slug is much shorter than the bounding steady-velocity cases — this demonstrates that the observed behaviour is not simply due to differences in nominal post-shock conditions. It should also be highlighted that this analysis has only been performed for one tube diameter (225 mm) and fill pressure (26.6 Pa). It is anticipated that these effects will be more pronounced for smaller shock tubes, or for lower initial pressures.

The analysis of Figure 6.7 shows that a moderate deceleration rate preserves the shock history in the test slug. However, in terms of selecting a valid ‘equilibrium’ region there will be a fixed amount of the test slug visible through the observation window. In the cases of Figure 6.5, at most 12 points were visible — equivalent to 2.4 m of shock

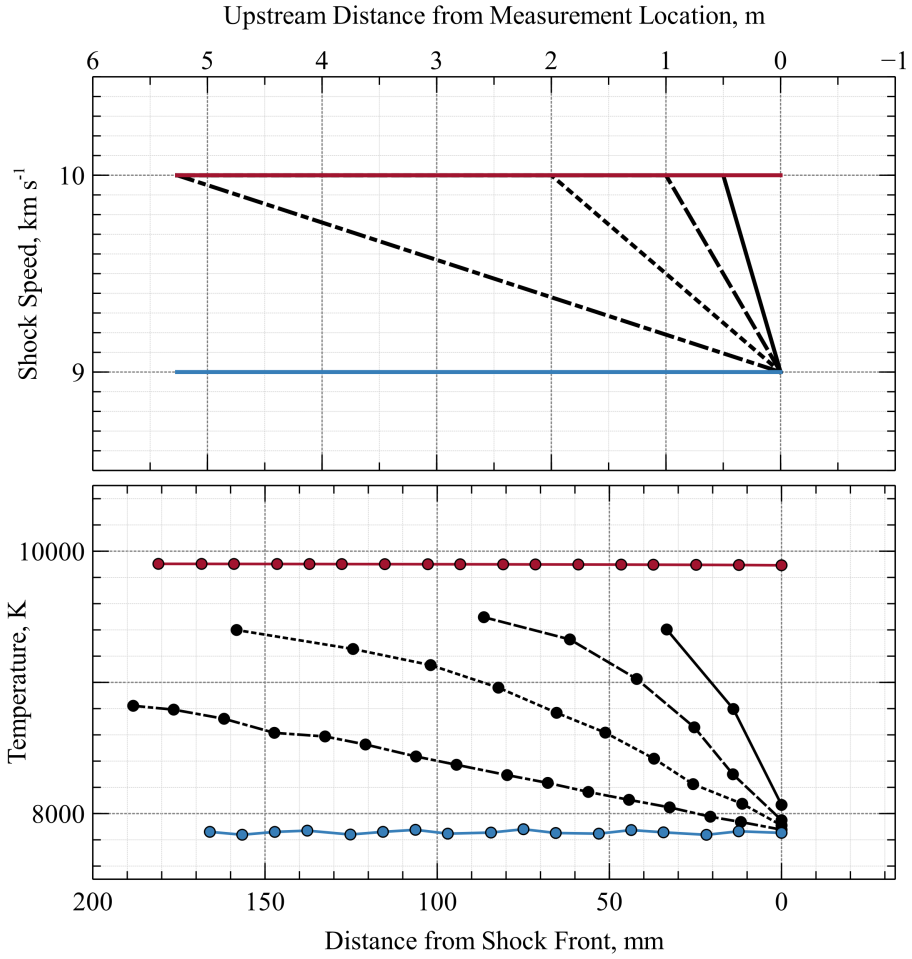


Figure 6.7 – Numerical investigation of the influence of deceleration rate on the test slug length. The top half of the figure shows simulated shock speed profiles along the shock tube. The bottom half shows the resulting temperature trends through the shock-layer. In all simulations the initial Lagrange point spacing is 200 mm.

travel. As a result, if the trajectory is reasonably flat for that distance along the shock tube then the condition is likely unaffected by SSV effects. This suggests that initial velocity variations during shock establishment (for example, due to a reflected shock at the secondary diaphragm) are less important if they occur upstream of the measured region.

Finally, this analysis shows that — depending on the shock deceleration rate — the presence of a flat region in post-shock radiance may not correspond to equilibrium. If the deceleration rate is moderate, an effectively monotonic rise in radiance can be observed and a steady state is never achieved. However, if there are more rapid decelerations then the majority of the test slug is consumed and a local maximum will appear at the

interface between the driver and driven gas. An example of this is seen for T6s188 in Figure 6.5, where the radiance reaches a pseudo-plateau (which does not correspond to any physically-meaningful value) at approximately 55 mm. This could be misinterpreted as the equilibrium region using some metrics (e.g. Brandis et al., 2010a). This may also suggest why certain past experiments have appeared to achieve radiance levels closer to equilibrium than might be expected: less of the shock history is visible, and so the maximum level of radiance observed is far below that which would be expected given the shock speed even a metre further upstream. Depending on the magnitude of the deceleration, this could also be affected by vortices at the interface which result in a departure from both the nominal test condition and the prediction of the LASTA code.

Overall, this assessment adds further motivation to the goal of achieving a steady shock speed profile: as well as causing undesirable gradients through the test slug; it also truncates it significantly. Given the challenges in achieving a perfectly uniform shock speed, it is likely that for many applications that the shock-layer must be rebuilt with the LASTA code (or an equivalent formulation) to properly extract chemical kinetic rates and the magnitude of shock-layer radiation. This in turn will require improved facility diagnostics and performance development, especially in the areas of reduced SSV and in the accurate, high-resolution measurement of shock speed.

6.5 Electron Density Measurements

In Chapter 2, it was highlighted that previous studies in shock tubes had shown excesses in electron density. The deceleration of the shock was posited as a potential cause of this discrepancy. Here, this link is investigated using the same fundamental approach as undertaken in the preceding radiance measurements: different shock speed profiles are generated, and the spatial trends in electron density determined.

In this section, the electron density in the shock-layer is determined using Stark broadening. A full description of this technique, including specific details of its application in this thesis, is provided in Appendix C. A very brief overview is first included here. The SSV test cases for the electron density are then summarised, after which the experimental results are presented and compared to the prediction of the LASTA code. Finally, historic

electron density measurements from the EAST facility are revisited and explanation of those results attempted.

6.5.1 Stark Broadening Methodology

The presence of free electrons in the flow causes widening of spectral lines through a mechanism known as Stark broadening. The locally-inhomogeneous distribution of electrons and ions in the plasma produces gradients in the electrostatic potential of the atomic and molecular nuclei. This effect perturbs the energy (and hence observed wavelength) of electronic transitions. The measured line width is thus a function of electron density. A common diagnostic approach used for high temperature plasmas is to measure the degree of broadening of a spectral line due to the Stark effect, and then infer the electron population from this measurement. In the experiments presented here, the Balmer-α line of atomic hydrogen at 656.6 nm is measured in high resolution using the Red OES system described in Chapter 5 with a 1200 Grooves/mm grating and slit width of 20 µm.

6.5.2 T6 Electron Density Experiments

Here, electron density measurements are undertaken at two free-stream pressures. The first, at 0.1 Torr, have reasonably flat shock trajectories, as shown in the upper half of Figure 6.8. At EAST, the 10.5 km s^{-1} condition was shown to match well with predictions, whilst the agreement found for 10 km s^{-1} was also reasonable. These two conditions therefore act as benchmarking test cases to validate the Stark broadening measurements and the electron density predictions of LASTA. The details of these cases are provided in Table 6.2.

The second pressure considered is 0.2 Torr, in line with the radiance measurements presented in Section 6.3. The motivation for the selection of these conditions is identical to that previously discussed for those measurements. At this pressure, the degree of shock deceleration was again varied to produce differing gradients in the test slug. The shots considered in this work are shown in the lower portion of Figure 6.8, with the key parameters again summarised in Table 6.2. Comparing these tests with the radiance

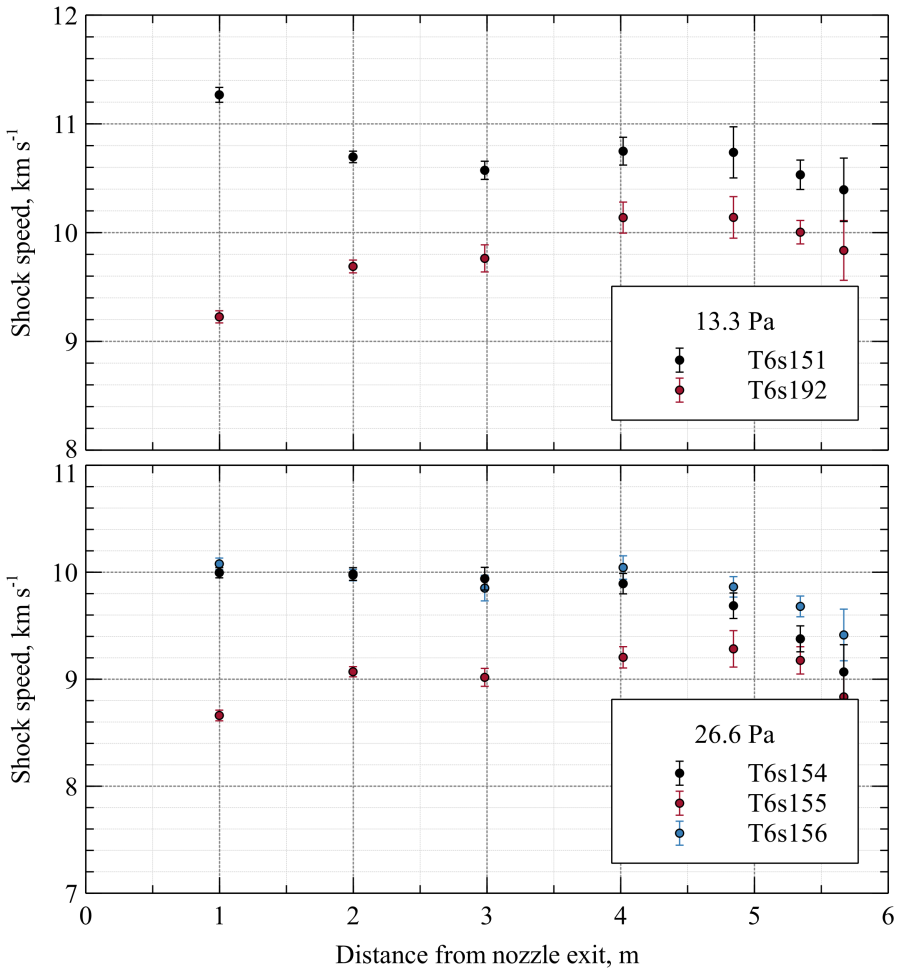


Figure 6.8 – Measured shock speed variation for the T6 electron density measurements.

test cases of Figure 6.3 and Table 6.1, it can be seen that these are broadly similar in final shock velocity and deceleration rate.

Electron Density Measurements at 0.1 Torr

The electron density measurements at an initial pressure of 0.1 Torr are presented in Figure 6.9. As described in Appendix C.2, the fit uncertainty is assessed at 5 mm intervals; these locations are depicted by markers. It can be assumed that the error at these points is representative of the uncertainty at intermediate positions. Included in these plots is the radiance between 648 nm–649 nm, corresponding to a feature of atomic nitrogen. This allows comparison of the shock-layer radiation to the electron density profile and, unlike the hydrogen, should not vary in initial concentration from test-to-test. Also shown

Table 6.2 – Measured shock speed characteristics for the SSV electron density test cases. Here, $U_{s,f}$ is the final shock speed, $U_{s,m}$ the mean of the last three measurements and $\Delta U_{s,max}$ the maximum percentage variation of the profile from the final measurement.

P_1, Pa	Shot	$U_{s,f}$, km s^{-1}	$U_{s,m}$, km s^{-1}	$\Delta U_{s,max}$, %
13.3	T6s151	10.39 ± 0.29	10.55 ± 0.13	8.4
	T6s192	9.84 ± 0.27	9.98 ± 0.11	-6.2
26.6	T6s154	9.07 ± 0.25	9.45 ± 0.09	10.2
	T6s155	8.83 ± 0.23	9.09 ± 0.08	5.1
	T6s156	9.41 ± 0.24	9.72 ± 0.10	7.1

is the nominal CEA equilibrium value for electron density based on the mean of the final three shock speeds. The LASTA prediction of the spatial variation in electron number density is also shown.

The results presented for T6s192 in Figure 6.9 show excellent agreement between the experimental measurement, the nominal CEA equilibrium electron density and the prediction of LASTA. Comparison of the mean shock speed with the profile shown in Figure 6.8 and values provided in Table 6.2 show that at approximately 7.5 m and at the end of the tube there is a departure of the velocity profile from the nominal average value. This is very well captured by LASTA, which consequently allows the measured fluctuations in electron density throughout the shock-layer to be directly linked to the shock velocity along the length of the tube.

Figure 6.9 also shows equivalent results for T6s151 at 10.5 km s^{-1}. Again, there is excellent agreement between the experimental measurement, CEA equilibrium value and the LASTA prediction during the test flow. Based on the radiation trace and the electron density variation, it can be seen that the slug is truncated at approximately 70 mm behind the shock front. This is not captured by LASTA given the final shock speed measurement still suggests a flat trajectory. This could be improved in future with better resolution of the shock speed after the windows. However, given the aim of this analysis was to validate the Stark measurement of electron density this comparison is still considered good.

Overall, a close agreement between the predicted, computational and measured electron density trends at the 0.1 Torr condition is found. This suggests that the current

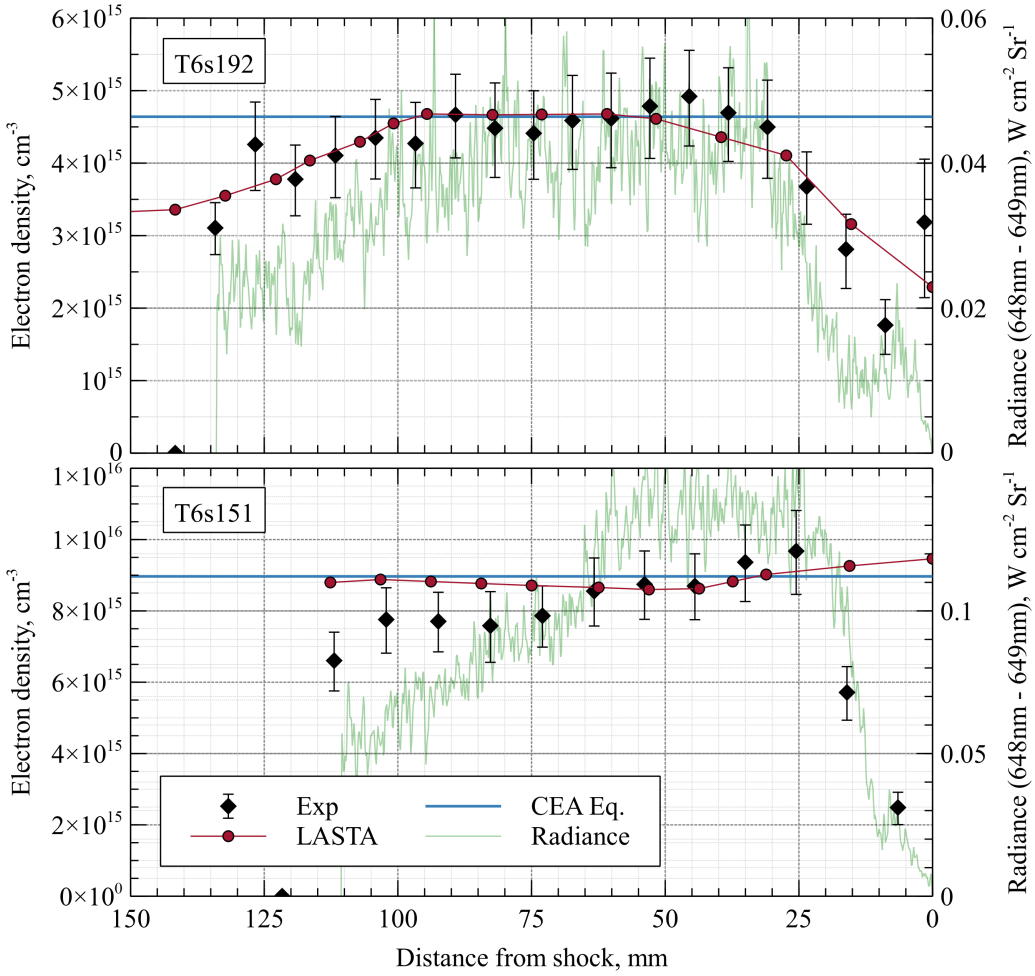
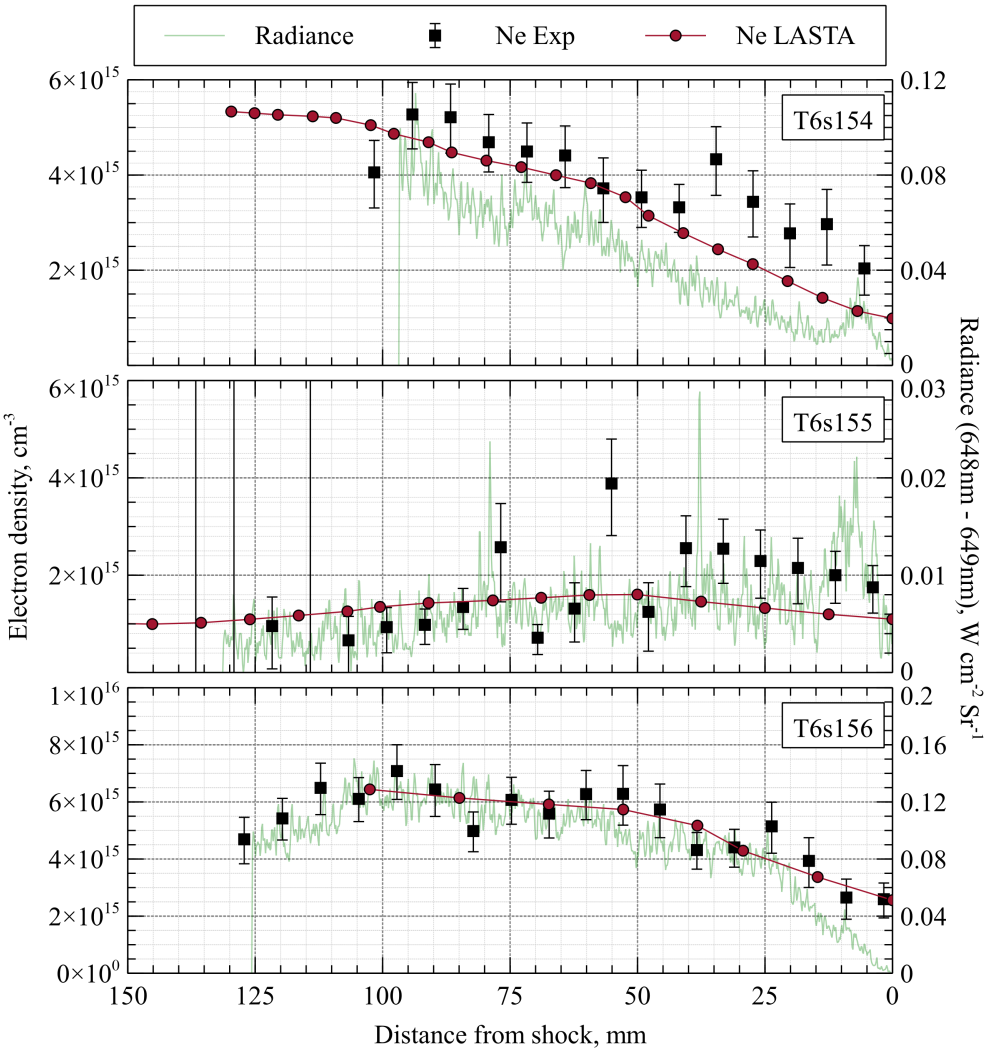


Figure 6.9 – Experimental electron density results at the 0.1 Torr condition. These are compared to the nominal equilibrium value (based on the averaged shock speed) and the predictions of LASTA. In both cases the LASTA results have been referenced to coincide with the shock location as determined from the rise in radiance.

methodology is reliable and can be used to investigate the effects of SSV on the test slug electron density distribution.

Electron Density Measurements at 0.2 Torr

Figure 6.10 shows comparison of experimental measurements for the different SSV profiles of Figure 6.8. Again, the measured radiance of the atomic nitrogen line is shown for the three cases. It can be seen that there is reasonable agreement in the magnitudes of the non-equilibrium peaks, suggesting similar shock speeds at the measurement location. The trends are also qualitatively similar to the radiance results previously



Experimental electron density results at the 0.2 Torr condition. In all cases the LASTA results have been referenced to coincide with the start of the non-equilibrium peak.

Figure 6.10 –]

discussed in Section 6.3.

The trends in post-shock electron density are shown in Figure 6.10 for all three conditions. It can be seen that after an initial non-equilibrium region there is strong agreement between the observed trends in electron density and the predictions of LASTA based on the measured shock speed profile. On the whole, the data for each test agrees with LASTA within the uncertainty and, crucially, the trends disagree with one another. It should be highlighted that if the final measured shock speed were taken as the nominal condition, the 'equilibrium' value would be equal to the LASTA prediction

at 0 mm. The departure from this value can thus be seen to be directly correlated with the shock trajectory.

There is a slight deviation of the LASTA result from the measurement near the start of the slug for tests T6s154 and T6s155. This is attributed to processes in the non-equilibrium region, both in the form of an increased electron density and in translational temperature which would introduce additional Doppler broadening. This requires an extension of LASTA to non-equilibrium thermochemistry to investigate fully. In addition, there is noise in the measurement of T6s155 between approximately −50 mm to −80 mm which appears to be greater than the uncertainty. The reason for this is not clear. At this condition the electron density is very sensitive to temperature, and so it is possible that either unresolved velocity fluctuations in the shock profile or transient pressure waves in the test slug could be the root cause.

Overall, the trends in electron density from both the numerical prediction and experimental measurement exhibit close similarity. Notably, the trends in electron density are very similar in all cases, and deviate significantly from one another. These results further confirm that the shock profile has a lasting influence on the test slug and can result in electron densities in excess of equilibrium.

6.5.3 Revisiting EAST Electron Density Measurements

The experimental results from T6 have both demonstrated evidence of shock history effects in the test slug and validated the LASTA code's prediction of the equilibrium thermochemistry in the shock-layer. This analysis is now extended to results from the EAST facility. This is undertaken to cross-validate the conclusions from the results already presented in this chapter and to attempt to explain historic discrepancies in the EAST data, as identified by Cruden (2012b).

To analyse the EAST results using LASTA, shock speed profiles are taken from the online datasets. Typically, the close spacing of shock timing stations at the observation window at EAST results in a significant noise in the velocity measurement. This data is fit with a polynomial by the investigators there to determine the nominal shock speed. To determine an input profile for LASTA, these closely-spaced measurements are first

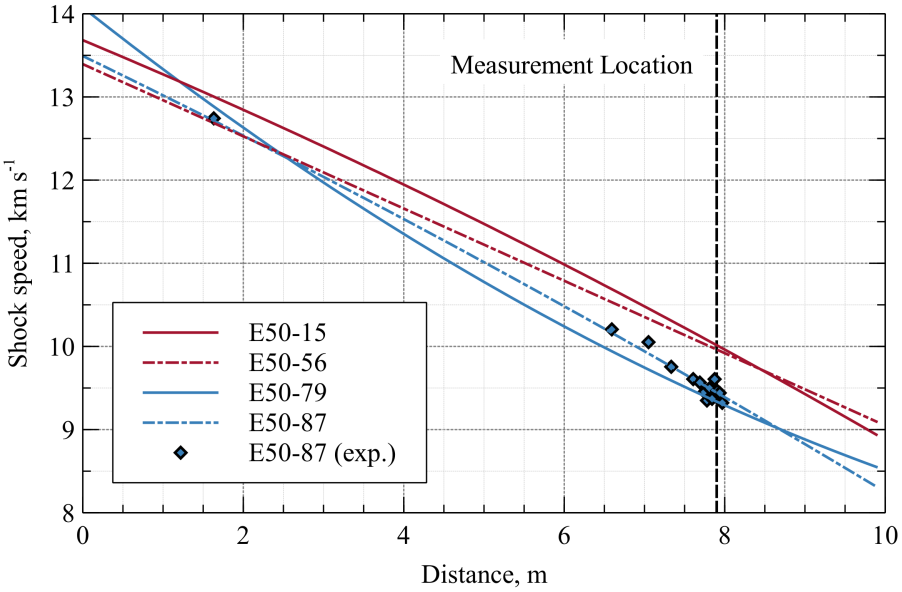


Figure 6.11 – EAST shock speed profiles for electron density analysis. The curves represent the polynomial trajectory used an an input to LASTA. The original experimental measurements for E50-87 are given as points for comparison.

averaged. A quadratic curve is then fit to the discrete shock speeds. This typically captures the overall trend well, but the shock speed at the test section is not exactly matched in the curve of best fit. The final shock speed measurement is then adjusted to give agreement between the polynomial shock profile and the nominal shock speed at the measurement location. Typically, the variation required is on the order of one percent and does not significantly alter the upstream profile. The resultant shock trajectories are given in Figure 6.11; note the substantial change in shock speed along the length of the tube in all cases. Also shown are the original experimental points for E50-87 to enable comparison with the resulting fit; this is representative of the entire dataset.

The results of the comparison between the previously-published EAST data and the predictions of LASTA are provided in Figure 6.12. Also shown is the expected equilibrium concentration based on the final shock speed. It can be seen that at the shock the LASTA result agrees with this value; this confirms that the tuning of the shock speed profile has given the correct velocity at the measurement location.

In general, the electron density compares well between the predictions of LASTA and the previous experiments at EAST. In the case of the 0.2 Torr measurements in the

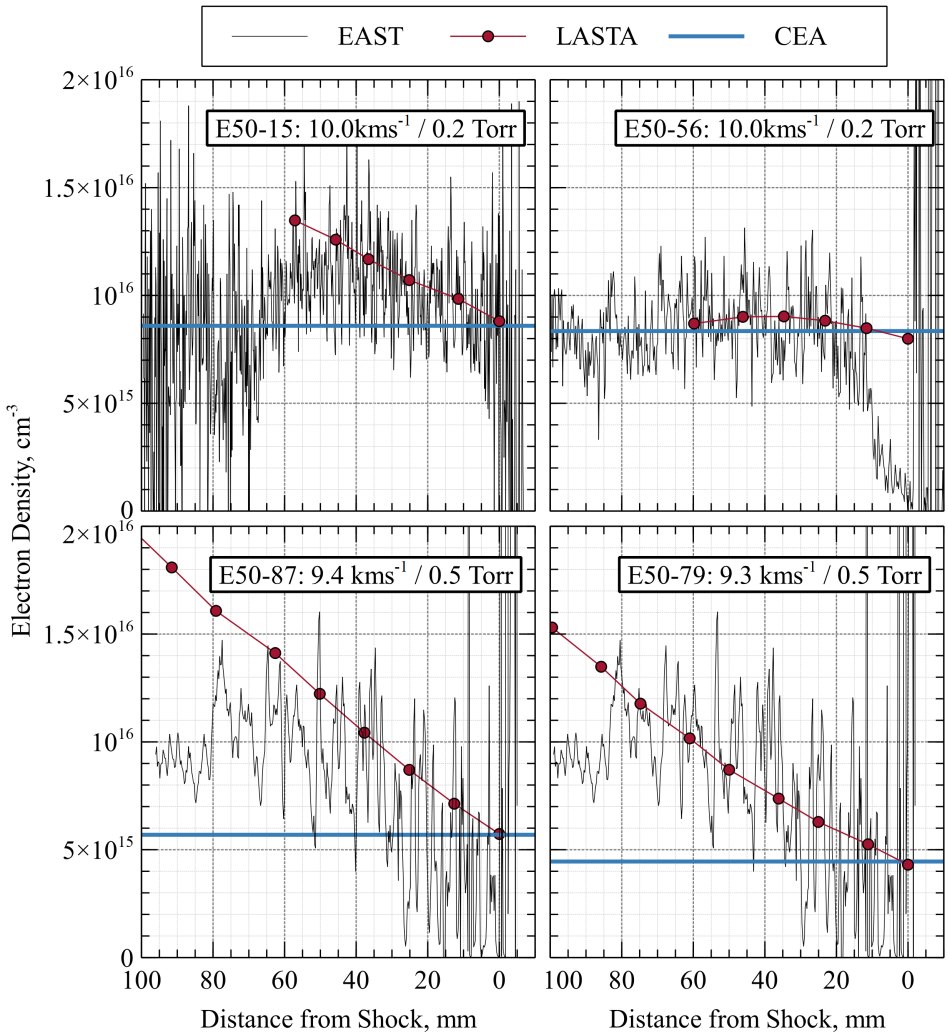


Figure 6.12 – Comparison between electron density measurements at EAST and the prediction of LASTA. The EAST data is replotted from Cruden (2012b).

upper portion of the figure, the slug length is also reasonably well captured. There is worsening agreement near the end of the slug for the 0.5 Torr cases. This is attributed to a wave effect which is not captured by the shock speed profile. In the EAST measurements, there are no shock timing stations after the window, and reasonably few along the length of the tube upstream; this means that exact rebuilding of the finer detail of the trajectory was not possible.

Despite some differences, there is again an overall good agreement in the trends of electron density in the shock-layer. In combination with the results already shown from the T6 AST, it is therefore concluded that shock speed variation is indeed the most likely

cause of the observed departures from equilibrium in the original data. Furthermore, this implies an equivalent explanation of similar discrepancies in equilibrium radiance as presented by Brandis et al. (2017), and originally discussed in the motivation section of Chapter 1, at velocities below $10\,\mathrm{km\,s^{-1}}$. This will be explicitly confirmed in future analysis of an extended set of the EAST data.

6.6 Summary

In summary, this chapter has shown that the spatial variation in post-shock species concentrations and radiative emission is intrinsically linked to the shock speed profile. This was demonstrated by developing decelerating test cases in the T6 AST and analysing both the emission of an atomic oxygen feature and the trends in electron density within the shock-layer. Using the LASTA and NEQAIR codes, the resulting variations were conclusively connected to the measured shock speed profile. This analysis was then extended to analyse historic discrepancies from the EAST facility, confirming SSV as their root cause.

The analysis in this chapter also found that the appearance of the test slug is closely linked to the deceleration rate, and that large decelerations can both significantly reduce the test time and introduce local maxima in the radiation profile which may be wrongly interpreted as equilibrium. Recommendations regarding allowable degrees of SSV (depending on the experimental goals) were made and guidelines to assist choosing a representative shock speed value for computational comparisons proposed. It was concluded that LASTA-like computations should form a fundamental component of the analysis of high-enthalpy shock tube experiments. Further recommendations are made in the subsequent chapter.

A good thesis is a finished thesis. A great thesis is a published thesis. A perfect one is neither.

— Anon.

7 Conclusions & Recommendations

Contents

7.1 Conclusions and Contributions 206
7.2 Recommendations for Future Work 209

The primary goal of this thesis was to establish a new ground test facility for the investigation of shock-layer radiation. In Chapter 1, this aim was partitioned into four objectives: to commission a new high-enthalpy test facility, to develop a bespoke operational mode specific to shock-layer radiation studies, to benchmark emission measurements in said mode against established results from the literature and, finally, to investigate historic discrepancies in data from other facilities.

In this chapter, the conclusions of the preceding work are synthesised. If these are compared to the originally stated aims of the work it can be seen that, in general, the objectives were achieved. The original contributions of this thesis to the wider field of experimental aerothermodynamics are also highlighted.

This thesis represents the first test campaign undertaken in a new ground test facility. The results presented here thus provide a starting point for many new avenues of research. There is consequently extensive scope to build upon the work presented in this thesis, both in terms of improvements which could be made to the facility and in the undertaking

of further analysis based upon the experimental results. Suggestions for future work based on these considerations are included here.

7.1 Conclusions and Contributions

In this section, the conclusions of the preceding chapters are summarised. These are also considered in the wider context of the aims of this thesis, with key contributions discussed.

7.1.1 A New Ground Test Facility

In Chapter 1, it was concluded that there was a need within Europe for a new high-enthalpy test facility which would extend existing aerothermodynamic experimental capability. Noted shortcomings were the capacity to reproduce the non-equilibrium portion of the shock-layer, the lack of a high-enthalpy shock tube facility and the need for higher performance to support future missions — including sample return trajectories.

A large component of this thesis was the commissioning of a new, high-enthalpy, multi-mode ground test facility. It was shown that the new experimental test-bed — T6 — can reach conditions relevant to high-speed atmospheric flight, shock-layer radiation and Mars sample return. In all cases, good quality test flows were observed and the facility performance was found to compare favourably to the predictions of numerical calculations. As a direct consequence of this work, many of the aforementioned shortcomings in European aerothermodynamic test capability have been addressed. A new research facility is therefore available to support future missions and to provide new insights into high-enthalpy flow phenomena.

7.1.2 The Aluminium Shock Tube

Many situations in which shock-layer radiation is critical occur under conditions of high altitude or low volumetric radiance. A new facility mode, the T6 AST, was therefore envisioned to provide a means of investigating these cases. The AST was specifically designed for shock-layer radiation studies, incorporating significant additional infrastructure (including high-vacuum pumping systems and a new Pitot rake), diaphragms at both ends of the tube and wall-integrated windows. The main feature of the AST is

a large (225 mm) bore, which was expected to yield improved signal-to-noise and test time characteristics. This new mode was successfully manufactured, pressure tested, installed and commissioned.

During the first test campaign of the T6 AST, 165 tests were completed. Over this period, the ability of the facility to achieve conditions important to radiative heating in the atmospheres of Earth, Mars and Titan was established. The performance of the new mode was shown to be close to the predictions of the PITOT code, albeit with a pressure-dependent discrepancy which was attributed to the intermediate nozzle. Despite this, good quality shock speed profiles and test flows were observed across a range of conditions, suggesting that this shock tube configuration functions well. A comparison of measured test times versus the predictions of Mirels was also found to give favourable agreement, demonstrating that these analysis tools can be used to predict the experimental performance of the AST. This new mode is now available for future studies of shock-layer radiation. A large body of performance data has also been collected which will enable high-fidelity computations of the facility flow and aid in the planning of future test campaigns.

7.1.3 Shock-Layer Radiation Experiments

The work undertaken for this thesis established a new measurement technique within the Oxford Hypersonics Group: emission spectroscopy. A full OES system was specified, purchased and installed. Simultaneous ultraviolet and visible/near-infrared measurements were undertaken of radiating air shocks at several conditions. These measurements were fully calibrated in terms of spatial position, wavelength and spectral radiance, permitting measurement of the spatial and spectral evolution of absolute emission throughout the shock-layer. For all conditions, it was shown that a significant region of steady, post-shock equilibrium could be achieved in the AST. A full uncertainty analysis of these experiments was also undertaken, placing confidence bounds on the data. These results institute the T6 AST as one of the only sources of such data in the world and provide a new dataset for the comparison of *ab initio* models and computational tools.

7.1.4 Cross-Facility Comparisons

The measurements made of shock-layer radiation in the T6 AST were compared to the NASA Electric Arc Shock Tube. Overall, good agreement was found between the two facilities in both the equilibrium and non-equilibrium portions of the shock-layer. This is especially true of the Red OES data, which showed excellent consistency both between shots and in comparison to EAST. The equilibrium portion of the shock-layer from both facilities was also compared to the NEQAIR code; the resulting comparison showed good qualitative similarity. Finally, a condition designed to match the plasma torch data of Laux (1993) was developed. This was shown to match the pressure and temperature of the ICP torch results, thereby providing a directly comparable test case and 'closing the loop' between available datasets from shock tubes and ICP facilities.

The availability of new cross-facility comparison data enabled identification of similar areas of disagreement with numerical tools. Notably, the N_2 (1+) band was shown to exceed the NEQAIR prediction across a range of conditions. This was also found to be the case when comparing to the plasma torch data of Laux (1993). Modelling of the AST results with other simulation tools is recommended. The new T6 data, which demonstrates large regions of steady post-shock radiance and minimal shock speed variation, will continue to provide a useful test case for this problem. Additionally, the background in the NIR for the higher speed Condition III was shown to generally agree with the NEQAIR prediction within the uncertainty of the measurement. This suggests that more excessive levels at EAST may indeed be caused by excess electron density, as this quantity was determined to be equilibrated in the T6 experiments.

7.1.5 Shock Speed Variation Effects

The results presented in Chapter 6 conclusively demonstrated through a combined experimental-numerical approach that the shock trajectory along the length of a high-enthalpy shock tube directly influences the observed trends in shock-layer radiation. This confirms the hypothesis of several authors, including Light (1973) and Brandis et al. (2010a). From this foundation, shock deceleration was confirmed as the source of excess electron densities in the previously published work of Cruden (2012b). These

measurements were also shown to be matched well by the assumption of thermochemical equilibrium after the initial post-shock non-equilibrium region.

A key conclusion of this thesis is thus that there is an intrinsic coupling between the desired experimental measurement and the performance of the facility. Notably, flat shock trajectories must be generated and/or a sufficiently validated computational analysis technique (such as LASTA) used to interpret the results. It is further concluded here that future publications of shock-layer radiation experiments must also present facility diagnostics: ideally, static pressures and Pitot pressures would be included, but shock-speed variation should be a minimum requirement. In general, performance can show large deviation from numerical predictions and so this would ideally take the form of experimental measurements. This means that additional instrumentation may need to be added to existing facilities. In presenting SSV data, it has been found during internal discussions that distance-time plots are difficult to interpret. The presentation of said data as average shock speed as a function of distance is hence proposed as the conventional means of showing this parameter.

7.2 Recommendations for Future Work

In this section, recommendations for future work are made. Here, these have been divided into two categories: Section 7.2.1 discusses mostly physical improvements, alterations or additions which could be used to enhance tunnel operation and/or the quality of the collected data. Section 7.2.2 then discusses recommendations for future research and exploitation of the new results.

7.2.1 Facility Improvements

A key outcome from these first experiments performed in T6 was an improved understanding of the experimental methodologies. Several direct improvements of these immediately suggest themselves; it is recommended that these be adopted wherever possible.

Free-Piston Driver Enhancement

As discussed in Chapter 3, the T6 free-piston driver was repurposed from the decommissioned T3 facility designed originally by Stalker (1966). This was the first research-scale tunnel of its type, and since that time significantly more has been learnt regarding the operation of such designs (Stalker, 2006; Gildfind et al., 2016; Hannemann et al., 2016). An obvious means of enhancing the T6 driver would be to implement the improvements seen on later facilities. Many of these are subtle and intended to improve the ease of facility operation; a comprehensive discussion would thus be esoteric even in the context of this thesis, but it is noted that general mechanical design improvements to improve tunnel operation, alignment and maintenance would greatly increase experimental throughput.

More modern free-piston designs incorporate a pressure sensor at the upstream face of the primary diaphragm. This allows characterisation of new driver conditions without the use of blank-off testing (see Section 3.3.1). Another key advantage is that the rupture pressure of the diaphragm is directly known, rather than being inferred from other facility measurements or from static rupture tests e.g. Stennett et al. (2019). This capability would greatly aid in the understanding of facility performance and in comparisons to computational tools. However, it is acknowledged that addition of a pressure tap is complicated by pressure rating requirements. An alternative would be to use a similar approach to that of Gildfind et al. (2019), wherein an on-board sensor is mounted on the front of the piston. This is relatively straight-forward to implement and requires no modification of the core facility components.

Improvements are also possible to increase the performance or operability of the free-piston driver. The development of a lightweight piston enables tuned operation at higher compression ratios; this was notably done in the thesis of Gildfind (2012) for the X2 facility. Some tests in this work showed evidence of shock attenuation due to expansion wave arrival; this could be mitigated through use of a lighter piston. Preliminary calculations based on the work of Itoh et al. (1999) suggest a piston mass of 12 kg would be ideal for Driver Condition C in T6. Alternatively, development of a new driver condition with approximately 80 MPa rupture pressure would allow tuned operation with the current 36 kg piston at a compression ratio of 60. Performance could also be improved

by increasing the length of the compression tube, as was done when refining the T3 design for the T4 Shock Tunnel (Stalker and Morgan, 1988). This could best be achieved by sleeving and re-honing the in-line reservoir bore, allowing extension to approximately 9 m in length. This alteration would also allow conversion of the facility to load the piston from the rear, which would remove the mechanical complexity of translating the downstream components laterally in order to return the piston after the shot. Removal of this process would permit longer shock tubes to be installed, including a secondary driver section for ExT mode. This change would also eliminate the down-time associated with replacement of the piston launcher seals, as these would be easily accessible. This latter issue could alternatively be resolved by inverting the piston-launcher mating geometry to position said seals on the piston; this change would be possible to implement concurrently with the design of a new piston.

General Facility Improvements

A major component of this thesis was the general commissioning of T6 in all of its operating modes. The conclusions of this process (as detailed in Section 3.7) made several recommendations for future work and development. A key recommendation is the trialling of less ductile diaphragms, which may improve shock speed variation characteristics in SST mode. In addition, the initial gradient in the shock speed profile has been posited as the root cause of performance loss when using a secondary driver. It is likely the performance capability of the SST and AST could be significantly enhanced through the resolution of this issue. A longer version of Shock Tube 1 (which acts as the secondary driver) could also resolve this as it would provide more distance over which the shock speed profile could stabilise. Although currently restricted by space constraints, the ideal solution would be to construct an additional barrel upstream of Shock Tube 1, which also would allow the ExT mode to also operate with a secondary driver. This could extend the operating envelope of this mode even further into the realm of proposed MSR trajectories. The addition of a nozzle for the ExT mode, as well as construction of further nozzles for RST mode, is also recommended.

There are several opportunities for the inclusion of additional instrumentation in the suite of measurement techniques currently available. A useful addition, especially for any campaigns using a test model, would be the addition of a recoil sensor. Doherty et al. (2015) comment that the linear voltage displacement transducer used for this purpose on T4 provides a repeatable means of triggering experimental apparatus (e.g. fuel injection systems) before the flow arrival. It also allows exact knowledge of the position of the model relative to the nozzle exit without the use of high-speed video. Secondly, it is recommended that static pressure measurement capability be developed, either as a rake-mounted probe or as a nozzle outlet wall-mounted pressure transducer. This allows better characterisation of the free-stream (including the degree of non-equilibrium) than is possible with Pitot measurements alone. Finally, the introduction of sputtering processes at the laboratory would enable coating of gauges with various materials. Notably, this would remove issues of ionisation for very high-enthalpy flows. This could be used to perform fast-response measurements of test time using heat flux methods, as well as for assessment of catalytic effects (Kim and Park, 2019).

Aluminium Shock Tube Infrastructure

Many of the physical design solutions and sub-systems were trialled for the first time during the AST campaign. Based on the operational experience gained during this period, several improvements should be implemented. Firstly, whilst the high-vacuum system did operate adequately it was found that several components were of insufficient diameter to allow rapid evacuation. A larger turbo-molecular pump would greatly help in this area. The pipework used for filling of the facility was also too long for the ultimate pressures used, resulting in extended settling times for measurements of initial pressure. Both of these issues could be improved by redesign of the pipework. Experience has shown that Parker EO-2 fittings gave a better and more repeatable seal than KF series vacuum components. This should be considered in future specifications of tunnel infrastructure. It was also found that the ports in the AST itself were insufficiently sized; these are limited by structural requirements and a desire to minimise disturbances to the flow. An ideal solution would be to construct an additional pressure vessel, akin to a miniature

test section, which would interface between the dump tank and aluminium tube. This would allow the addition of much larger ports for pumping and on which to mount pressure gauges. This could still be separated from the rest of the Test Section with a diaphragm to prevent contamination. The new AST Pitot rake could also be incorporated into this arrangement, permitting optical access. A comparison of the spectrum measured using the wall-integrated windows with that observed as the shock emerges from the end of the tube (i.e. the approach used by Brandis et al. (2007) and Jacobs (2011a) and, later, Collen et al., 2019) would also be enabled through this approach, allowing cross-validation of these measurement methods.

Spectroscopy System

Overall, the optical design used for the spectroscopic measurements in Chapter 5 was found to function well. One inherent issue in the design was the use of a telescopic optical arrangement; this results in greater spatial blurring away from the optical axis. It is therefore recommended that a modification similar to that of Greenberg et al. (2009) at EAST is made, wherein a telecentric optical arrangement is implemented. Such a design results in all chief rays originating from the tube axis travelling parallel to one another. This is theoretically simple to achieve, requiring only the purchase of sufficiently large mirrors and possibly some smaller customised optical components. It is also recommended that the laboratory space be better configured by moving the High Density Tunnel to another building, to allow removal of the additional folding mirror in the optical chain of the Blue OES.

The spectrograph and intensified camera used for the Blue OES were provided on loan from NASA Ames. This work has demonstrated the value of such a system to the experimental work undertaken on the T6 AST; purchase of a new system owned by the Oxford Hypersonics Group would therefore worthwhile. Based on operational experience gained, an intensified sCMOS is recommended over a traditional ICCD design. These allow much faster collection of calibration images — reducing both uncertainty and turn-around times — and exhibit improved dynamic range characteristics. Alternatively, new electron-multiplied ICCD technologies can offer an order-of-magnitude increase in

gain over typical ICCDs: their suitability for shock-layer radiation experiments should be investigated. If a telescopic optical set-up continues to be used then it is also suggested that a spectrograph with a longer entrance slit be adopted, to reduce the demagnification requirement of the optics and to allow identical optical paths for both OES channels. Finally, it was found that the calibration time required for the Blue OES was in many cases the limiting factor in the facility turn-around. Methods to improve the ease of this process would greatly aid the experimental process. Means of parallelising calibration tasks, for example an automated traverse for the D_2 lamp, or employing two window holders used in alternation (with the transmissivity assessed on the bench-top) should also be explored.

Improved Shock Trajectory Measurement

The results of Chapter 6 demonstrate the requirement for high resolution shock speed measurement along the length of the facility. Experience in analysing the shock tube flow using LASTA has also revealed that a measure of the shock speed variation after the windows would be useful. The addition of more shock timing stations along the length of the tube would achieve both aims. However, error in the calculated shock speed increases as transducer spacing is reduced due to the time-of-flight approach used: the uncertainty in arrival time and inter-sensor distance is equivalent, leading to proportionally higher error bounds. This could be negated to an extent through the approach of James et al. (2019a), where photodiodes (with very short rise times) and an order-of-magnitude higher data acquisition sampling frequency were found to greatly improve shock velocity determination for Gas Giant entry conditions. However, the number of transducers is limited by structural strength requirements and currently available, very high-speed data acquisition cards reduce the number of usable data channels. It is therefore recommended that a new facility instrumentation based on the work of Dufrene et al. (2012) be implemented, wherein microwaves were used to detect the motion of the shock in the LENS XX expansion tube. The arrangement of this device is reproduced in Figure 7.1, wherein a standing wave is established in the shock tube using an antenna; the ionisation behind the shock causes reflection of these waves and hence the shock speed can be measured. The authors show there is sufficient electron

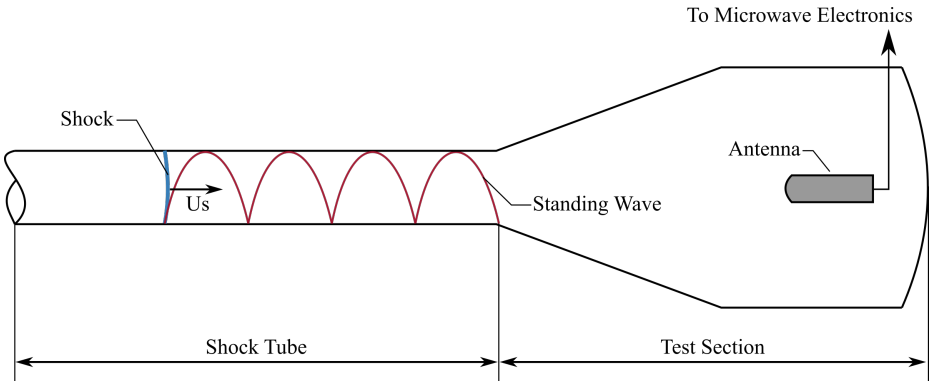


Figure 7.1 – A microwave shock tracking system. Adapted from Dufrene et al. (2012).

density at velocities above 2.5 km s^{-1} in air for this technique to used, with uncertainty less than 1 %. The worst-case resolution of this technique is stated to be one tube diameter (i.e. 225 mm in the AST), but it is proposed that more sophisticated signal processing techniques would enable resolution on the order of 10 mm. This would enable complete rebuilding of the shock profile, and would additionally be useable in every mode of T6 without requiring modification of several large facility components.

7.2.2 Further Work

Here, future research directions based on the scientific findings of this thesis are proposed.

Further T6 Testing

For the majority of the T6 operating modes only a handful of conditions have been tested. These were sufficient to demonstrate the capability of the facility; however, more testing should be undertaken to fully explore the performance envelope. Vastly more conditions will be tested as the facility sees increasing use in future research efforts. However, understanding of the facility performance, operation and flow quality is a crucial component of planning these programmes. It is therefore recommended that, wherever possible, future campaigns perform some degree of systematic performance characterisation of the operating mode. The tunnel operating procedures established in this work enabled up to six tests per day to be run; this is likely to increase in a less complex operating mode and following imminent infrastructure upgrades. This additional bandwidth could thus be used in part for performance characterisation, establishing a

dataset which can be used to define the test envelope, compare to computational tools and inform to future test programmes.

Computational Analysis of AST Nozzle

Whilst this work successfully characterised the performance of the AST and highlighted disparities between the experimental measurements and numerical tools, full explanation of the observed differences will require viscous, axisymmetric CFD simulation. Insufficient time remained in this project to undertake this, but the methodology is well-established (e.g. Gildfind et al., 2018). The main challenge to the full-scale simulation of a transient, high-enthalpy facility is computational time; sufficient super-computer resource is available within the University to perform this analysis. Alternatively, it is recommended that the FROSST solver of Satchell et al. (2021a) be extended to include (at least) equilibrium thermochemistry and the ability to simulate facility area changes. This would also greatly decrease the required computational time, therefore enabling a parametric design study of the nozzle geometry to be undertaken.

Non-Equilibrium Analysis

This thesis has focused on the equilibrium region of hypervelocity air shock-layers. There is thus substantial scope to investigate the non-equilibrium processes using the data presented here. This will require full characterisation of the optical path and camera to accurately model the spatial blurring of the non-equilibrium peak. Measurements which would enable this to be done have already been completed. Given the conclusions of Section 6.4.1, the non-equilibrium assessment should be done in combination with LASTA to ensure there is minimal variation in the nominal temperature across the non-equilibrium region. A comparison with computational results using established models in the literature should then be performed (see, for example, the analysis methodology of Cruden and Brandis, 2020). It is recommended here that this be done for cases which agree well with numerical tools at equilibrium to minimise errors caused by radiative modelling constants. When the agreement for these cases is fully understood, the analysis

should then be extended to fully investigate the coupling between the shape of the non-equilibrium region and shock speed variation.

Utilisation of the Full Shock-Layer Radiation Dataset

The results presented in this thesis represent a fraction of the total experimental dataset. There is thus extensive scope for the further analysis of this data. Possible applications include the validation of numerical models and the determination of non-equilibrium processes, including thermochemical rates. There are also experimental results from both Mars and Titan atmospheres which should be compared to previous results in the literature. It is thus a recommendation of this thesis that an accurate catalogue of tests completed in these campaigns be made available, including details of the experimental measurements for each test and their quality, following the example of Cruden (2017). The resulting resource could then be utilised by other researchers for a range of uses far beyond what could be speculated here.

Further Plasma Torch Comparison

It was found in this work that there is a difference at equivalent conditions between the shock tube, plasma torch data and the predictions of NEQAIR at equivalent conditions. The T6 data should thus be simulated with the SPECAIR code, where good agreement with the torch is seen (Tibère-Inglesse et al., 2018), and a comparison of modelling parameters made. This analysis should also be repeated at other conditions of overlap between the T6 and plasma torch datasets to investigate trends in equilibrium temperature. Finally, a key difference between the two facility types is the presence of a wall boundary layer in the shock tube experiments. It is recommended that finite-rate simulations of the boundary layer be undertaken, to explore the magnitude of these effects. Again, this could be included in a future version of the FROSST code (Satchell et al., 2021a).

Extended Optical Diagnostics

This work implemented a dual-channel emission spectroscopy system, covering the ultraviolet to near infrared. This diagnostic was chosen as it maximised the value of the collected data whilst still being achievable in the duration of the project. However, from

this baseline there is scope to extend the optical diagnostic capability. As discussed in Section 2.2.2, absorption and laser techniques can allow many additional properties of the flow to be determined. Absorption spectroscopy of N_2 vibrational levels to determine whether this species is in thermal equilibrium would be a useful measurement. Development of more specific diagnostics will be dictated by the needs of future research projects. However, it is strongly recommended that the capability to perform emission measurements in the VUV be developed. This is of general applicability for a range of radiative heating scenarios, including for Earth, Titan and Mars. VUV measurements also allow spectroscopic analysis of transitions closer to the ground state; species number densities, gas temperatures and the degree of non-equilibrium can thus be extracted with greater accuracy.

Reinterpretation of Shock Speed Variation in Impulse Facilities

A key conclusion of this thesis is that the shock trajectory influences the observed post-shock trends in both radiance and species populations. This was shown to be the source of discrepancies previously noted at the EAST facility. It is therefore recommended that past high-enthalpy shock tube measurements be revisited in the context of this finding. This may change the identified areas of equilibrium in some cases. Further, it is recommended that the LASTA code be extended to model non-equilibrium thermochemistry. This will allow full comparison of differing rate models to shock tube data. Although for the air tests shown here the area of non-equilibrium was found to be relatively small, other atmospheres — e.g. Titan (Brandis and Cruden, 2017b) — can require more than 100 mm to reach equilibrium. The shock history will thus have a greater impact on finite-rate thermochemistry comparisons for these atmospheres; the magnitude of this impact should be quantified. Finally, the analysis of shock history effects should be extended to the other operating modes (i.e. RST and ExT mode) to investigate test gas non-uniformities in these facility types.

Appendices

A

Arrangement of Facility Infrastructure

Contents

A.1 Diagram Summary 221

The purpose of this appendix is to capture the layout of the T6 Stalker Tunnel infrastructure. Specifically, the record here reflects the arrangement used for the first campaign of the new Aluminium Shock Tube mode. This is included to aid future planning of facility upgrades and to provide a comprehensive account of the experimental apparatus.

A.1 Diagram Summary

The presented diagram shows the pipework system and general arrangement of the facility, including the positioning of pressure gauges, pipework, vacuum pumps and gas bottles. This diagram is primarily the work of Doherty and McGilvray (2018), who designed the vast majority of the infrastructure and logic to support its operation. A full description of the components and their specifics is given in that report. Hal Surtell and Bill Godfrey are also acknowledged for their significant technical contribution to the final design. A description of the operating procedure used is provided in Section 4.2.5.

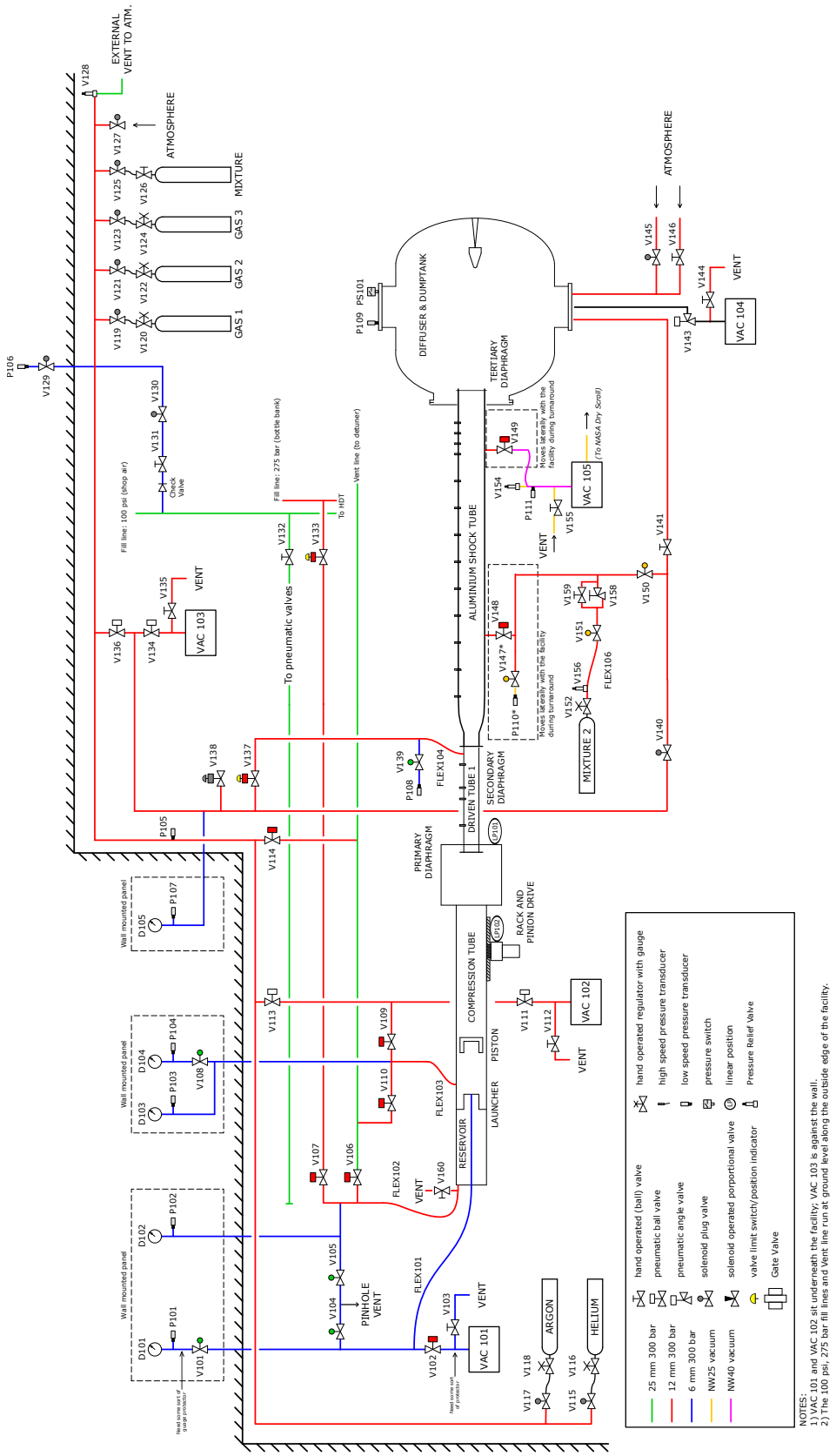


Figure A.1 – Layout of T6 in AST mode. Adapted from Doherty and McGilvray (2018).

B

Spectroscopic Calibration & Uncertainty

Contents

B.1 Details of Calibration 223
B.2 Details of Uncertainty Analysis 235
B.3 Estimated Uncertainties 240
B.4 Summary 242

The purpose of this appendix is two-fold: first, it aims to give a thorough explanation of the calibration procedure used for the Red and Blue OES channels, described in Section 5.2. Providing a full description of the process there was judged excessive the in the wider context of the chapter. Secondly, this appendix details the uncertainty analysis of the measured spectra, and places confidence bounds on the presented results.

B.1 Details of Calibration

In this section, the alignment and calibration procedures used for the Red and Blue OES systems are described in detail. The process to map pixels on the camera sensor to spatial position and to wavelength is first explained. The required steps to calibrate the system to make measurements of absolute spectral radiance is then described.

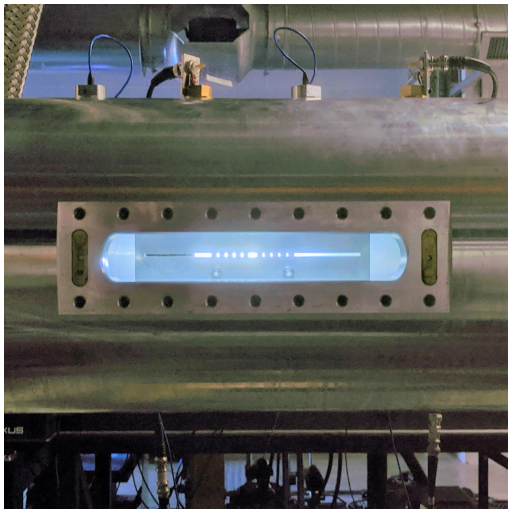
B.1.1 Optical System Alignment and Characterisation

The combination of optical system and spectrograph creates a 2-D map of intensity on the camera sensor. Some method is thus required to assign each pixel (1) a spatial location in the tube and (2) a wavelength value. Furthermore, the goal of these experiments was to determine absolute intensities of the emitted radiation behind the shock. A means of converting the measured signal (in sensor counts) to a physically meaningful value (in units of spectral radiance) is also necessary. This enables direct comparison to other facilities and to computational predictions. The procedure reported here is largely based on that used at the EAST facility, described by Cruden (2014). There are three reasons for its detailed inclusion here: firstly, for completeness in the description of the work undertaken in this thesis. Second, to highlight any differences in the specifics of the implementation (notably in the stitching of the Deuterium lamp images). Finally, the process is described fully in order to support the uncertainty analysis which follows in the second part of this appendix.

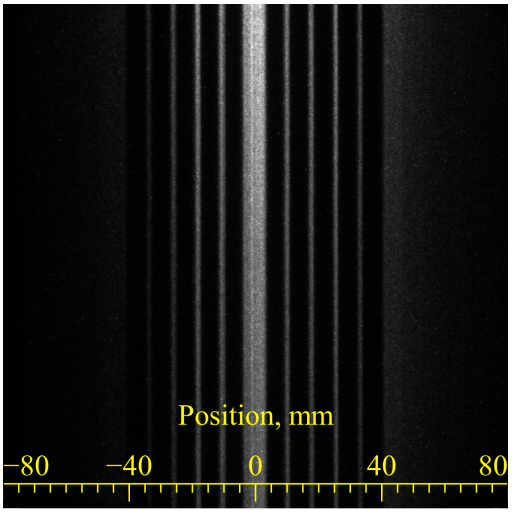
Spatial Calibration

Spatial calibration involves mapping one dimension of the camera sensor to physical positions along the axis of the tube. This ultimately allows spatial resolution of the measured shock layer. In addition, the spatial calibration procedure is useful during the alignment of the optics, specifically to help focus the optical systems on the centreline of the tube, ensure the imaged line is parallel to the tube axis and to determine the actual magnification and field-of-view of the installed system.

To achieve spatial calibration in the AST experiments a machined alignment bracket and plate were designed. The bracket locates on the surface of the window slot in the wall of the shock tube. This enables the alignment plate to be positioned exactly on the tube centreline. The plate consists of a series of holes and slots, which allow the optical system to be focused, the optical axis to be located spatially and the relation between pixel spacing and spatial distance (i.e. pixels mm^{-1}) to be determined. An LED light source is placed behind the plate to enable detection by the imaging system and visual identification of the image position and focus during alignment. A mask is placed on



(a) View of the T6 AST during spatial calibration. The calibration plate is visible on the tube centreline, where it is back-illuminated. Note that the window on the near side of the tube has been removed.



(b) Spatially calibrated image of the Alignment Plate for the Red channel. The spatial variation in intensity is due to the directional nature of the LED source.

Figure B.1 – Summary of the spatial calibration arrangement and resulting calibration image.

the far surface of the alignment plate to prevent excessive illumination of the central holes. An image of this arrangement is shown in Figure B.1a.

The spatial axis of the camera was determined by taking an image with the alignment plate installed. The locations of the eight circular holes in the plate were then identified and assigned a position based on their relative distance from the centre, which is known to an accuracy of ±0.1 mm based on the manufacturing tolerances. Using this method, the extent of the field-of-view was determined; these values are reported in Table 5.1. The use of a precision mounting plate allowed for highly repeatable positioning of the spatial calibration assembly. The Red and Blue OES systems are therefore referenced to the same datum, and hence there is direct correspondence between the axial locations in the data presented for both channels.

Wavelength Calibration

The mapping of horizontal camera pixels to wavelength is achieved by taking calibration images of a source with distinct spectral features. The associated wavelength of these features is then used to determine the wavelength at each pixel. The spectrographs used in

these experiments have interchangeable gratings which can be re-oriented depending on the wavelength region of interest. A wavelength calibration must therefore be performed for each grating and central wavelength setting.

For the wavelength calibrations in this work a Princeton Instruments IntelliCal® Hg/Ne–Ar lamp was used. For the IsoPlane, this can be mounted directly to the front of the spectrograph. In the case of the Blue system, the device was located in the optical path as close to the focal point as possible. It was not necessary to include the optical system in this component of the calibration as the wavelength calibration is not dependent on the measured intensity of the lines.

An interactive MATLAB routine was written which allows the user to manually locate the main calibration lines in each wavelength image. The corresponding wavelengths, based on the NIST-traceable calibration standard for the lamp, are then provided. Given the central wavelength of the image is approximately known this is typically straightforward. The result is a mapping of discrete pixel locations to wavelength values, between which linear interpolation is applied. This has the advantage of accounting for any non-linearity in the distribution of wavelength across the detector, although for the two imaging spectrometer arrangements used in this work this was not found to be present to any significant extent.

Instrument Function

In a spectrometer, the internal optical chain forms an image of the entrance slit on the exit focal plane. The signal measured by the camera is thus a convolution of the 'real' spectrum with this image, known as the instrument function. Characterisation of this shape is important for comparison with simulated spectra, as described in Section 5.3.3. In addition, the Stark broadening measurements presented in Section 6.5 require fitting of the experimental line shape to determine its Lorentzian width. The instrumental broadening must therefore be known as accurately as possible, so that its contribution can be accounted for. This must be characterised for each combination of slit width, grating and centre wavelength used.

In this thesis, the instrument function is characterised by fitting a curve to the wavelength calibration image. A single, high intensity line which is free from other features is selected. The source in the IntelliCal® is a low pressure arc discharge, and as such the physical causes of broadening in the emission (i.e. natural, Doppler and pressure broadening) are very small.[1] It is therefore assumed that their influence is negligible in the measured line shape, and that the resulting fit describes the instrument function alone.

For the emission measurements presented in this chapter, comparatively coarse gratings of 150 Grooves/mm were used to give a wide spectral bandpass. For the Red channel, the slit width was approximately 100 µm. It was found that the reading on the micrometer used for adjustment of slit width on the Blue spectrometer had an unknown offset; the exact value of the setting was thus not possible to determine. However, to somewhat offset the smaller solid angle of the optical system and the lower sensitivity of the camera, the slit was opened to a greater degree than on the Red channel. This is reflected in the greater broadening of the emission spectra from the Blue OES system presented in Chapter 5. This was not expected to significantly impact the the results, given that the majority of the features in the Blue are molecular bands, which overlap extensively.

The fitting of the line shape was accomplished using the Peakfit scripts of O'Haver (2021), an open-source toolset for fitting a range of peak shapes to overlapping or noisy experimental data. In choosing a suitable line shape, a key consideration was that it must also be implemented in NEQAIR to allow comparison with computed spectra. Based on the work of Cruden (2014), a linear Gaussian-Lorenztian blended shape was used for the Red channel. This was available as a default option in the Peakfit toolbox and so could be directly used. The equation for this line shape is given in Equation (B.1). An example of the resulting fit is shown in Figure B.2; this is typical of the line width found for all tests using this configuration. Although the fit is generally good, an asymmetric broadening feature is seen on the violet side of the line shape. This is a coma effect, as the IsoPlane is optimised for a single grating groove width (1200 Grooves/mm). The line shape could be

[1] These broadening mechanisms are discussed in more detail in Appendix C.

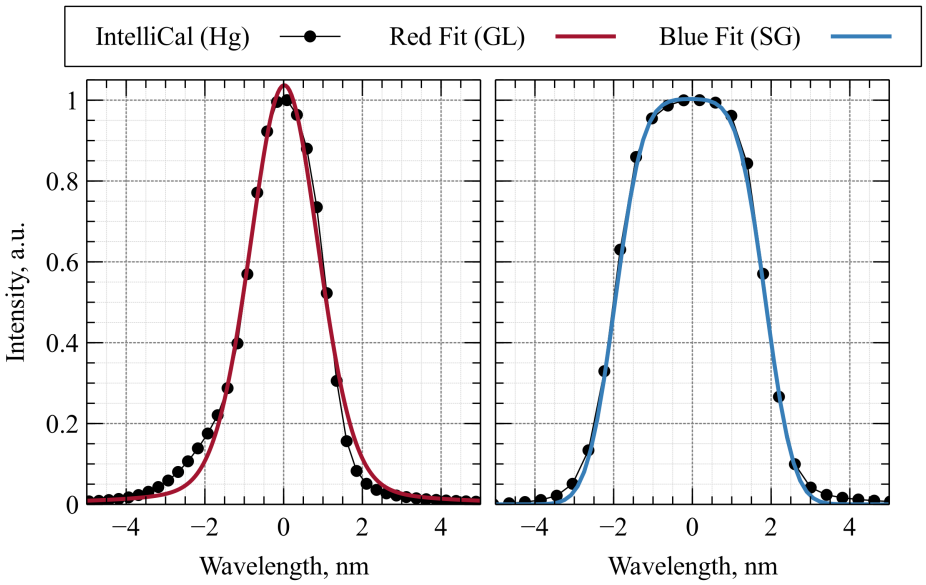


Figure B.2 – Comparison of measured and calculated line shapes for the AST OES systems. The markers represent the locations of individual pixels. The red data is fit with a Gaussian-Lorenztian blend of width 2.082 nm and $m_{GL} = 0.76$. The blue fit is a smeared Gaussian, with w_G = 1.361 nm and w_B =19.750 nm.

better modelled using an asymmetric function (e.g. a exponentially-broadened Gaussian) but this was not considered necessary for the current work.

$$ILS_{GL}(\lambda_0, w_G, m_{GL}) = m_{GL}\,\mathscr{G}(\lambda_0, w_G) + (1 - m_{GL})\,\mathscr{L}(\lambda_0, w_G) \tag{B.1}$$

For the blue channel, the large slit width resulted in a line shape with a flattened top. This is also the case for the infrared spectrometer channel at EAST, and so a smeared Gaussian (a convolution of a Gaussian curve with a rectangular (boxcar) window, which was found to describe the observed shape well) is implemented in NEQAIR. However, this was not available within the default Peakfit toolbox and so a modification to fit this line shape was added, as shown in Equation (B.2). The resulting fit of the Blue instrument function is shown in Figure B.2. This is again typical of all tests presented in this work.

$$ILS_{SG}(\lambda_0, w_G, w_B) = \mathscr{G}(\lambda_0, w_G) * \mathscr{B}(\lambda_0, w_B) \tag{B.2}$$

B.1.2 Absolute Intensity Calibration

The primary means of absolute spectral radiance calibration is a Bentham Instruments SRS8 quartz-tungsten-halogen integrating sphere (IS), with valid calibration above 300 nm. A second calibration standard is therefore required for the Blue OES system below this limit, which is achieved using a McPherson Model 632 deuterium lamp (referred to here as the D_2 source). As the IS calibration is common to both systems this is described first, after which the additional steps necessary for the D_2 lamp are included.

Integrating Sphere Calibration

A high-level summary of the calibration process is as follows: a full-field calibration of the camera is undertaken, the aim of which is to produce a 'calibration surface' (C), with units of 'counts per second per spectral radiance': counts $s^{-1}(W\,cm^{-2}\,sr^{-1}\,\mu m^{-1})^{-1}$. This can then be used to convert the 'counts per second' measured in the experiment to a value of absolute spectral radiance. By placing the calibration source in the imaging plane, all transmission losses in the optical chain and intensity variations (e.g. due to vignetting) across the field of view are taken into account.

The calculation required to generate this surface is given in Equation (B.3). This represents the main steps required to complete the calibration: a calibration image (S) is taken, erroneous signal due to pedestal effects (p) and background noise (B) is subtracted, and finally the remaining signal is divided by the known spectral radiance of the source (I) and the exposure time used for the calibration (t_{cal}) to arrive at the calibration surface for the optical system.

$$C(x,\lambda) = \frac{S_{cal}(x,\lambda) - p_{cal}(x,\lambda) - B_{cal}(x,\lambda)}{I_{source}(\lambda) \times t_{cal}} \tag{B.3}$$

The detailed steps required for the IS calibration are shown in Figure B.3. The following text describes these stages in detail. In these images, a similar convention to that used for the presentation of the 2D spectral data in Figure 5.2 is adopted. The majority of plots represent the 2D data on the intensified camera array. Cross-sections through this array are shown as functions of distance (a, b) and wavelength (i, ii, iii, iv). This discussion

assumes that a calibration relating the camera pixels to both wavelength and spatial location has first been completed; this has already been described fully in Appendix B.1.1.

In **Step 1**, an example of a single calibration image taken of the IS is shown. The IS has an outlet window diameter of 50 mm; the field-of-view is in excess of 150 mm. The integrating sphere thus fills only a portion of the observed spatial region. Several images of the IS must therefore be taken to calibrate the entirety of the camera sensor.

The raw recorded image is represented by the full-field, grey region (S_{cal}). This is a superposition of three contributing sources: the desired signal from the IS, the 'pedestal' due to scattered light from the broadband source, and a background due to thermal and read noise from the camera. The background is found by taking an image with the source powered off, but with equivalent exposure settings. This is directly subtracted from the measured image. The pedestal (visible as an augmentation in intensity above the background level, which increases near to the edges of the source) is removed using the method of Cruden (2014): first, the edges of the IS are identified. Away from the spatial location of the source, the intensity is subtracted to give zero counts. In the portion of the sensor actually covered by the IS image the values of the pedestal at either edge are linearly interpolated across the illuminated region and subtracted. This is performed for each wavelength to account for any spectral dependency. The result is shown here in red, where the background-subtracted IS image now ideally forms a boxcar-like function in spatial cross-section (a). The overall intensity is slightly reduced in comparison to the raw image; typically, the relative effect is largest at wavelengths with lower intensity. This process is then repeated for each calibration image.

Step 2 involves the combination of the individual IS images. As shown in the diagram, the IS images are taken with a significant amount of overlap — typically, approximately 10 are required to cover the whole field-of-view. These must be stitched together to give a continuous surface (still with units of counts). This is done by detecting the edge of the IS in each image to determine the centre of the source. An allowable extent either side of the centre is defined, which allows extraction of a 'core region' (free of edge-blurring effects). These core regions are then combined by averaging areas of overlap. This results in a continuous surface which accounts for any vignetting effects in the optical system.

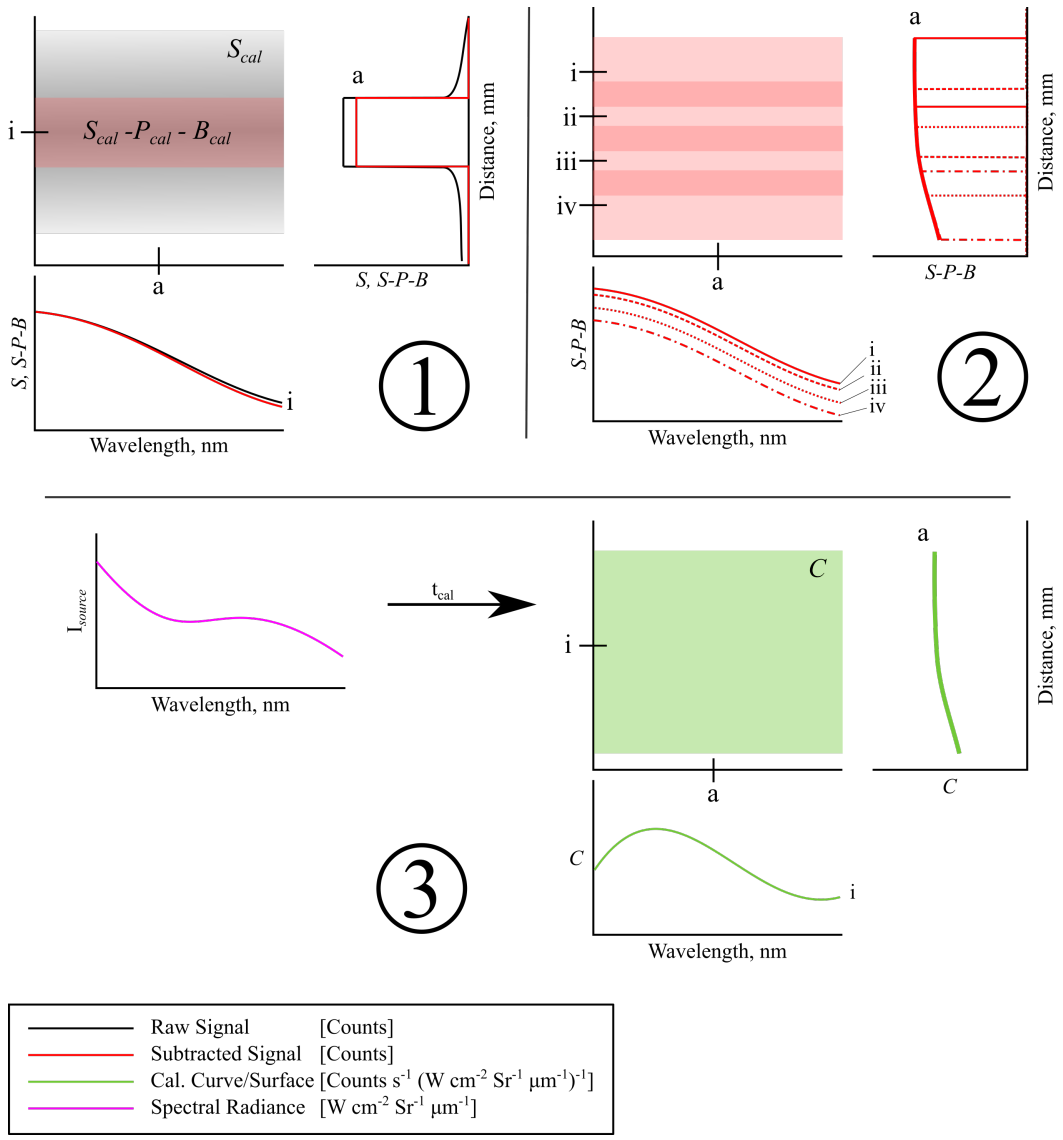


Figure B.3 – Diagram of OES system calibration process above 300 nm.

Finally, in **Step 3** the known spectral radiance of the IS (I_{source}) is used to generate the calibration surface. This is done by interpolating the manufacturer-provided values for the spectral radiance of the lamp as a function of wavelength. An element-wise division is then performed for each wavelength pixel, and this is repeated at every spatial location. The result is finally normalised by the exposure time to give the desired calibration surface, (C). This represents the transfer function of spectral radiance in the AST to camera counts, with units of counts $s^{-1}(W\,cm^{-2}\,sr^{-1}\,\mu m^{-1})^{-1}$.

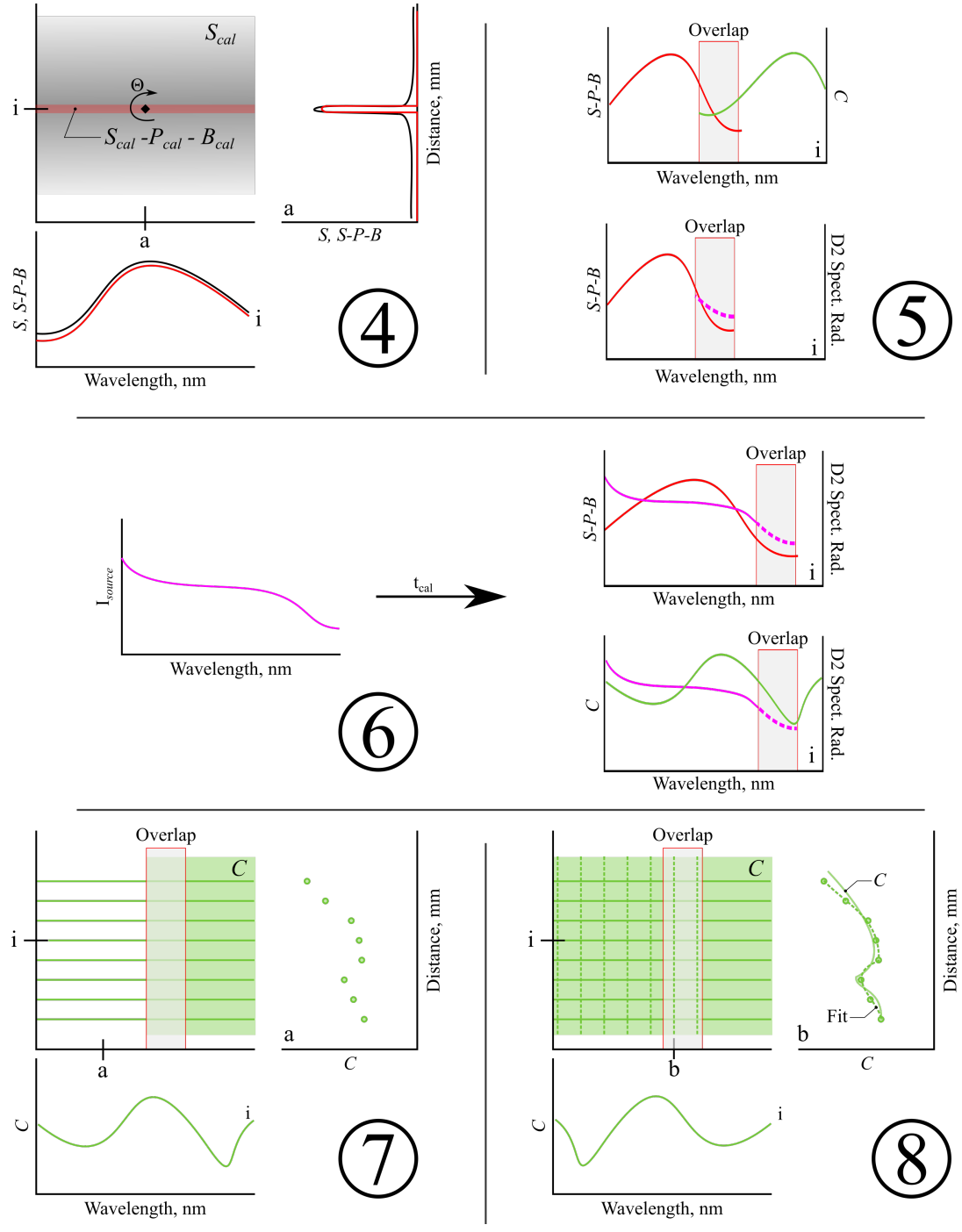


Figure B.4 – Diagram of additional steps required to calibrate the Blue OES system below 300 nm. The plot key is identical to that shown in Figure B.3

Deuterium Calibration

The additional steps required to generate the calibration surface for the D_2 lamp are shown in Figure B.4. At a glance, it can be seen that the process is significantly more involved

than that for the IS images. This complexity is driven by two key considerations: first, the lamp has an outlet diameter of approximately 1 mm and as such acts essentially as a point source. Whilst the lamp does have an absolute calibration, in practice its small spatial extent means that the image under-fills the spectrograph slit. The second complication is that the small spatial extent of the D_2 lamp makes capturing overlapping images across the whole field-of-view highly impractical. Instead, a means of stitching together images of the lamp at discrete spatial locations is required. The solutions to both of these issues are discussed in the subsequent paragraphs.

Step 4 shown in Figure B.4 is identical in principle to **Step 1** of Figure B.3, wherein the background and pedestal are subtracted from each of the D_2 lamp images. Typically a different exposure time is required for the D_2 and IS images; as such, a separate background is required. The only nuance of note is that the PIMAX-2 camera mounts to the Blue OES system spectrometer using a rotational attachment. There is thus a small angular offset between the camera sensor and the image plane. This is adjusted by calculating the difference in pixel location of the peak of the lamp at the extremes of the sensor for each image. An average value of angular offset is determined and then all images (including those from the IS) rotated accordingly. This is not required for the Red OES system due to a different mounting design.

In **Step 5**, a single lamp image (centred at cross-section i) is considered. It was previously stated that, due to under-filling of the spectrograph slit, the actual spectral radiance of the source is not known. This is corrected by effectively calibrating the lamp image using the calibration surface C, generated in **Step 3**. The IS has a valid calibration down to 300 nm; the D_2 lamp covers the range 116 nm to 410 nm. An overlap region is thus defined (here taken to be 350 nm to 400 nm) wherein both sources are concurrently within their calibration ranges, exhibit acceptable signal-to-noise, and any wavelength-dependent difference in optical transmission is expected to be small. The D_2 lamp image is thus calibrated across this small range, shown as the dashed magenta line in the diagram.

The same specific lamp image is still addressed in **Step 6**. The manufacturer again provides a known calibration curve for the lamp. Using the determined spectral radiance in the overlap region, this calibration curve is scaled by a constant factor to give the best

fit between the measured and nominal emission of the lamp in the overlap region. This is shown in the upper right diagram of **Step 6**, wherein the solid magenta calibration curve (from the D_2 source) lies on top of the (measured) dashed magenta signal in the overlap region. This scaled spectral radiance can then be used with the measured counts below the overlap wavelengths to calculate the calibration surface at this specific spatial location. This is shown in green in the lower right figure of **Step 6**.

The aforementioned process is repeated for each D_2 calibration image; the result is shown in **Step 7**. Here, at the longer wavelengths a full-field calibration surface from the output of the IS calibration is known. Each D_2 image has also provided a continuous calibration curve — at a single spatial location — across the desired wavelength range. These are shown as horizontal green lines. Note that these have been significantly thinned here for clarity; in reality approximately 20 spatial locations (corresponding to $\sim$10 mm intervals) are used. The final step required to generate the full calibration surface is to stitch together these discrete spatial points. Cross-section *a* gives an example of the shorter wavelengths before this process: here, a single wavelength is considered, which is calibrated at fixed points in space. These are then connected by fitting a fifth-order polynomial to the data, which was found to accurately capture the observed spatial variations across the sensor. It should be noted that this approach is different to that used by Cruden (2014), where the spatial variation of the intensity is first estimated from the IS calibration surface and then subtracted from the discrete D_2 lamp measurements.

The resulting stitched calibration surface (covering the whole wavelength region of interest) is shown in **Step 8**. Here, the vertical lines represent the values at all spatial points, interpolated from the polynomial fit. Note that this is done at each pixel, and as such these lines have an equivalent density to the green full-field calibration surface from the IS. In the overlap region, the goodness of the fit can be assessed by comparing the stitched D_2 images (at discrete spatial locations) to the full-field surface from the IS. This is shown in cross-section *b*, wherein both the fit and calibration surface curves are visible.

$$R(x,\lambda) = \frac{S_{exp}(x,\lambda) - p_{exp}(x,\lambda) - B_{exp}(x,\lambda)}{C(x,\lambda) \times t_{exp}} \tag{B.4}$$

Calibration of Shot Data

Using the final calibration surface, the measured counts can be calculated identically to **Step 1**. The process is given by Equation (B.4). In the same manner as the calibration images, the background signal and pedestal are subtracted. The signal (in counts) is then divided by the exposure time and the calibration surface to give a value for the absolute spectral radiance (in $\mathrm{W\,cm^{-2}\,sr^{-1}\,\mu m^{-1}}$) at each pixel.

B.2 Details of Uncertainty Analysis

In this section, the approach taken to perform the uncertainty analysis is outlined. The variables in considered in the calculation — and the bounds placed upon them — are then detailed.

B.2.1 Uncertainty Approach

The methodology used here to calculate the uncertainty is based on theory from the text of Coleman and Steele (2018) and the work of Moffat (1988). Following the approach of Doherty et al. (2015), a perturbation analysis of the calibration and shot data conversion scripts was performed. A summary only is given here: the MATLAB scripts used for post-processing constitute a function which take a series of input variables, represented by Equation (B.5a). The uncertainty in the output of these scripts can thus be calculated via the root-sum-square of the uncertainties of the inputs due to bias (or systematic) error and random (or precision) error as shown in Equation (B.5b). These uncertainties can be calculated by determining the sensitivity of the output to changes in each input variable, as shown in Equations (B.5c) and (B.5d). This is done by perturbing each variable individually by the maximum uncertainty and determining the difference of the output from the nominal.

The above process is repeated for all input variables, at both the maximum and minimum extents of the uncertainty bound. It is assumed that there is no covariance between these. In the case of asymmetric uncertainties, the sensitivities are weighted according to their distance from the nominal value; this results in maximum errors of $\mathcal{O}(3)$.

$$Y = f(X_1, X_2, \dots, X_N) \tag{B.5a}$$

$$\delta Y^2 = \sqrt{\sum_{i=1}^{N} \beta_i^2} + \sqrt{\sum_{i=1}^{N} \sigma_i^2} \tag{B.5b}$$

$$\beta_i = \frac{\partial Y}{\partial X_{i,\beta}} \delta X_{i,\beta} \tag{B.5c}$$

$$\sigma_i = \frac{\partial Y}{\partial X_{i,\sigma}} \delta X_{i,\sigma} \tag{B.5d}$$

It should be noted that the combined uncertainty given in Equation (B.5b) gives the value for uncertainty at each pixel. However, the quantities presented for spectral data in Chapters 5 and 6 are either averaged (in the case of equilibrium spectral radiance) or integrated (for radiance and the NEM calculations). Thus, the bias and random errors must be treated separately. Here, the bias errors are assumed to sum at each pixel (Coleman and Steele, 2018) and the random errors to combine as the root-sum-square. The total uncertainty for the calculated value is then combined as shown in Equation (B.5b).

B.2.2 Considered Uncertainties

Here, the variables considered in the uncertainty analysis are outlined and justifications made for their stated error bounds. Fundamentally, these relate to the variables in Equations (B.3) and (B.4). An uncertainty bound on the calibration surface is first determined; this is then propagated through the calculation of spectral radiance from the shot data.

A Note on Shot Noise

As will be seen, the main contributor to the random uncertainty at each pixel is the shot noise. The following interpretation is adapted from Dussault and Hoess (2004): the emission of photons is a discrete process, which is important over the short exposure times (i.e. less than 1 μs) used in the experiments presented here. As such, the arrival of photons at the camera can be described by a Poisson distribution, with a standard deviation equal to the square root of the number of photons which arrive at the detector. Typically this value is taken to represent the precision uncertainty in the optical signal, i.e. $\delta N_{ph} = \sqrt{N_{ph}}$.

It is important to note that this uncertainty bound does not represent the shot noise as measured on the camera in counts. Both the cameras used in this work are intensified; this means a variable-gain intensifier sits in front of the camera sensor to enhance the low numbers of incident photons (due to the short exposure time) up to measurable levels. In short, this works using the following process (e.g. Oxford Instruments Andor, 2021): on the object side of the sensor, a photocathode converts incoming photons into photoelectrons. These then enter the microchannel plate (MCP) which consists of a thin glass disc perforated with holes of approximately 5 µm. A significant potential difference ($\geq$200 V) can be set across this plate. If a photoelectron has sufficient energy, it dislodges additional electrons when it contacts the walls of these channels, which in turn generate further electrons in a cascade effect. These generated electrons then finally arrive at a phosphor film, where they are converted into light which can be detected by the camera sensor.

The arrival of a photon at the camera will produce a photoelectron with some quantum efficiency; this photoelectron may (not) cause an electron cascade within the MCP. The shot noise in counts is thus a composite Poisson process (Liu et al., 2006). For a given number of photons arriving at the detector, the counts can be calculated using expression of Equation (B.6a). This calculation effectively represents the conversion rate of incident photons to camera counts, considering the efficiency of the photocathode, the gain factor with which the MCP generates additional electrons and the sensitivity of the sensor's conversion of said electrons to counts.

Considering the shot noise due to photons arriving at the detector, the resulting counts can be written as shown in Equation (B.6b). Here, F is an additional noise factor which is introduced to account for the non-ideal operation of the intensifier (i.e. that a photoelectron can produce differing degrees of electron cascade in the MCP). Typically, this has a value between 1.3 and 2 and reduces at higher gain levels (Liu et al., 2006; Dussault and Hoess, 2004). In this work, it is conservatively taken to be equal to 2. This expression can be rewritten in terms of the measured counts as shown in Equation (B.6c). This form removes any dependency on the quantum efficiency, which is not known precisely for either camera. This approach also has the advantage of greatly simplifying the analysis, as said efficiency

is wavelength-dependent. This expression also shows that the actual shot noise is greater than the square root of the counts by a factor of $\sqrt{GE^{-1}}F$. The GE^{-1} product is known: this was calculated from the calibration sheet provided with the Andor Intensified sCMOS camera and taken directly from the manual for the Princeton Instruments PIMAX-2. These were found to have values of 1870 and 80 counts per photoelectron respectively.

$$N_c = \eta N_{ph} G E^{-1} \tag{B.6a}$$

$$\delta N_c = \sqrt{\eta N_{ph}} G E^{-1} F \tag{B.6b}$$

$$\delta N_c = \sqrt{N_c}\sqrt{G E^{-1}} F \tag{B.6c}$$

Uncertainty Bounds

As described in Appendix B.1, there are up to three connected processes in the conversion of the measured shot data into an absolute spectral radiance. These are: the calculation of a full-field calibration surface with the IS, the additional generation of a stitched calibration surface for the D_2 lamp, and finally the use of this calibration to process the shot data. The overarching equations required for this method are given in Equations (B.3) and (B.4). Here, bounds are set on these variables as given in Table B.1.

The justification for these bounds goes as follows: the shot noise has already been discussed, but two technicalities are noted. First, this should be calculated after the background subtraction, as this does not originate from the Poisson nature of the incident light. Secondly, the calibration images are averaged over either 100 or 5 images for the Red and Blue OES systems respectively[2]; this must be accounted for when determining the shot noise. For the background, uncertainty is calculated from the standard deviation of the background image in a region of the sensor which is not covered by the intensifier.

The remaining three terms are bias errors, as they provide a constant offset which will not be improved by averaging of the spectra. The stated error in the manufacturer's calibration of the IS and a tolerance on the wavelength calibration are conceptually straight-forward. The pedestal correction has a bound of 25 % applied; this is to account

[2]The difference in accumulation number is due to differing readout rates of the two cameras.

Table B.1 – Summary of the sources and magnitudes of the uncertainties considered in this analysis.

Step	Param.	Uncertainty	Type
IS Calibration	S_{cal}	Shot noise, Equation (B.6c)	Precision
	B_{cal}	$\pm 2\sigma$	Precision
	P_{cal}	±25 %	Bias
	I_{IS}	∼5 %, $f(\lambda)$	Bias
	λ	±4 px	Bias
D_2 Calibration	Θ	$\pm 2\sigma$	Bias
	I_{D2}	7 % (Constant over 172 nm–410 nm)	Bias
	f_{wl}	$\pm 2\sigma$	Precision
	C	Determined from previous step	Bias
	f_x	$\pm 2\sigma$	Precision
Shot Analysis	S_{exp}	Shot noise, Equation (B.6c)	Precision
	B_{exp}	$\pm 2\sigma$	Precision
	P_{exp}	25 %, −100 %	Bias
	C	Determined from previous step	Bias

for unknowns in the subtraction across the IS region, which may not be adequately captured using a linear interpolation.

With the exception of the I_{D2} term (which is again a manufacturer-stated tolerance on the lamp calibration) the D_2 calibration uncertainties are mostly related to the multiple fitting steps required. As discussed in Appendix B.1.2, the rotation correction for the camera is found by averaging the calculated angular offset for each of the images. A two-sigma (95 %) confidence interval is thus placed on this mean value, which forms a bias in the calibration. An identical bound is placed on both the fit of the D_2 calibration curve to the measured data (f_{wl}) and on the spatial fit between each D_2 lamp calibration curve (f_x). It is assumed these are distorted by random error which will tend to the mean when considering average or integrated spectra. Finally, the IS calibration surface is required to initially scale the D_2 signal; this is assumed to act as a 'fossilised' (in the terminology of Moffat, 1988) uncertainty and hence is treated as a bias error.

The shot calibration uncertainties are mostly identical to the previous steps. The only exception is the pedestal for the shot, which has a lower limit set of −100 %. This is done as some conditions can exhibit precursor radiation, which makes identification of

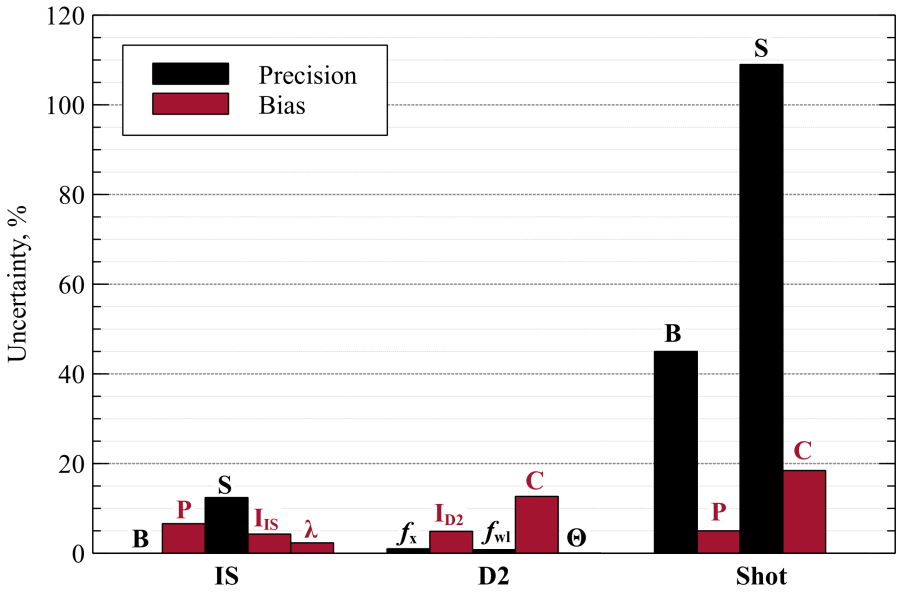


Figure B.5 – Error budget for the different stages of the calibration and shot data conversion processes, with test T6s186 used as an example. The stated uncertainties are the individual contributions from each source; these are evaluated at each pixel and then averaged at the middle of the sensor to give an estimate of their comparative magnitudes.

the correct pedestal magnitude challenging. This bound therefore covers the eventuality that all of the observed radiance ahead of the shock front is part of the real signal. In either case, the impact is comparatively small. The calibration surface is again treated as a bias uncertainty.

B.3 Estimated Uncertainties

In this section, uncertainty results are presented for the three test conditions developed in Chapter 4 and analysed in Chapter 5. These represent the total error bound on the measurement. Figure B.5 first compares the relative magnitude of each source of uncertainty. The stated values are the relative size of the uncertainty bound for an illustrative example; here, the Blue OES system calibration for T6s186 is used. The presented values are calculated at each pixel and then averaged over the middle of the sensor. This representation allows comparison of the relative contribution from each of the sources and could assist in future optimisation of the experimental arrangement.

For the calibration, the largest contributors to the uncertainty are typically the

calibration sources and the shot noise. A positive conclusion of this analysis is that the multiple fitting processes required for the additional D_2 steps (i.e. the values for Θ, f_x and f_{wl}) do not significantly contribute to the uncertainty. This builds confidence in the robustness of the post-processing methods applied in this work.

In terms of the shot data, the overall uncertainty on each pixel is high. This is dominated by the shot noise and, to a lesser extent, the background. These are both relatively larger than their equivalents in the calibration images. The primary cause of this is that the calibration images are averaged over a large number of accumulations (100 for the Red OES system and 5 for the Blue). This tends to reduce the precision errors of the images. The total number of accumulations must therefore be considered when determining these noise magnitudes for the calibration images. A secondary cause of the observed differences is that the absolute number of counts is typically smaller in the test; the background is therefore a larger component of the signal and the shot noise is comparatively greater. Although when viewed in the context of a single pixel these errors seem large, in practice many pixels are averaged to perform comparisons of the spectral data. As can be observed in Figure B.6, this tends to shift the absolute uncertainty towards the bias values.

The procedure discussed in Appendix B.2 is here applied to three tests, covering the conditions which are the focus of Chapter 5. The three key parameters used in this work (equilibrium spectral radiance, the spectral NEM and integrated radiance) are presented here. Figures B.6 and B.7 show the spatially and spectrally resolved errors for each metric, for shots T6s159, T6s160 and T6s166. Results from both channels are shown. In terms of the radiance results of Figure B.6, the overall uncertainties typically align well. This is due to the large number of pixels included in the integration, which tends to reduce precision error. Based on this result, a rule-of-thumb value of 25 % can be defined for the total integrated radiance using this optical arrangement. This is of potential use during future test campaigns, where methods for rapid assessment of shot quality are valuable.

Figure B.7 shows the spectrally-resolved uncertainty for the three conditions. These values can be considered generally representative of all tests. In general, it can be observed that the level of uncertainty is reasonable in the context of high-enthalpy

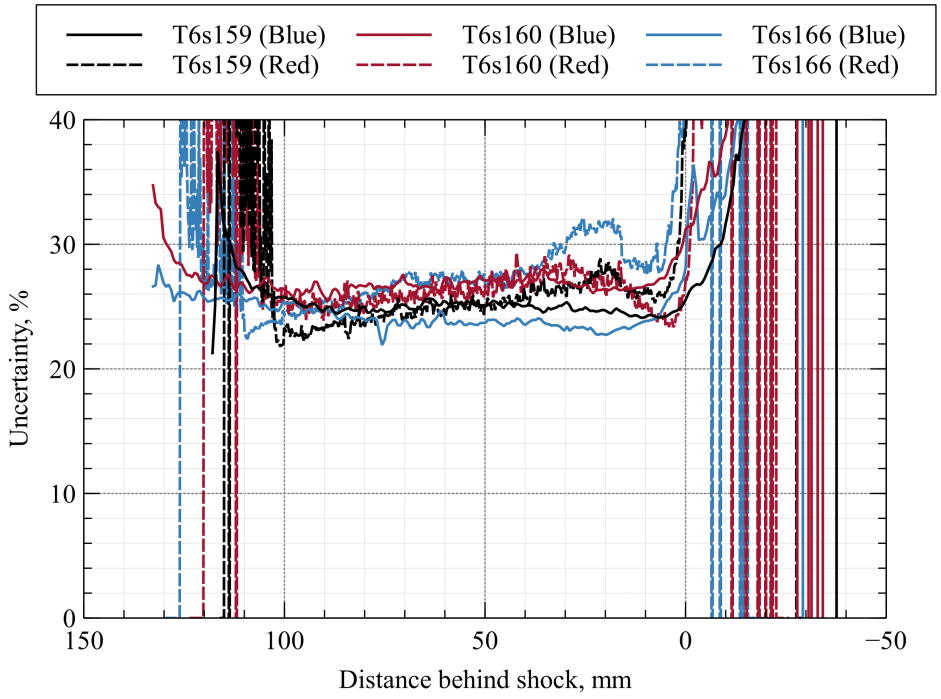
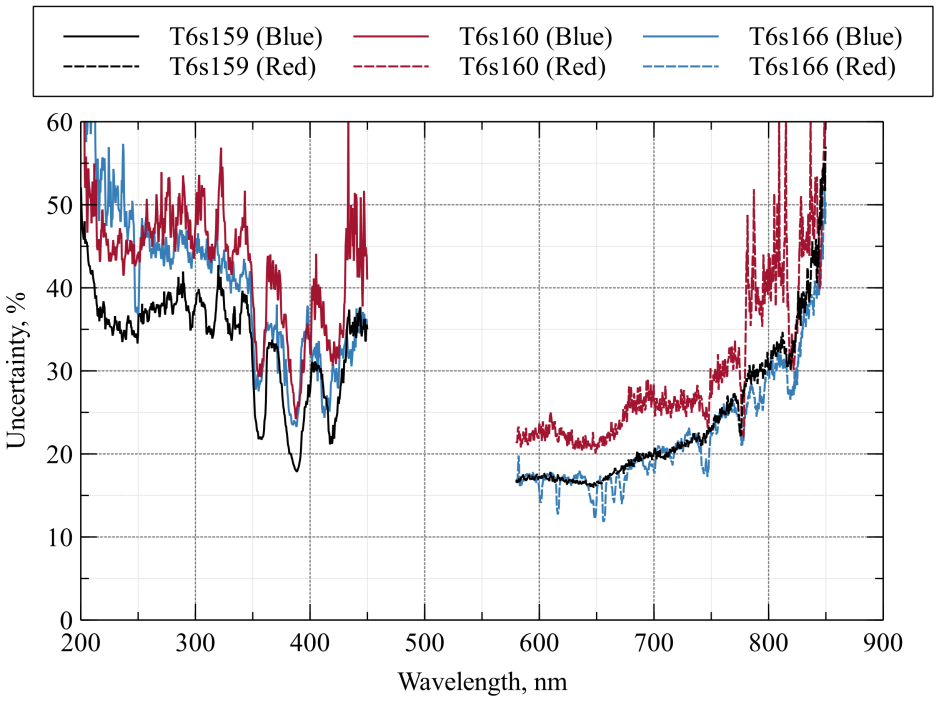


Figure B.6 – Representative overall uncertainty in post-shock radiance. The blue data is averaged from 200 nm to 450 nm; the Red is from 600 nm to 825 nm. The noise at either edge of the image represents the end of the shock-layer in the measurement — not the extent of the field-of-view.

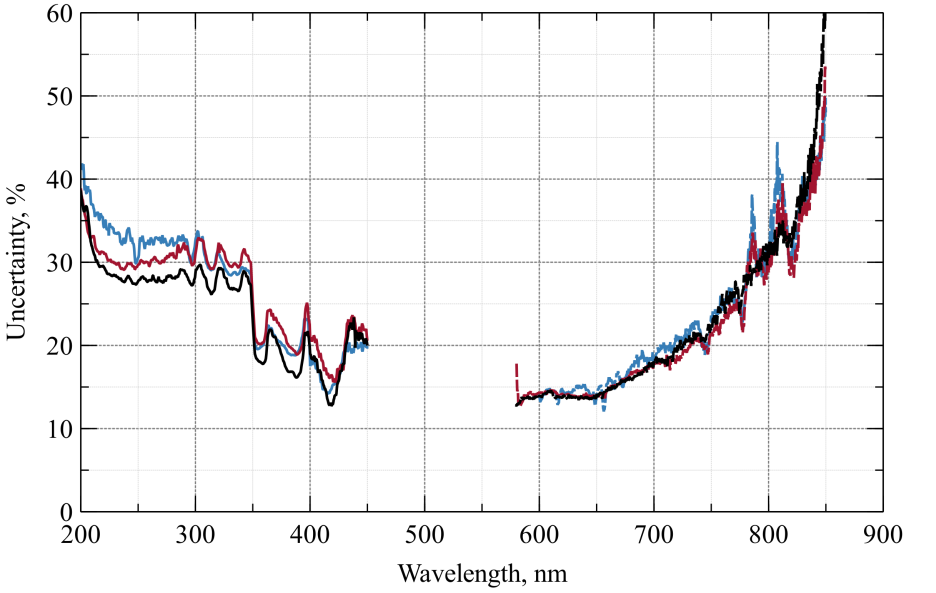
plasma diagnostics. In the case of the Red data, uncertainties as low as 15 % are estimated for some parts of the spectrum. Notably, where there is high intensity, or large integration limits, the overall uncertainties are significantly reduced. This is particularly apparent for the molecular bands in the UV data and for the atomic features visible in the NIR for T6s166. Overall, confidence in the NEM results is higher than the equilibrium radiance for the cases presented here. This is due not only to a higher intensity in this region, but is also due to the 40 mm integration distance used, *c.f.* 10 mm for the equilibrium spectra. This highlights another important advantage of achieving a large amount of post-shock equilibrium (as is the case for all presented cases in the T6 AST): precision uncertainty can be significantly reduced, leading to increased confidence in the emission data.

B.4 Summary

This appendix provided enhanced details of the methodologies which underpin the emission spectroscopy measurements used in this work. An in-depth overview of the



(a) Equilibrium spectral radiance, averaging a 10 mm spatial extent.



(b) Spectral non-equilibrium metric.

Figure B.7 – Comparison of uncertainty as a function of wavelength for three shots at the conditions discussed in Chapter 5.

calibration and post-processing procedure was first provided, to compliment the discussion in the main text. This was largely based on the approach taken by Cruden (2014); specifics of the implementation particular to this work were specifically identified.

A perturbation-based uncertainty analysis was then formulated. Based on the description in the preceding section, key variables for this assessment were identified. Error bounds were then estimated for these parameters. Using a MATLAB-based function to wrap around the existing calibration scripts, said variables were perturbed; the sensitivity of the calibration surface and processed shot data at each pixel could thus be established.

Finally, examples of this approach were shown for shots representative of the core conditions studied in this work. An uncertainty budget was presented, which was seen to aid identification of the largest contributing factors in the overall experimental error. Crucially, the sensitivity to the fitting processes used in the calibration scripts was determined to be low. Uncertainties presented for measurements of equilibrium spectral radiance, integrated radiance and the spectral non-equilibrium metric were shown to have good consistency, and to be of a reasonable magnitude given the nature of these experiments.

C

Stark Broadening Approach

Contents

C.1 Line Broadening Considerations 245
C.2 Stark Broadening: Uncertainty Quantification 249

The purpose of this appendix is to describe the methodology used for the Stark broadening measurements of Chapter 6. A brief description of the theory of line broadening is first given, after which the method used to determine the Stark width from the experimental spectra is discussed. The means by which the uncertainty for this measurement is calculated is also outlined.

C.1 Line Broadening Considerations

Electronic transitions occur between discrete energy levels, and thus ideally a spectral line would be observed at a single wavelength. This is reflected in Equation (5.4), which shows that an atomic transition has an associated nominal wavelength, λ_0. In practice, physical processes in the plasma, and inherent properties of the measurement method, cause the transition energy to be distributed over a range of wavelengths. This is known as 'line broadening'.

As will be discussed, the degree of Stark broadening can be used to infer the electron density of the plasma. However, the observed line shape will be the convolution of several broadening mechanisms. Before the Stark width can be extracted, these other sources of broadening must be accounted for in order to remove bias from the measurement. The largest contributor to the measured broadening is due to the instrument function (as discussed in Appendix B), but all mechanisms are considered here for completeness. The theory in this discussion is largely based on the text of Griem (2005); the analysis methodology used follows the work of Cruden (2012b).

Natural Natural broadening occurs due to the uncertainty principle. Each excited state has a mean lifetime after which it is expected to spontaneously decay, emitting a photon and falling to a lower energy. However, there is an uncertainty in the duration of this lifetime and so, through Heisenberg's Uncertainty Principle, in the exact energy of the transition. The broadening can be calculated by considering the lifetimes of the upper and lower states of the transition. For H-α, this is between principle quantum numbers $\mathscr{N} = 3 \rightarrow 2$. Following Takama and Suzuki (2009), the natural width can be calculated using Equation (C.1) by considering the allowed transitions of both the upper and lower states to all levels below their own. Here, the expression is presented as a function of the Einstein coefficients, which can be found from tabulated data e.g. Wiese et al. (1966). Using the corresponding values for hydrogen, the natural line width for the H-α transition is found to be 1.3×10^{-4} nm and is thus entirely negligible for the current analysis.

$$\Delta\lambda_N = \frac{\lambda_0^2}{2\pi c}\left(\sum_{\mathscr{N}=1}^{2} A_{3\mathscr{N}} + A_{21}\right) \tag{C.1}$$

Doppler During a radiative transition, the emitting particle is not stationary relative to the observer, due to thermal motion. This movement results in the emitted photon being either red- or blue-shifted depending on the instantaneous magnitude and direction of the particle's velocity. This results in a Gaussian broadening of the line shape, which can be calculated using Equation (C.2). The relative magnitude of this broadening mechanism for the current experiments is discussed further at the end of this section.

$$\Delta\lambda_D = \lambda_0 \sqrt{\frac{8\mathscr{R}T\ln(2)}{c^2}} \tag{C.2}$$

Pressure Broadening Pressure broadening occurs due to interactions of the radiator with nearby particles in the gas. The character of this broadening depends on whether the second particle is of the same ('resonance' broadening) or different ('van der Waals' broadening) species. The underlying physics of these processes is complex and so a full explanation is not attempted here; the reader is again directed to the texts of Thorne et al. (1999) and Griem (2005). In practice, the contributions can be calculated using semi-empirical correlations such as that of Laux (1993). Alternatively, Cruden (2012b) provides an expression which is employed in the NEQAIR code which is shown in Equation (C.3). Here, the first term represents the resonance broadening and the second that due to van der Waals mechanisms.

$$\Delta\lambda_{P,i} = \left(1.33\times10^{-30}\sqrt{\frac{2}{M_i}}n_i + 5.85\times10^{-31}\sqrt{\frac{2}{M_{avg}}}\left(n_{tot}-n_i-n_e\right)\right)\sqrt{T}\ \lambda_0^2 \tag{C.3}$$

Stark Broadening In a plasma, the locally non-homogenous distribution of ions and free electrons leads to a spatially-varying electric field. This field perturbs the usual electrostatic potential between the nucleus and bound electrons, causing an asymmetric energy difference in the direction of the external field. For hydrogen, the broadening due to this effect is symmetric and Lorentzian in shape. The width of this curve is directly related to the electron density. For the H-α line, Cruden (2012b) gives an approximate formula, shown in Equation (C.4), based on the tabulated data of Gigosos and Cardeñoso (1996) for the electron density (in cm^{-3}) as a function of this Lorentzian width.

$$n_e = 9.87\times10^{16}\ w_{L,\alpha}^{1.65} \tag{C.4}$$

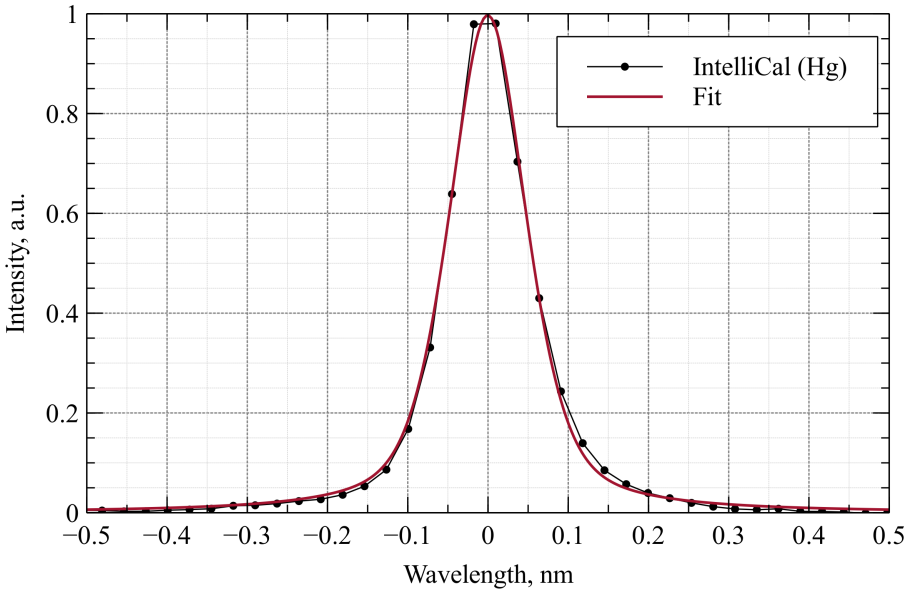


Figure C.1 – An example of the measured and modelled instrument function for the 1200 Grooves/mm grating used for the presented Stark broadening measurements. In this case, the resulting fit had a FWHM of 0.1146 nm with 51.46 % Gaussian character. The RMS fit error for this case was 0.87 %.

Instrumental Broadening The broadening mechanisms discussed up to this point have occurred due to physical processes in the plasma. However, the instrumental broadening also contributes to the measured line shape and this contribution must be accounted for to extract an accurate measure of the Stark width. To characterise the instrument function for these tests the approach used was identical to that discussed in Appendix B.1.1. The high-resolution grating line shape was found to be fit very well by the linear Gaussian-Lorentzian function of Equation (B.1). The resultant fit is shown in Figure C.1, where the full width at half maximum (FWHM) was found to be 1.15 Å with RMS error of 0.87 %. This quality of fit is representative of all high-resolution instrument functions used for the measurements of Chapter 6.

In the work of Cruden (2012b), the relative contributions of the Doppler and pressure broadening were assessed for a range of conditions, which were inclusive of the cases considered in this work. It was found that, for the H-α line, the Doppler broadening contribution to the line shape was less than 5 % for electron densities above 4×10^{14} cm^{-3}. This is generally much lower than any of the conditions analysed here. The pressure

broadening was found to have a 5 % effect at shock speeds less than 9 km s^{-1} at at free-stream pressure of 133 Pa. All cases considered in this work are above this velocity and significantly below this pressure, and so it is expected that the effect of pressure broadening will be also negligible.

C.1.1 Lorentzian Fitting Procedure

To determine the Stark width of the measured H-α line, the peakfit toolbox (O'Haver, 2021) was modified to fit the measured spectral data using the convolution of the ILS and a Lorentzian function. This approach avoids the excessive noise generated by deconvolving the spectrum using the instrument function. Given that the ILS is invariant and the parameters known from the measurement of the line shape, (discussed in Appendix C.1) the only free variable in this fit is the Lorentzian width; this is assumed to be entirely due to the Stark effect. The determined FWHM is then used to calculate the electron number density using Equation (C.4).

To extract the variation in electron density through the shock-layer the data is first smoothed spatially to reduce noise. For the validation tests of Figure 6.9, a 37 pixel[1] averaging window was used corresponding to approximately 5 mm intervals. For the lower speed tests, it was found that more averaging was needed to produce a smooth signal; in Figure 6.10 all traces have been smoothed by the same amount for consistency: 67 px, or 10 mm. The electron density and uncertainties are calculated and presented at 5 mm intervals; the values are found to be consistent between spatial locations and thus can be said to also represent the uncertainty in the intermediate positions.

C.2 Stark Broadening: Uncertainty Quantification

There are three main sources of error in the Stark measurement: the contribution of other broadening mechanisms to the measured Lorentzian width, the error in the fit of the line shape and the uncertainty in the data reduction equation used to calculate the electron density. Based upon the discussion of Appendix C.1, it is assumed that the

[1]Note again that 2×2 binning is used for the sCMOS camera, and so this refers to the effective super-pixels.

influence of natural, Doppler and pressure broadening mechanisms are negligible. In addition, the main effect of these mechanisms would be to introduce a bias error in the measurement, which would not greatly change the conclusions drawn regarding differing spatial trends in the shock-layer due to deceleration.

The fitting error is estimated using a resampling residuals 'bootstrapping' approach. In summary, the line shape is first fit using the method outlined in Appendix C.1. The residual errors between this fit and the original data are then calculated; these are treated as an estimator of the noise. Each data point of the determined line shape is then perturbed by a randomly sampled residual value, creating a synthetic response variable which is distorted by noise of a magnitude representative of the real data. This artificial curve is then fit using the original method. This process is repeated for 500 iterations, resulting in a statistically significant distribution of fit Lorentzian widths. This allows the sample mean and standard error to be calculated. Here, the fitting error used corresponds to a 95 % confidence interval of this distribution.

Finally, the components of the error in Equation (C.4) are stated by Cruden (2012b) to be 6 % due to the fitting of tabulated data, 4 % due to the assumption of a reduced ion mass of 1.0 and 3 % from the simulations used to generate the original data by Gigosos and Cardeñoso (1996). It is assumed that these are independent; the root-sum-square error in the Stark broadening equation is thus estimated to be 8 %. This is applied to the limits of the confidence interval determined from the line shape fit to give a final maximum and minimum bound on the calculated electron density.

References

ALLEN, M. G. and KESSLER, W. J. (1996). "Simultaneous water vapor concentration and temperature measurements using 1.31-micron diode lasers". *AIAA journal* 34.3, pages 483–488.

ANDERSON JR., J. D. (1989). *Hypersonic and High Temperature Gas Dynamics*. McGraw-Hill Series in Aeronautical and Aerospace Engineering. McGraw-Hill. ISBN: 0-07-001671-2.

ANDRIANATOS, A., GILDFIND, D., and MORGAN, R. (2016). "Preliminary Development of High Enthalpy Conditions for the X3 Expansion Tube". In: *20th Australasian Fluid Mechanics Conference*.

ANDRIANATOS, A., GILDFIND, D., and MORGAN, R. (2015). "A study of radiation scaling of high enthalpy flows in expansion tubes". In: *7th Asia Pacific International Symposium on Aerospace Technology*.

— (2019). "Testing a full-scale Hayabusa model in a large expansion tube". In: *APISAT 2019: Asia Pacific International Symposium on Aerospace Technology*. Engineers Australia, page 43.

BAKOS, R. and ERDOS, J. (1995). "Options for enhancement of the performance of shock-expansion tubes and tunnels". In: *33rd Aerospace Sciences Meeting and Exhibit*.

BAKOS, R. J. and MORGAN, R. G. (1994). "Chemical recombination in an expansion tube". *AIAA journal* 32.6, pages 1316–1319.

BANERJI, N., LEYLAND, P., FAHY, E., and MORGAN, R. (2018). "Venus Entry Flow over a Decomposing Aeroshell in X2 Expansion Tube". *Journal of Thermophysics and Heat Transfer* 32.2, pages 292–302.

BARNHARDT, M. D., BRANDIS, A. M., WRIGHT, M. J., and HUGHES, M. F. (2019). *Recent advancements in modeling and simulation of entry systems at NASA*. Technical report. NASA.

BECK, W. H. and MACKIE, J. C. (1978). "Application of the shock tube unsteady expansion wave technique to the study of chemical reactions". *Journal of Physics D: Applied Physics* 11.9, page 1249.

BENSASSI, K. and BRANDIS, A. M. (2019). "Time accurate simulation of nonequilibrium flow inside the NASA Ames Electric Arc Shock Tube". In: *AIAA Scitech 2019 Forum*, page 0798.

BERGER, E. (2020). *Thanks to SpaceX, NASA regains a capability it lost for a decade*. URL: `https://arstechnica.com/science/2020/11/nasas-big-bet-on-spacex-and-commercial-space-pays-off/` (visited on May 17, 2021).

BOGDANOFF, D. W. and CRUDEN, B. A. (2016). *Optimizing Facility Configurations and Operating Conditions for Improved Performance in the NASA Ames EAST 24 Inch Shock Tube*. Technical report. NASA.

BOSE, D., MCCORKLE, E., BOGDANOFF, D., and ALLEN, G. (2009). "Comparisons of air radiation model with shock tube measurements". In: *47th AIAA Aerospace Sciences Meeting Including The New Horizons Forum and Aerospace Exposition*, page 1030.

BOYD, I. D. and JENNISKENS, P. M. (2010). "Modeling of stardust entry at high altitude, part 2: Radiation analysis". *Journal of Spacecraft and Rockets* 47.6, pages 901–909.

BOYER, A. G. (1965). *Design, Instrumentation and Performance of the UTIAS 4-in. x 7-in. Hypersonic Shock Tube*. Technical Report 99. Institute for Aerospace Studies, University of Toronto.

BRANDIS, A. M., MORGAN, R. G., LAUX, C. O., MAGIN, T., MCINTYRE, T., and JACOBS, P. A. (2007). "Nonequilibrium radiation measurements and modelling relevant to Titan entry". In: *Proceedings of the 16th Australasian Fluid Mechanics Conference, 16AFMC*. Volume 1. School of Engineering, The University of Queensland, pages 594–601.

BRANDIS, A. (2012). "Validation of shock layer radiation: perspectives for test cases". *ESA Special Publication* 714, page 24.

— (2018). "Overview of recent EAST testing, modeling & analysis". In: *12th International Workshop on Shock Tube Technology*.

BRANDIS, A., CRUDEN, B., and JOHNSTON, C. (2019). "Shock Tube Measurements of Radiative Heating for Titan and Nitrogen". In: *8th International Workshop on Radiation of High Temperature Gases*.

BRANDIS, A., CRUDEN, B., PRABHU, D., BOSE, D., MCGILVRAY, M., and MORGAN, R. (2010a). "Analysis of air radiation measurements obtained in the EAST and X2 shocktube facilities". In: *10th AIAA/ASME Joint Thermophysics and Heat Transfer Conference*.

BRANDIS, A., JOHNSTON, C., PANESI, M., CRUDEN, B., PRABHU, D., and BOSE, D. (2013). "Investigation of nonequilibrium radiation for Mars entry", page 1055.

BRANDIS, A. M., SAUNDERS, D., JOHNSTON, C., CRUDEN, B., and WHITE, T. (2020). "Radiative heating on the after-body of Martian entry vehicles". *Journal of Thermophysics and Heat Transfer* 34.1, pages 66–77.

BRANDIS, A. M. and CRUDEN, B. A. (2017a). "Benchmark Shock Tube Experiments of Radiative Heating Relevant to Earth Re-entry". In: *55th AIAA Aerospace Sciences Meeting*.

— (2017b). "Titan Atmospheric Entry Radiative Heating". In: *47th AIAA Thermophysics Conference*.

— (2018). "Shock tube radiation measurements in nitrogen". In: *2018 Joint Thermophysics and Heat Transfer Conference*, page 3437.

— (2019). *NEQAIR v15.0 release notes: Nonequilibrium and equilibrium radiative transport and spectra program*. Technical report. NASA Ames Research Center.

BRANDIS, A. M. and JOHNSTON, C. O. (2014). "Characterization of stagnation-point heat flux for Earth entry". In: *45th AIAA Plasmadynamics and Lasers Conference*.

BRANDIS, A. M., JOHNSTON, C. O., and CRUDEN, B. A. (2016). "Non-equilibrium radiation for Earth entry". In: *46th AIAA Thermophysics Conference*, page 3690.

BRANDIS, A. M., LAUX, C. O., MAGIN, T., MCINTYRE, T. J., and MORGAN, R. G. (2014). "Comparison of Titan Entry Radiation Shock-Tube Data with Collisional-Radiative Models". *Journal of Thermophysics and Heat Transfer* 28.1, pages 32–38.

BRANDIS, A. M., MORGAN, R. G., MCINTYRE, T. J., and JACOBS, P. A. (2010b). "Nonequilibrium radiation intensity measurements in simulated Titan atmospheres". *Journal of Thermophysics and Heat Transfer* 24.2, pages 291–300.

BRANDIS, A., JOHNSTON, C., CRUDEN, B., PRABHU, D., and BOSE, D. (2015). "Uncertainty analysis and validation of radiation measurements for Earth reentry". *Journal of Thermophysics and Heat Transfer* 29.2, pages 209–221.

BRANDIS, A., JOHNSTON, C., CRUDEN, B., and PRABHU, D. (2017). "Equilibrium radiative heating from 9.5 to 15.5 km/s for earth atmospheric entry". *Journal of Thermophysics and Heat Transfer* 31.1, pages 178–192.

BUGEL, M., REYNIER, P., and SMITH, A. (2011). "Survey of European and major ISC facilities for supporting Mars and sample return mission aerothermodynamics and tests required for thermal protection system and dynamic stability". *International Journal of Aerospace Engineering* 2011.

BUTTSWORTH, D., MORGAN, R., and JENNISKENS, P. (2013). "Near-ultraviolet emission spectroscopy of the Hayabusa reentry". *Journal of Spacecraft and Rockets* 50.6, pages 1109–1120.

CAPRA, B. R. (2006). "Aerothermodynamic Simulation of Subscale Models of the FIRE IIand Titan Explorer Vehicles in Expansion Tubes". PhD thesis. University of Queensland.

CAPRA, B. R. (2007). "Aerothermodynamic simulation of subscale models of the FIRE II and Titan Explorer vehicles in expansion tubes." PhD thesis. University of Queensland.

CHAN, W. Y., JACOBS, P. A., SMART, M. K., GRIEVE, S., CRADDOCK, C. S., and DOHERTY, L. J. (2018). "Aerodynamic design of nozzles with uniform outflow for hypervelocity ground-test facilities". *Journal of Propulsion and Power* 34.6, pages 1467–1478.

CHANDEL, D., NOMPELIS, I., CANDLER, G. V., and BRANDIS, A. M. (2019). "CFD Predictions of High Enthalpy Shocks in Nitrogen". In: *AIAA Aviation 2019 Forum*, page 3078.

COLEMAN, H. W. and STEELE, W. G. (2018). *Experimentation, validation, and uncertainty analysis for engineers*. John Wiley & Sons.

COLLEN, P. L. and DOHERTY, L. J. (2018). *Aluminium Shock Tube Hydraulic Pressure Test: Stress Analysis*. Technical report T6-TR-2017-01. University of Oxford.

COLLEN, P., DOHERTY, L. J., SUBIAH, S. D., SOPEK, T., JAHN, I., GILDFIND, D., PENTY GERAETS, R., GOLLAN, R., HAMBIDGE, C., MORGAN, R., et al. (2021). "Development and commissioning of the T6 Stalker Tunnel". *Experiments in Fluids* 62.11, pages 1–24.

COLLEN, P. L., DOHERTY, L. J., and MCGILVRAY, M. (2019). "Measurements of radiating hypervelocity air shock layers in the T6 Free-Piston Driven Shock Tube". In: *International*

Conference on Flight Vehicles, Aerothermodynamics and Re-entry Missions & Engineering. ESA Conference Bureau.

CRUDEN, B. (May 2011). "Absolute radiation measurement during planetary entry in the NASA Ames Electric Arc Shock Tube facility". In: volume 1333. DOI: 10.1063/1.3562792.

— (2012a). "Radiance measurement for low density Mars entry". In: *43rd AIAA Thermophysics Conference*, page 2742.

CRUDEN, B., MARTINEZ, R., GRINSTEAD, J., and OLEJNICZAK, J. (2009). "Simultaneous vacuum-ultraviolet through near-IR absolute radiation measurement with spatiotemporal resolution in an electric arc shock tube". In: *41st AIAA Thermophysics Conference*, page 4240.

CRUDEN, B. A., BRANDIS, A. M., and PRABHU, D. K. (2014). "Measurement and characterization of mid-wave infrared radiation in CO2 shocks". In: *11th AIAA/ASME Joint Thermophysics and Heat Transfer Conference*, page 2962.

CRUDEN, B. A., BRANDIS, A. M., WHITE, T. R., and BOSE, D. (2015). "Radiative heating for MSL entry: Verification of simulations from ground test to flight data". In: *53rd AIAA Aerospace Sciences Meeting*.

CRUDEN, B. A. (2012b). "Electron density measurement in reentry shocks for lunar return". *Journal of Thermophysics and Heat Transfer* 26.2, pages 222–230.

— (2014). *Absolute radiation measurements in Earth and Mars entry conditions*. Technical report STO-AVT-218-VKI. NATO.

— (2017). *Electric Arc Shock Tube (EAST) Test Data*. URL: https://data.nasa.gov/docs/datasets/aerothermodynamics/EAST/index.html (visited on May 19, 2021).

CRUDEN, B. A. and BOGDANOFF, D. W. (2017). "Shock radiation tests for Saturn and Uranus entry probes". *Journal of Spacecraft and Rockets* 54.6, pages 1246–1257.

CRUDEN, B. A. and BRANDIS, A. M. (2014). "Updates to the NEQAIR radiation solver". In: European Space Agency St. Andrews, UK.

— (2017). "Measurement of radiative non-equilibrium for air shocks between 7-9 km/s". In: *47th AIAA Thermophysics Conference*, page 4535.

— (2019). "Revised shock layer radiation modeling for air". In: *8th International Workshop on Radiation of High Temperature Gases for Space Missions*.

— (2020). "Measurement of radiative nonequilibrium for air shocks between 7 and 9 km/s". *Journal of Thermophysics and Heat Transfer* 34.1, pages 154–180.

CRUDEN, B. A., BRANDIS, A. M., and JOHNSTON, C. O. (2018). "Development of a Radiative Heating Margin Policy for Lunar Return Missions". *Journal of Thermophysics and Heat Transfer* 32.2, pages 303–315.

CRUDEN, B. A., PRABHU, D., and MARTINEZ, R. (2012). "Absolute radiation measurement in Venus and Mars entry conditions". *Journal of Spacecraft and Rockets* 49.6, pages 1069–1079.

CRUDEN, B. A., TANG, C. Y., OLEJNICZAK, J., AMAR, A. J., and TANNO, H. (2021). "Characterization of radiative heating anomaly in high enthalpy shock tunnels". In: *AIAA Scitech 2021 Forum*, page 0103.

DANEHY, P. M., BATHEL, B. F., JOHANSEN, C. T., WINTER, M., O'BYRNE, S., and CUTLER, A. D. (2013). "Hypersonic Nonequilibrium Flows: Fundamentals and Recent Advances". In: edited by E. JOSYULA. AIAA. Chapter Molecular-based optical diagnostics for hypersonic nonequilibrium flows, pages 343–470.

DAVIES, W. and BERNSTEIN, L. (1969). "Heat transfer and transition to turbulence in the shock-induced boundary layer on a semi-infinite flat plate". *Journal of Fluid Mechanics* 36.1, pages 87–112.

DE CROMBRUGGHE, G., GILDFIND, D., ZANDER, F., MCINTYRE, T., and MORGAN, R. (2014). "Design of test flows to investigate binary scaling in high enthalpy CO2-N2 mixtures". In: *Proceedings of the 19th Australasian Fluid Mechanics Conference, AFMC 2014*. RMIT University, pages 325–1.

DILLMAN, R. and CORLISS, J. (2008). "Overview of the Mars Sample Return Earth Entry Vehicle". In: *Sixth International Planetary Probe Workshop*.

DOHERTY, L. J. and MCGILVRAY, M. (2018). *PLC Design Brief for the T6 Stalker Tunnel and High Density Tunnel*. Technical report HYP-TR-2015-01. University of Oxford.

DOHERTY, L. J., SMART, M. K., and MEE, D. J. (2015). "Experimental Testing of an Airframe-Integrated Three-Dimensional Scramjet at Mach 10". *AIAA Journal* 53.11, pages 3196–3207. DOI: 10.2514/1.J053785.

DOOLABH, A. (2016). "A Concept Study for a Piston Driven sCO2 Turbine Test Facility". Dissertation. University of Queensland.

DOOLAN, C. and JACOBS, P. (1996). "Modeling mass entrainment in a quasi-one-dimensional shock tube code". *AIAA Journal* 34.6, pages 1291–1293.

DREIER, C. (2020). *The cost of Perseverance, in context*. URL: https://www.planetary.org/articles/cost-of-perseverance-in-context (visited on June 7, 2021).

DUFF, R. E. (1959). "Shock-tube performance at low initial pressure". *The Physics of Fluids* 2.2, pages 207–216.

DUFRENE, A., MACLEAN, M., and HOLDEN, M. (2012). "Development of microwave plasma diagnostics for expansion tunnel characterization". In: *50th AIAA Aerospace Sciences Meeting including the New Horizons Forum and Aerospace Exposition*, page 369.

DUFRENE, A., SHARMA, M., and AUSTIN, J. (2007). "Design and characterization of a hypervelocity expansion tube facility". *Journal of Propulsion and Power* 23.6, pages 1185–1193.

DUSSAULT, D. and HOESS, P. (2004). "Noise performance comparison of ICCD with CCD and EMCCD cameras". In: *Infrared Systems and Photoelectronic Technology*. Volume 5563. International Society for Optics and Photonics, pages 195–204.

EBERHART, M. and LOEHLE, S. (2019). "Light-Field Imaging for Plasma Wind-Tunnel Application". *Journal of Thermophysics and Heat Transfer* 33.2, pages 407–415.

EICHMANN, T. N., MCINTYRE, T. J., BISHOP, A. I., VAKATA, S., and RUBINSZTEIN-DUNLOP, H. (2007). "Three-dimensional effects on line-of-sight visualization

measurements of supersonic and hypersonic flow over cylinders". *Shock waves* 16.4-5, pages 299–307.

ERDMAN, P. W., ZIPF, E. C., ESPY, P., HOWLETT, C., LEVIN, D. A., LODA, R., COLLINS, R. J., and CANDLER, G. V. (1993). "Flight measurements of low-velocity bow shock ultraviolet radiation". *Journal of Thermophysics and Heat Transfer* 7.1, pages 37–41.

ERDOS, J., CALLEJA, J., and TAMAGNO, J. (1994). "Increase in the hypervelocity test envelope of the HYPULSE shock-expansion tube", page 2524.

ESTEC CONCURRENT DESIGN FACILITY (2019). *A Mission to the Ice Giants – Neptune and Uranus*. Technical report. ESA.

FAHY, E. (2016). "Superorbital Re-entry Shock Layers: Flight and Laboratory Comparisons". PhD thesis. University of Queensland.

FAHY, E., BUTTSWORTH, D., GOLLAN, R., JACOBS, P., and MORGAN, R. G. (2016). "Experimental and computational fluid dynamics studies of superorbital Earth re-entry".

FAY, J. A. and RIDDELL, F. R. (1958). "Theory of stagnation point heat transfer in dissociated air". *Journal of the Aerospace Sciences* 25.2, pages 73–85.

FLETCHER, D. G. (2004). "Fundamentals of Hypersonic Flow - Aerothermodynamics". *Lecture Series on Critical Technologies for Hypersonic Vehicle Development, Von Karman Institute, Rhode-St-Genise, Belgium*, pages 10–14.

FORTUNE BUSINESS INSIGHTS (2020). *Space Launch Services Market*. URL: `https://www.fortunebusinessinsights.com/industry-reports/space-launch-services-market-101931` (visited on May 17, 2021).

FUJITA, K., SUZUKI, T., TAKAYANAGI, H., OZAWA, T., NOMURA, S., TAKIZAWA, N., MATSUYAMA, S., LEMAL, A., and MIZUNO, M. (2017). "Research on shock-induced aerothermodynamics for future planetary explorations". In: *International Symposium on Shock Waves*. Springer, pages 57–64.

FUJITA, K., SATO, S., ABE, T., and EBINUMA, Y. (2002). "Experimental investigation of air radiation from behind a strong shock wave". *Journal of Thermophysics and Heat Transfer* 16.1, pages 77–82.

GAZARIK, M. J., WRIGHT, M. J., LITTLE, A., CHEATWOOD, F. M., HERATH, J. A., MUNK, M. M., NOVAK, F. J., and MARTINEZ, E. R. (2008). "Overview of the MEDLI Project".

GESSMAN, R. J. (2001). "An experimental investigation of the effects of chemical and ionizational nonequilibrium in recombining atmospheric pressure air plasmas". PhD thesis. Stanford University.

GIGOSOS, M. A. and CARDEÑOSO, V. (1996). "New plasma diagnosis tables of hydrogen Stark broadening including ion dynamics". *Journal of Physics B: Atomic, Molecular and Optical Physics* 29.20, page 4795.

GILDFIND, D. E. (2012). "Development of high total pressure scramjet flow conditions using the X2 expansion tube". PhD Thesis. University of Queensland.

GILDFIND, D. E., HINES, T., JACOBS, P. A., STENNETT, S., and DIMITRIJEVIC, I. (2019). "Use of acceleration and optical waypoint measurements to estimate piston trajectory in an impulse facility". *Shock Waves* 29.6, pages 873–899.

GILDFIND, D. E., JACOBS, P. A., and MORGAN, R. G. (2013). "Vibration Isolation in a free-piston driven expansion tube facility". *Shock Waves* 23, pages 431–438.

GILDFIND, D. E., JAMES, C. M., TONIATO, P., and MORGAN, R. G. (2015). "Performance considerations for expansion tube operation with a shock-heated secondary driver". *Journal of Fluid Mechanics* 777, pages 364–407.

GILDFIND, D. E., MORGAN, R. G., and JACOBS, P. A. (2016). "Expansion tubes in Australia". In: *Experimental Methods of Shock Wave Research*. Springer, pages 399–431.

GILDFIND, D., JACOBS, P., MORGAN, R., CHAN, W., and GOLLAN, R. (2018). "Scramjet test flow reconstruction for a large-scale expansion tube, Part 2: axisymmetric CFD analysis". *Shock Waves* 28.4, pages 899–918.

GNOFFO, P. A. (1999). "Planetary-entry gas dynamics". *Annual Review of Fluid Mechanics* 31.1, pages 459–494.

— (1989). *Conservation equations and physical models for hypersonic air flows in thermal and chemical nonequilibrium*. Volume 2867. National Aeronautics and Space Administration.

GOOZEE, R. J. (2003). "Simulation of a complete shock tunnel with parallel computer codes". PhD thesis. The University of Queensland.

GOOZÉE, R. J., JACOBS, P. A., and BUTTSWORTH, D. R. (2006). "Simulation of a complete reflected shock tunnel showing a vortex mechanism for flow contamination". *Shock Waves* 15.3-4, pages 165–176.

GORDON, S. and MCBRIDE, B. J. (Oct. 1994). *Computer Program for Calculation of Complex Chemical Equilibrium Compositions and Applications: I. Analysis*. NASA Reference Report NASA RP-1311. NASA Lewis Research Center, Cleveland, OH.

GOULARD, R. (1961). "The coupling of radiation and convection in detached shock layers". *Journal of Quantitative Spectroscopy and Radiative Transfer* 1.3-4, pages 249–257.

GREENBERG, R. B., CRUDEN, B. A., GRINSTEAD, J. H., and YEUNG, D. (2009). "Collection optics for imaging spectroscopy of an electric arc shock tube". In: *Novel Optical Systems Design and Optimization XII*. International Society for Optics and Photonics.

GRIEM, H. R. (2005). *Principles of plasma spectroscopy*. 2. Cambridge University Press.

GRIMALDI, C., MCGUIRE, S., TIBÈRE-INGLESSE, A. C., and LAUX, C. O. (2021). "Infrared radiation measurements of a recombining CO2 plasma at atmospheric pressure". In: *AIAA Scitech 2021 Forum*, page 0104.

GRINSTEAD, J. H., WILDER, M. C., REDA, D. C., CORNELISON, C. J., CRUDEN, B. A., and BOGDANOFF, D. W. (2010). *Shock tube and ballistic range facilities at NASA Ames Research Center*. Technical report. NATO RTO-EN-AVT-186.

GU, S. (2018). "Mars entry afterbody radiative heating: an experimental study of nonequilibrium CO2 expanding flow". PhD thesis. University of Queensland.

GÜLHAN, A., THIELE, T., SIEBE, F., KRONEN, R., and SCHLEUTKER, T. (2019). "Aerothermal measurements from the ExoMars Schiaparelli capsule entry". *Journal of Spacecraft and Rockets* 56.1, pages 68–81.

GUPTA, R. N., LEE, K. P., THOMPSON, R. A., and YOS, J. M. (1989). "A review of reaction rates and thermodynamic and transport properties for the 11-species air model for chemical and thermal non-equilibrium calculations to 30000 K". *NASA Technical Memorandum* 101, page 528.

HANNEMANN, K., ITOH, K., MEE, D. J., and HORNUNG, H. G. (2016). "Free Piston Shock Tunnels HEG, HIEST, T4 and T5". In: *Experimental Methods of Shock Wave Research*. Springer, pages 181–264.

HANNEMANN, K., SCHRAMM, J. M., WAGNER, A., KARL, S., and HANNEMANN, V. (2010). *A Closely Coupled Experimental and Numerical Approach for Hypersonic and High Enthalpy Flow Investigations Utilising the HEG Shock Tunnel and the DLR TAU Code*. Technical report. German Aerospace Centre Braunschweig.

HANSON, R. K. and DAVIDSON, D. F. (2014). "Recent advances in laser absorption and shock tube methods for studies of combustion chemistry". *Progress in Energy and Combustion Science* 44, pages 103–114.

HAYNE, M. J. (2004). "Hypervelocity flow over rearward-facing steps". PhD thesis. University of Queensland.

HAYNE, M. J., MEE, D. J., GAI, S. L., and MCINTYRE, T. J. (2007). "Boundary layers on a flat plate at sub-and superorbital speeds". *Journal of Thermophysics and Heat Transfer* 21.4, pages 772–779.

HERMANN, T., LÖHLE, S., ZANDER, F., and FASOULAS, S. (2017). "Measurement of the aerothermodynamic state in a high enthalpy plasma wind-tunnel flow". *Journal of Quantitative Spectroscopy and Radiative Transfer* 201, pages 216–225.

HERMANN, T., LÖHLE, S., ZANDER, F., FULGE, H., and FASOULAS, S. (2016). "Characterization of a reentry plasma wind-tunnel flow with vacuum-ultraviolet to near-infrared spectroscopy". *Journal of Thermophysics and Heat Transfer* 30.3, pages 673–688.

HOLDEN, M. S., WADHAMS, T. P., and MACLEAN, M. (2008). "Experimental Studies in the LENS Supersonic and Hypersonic Tunnels for Hypervelocity Vehicle Performance and Code Validation". In: *15th AIAA International Space Planes and Hypersonic Systems and Technologies Conference*.

HOLLIS, B. R. (2012). "Blunt-body entry vehicle aerotherodynamics: Transition and turbulent heating". *Journal of Spacecraft and Rockets* 49.3, pages 435–449.

HOLLIS, B. R. and PRABHU, D. K. (2013). "Assessment of laminar, convective aeroheating prediction uncertainties for Mars-entry vehicles". *Journal of Spacecraft and Rockets* 50.1, pages 56–68.

HOOKER, W. J. (1961). "Testing Time and Contact-Zone Phenomena in Shock-Tube Flows". *The Physics of Fluids* 4.12, pages 1451–1463.

HORNUNG, H. (1990). "Role and techniques of ground testing for simulation of flows up to orbital speed". In: *16th Aerodynamic Ground Testing Conference*, page 1377.

HORNUNG, H., STURTEVANT, B., BELANGER, J., SANDERSON, S., BROUILLETTE, M., and JENKINS, M. (1992). "Performance data of the new free-piston shock tunnel T5 at GALCIT". In: *Shock Waves*. Springer, pages 603–610.

HORNUNG, H. G. (2010). *Ground testing for hypervelocity flow, capabilities and limitations*. Technical report. California Inst of Tech Pasadena Graduate Aerospace Labs.

HURLE, I. R., RUSSO, A. L., and HALL, J. G. (1964). "Spectroscopic studies of vibrational nonequilibrium in supersonic nozzle flows". *The Journal of Chemical Physics* 40.8, pages 2076–2089.

ITOH, K., UEDA, S., KOMURO, T., SATO, K., TAKAHASHI, M., MIYAJIMA, H., TANNO, H., and MURAMOTO, H. (1998). "Improvement of a Free Piston Driver for a High-Enthalpy Shock Tunnel". *Shock Waves* 8.4, pages 215–233.

ITOH, K., UEDA, S., KOMURO, T., SATO, K., TANNO, H., and TAKAHASHI, M. (1999). "Hypervelocity aerothermodynamic and propulsion research using a high enthalpy shock tunnel HIEST". In: *9th International Space Planes and Hypersonic Systems and Technologies Conference*, page 4960.

JACOBS, C. (2011a). "Radiation in low density hypervelocity flows". PhD thesis. University of Queensland.

JACOBS, C., MCINTYRE, T., MORGAN, R., BRANDIS, A., and LAUX, C. (2015). "Radiative heat transfer measurements in low-density Titan atmospheres". *Journal of Thermophysics and Heat Transfer* 29.4, pages 835–844.

JACOBS, P. A. (2011b). *A microcontroller-based delay generator for predicting shock arrival in the X2 expansion tube*. Technical report 2011/05. University of Queensland.

JACOBS, P., GOLLAN, R., POTTER, D., ZANDER, F., GILDFIND, D., BLYTON, P., CHAN, W., and DOHERTY, L. (2011). *Estimation of high-enthalpy flow conditions for simple shock and expansion processes using the ESTCj program and library*. Technical Report. University of Queensland.

JACOBS, P. and GOLLAN, R. (2016). "Implementation of a compressible-flow simulation code in the D programming language". *Applied Mechanics and Materials* 846, pages 54–60.

JACOBS, P. A. (Nov. 1998). *Shock Tube Modelling with L1d*. Research Report 13/1998. Brisbane, Australia: The University of Queensland, Department of Mechanical Engineering.

JAMES, C. M., COX, D., KOMONEN, A., BARLTROP, L., WIKNER, D. R., MCINTYRE, T. J., et al. (2019a). "Detecting shock arrival in expansion tubes and shock tunnels using high frequency photodiodes". In: *APISAT 2019: Asia Pacific International Symposium on Aerospace Technology*, page 584.

JAMES, C. M., BIRCH, B., SMITH, D. R., CULLEN, T. G., MILLARD, T., VELLA, S., LIU, Y., MORGAN, R. G., STERN, N., and BUTTSWORTH, D. (2019b). "Testing of Ultra Fast Response, Durable Co-axial Thermocouples for High Enthalpy Impulse Facilities". In: *AIAA Aviation 2019 Forum*, page 3007.

JAMES, C. M., CULLEN, T. G., WEI, H., LEWIS, S. W., GU, S., MORGAN, R. G., and MCINTYRE, T. J. (2018a). "Improved test time evaluation in an expansion tube". *Experiments in Fluids* 59.5, page 87.

JAMES, C. M. (2019). "Using a simplified Canny edge detector to detect shock arrival in expansion tubes and shock tunnels". In: *Proceedings of the 32nd International Symposium on Shock Waves*.

JAMES, C., GILDFIND, D., LEWIS, S., MORGAN, R., and ZANDER, F. (2018b). "Implementation of a state-to-state analytical framework for the calculation of expansion tube flow properties". *Shock Waves* 28.2, pages 349–377.

JOHNSTON, C., BRANDIS, A., and SUTTON, K. (2012). "Shock layer radiation modeling and uncertainty for Mars entry". In: *43rd AIAA Thermophysics Conference*.

JOHNSTON, C. O. and BRANDIS, A. M. (2015a). "Aerothermodynamic Characteristics of 16-22 km/s Earth Entry". In: *45th AIAA Thermophysics Conference*, page 3110.

— (2015b). "Features of afterbody radiative heating for Earth entry". *Journal of Spacecraft and Rockets* 52.1, pages 105–119.

JOHNSTON, C. O. (2021). "Evaluating Shock-Tube Informed Biases for Shock-Layer Radiative Heating Simulations". *Journal of Thermophysics and Heat Transfer* 35.2, pages 349–361.

JOHNSTON, C. O., GNOFFO, P. A., and SUTTON, K. (2009). "Influence of ablation on radiative heating for Earth entry". *Journal of Spacecraft and Rockets* 46.3, pages 481–491.

JOHNSTON, C. O., MAZAHERI, A., GNOFFO, P., KLEB, B., and BOSE, D. (2013). "Radiative heating uncertainty for hyperbolic Earth entry, Part 1: Flight simulation modeling and uncertainty". *Journal of Spacecraft and Rockets* 50.1, pages 19–38.

JOHNSTON, C. O., WEST, T. K., and BRANDIS, A. M. (2019). "Features of afterbody radiative heating for Titan entry". In: *AIAA Aviation 2019 Forum*, page 3010.

KAMEL, M., MORRIS, C., THURBER, M., WEHE, S., and HANSON, R. (1995). "New expansion tube facility for the investigation of hypersonic reactive flow". In: *33rd Aerospace Sciences Meeting and Exhibit*, page 233.

KIM, I. and PARK, G. (2019). "Experimental study of oxygen catalytic recombination on a smooth surface in a shock tube". *Applied Thermal Engineering* 156, pages 678–691.

KLICHE, D., MUNDT, C., and HIRSCHEL, E. H. (2011). "The hypersonic Mach number independence principle in the case of viscous flow". *Shock Waves* 21.4, pages 307–314.

KOLESNIKOV, A. F. (1999). *Extrapolation from high enthalpy tests to flight based on the concept of local heat transfer simulation*. Technical report Measurement Techniques for High Enthalpy and Plasma Flows. VKI.

KOTOV, D. V., YEE, H. C., PANESI, M., PRABHU, D. K., and WRAY, A. A. (2014). "Computational challenges for simulations related to the NASA electric arc shock tube (EAST) experiments". *Journal of Computational Physics* 269, pages 215–233.

KRAMIDA, A., RALCHENKO, Y., READER, J., and NIST ASD TEAM (2020). *NIST Atomic Spectra Database (ver. 5.8)*. URL: `https://physics.nist.gov/asd` (visited on May 23, 2021).

KRISHNA, Y. et al. (2016). "Tunable diode laser absorption spectroscopy as a flow diagnostic Tool: a review". *Journal of the Indian Institute of Science* 96.1, pages 17–28.

KURTZ, J., AIZENGENDLER, M., KRISHNA, Y., WALSH, P., and O'BYRNE, S. B. (2015). "Flight test of a rugged scramjet-inlet temperature and velocity sensor". In: *53rd AIAA Aerospace Sciences Meeting*, page 0110.

LAUX, C. O., SPENCE, T. G., KRUGER, C. H., and ZARE, R. N. (2003). "Optical diagnostics of atmospheric pressure air plasmas". *Plasma Sources Science and Technology* 12.2, page 125.

LAUX, C. O. (1993). "Optical diagnostics and radiative emission of air plasmas". PhD thesis. Stanford university.

LE PAGE, L. M., BARRETT, M., O'BYRNE, S., and GAI, S. L. (2020). "Laser-induced fluorescence velocimetry for a hypersonic leading-edge separation". *Physics of Fluids* 32.3, page 036103.

LEIBOWITZ, M. (2020). "Hypervelocity Shock Tunnel Studies of Blunt Body Aerothermodynamics in Carbon Dioxide for Mars Entry". PhD thesis. California Institute of Technology.

LEMAL, A., JACOBS, C. M., PERRIN, M.-Y., LAUX, C. O., TRAN, P., and RAYNAUD, E. (2016). "Prediction of nonequilibrium air plasma radiation behind a shock wave". *Journal of Thermophysics and Heat Transfer* 30.1, pages 197–210.

LEVIN, D. A. (2014). "Hypersonic Nonequilibrium Flows: Fundamentals and Recent Advances". In: edited by E. JOSYULA. AIAA. Chapter Radiation from Hypersonic Bodies—A Window on Non-Equilibrium Processes, pages 159–201.

LEWIS, S. (2017). "Laminar Mirels Solver (python script)". XLabs Shot Analysis Repository, Centre for Hypersonics, University of Queensland.

LEWIS, S. W., MORGAN, R. G., MCINTYRE, T. J., ALBA, C. R., and GREENDYKE, R. B. (2016). "Expansion tunnel experiments of earth reentry flow with surface ablation". *Journal of Spacecraft and Rockets* 53.5, pages 887–899.

LEYLAND, P., MCINTYRE, T., MORGAN, R., JACOBS, P., ZANDER, F., SHEIKH, U., EICHMANN, T., FAHY, E., JOSHI, O., DUFFA, G., et al. (2013). "Radiation-ablation coupling for capsule reentry heating via simulation and expansion tube investigations". In: *Proceedings of the 5th European Conference for Aeronautics and Space Sciences (EUCASS)*. CONF.

LIGHT, G. C. (1973). "Test gas properties behind a decelerating shock wave in a shock tube". *The Physics of Fluids* 16.5, pages 624–628.

LIN, X., YU, X. L., LI, F., ZHANG, S. H., XIN, J. G., and CHANG, X. Y. (2013). "CO concentration and temperature measurements in a shock tube for Martian mixtures by coupling OES and TDLAS". *Applied Physics B* 110.3, pages 401–409.

LINO DA SILVA, M. and BECK, J. (2011). "Contribution of CO2 IR radiation to Martian entries radiative wall fluxes". In: *49th AIAA Aerospace sciences meeting including the new horizons forum and aerospace exposition*, page 135.

LIU, Z., HUNT, W., VAUGHAN, M., HOSTETLER, C., MCGILL, M., POWELL, K., WINKER, D., and HU, Y. (2006). "Estimating random errors due to shot noise in backscatter lidar observations". *Applied optics* 45.18, pages 4437–4447.

LOEHLE, S., HERMANN, T., and ZANDER, F. (2018). "Experimental assessment of the performance of ablative heat shield materials from plasma wind tunnel testing". *CEAS Space journal* 10.2, pages 203–211.

LOEHLE, S., FASOULAS, S., HERDRICH, G. H., HERMANN, T. A., MASSUTI-BALLESTER, B., MEINDL, A., PAGAN, A. S., and ZANDER, F. (2016a). "The plasma wind tunnels at the institute of space systems: current status and challenges". In: *32nd AIAA Aerodynamic Measurement Technology and Ground Testing Conference*, page 3201.

LOEHLE, S., HERMANN, T. A., ZANDER, F., FULGE, H., and MARYNOWSKI, T. (2014). "Ablation radiation coupling investigation in Earth re-entry using plasma wind tunnel experiments". In: *11th AIAA/ASME Joint Thermophysics and Heat Transfer Conference*, page 2250.

LOEHLE, S., HERMANN, T. A., ZANDER, F., and MARYNOWSKI, T. (2016b). "Echelle spectroscopy for high enthalpy flow diagnostics", page 3691.

LÖHLE, S., VACHER, D., MENECIER, S., DUDECK, M., LIEBHARD, H., MARINOWSKI, T., HERDRICH, G., FASOULAS, S., and ANDRÉ, P. (2010). "Measurement campaigns on Mars entry plasmas using ICP torches. Characterization by emission spectroscopy and probes techniques". In: *Proceedings of the 4th International Workshop on Radiation and High Temperature Gases in Atmospheric Entry*.

LU, F. K. and MARREN, D. E., editors (2002). *Advanced Hypersonic Test Facilities*. Volume 198. Progress in Astronautics and Aeronautics. American Institute of Aeronautics and Astronautics.

MACDONALD, M. E., BRANDIS, A. M., and CRUDEN, B. A. (2018). "Temperature and CO number density measurements in shocked CO and CO2 via tunable diode laser absorption spectroscopy". In: *2018 Joint Thermophysics and Heat Transfer Conference*, page 4067.

MACDONALD, M. E., JACOBS, C. M., LAUX, C. O., ZANDER, F., and MORGAN, R. G. (2015). "Measurements of air plasma/ablator interactions in an inductively coupled plasma torch". *Journal of Thermophysics and Heat transfer* 29.1, pages 12–23.

MACLEAN, M., DUFRENE, A., and HOLDEN, M. (2013). "Spherical capsule heating in high enthalpy carbon dioxide in LENS-XX expansion tunnel". In: *51st AIAA Aerospace Sciences Meeting including the New Horizons Forum and Aerospace Exposition*, page 906.

MACLEAN, M. and HOLDEN, M. (2006). "Numerical assessment of data in catalytic and transitional flows for Martian entry". In: *9th AIAA/ASME Joint Thermophysics and Heat Transfer Conference*, page 2946.

MARSCHALL, J. and FLETCHER, D. G. (2010). "High-enthalpy test environments, flow modeling and in situ diagnostics for characterizing ultra-high temperature ceramics". *Journal of the European Ceramic Society* 30.11, pages 2323–2336.

MATSUI, M. and MORITA, R. (2021). "Development of high-sensitivity laser absorption spectroscopy system for number density measurement of atomic oxygen in optically thick plasma". *Transactions of the Japan Society for Aeronautical and Space Sciences, Aerospace Technology Japan* 19.3, pages 447–451.

MCGILVRAY, M., MORGAN, R., POTTER, D., BUTTSWORTH, D., and MCINTYRE, T. (2010a). *Shock tube measurements in the X2 facility of radiation from CEV re-entry conditions.* Technical report. University of Queensland.

MCGILVRAY, M., DOHERTY, L. J., MORGAN, R. G., GILDFIND, D., JACOBS, P., and IRELAND, P. (2015). "T6: The Oxford University Stalker Tunnel". In: *20th AIAA International Space Planes and Hypersonic Systems and Technologies Conference*.

MCGILVRAY, M., JACOBS, P. A., MORGAN, R. G., GOLLAN, R. J., and JACOBS, C. M. (2009). "Helmholtz resonance of pitot pressure measurements in impulsive hypersonic test facilities". *AIAA Journal* 47.10, pages 2430–2439.

MCGILVRAY, M., MORGAN, R. G., and JACOBS, P. A. (2010b). "Scramjet Experiments in an Expansion Tunnel: Evaluated Using a Quasi-Steady Analysis Technique". *AIAA Journal* 48.8, pages 1635–1646. DOI: 10.2514/1.J050024. eprint: https://doi.org/10.2514/1.J050024. URL: https://doi.org/10.2514/1.J050024.

MCGUIRE, S. D., TIBERE-INGLESSE, A. C., MARIOTTO, P. B., CRUDEN, B. A., and LAUX, C. O. (2020). "Measurements and modeling of CO 4th positive (A–X) radiation". *Journal of Quantitative Spectroscopy and Radiative Transfer* 245, page 106855.

MCINTYRE, T. J., EICHMANN, T. N., JACOBS, C., POTTER, D., MCGILVRAY, M., JACOBS, P., and MORGAN, R. (2011). "Shock tube and expansion tunnel measurements of high temperature radiating flows". In: *Proceedings of the 4th International Workshop on Radiation of High Temperature Gases in Atmospheric Entry*. Volume 689, page 37.

MILOS, F. S. (1997). "Galileo probe heat shield ablation experiment". *Journal of Spacecraft and Rockets* 34.6, pages 705–713.

MIRELS, H. (1963). "Test Time in Low-Pressure Shock Tubes". *The Physics of Fluids* 6.9, pages 1201–1214.

— (1964). "Shock tube test time limitation due to turbulent-wall boundary layer". *AIAA Journal* 2.1, pages 84–93.

MITCHELTREE, R. A. and GNOFFO, P. A. (1991). "Thermochemical nonequilibrium issues for Earth re-entry of Mars mission vehicles". *Journal of Spacecraft and Rockets* 28.5, pages 552–559.

MOFFAT, R. J. (1988). "Describing the uncertainties in experimental results". *Experimental thermal and fluid science* 1.1, pages 3–17.

MORGAN, R. G., MCINTYRE, T. J., JACOBS, P. A., BUTTSWORTH, D. R., MACROSSAN, M. N., GOLLAN, R. J., CAPRA, B. R., BRANDIS, A. M., POTTER, D., EICHMANN, T., et al. (2006). "Impulse facility simulation of hypervelocity radiating flows". *European Space Agency (Special Publication)* 629, pages 1–6.

MORGAN, R., MCINTYRE, T., BUTTSWORTH, D., JACOBS, P., POTTER, D., BRANDIS, A., GOLLAN, R., JACOBS, C., CAPRA, B., MCGILVARY, M., et al. (2008). "Impulse facilities for the simulation of hypersonic radiating flows". In: *38th Fluid Dynamics Conference and Exhibit*, page 4270.

MORGAN, R., MCINTYRE, T., and SHEIKH, U. (2011). "Simulation of Radiating Flows in Impulsive Facilities". In: *49th AIAA Aerospace Sciences Meeting including the New Horizons Forum and Aerospace Exposition*, page 250.

MORGAN STANLEY (2020). *Space: Investing in the Final Frontier*. URL: https://www.morganstanley.com/ideas/investing-in-space (visited on May 17, 2021).

MUNDT, C. (2016). "Development of the New Piston-Driven Shock-Tunnel HELM". In: *Experimental Methods of Shock Wave Research*. Springer, pages 265–283.

MUNDT, C., BOYCE, R. R., JACOBS, P. A., and HANNEMANN, K. (Mar. 2007). "Validation study of numerical simulations by comparison to measurements in piston-driven shock-tunnels". *Aerospace Science and Technology* 11.2-3, pages 100–109.

NASA (Oct. 1976). *U.S. Standard Atmosphere 1976*. Technical Memorandum X-74335. NASA.

— (2020). *Moon to Mars*. URL: https://www.nasa.gov/topics/moon-to-mars (visited on May 17, 2021).

NEELY, A. J., STALKER, R. J., and PAULL, A. (1991). "Hypervelocity Flows of Argon Produced in a Free Piston Driven Expansion Tube". In: *Shock Waves*. Volume 2. Sendai, Japan: Springer Verlag, pages 997–1004.

NELESSEN, A., SACKIER, C., CLARK, I., BRUGAROLAS, P., VILLAR, G., CHEN, A., STEHURA, A., OTERO, R., STILLEY, E., WAY, D., EDQUIST, K., MOHAN, S., GIOVINGO, C., and LEFLAND, M. (2019). "Mars 2020 Entry, Descent, and Landing System Overview". In: *2019 IEEE Aerospace Conference*, pages 1–20.

NICHOLS, R. H. and NELSON, C. (2004). "Wall function boundary conditions including heat transfer and compressibility". *AIAA journal* 42.6, pages 1107–1114.

NOEDING, P. and MARTINEZ SCHRAMM, J. (2014). "Numerical rebuilding of shock tube experiments in co2 flow under conditions relevant for Mars entry probes". In: *11th AIAA/ASME Joint Thermophysics and Heat Transfer Conference*, page 2549.

O'CALLAGHAN, J. (2021). *Three Spacecraft Are About To Arrive At Mars. Here's Everything You Need To Know About Them*. URL: https://www.forbes.com/sites/jonathanocallaghan/2021/02/08/three-spacecraft-are-about-to-arrive-at-mars-heres-everything-you-need-to-know-about-them/ (visited on May 17, 2021).

O'HAVER, T. C. (2021). *Interactive signal processing tools*. URL: https://terpconnect.umd.edu/~toh/spectrum/SignalProcessingTools.html (visited on May 22, 2021).

OLDFIELD, M. L. G. (2008). "Impulse response processing of transient heat transfer gauge signals". *Journal of turbomachinery* 130.2.

OLEJNICZAK, J., PRABHU, D., WRIGHT, M., TAKASHIMA, N., HOLLIS, B., SUTTON, K., and ZOBY, E. V. (2003). "An analysis of the radiative heating environment for aerocapture at Titan". In: *39th AIAA/ASME/SAE/ASEE Joint Propulsion Conference and Exhibit*.

OSWATITSCH, K. and RUEDINGER (1980). *Contributions to the Development of Gasdynamics*. Springer.

OXFORD INSTRUMENTS ANDOR (2021). *An Introduction to ICCD Cameras*. URL: https://andor.oxinst.com/learning/view/article/intensified-ccd-cameras (visited on June 2, 2021).

PALMER, G., PRABHU, D., BRANDIS, A., EICHMANN, T., POTTER, D., and MCINTYRE, T. (2011a). "Numerical simulation of radiation measurements taken in the X2 facility for Mars and Titan gas mixtures". In: *42nd AIAA Thermophysics Conference*, page 3768.

PALMER, G., PRABHU, D., TANG, C., and BROWN, J. (2011b). "Coupled fluids-radiation analysis of a high-mass Mars entry vehicle". In: *42nd AIAA Thermophysics Conference*, page 3495.

PALMER, R. A. (1999). "Measurement of heat transfer in superorbital flows". PhD thesis. University of Queensland.

PANNIER, E. and LAUX, C. O. (2019). "RADIS: A nonequilibrium line-by-line radiative code for CO2 and HITRAN-like database species". *Journal of Quantitative Spectroscopy and Radiative Transfer* 222, pages 12–25.

PARK, C. (1985). *Nonequilibrium Air Radiation (NEQAIR) Program: User's manual*. Technical report TM 86707. NASA.

— (1989). "Assessment of two-temperature kinetic model for ionizing air". *Journal of Thermophysics and Heat Transfer* 3.3, pages 233–244.

— (1990). *Nonequilibrium Hypersonic Aerothermodynamics*. Wiley, New York.

— (1993). "Review of chemical-kinetic problems of future NASA missions. I-Earth entries". *Journal of Thermophysics and Heat transfer* 7.3, pages 385–398.

PARKER, R., WAKEMAN, T., HOLDEN, M., and MACLEAN, M. (2006). "Measuring nitric oxide freestream concentration using quantum cascade lasers at CUBRC". In: *44th AIAA Aerospace Sciences Meeting and Exhibit*, page 926.

PAULL, A. and STALKER, R. J. (1992). "Acoustic waves in shock tunnels and expansion tubes". In: *Shock Waves*. Springer, pages 697–704.

PENTY GARAETS, R. (2019). "Development and testing of a diamond calorimeter heat transfer gauge". PhD thesis. University of Oxford.

PENTY GERAETS, R. T., MCGILVRAY, M., DOHERTY, L. J., MORGAN, R. G., JAMES, C. M., and BUTTSWORTH, D. R. (2020). "Development of a Fast-Response Diamond Calorimeter Heat Transfer Gauge". *Journal of Thermophysics and Heat Transfer* 34.1, pages 193–202. DOI: 10.2514/1.T5688.

POTTER, D. F. (2011). "Modelling of radiating shock layers for atmospheric entry at Earth and Mars". PhD thesis. University of Queensland.

POTTER, S. (2020). *NASA Moves Forward with Campaign to Return Mars Samples to Earth*. https://www.nasa.gov/press-release/nasa-moves-forward-with-campaign-to-return-mars-samples-to-earth. accessed 29/12/20. NASA.

RAICHE, G. and DRIVER, D. (2004). "Shock layer optical attenuation and emission spectroscopy measurements during arc jet testing with ablating models", page 825.

RAMJATAN, S., LANI, A., BOCCELLI, S., VAN HOVE, B., KARATEKIN, Ö., MAGIN, T., and THOEMEL, J. (2020). "Blackout analysis of Mars entry missions". *Journal of Fluid Mechanics* 904.

REED, T. B. (1961). "Induction-coupled plasma torch". *Journal of Applied Physics* 32.5, pages 821–824.

REYNIER, P. (2016). "Survey of high-enthalpy shock facilities in the perspective of radiation and chemical kinetics investigations". *Progress in Aerospace Sciences* 85, pages 1–32.

RICHARDSON, N. R. (1966). *Project FIRE Instrumentation for Radiative Heating and Related Measurements*. Technical report TN D-3646. NASA.

ROBERTS, G. T., MORGAN, R. G., and STALKER, R. J. (1995). "Influence of secondary diaphragm on flow quality in expansion tubes". In: *Shock Waves@ Marseille I*. Springer, pages 203–208.

ROSHKO, A. (1960). "On Flow Duration in Low-Pressure Shock Tubes". *The Physics of Fluids* 3.6, pages 835–842.

ROTHKOPF, E. and LOW, W. (1974). "Diaphragm opening process in shock tubes". *The Physics of Fluids* 17.6, pages 1169–1173.

ROY, S., GORD, J. R., and PATNAIK, A. K. (2010). "Recent advances in coherent anti-Stokes Raman scattering spectroscopy: Fundamental developments and applications in reacting flows". *Progress in Energy and Combustion Science* 36.2, pages 280–306.

SASOH, A., OHNISHI, Y., RAMJAUN, D., TAKAYAMA, K., OTSU, H., and ABE, T. (2001). "Effective test time evaluation in high-enthalpy expansion tube". *AIAA journal* 39.11, pages 2141–2147.

SATCHELL, M. (2021). "Numerical simulation and modeling of shock tube experiments". PhD thesis. University of Oxford.

SATCHELL, M., COLLEN, P., MCGILVRAY, M., and DI MARE, L. (2021a). "Numerical simulation of shock tubes using shock tracking in an overset formulation". *AIAA Journal*, pages 1–11.

SATCHELL, M., GLENN, A., COLLEN, P., PENTY-GERAETS, R., MCGILVRAY, M., and DI MARE, L. (2021b). "Analytical method of evaluating nonuniformities in shock tube flows: application". *AIAA Journal*, pages 1–8.

SATCHELL, M., MCGILVRAY, M., and DI MARE, L. (2021c). "Analytical method of evaluating nonuniformities in shock tube flows: theory and development". *AIAA Journal*, pages 1–15.

SENATE COMMITTEE ON COMMERCE, SCIENCE & TRANSPORTATION (2019). *Commerce Leaders Introduce the NASA Authorization Act of 2019*. URL: `https://www.commerce.senate.gov/2019/11/commerce-leaders-introduce-the-nasa-authorization-act-of-2019` (visited on May 17, 2021).

SHARMA, S. P. and PARK, C. (1990). "Operating characteristics of a 60-and 10-cm electric arc-driven shock tube". *Journal of Thermophysics and Heat Transfer* 4.3, pages 259–265.

SHARMA PRIYADARSHINI, M., MUNAFO, A., BRANDIS, A. M., CRUDEN, B. A., and PANESI, M. (2018). "One-dimensional modeling methodology for shock tubes: Application to the EAST facility". In: *2018 Joint Thermophysics and Heat Transfer Conference*, page 4181.

SHEIKH, U., MORGAN, R., ZANDER, F., EICHMANN, T., and MCINTYRE, T. (2012). "Vacuum ultraviolet emission spectroscopy system for superorbital re-entries". In: *18th AIAA/3AF*

International Space Planes and Hypersonic Systems and Technologies Conference, page 5807.

SIMPSON, C., CHANDLER, T., and BRIDGMAN, K. (1967). "Effect on shock trajectory of the opening time of diaphragms in a shock tube". *The Physics of Fluids* 10.9, pages 1894–1896.

SMITH, C. E. (1966). "The starting process in a hypersonic nozzle". *Journal of Fluid Mechanics* 24.4, pages 625–640.

SMITH, R. K., WAGNER, D. A., and CUNNINGHAM, J. (1998). "A survey of current and future plasma arc-heated test facilities for aerospace and commercial applications". In: *36th AIAA Aerospace Sciences Meeting and Exhibit*, page 146.

STALKER, R. J. (1967). "A study of the free-piston shock tunnel." *AIAA Journal* 5.12, pages 2160–2165.

STALKER, R. J. and MORGAN, R. G. (1988). "The University of Queensland free piston shock tunnel T-4: Initial operation and preliminary calibration". In: *Fourth National Space Engineering Symposium: Preprints of Papers*. Institution of Engineers, Australia, page 182.

STALKER, R. J. (1966). "The Free Piston Shock Tube". *Aeronautical Quarterly* 17, pages 351–370.

— (2006). "Modern Developments in Hypersonic Wind Tunnels". *Aeronautical Journal* 110.1103, pages 21–40.

STALKER, R. J., PAULL, A., MEE, D. J., MORGAN, R. G., and JACOBS, P. A. (Aug. 2005). "Scramjets and Shock Tunnels - The Queensland Experience". *Progress in Aerospace Sciences* 41.6, pages 471–513.

STALKER, R. (1972). "Development of a hypervelocity wind tunnel". *The Aeronautical Journal* 76.738, pages 374–384.

STALKER, R. and CRANE, K. (1978). "Driver gas contamination in a high-enthalpy reflected shock tunnel". *AIAA Journal* 16.3, pages 277–279.

STENNETT, S. J., GILDFIND, D. E., JACOBS, P. A., MORGAN, R. G., JAMES, C. M., TONIATO, P., et al. (2019). "The X3R reflected shock tunnel: A new, long-duration operating mode for the X3 expansion tube". In: *APISAT 2019: Asia Pacific International Symposium on Aerospace Technology*. Engineers Australia, page 1945.

STENNETT, S. J., GILDFIND, D., JACOBS, P., MORGAN, R., JAMES, C., and TONIATO, P. (2020). "The X3R Free-Piston Reflected Shock Tunnel: Australia's New Large-Scale, Long-Duration Hypersonic Testing Capability". In: *23rd AIAA International Space Planes and Hypersonic Systems and Technologies Conference*.

STENNETT, S. J., GILDFIND, D. E., JACOBS, P. A., and MORGAN, R. G. (2018). "Performance optimization of X3R: A new reflected shock tunnel mode for the X3 expansion tube". In: *2018 Aerodynamic Measurement Technology and Ground Testing Conference*.

SU, W., BRUNO, D., and BABOU, Y. (2018). "State-specific modeling of vibrational relaxation and nitric oxide formation in shock-heated air". *Journal of Thermophysics and Heat Transfer* 32.2, pages 337–352.

SUBIAH, S. D., COLLEN, P. L., DOHERTY, L. J., and MCGILVRAY, M. (2019). "Condition Development and Commissioning of the Oxford T6 Stalker Tunnel in Reflected Shock Tunnel

Mode". In: *International Conference on Flight Vehicles, Aerothermodynamics and Re-entry Missions & Engineering*.

SUTTON, K. and GRAVES, R. (1971). *A general stagnation-point convective heating equation for arbitrary gas mixtures*. Technical report TR R-736. NASA.

TAKAMA, Y. and SUZUKI, K. (2009). "Spectroscopic observation of translational-rotational nonequilibrium in low-density hydrogen plasma flow". *Journal of thermophysics and heat transfer* 23.3, pages 454–462.

TAKAYANAGI, H., LEMAL, A., NOMURA, S., and FUJITA, K. (2018). "Measurements of carbon dioxide nonequilibrium infrared radiation in shocked and expanded flows". *Journal of Thermophysics and Heat Transfer* 32.2, pages 483–494.

TAKAYANAGI, H., NOMURA, S., LEMAL, A., and FUJITA, K. (2017). "Measurements of Nonequilibrium Carbon Dioxide Infrared Radiation in an Exapnsion Tube". *AIAA* 1369.

TAKAYANAGI, H. and FUJITA, K. (2012). "Absolute radiation measurements behind strong shock wave in carbon dioxide flow for Mars aerocapture missions". In: *43rd AIAA Thermophysics Conference*, page 2744.

TAKAYANAGI, H., FUJITA, K., ISHIDA, H., YAMADA, K., and ABE, T. (2014). "Radiation intensity measurement in VUV wavelength region behind strong shock wave for future sample return missions". In: *11th AIAA/ASME Joint Thermophysics and Heat Transfer Conference*, page 2965.

TAKAYANAGI, H., NOMURA, S., and FUJITA, K. (2019). "Experimental radiation measurement from CO2 flow in shock tube and expansion tube". In: *International Conference on Flight Vehicles, Aerothermodynamics and Re-entry Missions & Engineering*.

TAMAGNO, J., BAKOS, R., PULSONETTI, M., and ERDOS, J. (1990). "Hypervelocity real gas capabilities of GASL's expansion tube (HYPULSE) facility". In: *16th Aerodynamic Ground Testing Conference*, page 1390.

TANNO, H., ITOH, K., KOMURO, T., and SATO, K. (2000). "Experimental Study on the Tuned Operation of a Free Piston Driver". *Shock Waves* 10.1, pages 1–7.

TANNO, H., KOMURO, T., LILLARD, R. P., and OLEJNICZAK, J. (2015). "Experimental study of high-enthalpy heat flux augmentation in shock tunnels". *Journal of Thermophysics and Heat Transfer* 29.4, pages 858–862.

TANNO, H., KOMURO, T., SATO, K., ITOH, K., ARAI, K., and YAMADA, K. (2016). "Basic characteristics of the free-piston driven expansion tube JAXA HEK-X". In: *32nd AIAA Aerodynamic Measurement Technology and Ground Testing Conference*.

TAUBER, M. E. and SUTTON, K. (1991). "Stagnation-point radiative heating relations for Earth and Mars entries". *Journal of Spacecraft and Rockets* 28.1, pages 40–42.

TAYLOR, R. L., CAMAC, M., and FEINBERG, R. M. (1967). "Measurements of vibration-vibration coupling in gas mixtures". 11.1, pages 49–65.

THORNE, A., LITZÉN, U., and JOHANSSON, S. (1999). *Spectrophysics: principles and applications*. Springer Science & Business Media.

TIBÈRE-INGLESSE, A. C., MCGUIRE, S. D., MARIOTTO, P., and LAUX, C. O. (2018). "Validation cases for recombining nitrogen and air plasmas". *Plasma Sources Science and Technology* 27.11, page 115010.

TOENNIES, J. P. and GREENE, E. F. (1957). "Dissociation Energies of Carbon Monoxide and Nitrogen from Reflected Shock Wave Studies". *The Journal of Chemical Physics* 26.3, pages 655–662.

TRIMPI, R. L. (1962). *A preliminary theoretical study of the expansion tube, a new device for producing high-enthalpy short-duration hypersonic gas flows*. Technical Report R-133. NASA.

TSAI, C.-Y., CHUE, R., NICHOLSON, C., and TYLL, J. (Jan. 2009). "Hypervelocity Capability of HyPulse Shock Tunnel for Radiative Heat Transfer Measurements at Lunar Reentries". In: *47th AIAA Aerospace Sciences Meeting*. ISBN: 978-1-60086-973-0. DOI: 10.2514/6.2009-1516.

VACHER, D., DUDECK, M., ANDRÉ, P., DA SILVA, M. L., FAURE, G., DUBOIS, M., HAMWI, A., MENECIER, S., and ROCHETTE, D. (2009). "Radiation from an ICP plasma torch in the near-UV to near-IR spectral region for a Titan-type N2-CH4 mixture". *Journal of technical physics* 50.3, pages 213–231.

WAGNER, A. (12–13 April 2018). "High Frequency Pressure Measurements in Shock Tunnels using Piezoelectric Transducers". In: *12th International Workshop on Shock Tube Technology*. Kakuda, Japan.

WALL, M. (2021). *China launches core module of new space station to orbit*. URL: https://www.space.com/china-launches-core-module-tianhe-space-station (visited on May 17, 2021).

WANG, Q., LI, J. W., LU, P., LI, J. P., ZHAO, W., and JIANG, Z. (2017). "Pressure and Heat Flux Calibration of the Long-test-duration Hypervelocity Detonation-driven Shock Tunnel". In: *21st AIAA International Space Planes and Hypersonics Technologies Conference*, page 2155.

WEI, H. (2017). "Air radiation in a superorbital expanding flow". PhD thesis. University of Queensland.

WEST IV, T. K., JOHNSTON, C. O., and HOSDER, S. (2017). "Uncertainty and sensitivity analysis of afterbody radiative heating predictions for Earth entry". *Journal of Thermophysics and Heat Transfer* 31.2, pages 294–306.

WHITE, D. R. (1958). "Influence of diaphragm opening time on shock-tube flows". *Journal of Fluid Mechanics* 4.6, pages 585–599.

WIESE, W. L., SMITH, M. W., and GLENNON, B. M. (1966). "Atomic transition probabilities. volume i. hydrogen through neon".

WILCOX, D. C. et al. (1998). *Turbulence modeling for CFD*. Volume 2. DCW industries La Canada, CA.

WILKE, C. R. (Apr. 1950). "A Viscosity Equation for Gas Mixtures". *The Journal of Chemical Physics* 18.4, pages 517–519.

WINDSOR, M. W., DAVIDSON, N., and TAYLOR, R. (1957). "Measurement of the vibrational relaxation time of CO behind a shock wave by infrared emission". *The Journal of Chemical Physics* 27.1, pages 315–316.

WINTER, M. W., TERRAZAS-SALINAS, I., HUI, F. C. L., WHITE, B., and TAUNK, J. S. (2019). "Measured Radiation Heat Flux to a Probe in a NASA Ames Arc Jet". *Journal of Thermophysics and Heat Transfer* 33.4, pages 1112–1126.

WITTLIFF, C. E. (1959). "The tailored-interface hypersonic shock tunnel". *Journal of the Aerospace Sciences* 26.4, pages 219–228.

WITZE, A. (2021). *Lift off! First flight on Mars launches new way to explore worlds*. URL: `https://www.nature.com/articles/d41586-021-00909-z` (visited on May 17, 2021).

WRIGHT, M., OLEJNICZAK, J., BROWN, J., HORNUNG, H., and EDQUIST, K. (2005). "Computational modeling of T5 laminar and turbulent heating data on blunt cones, part 2: Mars applications". In: *43rd AIAA Aerospace Sciences Meeting and Exhibit*, page 177.

YALIN, A. P., ZARE, R. N., LAUX, C., and KRUGER, C. H. (2002). "Temporally resolved cavity ring-downspectroscopy in a pulsed nitrogen plasma". *Appl. Phys. Lett.* 1408.81.

YAMADA, G., SUZUKI, T., TAKAYANAGI, H., and FUJITA, K. (2011). "Development of shock tube for ground testing reentry aerothermodynamics". *Transactions of the Japan Society for Aeronautical and Space Sciences* 54.183, pages 51–61.

YAMADA, G., TAKAYANAGI, H., SUZUKI, T., and FUJITA, K. (2012). "Shock layer radiation analysis using a hypervelocity shock tube (HVST)". *Transactions of the Japan Society for Aeronautical and Space Sciences* 55.1, pages 37–43.

YANES, N. J. and AUSTIN, J. M. (2019). "Nitric Oxide Spectroscopic Measurements in a Hypervelocity Stagnation Flow". In: *AIAA Scitech 2019 Forum*, page 0794.

ZANDER, F., GOLLAN, R. J., JACOBS, P. A., and MORGAN, R. G. (2014). "Hypervelocity shock standoff on spheres in air". *Shock Waves* 24.2, pages 171–178.

ZANDER, F., MARYNOWSKI, T., and LÖHLE, S. (2017). "High-Speed Imaging of High-Frequency Effects of a CO2 Plasma Flow". *Journal of Thermophysics and Heat Transfer* 31.2, pages 451–462.

ZOBY, E. V. and SULLIVAN, E. M. (1966). "Effects of corner radius on stagnation-point velocity gradients on blunt axisymmetric bodies". *Journal of Spacecraft and Rockets* 3.10, pages 1567–1567.